LUIZ GUSTAVO SOUSA VASCONCELLOS

ADVANCED COMPUTATIONAL FLUID DYNAMICS IN BLOODSTAIN PATTERN ANALYSIS: INVESTIGATING NON-NEWTONIAN PROPERTIES FOR FORENSIC APPLICATIONS

UNIVERSIDADE FEDERAL DE UBERLÂNDIA
FACULDADE DE ENGENHARIA MECÂNICA
PÓS-GRADUAÇÃO EM ENGENHARIA MECÂNICA
2024

LUIZ GUSTAVO SOUSA VASCONCELLOS

ADVANCED COMPUTATIONAL FLUID DYNAMICS IN BLOODSTAIN PATTERN ANALYSIS: INVESTIGATING NON-NEWTONIAN PROPERTIES FOR FORENSIC APPLICATIONS

Dissertation submitted to the Graduate Program in Mechanical Engineering at the Federal University of Uberlândia, as part of the requirements for the degree of Master in Mechanical Engineering.

Area of Concentration: Heat Transfer and Fluid Mechanics
Research Line: Computational Fluid Dynamics

Prof. Dr. Aristeu da Silveira Neto
Advisor

Prof. Dr. Daniel Dall'Onder dos Santos
Co-advisor

Prof. Dr. Gilmar Guimarães
Coordinator of the Graduate Program in Mechanical Engineering

Uberlândia, Minas Gerais
2024

Ficha Catalográfica Online do Sistema de Bibliotecas da UFU
com dados informados pelo(a) próprio(a) autor(a).

V331
2024

Vasconcellos, Luiz Gustavo Sousa, 1991-
Advanced Computational Fluid Dynamics in Bloodstain Pattern Analysis: Investigating Non-Newtonian Properties for Forensic Applications [recurso eletrônico] / Luiz Gustavo Sousa Vasconcellos. - 2024.

Orientador: Aristeu da Silveira Neto.
Coorientador: Daniel Dall'Onder dos Santos.
Dissertação (Mestrado) - Universidade Federal de Uberlândia, Pós-graduação em Engenharia Mecânica.
Modo de acesso: Internet.
Disponível em: http://doi.org/10.14393/ufu.di.2024.488
Inclui bibliografia.

1. Engenharia mecânica. I. Silveira Neto, Aristeu da , 1955-, (Orient.). II. Santos, Daniel Dall'Onder dos, 1986-, (Coorient.). III. Universidade Federal de Uberlândia. Pós-graduação em Engenharia Mecânica. IV. Título.

CDU: 621

Bibliotecários responsáveis pela estrutura de acordo com o AACR2:

Gizele Cristine Nunes do Couto - CRB6/2091
Nelson Marcos Ferreira - CRB6/3074

UNIVERSIDADE FEDERAL DE UBERLÂNDIA
Coordenação do Programa de Pós-Graduação em Engenharia Mecânica
Av. João Naves de Ávila, nº 2121, Bloco 1M, Sala 212 - Bairro Santa Mônica, Uberlândia-MG, CEP 38400-902
Telefone: (34) 3239-4282 - www.posmecanicaufu.com.br - secposmec@mecanica.ufu.br

ATA DE DEFESA - PÓS-GRADUAÇÃO

DEFENSE MINUTES - POSTGRADUATE

Graduate Program in:	Mechanical Engineering				
Defense of:	Academic Master's Dissertation, No. 647, PPGEM				
Date:	07/18/2024	Start time:	10:00 AM	End time:	2:00 AM
Student ID:	12222EMC003				
Student name:	Luiz Gustavo Sousa Vasconcellos				
Dissertation title:	ADVANCED COMPUTATIONAL FLUID DYNAMICS IN BLOODSTAIN PATTERN ANALYSIS: INVESTIGATING NON-NEWTONIAN PROPERTIES FOR FORENSIC APPLICATIONS				
Field of Concentration:	Heat Transfer and Fluid Mechanics				
Research Line:	Fluid Dynamics and Heat Transfer				
Linked Research Project:					

The Examination Committee, appointed by the Graduate Program in Mechanical Engineering Board, met via videoconference, composed of: Prof. Dr. João Marcelo Vedovotto - UFU; Prof. Dr. Paulo R. de Souza Mendes - PUC Rio; Prof. Dr. Daniel Attinger - USA; Prof. Dr. Aristeu da Silveira Neto - UFU, the candidate's advisor; and by Prof. Dr. Daniel Dall'Onder dos Santos - UFU, the candidate's co-advisor.

Commencing the proceedings, the chair, Dr. Aristeu da Silveira Neto, introduced the Examination Committee and the candidate, thanked the audience for their presence, and gave the floor to the student for the presentation of his work. The duration of the student's presentation and the time for questioning and response were in accordance with the Program's regulations.

Next, the chair granted the floor, in order, to the examiners, who proceeded to question the candidate. Upon conclusion of the questioning, which was conducted within the regulatory terms, the Committee, in a secret session, assigned the final result, considering the candidate: Passed

This defense is part of the necessary requirements for obtaining the Master’s degree.

The appropriate diploma will be issued after fulfilling the remaining requirements, in accordance with the Program's regulations, the pertinent legislation, and UFU's internal regulations.

There being no further business, the proceedings were concluded. This record was drafted, read, found to be in order, and signed by the Examination Committee.

Documento assinado eletronicamente por **Aristeu da Silveira Neto**, **Professor(a) do Magistério Superior**, em 18/07/2024, às 11:39, conforme horário oficial de Brasília, com fundamento no art. 6º, § 1º, do Decreto nº 8.539, de 8 de outubro de 2015.

Documento assinado eletronicamente por **Daniel Dall'Onder dos Santos**, **Professor(a) do Magistério Superior**, em 18/07/2024, às 11:41, conforme horário oficial de Brasília, com fundamento no art. 6º, § 1º, do Decreto nº 8.539, de 8 de outubro de 2015.

Documento assinado eletronicamente por **Daniel Etienne Attinger**, **Usuário Externo**, em 18/07/2024, às 11:46, conforme horário oficial de Brasília, com fundamento no art. 6º, § 1º, do Decreto nº 8.539, de 8 de outubro de 2015.

Documento assinado eletronicamente por **PAULO ROBERTO DE SOUZA MENDES**, **Usuário Externo**, em 18/07/2024, às 13:42, conforme horário oficial de Brasília, com fundamento no art. 6º, § 1º, do Decreto nº 8.539, de 8 de outubro de 2015.

Documento assinado eletronicamente por **João Marcelo Vedovotto**, **Professor(a) do Magistério Superior**, em 18/07/2024, às 13:52, conforme horário oficial de Brasília, com fundamento no art. 6º, § 1º, do Decreto nº 8.539, de 8 de outubro de 2015.

A autenticidade deste documento pode ser conferida no site https://www.sei.ufu.br/sei/controlador_externo.php?acao=documento_conferir&id_orgao_acesso_externo=0, informando o código verificador **5532220** e o código CRC **0F0C336F**.

Referência: Processo nº 23117.044547/2024-91 SEI nº 5532220

LUIZ GUSTAVO SOUSA VASCONCELLOS

ADVANCED COMPUTATIONAL FLUID DYNAMICS IN BLOODSTAIN PATTERN ANALYSIS: INVESTIGATING NON-NEWTONIAN PROPERTIES FOR FORENSIC APPLICATIONS

Approved Dissertation by the Graduate Program in Mechanical Engineering at the Federal University of Uberlândia.

Area of Concentration: Heat Transfer and Fluid Mechanics
Research Line: Computational Fluid Dynamics

Uberlândia, July 18, 2024.

Examination Committee:

Prof. Dr. Aristeu da Silveira Neto (UFU)
Advisor

Prof. Dr. Daniel Dall'Onder dos Santos (UFU)
Co-advisor

Prof. Dr. João Marcelo Vedovotto (UFU)
Internal member of the Examining Committee

Prof. Dr. Paulo R. de Souza Mendes (PUC-Rio)
External member of the Examining Committee

Prof. Dr. Daniel Attinger (Fellow, American Society of Mechanical Engineers)
External member of the Examining Committee

I dedicate this dissertation to my beloved wife, Monisa de Oliveira Vilela Vasconcellos, and our dear daughter, Manuela de Oliveira Vasconcellos.

Monisa, your courage and strength during the challenges we faced when moving to Uberlândia/MG, followed by the birth of our daughter Manuela, were truly inspiring. Your constant presence and unconditional support were the anchor that kept me steady throughout the entire process of my master's degree. Your dedication as a wife and mother is an endless source of admiration and gratitude.

Manuela, your arrival brought new light and joy into our days. Your contagious energy and your innocently and genuinely caring attitudes were a constant source of inspiration and motivation for me. You are our greatest gift and the reason why I strive to be the best father and human being possible.

To my esteemed advisor, Prof. Dr. Aristeu, I express my deep gratitude for your trust in my research project, even though it was so distinct from the conventional approaches of our laboratory. Your wise guidance and tireless support were instrumental to the success of this work.

I conclude this journey with a phrase that has long represented me: "A burning desire to be and to do is the starting point from which the dreamer must take off. Dreams are not born from indifference, laziness, or lack of ambition." (Napoleon Hill). May this work be just the beginning of many achievements inspired by the desire to make a difference.

With love, gratitude, and respect,
Luiz.

Acknowledgements

I sincerely thank the members of my advisory committee for their support and guidance throughout my research project: Dr. Aristeu da Silveira Neto, advisor, and Dr. Daniel Dall'Onder dos Santos, co-advisor.

To the professors who agreed to be part of the dissertation Examining Committee, contributing their extensive and valuable scientific knowledge: Dr. João Marcelo Vedovotto, Dr. Paulo R. de Souza Mendes and Dr. Daniel Attinger.

Additionally, I would like to acknowledge the support and valuable contributions of other professors, researchers and laboratory colleagues: Dr. Elie Luis Martínez Padilla, Dr. Pedro Henrique Augusto Vedovotto and M.Sc. João Emanuel Fermino Martini.

I am grateful to both the Federal University of Uberlândia/MG and the Computational Fluid Mechanics Laboratory (MFLab) for the essential resources and facilities for my work.

I am also immensely grateful to POLITEC - Official Forensic and Technical Identification of Mato Grosso, for granting me authorization for professional qualification licence.

My sincere thanks also go to my classmates, friends and family who provided emotional support and encouragement throughout my master's degree. I am especially grateful to Mrs. Vanilda and Mr. Luiz, my parents, Mr. Paulo Henrique, my brother, Mr. Iago Nonaka and Mr. Gabriel Sabino, M.Sc. candidates, M.Sc. João Emanuel Fermino Martini, and Dr. Pedro Henrique Augusto Vedovotto.

I thank the International Association of Bloodstain Pattern Analysts (IABPA) and the participants of the 40th Annual Conference of IABPA in Baltimore/MD, USA, for their intellectual contribution to my research.

The technical assistance of M.Sc. candidate Johnatas Teixera de Freitas and Dr. Millena Martins Villar was fundamental to the success of my project.

I cannot fail to express my gratitude to my originating agency, POLITEC, and all the colleagues, namely, who sacrificed for my professional growth:

- Official Criminal Experts
    - Adriano Mendes Pacheco
    - Ana Maria dos Anjos Xavier
    - Eduardo Pacheco e Souza da Silva
    - Fracisco Morais de Oliveira
    - Felipe Perinazzo Rambo
    - Geraldo Rambo

  - Gley Julio Pereira Soares
  - Henrique Mauro Rodrigues
  - Hudson de Sousa Guasti
  - Jacqueline Maciel Narvaes da Silva
  - Kairo Diego Araújo
  - Lenard Serrano
  - Maxsuel Alves de Souza
  - Nildeson Cândido da Silva
  - Rosemary de Souza Kanacilo
  - Tatiana de Souza Guasti Orlato
  - Waldemon Tadeu Victor Coelho

- Technical- administrative public agents:
  - Antônio Celso da Silva
  - Aurelino Duarte da Silva
  - César Martins dos Santos
  - David Cavalcante de Souza
  - Elizeu Moreira dos Santos
  - Éricka Christiane Meneghete Gaioto
  - João Inácio Dias
  - Jorge da Silva Caldeira
  - Cláudia Bastos Ferro
  - Liv de Oliveira Silva Cintra
  - Pedro Lopes Miranda
  - Romas Martins de Oliveira
  - Ivan Rodrigues de Lima

- POLITEC Management (for authorization to pursue the master's degree):
  - Rubens Sadao Okada - General Director
  - Mairo Fábio Camargo - Interiorization Director
  - Ariadne Nunes Ferreira de Matos - Regional Coordinator of Rondonópolis/MT
  - Rubens Pereira - Regional Coordinator of Rondonópolis/MT
  - Éder Jones da Silva - Criminalistics Manager

“Science does not build truth. Science builds knowledge.”
Unknown Author

VASCONCELLOS, L. G. S. **Dinâmica dos Fluidos Computacional Avançada na Análise de Padrões de Manchas de Sangue: Investigação das Propriedades Não Newtonianas para Aplicações Forenses**. 2024. 179f. Dissertação de Mestrado, Universidade Federal de Uberlândia, Uberlândia/MG, Brasil.

Resumo

Visando preencher uma lacuna significativa no entendimento científico, realizamos simulações de gotas de sangue humano e animal em queda livre e seu impacto em superfície sólida, explorando as propriedades não newtonianas do sangue. Os resultados revelaram que modelos constitutivos simples, como o power-law, são inadequados para contextos forenses devido a níveis de viscosidade não físicos em taxas de cisalhamento elevadas ou muito baixas. Comparações entre modelos mostraram variações substanciais na distribuição de viscosidade interna e na forma final das gotas, destacando a importância de modelos precisos para a análise forense. Este trabalho, embora não pioneiro, é um dos poucos no mundo a utilizar Dinâmica dos Fluidos Computacional (CFD) em Análise de Padrões de Manchas de Sangue (BPA), indicando um caminho promissor para a construção de um framework robusto para a interpretação de evidências de sangue. As simulações realizadas com o código MFSim posicionam esta pesquisa na vanguarda da mecânica dos fluidos forense, oferecendo novas ferramentas para a comunidade internacional de analistas de padrões de manchas de sangue e estabelecendo um caminho promissor para futuras investigações científicas.

Palavras-chave: Dinâmica dos Fluidos Computacional, Análise de Padrões de Manchas de Sangue, Fluidos não newtonianos, Método VoF

VASCONCELLOS, L. G. S. **Advanced Computational Fluid Dynamics in Bloodstain Pattern Analysis: Investigating Non-Newtonian Properties for Forensic Applications**. 2024. 179p. Master's Dissertation, Federal University of Uberlândia, Uberlândia/MG, Brazil.

Abstract

Aiming to fill a significant gap in scientific understanding, we conducted simulations of human and animal blood droplets in free fall and their impact on solid surfaces, exploring the non-Newtonian properties of blood. The results revealed that simple constitutive models, such as the power-law model, are inadequate for forensic contexts due to non-physical viscosity levels at high or very low shear rates. Comparisons between models showed substantial variations in internal viscosity distribution and the final shape of the droplets, highlighting the importance of accurate models for forensic analysis. This work, although not pioneering, is one of the few in the world to use Computational Fluid Dynamics (CFD) in Bloodstain Pattern Analysis (BPA), indicating a promising path towards constructing a robust framework for interpreting blood evidence. The simulations performed with the MFSim code position this research at the forefront of forensic fluid mechanics, offering new tools to the international community of bloodstain pattern analysts and establishing a promising path for future scientific investigations.

Keywords: Computational Fluid Dynamics, Bloodstain Pattern Analysis, Non-Newtonian Fluids, VoF Method

List of Figures

List of Tables

List of abbreviations and acronyms

	Scientific Terms
ACD	Acid Citrate Dextrose
AR	Aspect Ratio
BPA	Bloodstain Pattern Analysis
CFD	Computational Fluid Dynamics
CSF	Continuum Surface Force
CFL	Courant-Friedrichs-Lewy number
DNA	Deoxyribonucleic Acid
DNS	Direct Numerical Simulation
dpm	Discrete Phase Model
EDTA	Ethylenediaminetetraacetic Acid
FVM	Finite Volume Method
GNF	Generalized Newtonian Fluid
Hb	Hemoglobin
HCT	Hematocrit
IABPA	International Association of Bloodstain Pattern Analysts
IBM	Immersed Boundary Method
K-L	Non-identified meaning
l_{bot}	MFSim's base mesh
l_{top}	MFSim's finest mesh
MFSim	CFD simulation software from MFLab
ODE	Ordinary Differential Equation
RBC	Red Blood Cell
SI	International System of Units

SOP	Standard Operating Procedures
TVD	Total Variation Diminishing
VoF	Volume of Fluid
WBC	White Blood Cell
WBV	Whole Blood Viscosity

Institutions and Organizations

FEMEC	Mechanical Engineering Faculty
IEEE	Institute of Electrical and Electronics Engineers
LEAA	Law Enforcement Assistance Administration
MFLab	Fluid Mechanics Laboratory
UF	Federative Unit
UFU	Federal University of Uberlândia
US	United States
USA	United States of America

Units and Measurements

°C	Degrees Celsius
cm	Centimeter
kg	kilogram
L	Liter
m	Meter
mm	Millimeter
ml	Milliliter
mN	Millinewton
N	Newton

Pa	Pascal
s^{-1}	Per second (reciprocal second)

Mathematical Operators

det	Matrix determinant operator
erf	Gauss error function operator
erfc	Gauss complementary error function operator
exp	Exponential operator
lim	Limit operator
sinh	Hyperbolic sine operator
tg	Tangent operator

List of symbols

Primary Symbols

3D	Three-dimensional
A	Surface area
A_t	Cross-sectional area
α	Angle
α_1	Dimensionless parameter from K-L model
α_2	Dimensionless parameter from K-L model
$\approx$	Approximate
$\mathbf{a}$	Acceleration vector
a	Dimensionless parameter from Carreau-Yasuda, Cross or modified Powell-Eyring models
β	Angle
$\dot{\boldsymbol{\gamma}}$	Strain rate tensor
$\dot{\gamma}_{ij}$	Strain rate tensor in index notation
$\dot{\gamma}$	Scalar value of shear rate
C_D	Drag coefficient
D	Diameter
δ_{ij}	Kronecker delta function
Δ	Grid spacing or variation operator
d	Differential symbol
$\dot{m}$	Mass flow rate
E_k	Kinetic energy
F	Scalar value of force
$\mathbf{F}$	Force vector

$\mathbf{f}$	Force vector per unit of volume
G	Elasticity modulus
g_i	Gravitational acceleration vector in index notation
$\mathbf{g}$	Gravitational acceleration vector
$\int$	Integral operator
i	Index used in tensors
j	Index used in tensors
$I_{\mathbf{T}}$	First Galilean invariant of a generic tensor $\mathbf{T}$
$II_{\mathbf{T}}$	Second Galilean invariant of a generic tensor $\mathbf{T}$
$III_{\mathbf{T}}$	Third Galilean invariant of a generic tensor $\mathbf{T}$
L	Characteristic length
λ	Time constant
m	Mass
m	Fluid consistency index of power-law model or dimensionless parameter from modified Cross model
$\mathbb{R}^3$	Three-dimensional space
μ	Arithmetic mean
μ	Viscosity
μ^*	Viscosity ratio between dispersed and continuous phases
∇	Gradient operator
$\nabla\cdot$	Divergent operator
∇^2	Laplacian operator
n	Flow behavior index of power-law model or dimensionless parameter from Papanastasiou regularization
ν	Kinematic viscosity
Oh	Ohnesorge number

Ω	Rotation
p	Pressure
$\propto$	Proportionality symbol
Re	Reynolds number
ρ	Specific mass
ρ^*	Specific mass ratio between dispersed and continuous phases
t	Time
tr	Tensor trace operator
T	Temperature
$\mathbf{T}$	Generic tensor
$\mathbf{u}$	Velocity vector
u_i	Velocity vector in index notation
U	Characteristic velocity
u	Velocity vector component in x direction
v	Velocity vector component in y direction
V	Scalar value for velocity
w	Velocity vector component in z direction
We	Weber number
$\overline{AB}$	Straight segment from A to B
$\overline{\mu}$	Interface viscosity mean
$\overline{\rho}$	Interface specific mass mean
$\overline{u}$	Mean velocity
ϕ	Angle or indicator function for VoF method
ψ	Stream function
σ	Interfacial tension
$\mathbf{S}$	Strain rate tensor or position vector

S_{ij}	Strain rate tensor in index notation
τ	Shear stress
τ_0	Yield stress
τ_c	Yield stress from Casson model
τ_{ij}	Shear stress tensor in index notation
$\boldsymbol{\tau}$	Shear stress tensor
τ_y	Yield stress
φ	Simplified variable representing some terms
η	Viscosity for non-Newtonian fluid
η_0	Zero-shear rate viscosity
η_c	Infinite-shear rate viscosity from Casson model
η_∞	Infinite-shear rate viscosity
$\frac{D()}{Dt}$	Substantial derivative
$\frac{\partial()}{\partial()}$	Partial derivative
$\sum$	Summation operator
x	x-direction
y	y-direction
z	z-direction

Subscripts

c	Continuous phase or Casson
$crit$	Critical
d	Dispersed phase
$drop$	Droplet
g	Gas phase (continuous phase)
l	Liquid phase (dispersed phase)

max	Maximum
p	Particle
R	Relative

Contents

1 Introduction

1.1 Contextualization and background

The forensic expertise in Brazil still yearns for a solid and densely diffusive scientific development in various areas of forensic knowledge. The myriad of factors that interfere with the diffusion and interest in scientific knowledge in this community in Brazil limits the majority of these professionals to develop criminal forensic reports in which often outdated techniques are used, along with standardized but outdated writing sections. Despite this diatribe, it is clear that some areas of forensic expertise are in an advanced scientific stage, such as DNA examination laboratories, ballistic comparison laboratories, audio and video forensic laboratories, etc. However, the experts known as "on-call" - the majority in the Brazilian scenario - who usually assume the conduct of examinations and the reporting of *crimes against persons*, *crimes against property*, *traffic crimes*, and some other natures, often do not qualify enough, do not update themselves with new techniques and methodologies, do not conduct research in any of the areas they work in, thus producing results below what is possible and necessary. And this performance condition is not inexorable, as long as there is greater diffusion of certain knowledge to the forensic community.

Specifically in crime scenes involving individuals, we encounter the discipline of Bloodstain Pattern Analysis (BPA), which is further detailed in chapter 2. Briefly introducing the subject, we have here a highly significant discipline with the real capacity to decisively assist in the reconstruction - at least partially - of the dynamics that led to a particular crime scene.

A forensic expert willing to do so can seek training in BPA through various training programs offered by institutions around the world. Currently, there is a certain maturity in the field, where generic training programs are being broken down into various specificities such as:

- Bloodstain documentation
- Classification and terminology
- Surface interactions
- Forensic photography
- Physics and mathematics
- Fabrics and textiles

- Fluid dynamics

However, as observed by this master's student during the *40th Annual Conference of Bloodstain Pattern Analysts* (IABPA, 2023), the physical understanding of human blood fluid dynamics - especially with the aid of computational simulation tools - remains lacking. The international community embraces material experiments with blood (mostly non-human and synthetic), the development of mathematical models for some important questions (such as stain size, angle of impact, area of origin or the influence of relative humidity on bloodstain formation), but little is studied in depth about the physics involved in bloodstains, about the behavior of the fluid's intrinsic properties. And even with all these separate mathematical models, how can they be used together? This is the idiosyncrasy of the BPA forensic community.

Attinger et al. (2013) already mentioned this in their paper:

> There are currently no simulation tools that solve both the impact of a drop and the formation of a stain, but current simulation techniques are ready to address this challenge. These simulation tools could be used for investigating parameters that are difficult to investigate experimentally, such as the influence of viscosity, substrate wettability, or drop sizes and velocities.

1.2 Subject relevance

The current project is aimed at conducting groundbreaking computational simulations within the realm of fluid mechanics, with a specific focus on the forensic analysis of bloodstain patterns. Our study distinguishes itself by addressing a substantial gap in scientific understanding, given the scarcity of comprehensive investigations into computational fluid dynamics within the forensic domain on a global scale.

The objectives are well-defined: to execute computational simulations of both human and animal blood droplets in free fall and to scrutinize their impact upon a solid surface. These simulations will facilitate a deeper comprehension of the non-Newtonian properties of blood and their repercussions on the bloodstain patterns discernible at crime scenes.

The significance of this project cannot be underestimated. Through computational simulation, we envision the ability to replicate intricate real-world scenarios in the foreseeable future, thereby furnishing invaluable insights for forensic inquiries. For instance, we anticipate being able to pinpoint the origin of a blood droplet based on its morphology and dispersion characteristics, thereby furnishing unequivocal deductions grounded in physical principles to resolve criminal investigations.

Moreover, our project is pioneering and exclusive, as we leverage a bespoke computational code developed internally within the Fluid Mechanics Laboratory, MFLab, at the Federal University of Uberlândia/MG, Brazil. This distinctive approach empowers us to attain a level of granularity and accuracy unattainable through empirical experiments with blood samples.

1.3 Objectives

From a broader perspective, the objective falls within the formulation of knowledge regarding the physical behavior of human blood in conditions related to forensic essence, namely crime scenes containing human blood drops in the analyzed environment. This understanding, here explored in the form of freely falling droplets, entails extensive work implementing numerical routines in specific computational code, validations, reading related articles, aiming to solidify such knowledge.

Specifying the path to be followed in this journey, the following specific objectives can be defined:

- Numerically implement and validate - in MFSim - non-Newtonian viscosity models
- Model human blood using each previously implemented and validated non-Newtonian viscosity model in specific physical problems relevant to the forensic perspective
- Compare and discuss the results of the computational simulations performed
- Outline perspectives for future research on the subject

With the present work, it is hoped to provide a deep and solid contribution to the physical understanding of human blood fluid dynamics for the forensic community - especially for bloodstain pattern analysts - with this knowledge being convertible into enhancements in forensic practice related to the subject and also adherence to *Standard Operating Procedures - SOPs*.

1.4 Methodology and dissertation structure

This subsection provides an overview of the overall structure of the dissertation, including the organization of chapters and the topics covered in each chapter. It serves as a road map for the reader to understand how the research is presented and how the various components of the study are interconnected.

In chapter 2, *Bloodstain Pattern Analysis*, the criminal environment in which the object of study of this dissertation is found is presented. Crime data from Brazil is presented, demonstrating the factual need for technical-scientific improvement in the area, aiming to deliver excellent work to society. Furthermore, fundamental concepts of Bloodstain Pattern Analysis (BPA) will be introduced. This includes an overview of the physics behind bloodstain formation, types of bloodstains, and the significance of analyzing bloodstain patterns in forensic investigations.

In chapter 3, human blood will be classified based on its intrinsic characteristics, its properties, taking into account various bibliographies.

In chapters 4, 5, and 6, the laws of physics that guide all calculations to be performed in computational modeling are introduced. The entire fluid dynamics system is solved using balance equations presented in these chapters. The modification introduced in the equations to appreciate non-Newtonian behavior is also presented. Finally, the various rheological models implemented in the MFSim computational code and used in various studies with human blood are introduced.

In chapter 7, the reader is introduced to the computational code in which all simulations presented in this dissertation were performed: The MFSim.

The following chapter presents all validations performed with the MFSim computational code before starting any modeling for human blood. At this stage, all implementations for non-Newtonian fluid modeling had already been made, leaving only the validation of such additions to the code.

In chapter 9, *Performance analysis of blood's rheological models*, a basic comparison is made between the non-Newtonian viscosity models worked on, from the perspective of viscosity as a function of shear rate, comparing them with available material experiments. This chapter provides a prediction of the performance of such rheological models.

Next, in chapter 10, the results of the computational simulations for the free fall of a human blood droplet are presented, comparing the models used and discussing them.

In chapter 11, several proposed models for representing animal blood are presented, which were also computationally simulated and compared to the human blood models discussed in the previous chapter.

Finally, in chapter 12, the conclusions of this project are presented, along with proposals for future work that can be undertaken.

1.5 Expected contributions

The current research aims to deliver significant quantitative and qualitative outcomes, enhancing technical and scientific insights crucial for improving forensic practices in Bloodstain Pattern Analysis (BPA) at crime scenes. This study seeks to advance the understanding of human blood fluid dynamics, particularly through the use of computational modeling tools.

A key goal is to develop and validate diverse models addressing various physical phenomena, such as the interaction of blood droplets with different surfaces, adhesion properties, wettability, and varying shapes representing human blood volumes. Each aspect requires a thorough understanding from a physical perspective, implementation into computational frameworks, and subsequent validation.

By providing new and essential scientific knowledge on the fluid dynamic behavior of human blood at crime scenes, this research aims to empower forensic professionals to make more categorical inferences based on physical principles. Furthermore, it paves the way for future advancements in computational modeling, potentially serving as an auxiliary tool for reconstructing crime dynamics through the analysis of bloodstain patterns.

1.6 Study limitations

Despite exclusive dedication, the most significant limitation encountered was time. The extensive knowledge required to begin obtaining initial results in computational modeling highlights the need for additional time to overcome various challenges addressed in this dissertation. However, the current work is already sufficient to generate meaningful quantitative and qualitative results, contributing positively to BPA procedures at crime scenes.

There remains a considerable journey towards achieving more realistic computational simulations, necessitating the development and validation of multiple models for different physical phenomena, such as droplet-surface interactions, adhesion properties, wettability, and arbitrary shapes for the initial blood volume. These aspects must be thoroughly understood, implemented in computational code, and validated.

Moreover, a challenge lies in comprehending the mechanisms within open-source computational modeling codes. It is imperative for users and researchers to have a profound understanding of these processes throughout their simulations, as these codes often operate as "black boxes", limiting insights into their internal workings.

2 Bloodstain Pattern Analysis

2.1 Introduction

In Brazil, the official practice of criminal forensics is carried out by state and federal agencies, with 20 states operating independently from the Civil Judiciary Police (SILVA; BASTOS; OLIVEIRA, 2022). Official criminal forensics serves numerous criminal natures, including *crimes against persons*, a nature where bloodstains are commonly found and warrant categorical analysis using established methodologies (BEVEL; GARNER, 2008).

In the year 2021, the country recorded a total of 47,847 homicides, as presented in Fig. 1, being 33,039 by firearm. This corresponds to a rate of 15.4 firearm deaths per 100,000 inhabitants. Nine UFs showed positive variations compared to 2020, deserving attention: Amazonas (53.6 %), Amapá (37.2 %), Rondônia (33.2 %), Mato Grosso do Sul (27.0 %), and Piauí (26.9 %). Conversely, the largest negative variations were observed in Acre (-50.0 %), Goiás (-28.4 %), Federal District (-23.7 %), and Sergipe (-20.1 %). This positive variation in percentages during this period is likely associated with the increased availability of these firearms. As emphasized in previous editions of the *Violence Atlas*, there is a strong consensus in the scientific literature regarding the causal relationship between the increase in the circulation of firearms and the growth of homicide rates.

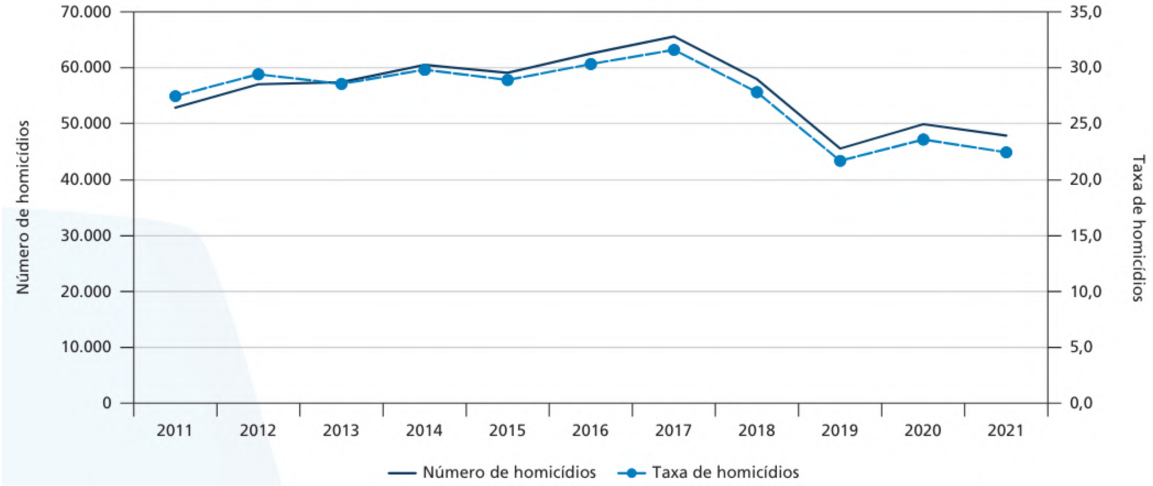

Figure 1 – Number of homicides in Brazil (2011-2021). Source: Cerqueira et al. (2023)

In the context of an exceptionally high number of crimes against persons, the quantity of crime scenes in which forensic experts operate becomes evident. These experts require an excellent knowledge of bloodstain patterns to interpret them correctly and extract information that, in many instances, would otherwise go unnoticed. Additionally, there are some specific conditions that can confuse the expert within his interpretation of the bloodstains. As exposed by Raymond, Smith e Liesegang (1996), there are several common situations where this could be relevant. The accused might have had a lawful encounter with a victim stained with blood or may assert self-defense. A law enforcement officer could be shot, leading to accusations of misconduct. Additional instances involve questionable deaths (such as distinguishing between homicide and suicide) or scenarios where multiple individuals have bled at the location, and their blood may have mixed. It's also possible that a combination of the aforementioned scenarios may have occurred.

2.2 Bloodstain Pattern Analysis: Beginning and function

The analysis of bloodstain patterns has a history of approximately 150 years from a scientific perspective. According to Bevel e Garner (2008), the first journal in which authors were able to discuss forensic topics related to blood analysis at crime scenes was the *Viertaljahresschrift fur gerichtliche Medizin (Quarter-Year Writings for Forensic Medicine)*, published in Germany between 1850 and 1940.

Furthermore, Bevel e Garner (2008) mentions an article from 1856 written by J. B. Lassaigne, *Neue Untersuchungen zur Erkennung von Blutflecken auf Eisen und Stahl (New Examination to Differentiate Bloodspots from Iron and Steel)*, in which he discusses some marks that appeared to be bloodstains, but were actually caused by insect activity.

Another interesting case is that of the criminologist Henry T. F. Rhodes, who in 1931 published his book *Some Persons Unknown*, in which he showed the evolution in blood identification and also the evolution of court requirements, where there was a transition from testimonies of the type "looks like blood" to "is blood" and, subsequently, to "is blood, and is human blood."

Bloodstain Pattern Analysis, commonly called BPA, is a forensic discipline that seeks to elucidate the facts behind a previous event, which is usually a crime. The dispersion, shape characteristics, volume, pattern, number and size of bloodstains are some of the parameters measured by an analyst. As formally stated by Bevel e Garner (2008), some basic bloodstain event types are:

- Blood dispersed from a point/area source by a force (e.g., impact patterns)
- Blood ejected over time from an object in motion (e.g., cast-off patterns)
- Blood ejected in volume over pressure (e.g., spurt and gush patterns)
- Blood dispersed as a function of gravity (e.g., drip, drip trails)
- Blood that accumulates and/or flows on a surface (e.g., pools and flows)
- Blood that is deposited through contact transfer (e.g., smears and pattern transfers)

Additionally, the information that can be obtained after further examination includes:

- The direction in which a stain was traveling when deposited
- The angle of impact
- The area of origin of impact patterns, in $\mathbb{R}^3$
- The direction from which a force was applied
- The nature of object(s) involved in creating the pattern
- In some instances, the approximate number of blows struck during an incident
- The relative position(s) in the scene of the suspect, victim, or other related objects during the incident
- Movement of individuals and/or objects during and after bloodshed
- Sequencing of multiple events associated with an incident

MacDonell (2009) mention that these further examinations will lead to significant considerations, in order of decreasing significance:

- The shape of individual bloodstains, which may allow their origin to be determined in three dimensions
- The size of the individual bloodstains, which suggests the kind of energy that was available for their production, if they were the result of an impact
- The distribution and concentration of a bloodstain pattern may suggest the distance between the origin of blood and the surface upon which it was deposited

Many proclaim Herbert MacDonell as the father of modern BPA. The report *Flight Characteristics and Stain Patterns of Human Blood*, by MacDonell et al. (1971), was the result of extensive research on the subject, being published by the Law Enforcement Assistance Administration (LEAA), where he worked at that time.

As cited by MacDonell (2009), bloodstain patterns, as physical evidence, must first be detected, preserved, examined, interpreted, and properly presented in court to utilize their evidentiary value. Contrary to what MacDonell says in his article, this master's student does not agree that blood's surface tension and viscosity properties are sufficiently similar to those of water that it is unnecessary to formulate an entirely new concept to deal with blood as a liquid.

And finally, we still have an good definition of BPA, by Kiely (2005), from an interesting perspective:

> This strictly observation-based forensic tool is a highly specialized crime scene procedure that is combined with the equally important skills involved in forensic photography. It is commonly used in homicide and suicide settings to determine the sequence of events, the distance of the shooter to the victim, self-defense, mental states such as intent, and a number of important crime scene dynamics that can be of inestimable use to both prosecutors and defense counsel.

2.3 Bloodstain Pattern Analysis: Terminologies

In the work *Bloodstain Pattern Analysis* by one of the greatest authorities on the subject, Bevel e Garner (2008), an important analysis of terminologies is carried out, in which the author demonstrates attention and relevance regarding the need for the physical perspective of terminologies. Starting with the subject matter itself, which has the following variations:

- Bloodstain pattern interpretation
- Blood spatter analysis
- Bloodstain spatter analysis
- Blood splatter analysis/interpretation
- Bloodstain pattern analysis

Bevel e Garner (2008) point to *Bloodstain Pattern Analysis* as the most suitable terminology for the subject. This is because the word *analysis* implies a structured and detailed approach to what will be examined at crime scenes. On the other hand, the word *interpretation* implies a subjective interpretation.

Furthermore, regarding the use of *pattern* rather than *spatter* or *splatter*, this is due to the variety of bloodstain types found at crime scenes, with which the forensic analyst will encounter.

Now, concerning other terms related to the analysis of bloodstain patterns at crime scenes, terms that will assist the forensic analyst in their analyses:

- *Angle of impact*: acute angle formed between the displacement vector or velocity vector and the surface with which the blood drop will come into contact
- *Arterial (spurt/gush)*: Jet of blood generated under pressure, usually due to the rupture of an artery or the heart
- *Atomized blood/Misting*: Bloodstain patterns characterized by a cloud of microscopic blood droplets. In the present work, the use of *atomized blood* is suggested instead of *misting*, due to the physical-theoretical concept of atomization, widely known and

used in engineering. Tryggvason, Scardovelli e Zaleski (2011) defines atomization as a striking process in which the mentioned clouds of droplets are produced. Atomization is usually produced by the ejection of liquids - at high speed - through injector nozzles. In the case of *atomized blood*, this refers, for example, to the high-speed impact of firearm projectiles on the human body, transferring a high linear momentum to the blood, which will atomize it

- *Blood into blood patterns*: Occurs when blood is deposited onto a previously created bloodstain pattern
- *Blowback effect*: Occurs when blood is deposited inside the barrel of a firearm after the shot has been fired
- *Capillary action*: Physically, the capillarity of a fluid refers to its ability to rise or fall in a capillary tube, which is a thin and narrow tube. This phenomenon is observed due to the combination of cohesive forces (attraction between molecules of the fluid itself) and adhesive forces (attraction between molecules of the fluid and the surface of the tube). Regarding this characteristic being observed at crime scenes, it refers to patterns formed, for example, when a bloodied hand, on any surface, is removed from it. Before complete separation of the hand and the surface, the blood permeating them remains attached to both surfaces due to surface tension, until the moment of complete separation, leaving a peculiar pattern on the surface (see Fig. 2)
- *Cast-off patterns*: The ones created from flung blood or projected from an object in motion or one that suddenly stops some motion (Fig. 3)
- *Clot*: A gelatinous mass formed by the confluence of blood cells in fibrin
- *Contact stain*: The ones created by the transfer of blood from one object to another through physical contact
- *Drip/Drip trail*: Trail of blood drops formed from an individual or object dripping blood while moving
- *Expectorate Spatter/Blood*: Bloodstain patterns created when blood is expelled from the mouth, nose, or respiratory system under pressure
- *Flow*: Described as the flow of a mass of blood due to gravity
- *Fly spot*: Bloodstains similar to spatter, but caused by fly activity
- *Impact site*: The point where the surface of an arbitrary object, holding a certain amount of linear momentum, encounters a source of blood and impacts it, transferring part of that linear momentum to that blood source

- *Non-spatter stains*: Bloodstain patterns that do not fit the descriptions above
- *Parent stain*: Bloodstains that originate satellite, secondary drops, which are ejected from this main drop after its contact with a surface
- *Primary Stain*: The main stain of any found pattern
- *Ricochet stain*: Blood that after impacting an object, has part of its volume separated from the main portion and ricochets off to another surface or simply falls freely due to gravity
- *Satellite Stain/Spatter*: Small secondary drops that separate from a larger drop after the impact of this latter against an arbitrary surface
- *Saturation stain*: When a portion of blood is absorbed by a permeable surface (Fig. 4)
- *Shadowing/Ghosting/Void*: Occurs when a secondary object retains - on its surface - a portion of a well-defined bloodstain, promoting a discontinuity of the bloodstain when removed from its initial position
- *Skeletonized Stain/Skeletonization*: Bloodstain that maintains its original shape and dimensions even when disturbed
- *Smear*: Encompasses various types of bloodstains generated by transfers between surfaces by contact with relative motion
- *Spatter Stains*: Stains resulting from the impact of free-flying drops on surfaces
- *Spines*: Characteristics of "lines" of blood formed at the edges of single drops after impact
- *Swipe*: When a bloodied object transfers part of that blood to another object or surface through relative motion
- *Wipe*: When the surface of any object comes into contact and is moved over a bloodstain adhered to another surface

Figure 2 – Distinct linear features are present in the pattern because of the capillary action. Source: Bevel e Garner (2008)

Figure 3 – Two cast-off patterns. The two distinct linear patterns on the cabinet are cast-off, produced by a bloody object that was swung right to left. Source: Bevel e Garner (2008)

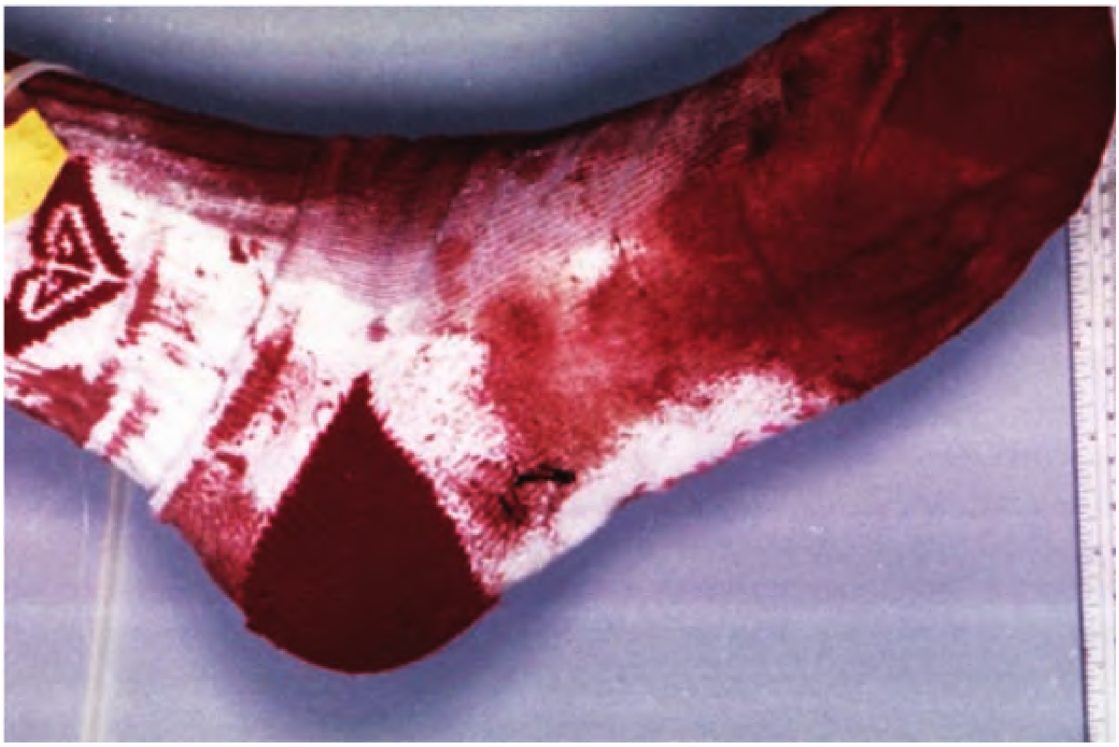

Figure 4 – A saturation stain on a sock. The location of the saturation along the full length of the top of the sock and lack of full saturation on the bottom assist in positioning the victim when the saturation occurred. Source: Bevel e Garner (2008)

Bevel e Garner (2008) proposed - in 2002 - an initial classification for bloodstains (Fig. 5), emphasizing that the difficulty in achieving consensus regarding nomenclature should not impede the prompt presentation of proposals by the forensic scientific community. Over time, new propositions are put forth by various scientific bodies worldwide, contributing to the consensus within the forensic community.

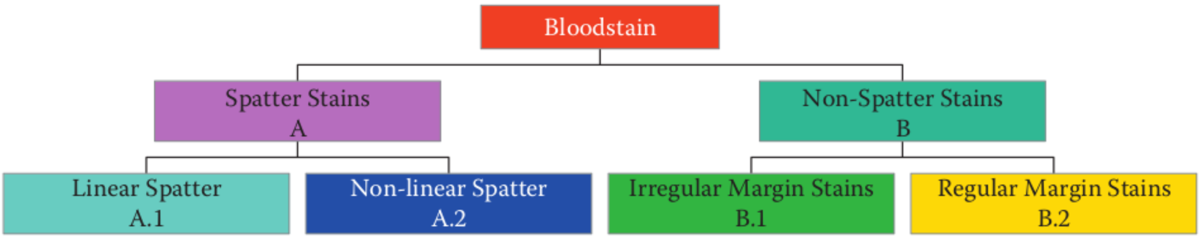

Figure 5 – The first three levels of the bloodstain taxonomy generate two primary categories (spatter and non-spatter) and four subcategories (linear spatter, non-linear spatter, regular margin stains, and irregular margin stains). Source: Bevel e Garner (2008)

2.4 Expert qualification

As a rule, the expert qualification to perform crime scene investigations as a bloodstain pattern analyst can vary a lot, depending on how many crime scenes the expert attended, how many and which courses the expert took, as well as the amount of knowledge in blood fluid dynamics.

Kiely (2005) mentioned some cases on USA, in which the courts were very willing to qualify experts on seemingly minimum bases.

In a case in the United States of America, for instance, a death row inmate appealed, arguing that the police officer who attended the crime scene was not sufficiently qualified to analyze bloodstains. However, the Supreme Court decided as follows, as excerpted from Kiely (2005):

> The court found that the detective qualified as a blood-spatter analysis expert because he had attended crime scene management classes, a homicide investigation class, and watched two training videos on blood-spatter analysis as part of his advanced officer training. “While this training is not extensive,” the court said, “it is significantly more extensive than the average person has received and is sufficient to allow the testimony to be heard by the jury.”44 The court, therefore, allowed the testimony to stand.

Another interesting case mentioned by Kiely (2005) was *Commonwealth v. Begley.* In this case, the physical explanation for the blowback pattern was crucial in solving the crime, due to the insufficient amount of blood found on a glove and inside the barrel of the questioned firearm.

Just as in the cases mentioned, there are countless others where the importance of the forensic expert’s qualification in analyzing bloodstain patterns can be perceived, knowing that this knowledge has the power to extract categorical information about aspects of the crime dynamics.

2.5 Scientific research and methodology for BPA

Chalmers (1999) mentions another author’s - J. J. Davies (1968) - definition: "Science is a structure built upon facts".

In a simpler manner, Laudan (1978) defines science as essentially a problem-solving activity. Aptly, it states that if problems are the focus of scientific thought, theories are the end result. Laudan (1978) asserts that theories matter, that they are cognitively significant insofar as they provide adequate solutions to problems.

Chalmers (1999) also cited a fact about Galileo, addressed by H. D. Anthony (1948):

> It was not so much the observations and experiments which Galileo made that caused the break with tradition as his attitude to them. For him,

> the facts based on them were taken as facts, and not related to some preconceived idea[...] The facts of observation might, or might not, fit into an acknowledged scheme of the universe, but the important thing, in Galileo's opinion, was to accept the facts and build the theory to fit them.

Finally, according to Chalmers (1999), facts can be assumed as the basis of science for three reasons:

- Facts are directly given to careful and unbiased observers through the senses
- Facts are prior to and independent of theory
- Facts constitute a firm and reliable foundation for scientific knowledge

In his work *The Logic of Scientific Discovery*, Popper (1959) discusses *scientific objectivity* and *subjective conviction*. Popper suggests that these philosophical terms are the subject of endless debates. However, he argues that the term "objective" is used to indicate that scientific knowledge must be justified and tested. He asserts that every new scientific theory should not necessarily be justified or verified but tested. On the other hand, subjective experience or the feeling of conviction can never justify a scientific statement.

Kuhn (1996) offers an intriguing approach to scientific research. Firstly, he defines the term "paradigm" as an accepted "model or pattern" within the community. However, the sense of the words "model" or "pattern" is not usual in their definition; their essence lies in their replicability. According to Kuhn, in science, the "model" or "pattern" is an object for further articulation or specification under new or more rigorous conditions. Thus, science progresses.

Drawing a parallel with the present work, the paradigm discussed here relates to the current understanding of the physical behavior of human blood in a forensic context.

Furthermore, it is worth mentioning a passage from Bacon (2011) about the importance of in-depth scientific research, returning to the understanding of the physical foundations of fluid dynamic phenomena:

> "The best demonstration is, by far, the experiment, provided it be made diligently and with caution. If we seek to apply it to other facts supposed to be similar, unless it be done rightly and methodically, it is fallacious. [...] it is necessary to extend the investigation to the most general of things."

Forensic disciplines have unnecessarily suffered in the past due to a lack of a consensus methodology. It is worth noting that in the legal context, forensic disciplines are often attacked by defense attorneys and prosecutors, attempting to discredit the work performed by forensic experts.

Therefore, the establishment of precise methodologies with a strong scientific basis becomes crucial to deter challenges.

Bevel e Garner (2008) proposes an eight-step methodology to bloodstain pattern analysts, addressing the "how" of applying the scientific method to bloodstain analysis:

- Become familiar with the entire scene
- Identify the discrete patterns among the many bloodstained surfaces
- Categorize these patterns based on an established taxonomy
- Evaluate aspects of directionality and motion for the pattern
- Evaluate angles of impact, points of convergence, and areas of origin
- Evaluate interrelationships among patterns and other evidence
- Evaluate viable source events to explain the pattern, based on all of the evidence
- Define a best explanation of the events

3 Blood features and classification

3.1 Introduction

Understanding the physical, physiological, and compositional characteristics of human blood plays a crucial role in various fields, ranging from medical research to forensic investigation. In the context of mechanical engineering, this understanding is fundamental for the computational modeling of blood fluid dynamics.

Viscosity, specific mass and composition are intrinsic factors that influence the behavior of blood during its flow through the blood vessels. Studies such as those by Chien (1970) emphasize the importance of these properties for a more accurate understanding of hemodynamic conditions.

Furthermore, the analysis of bloodstain patterns at crime scenes is an integral part of forensic investigation. The correct interpretation of these patterns requires knowledge not only of blood properties but also of how these characteristics manifest in different scenarios.

In the realm of computational modeling, comprehending the complex interaction between blood and vascular structures and, in our case, the random structures of a crime scene, is crucial for developing accurate models. Works like that of Perktold, Rappitsch e Grasser (1998) delve into hemodynamic modeling, emphasizing the need to consider the rheological properties of blood.

In conclusion, a comprehensive understanding of human blood characteristics is essential for advancements in both mechanical engineering and forensic investigation. The interdisciplinary nature of these fields highlights the importance of a holistic approach to enhance the understanding and practical application of this knowledge.

On the following sections some properties and characteristics of human blood, according to various sources in the field, will be introduced.

3.2 Blood's elements

Initially, I quote a passage from Windberger et al. (2017), where he classifies human blood from a characteristically holistic perspective:

> Blood was characterized as a shear-thinning viscoelastic fluid, showing different degree of thixotropy in relation to RBCs aggregation. Typically, at low shear rates, RBC aggregates and clusters, while at high shear rates singularly suspended RBCs contribute to plasma enhancement. It must be noted that low shear viscosity reflects the specific texture of blood at low shear which is given by the sum of all attracting forces in the respective sample, rather than showing RBCs aggregation alone.

The terms mentioned by Windberger et al. (2017) will be dissected below for a better understanding of their effects.

According to Weber e Lednev (2020), blood accounts for about 8 % of human body's weight or about 5.67 L.

Blood elements include erythrocytes (red blood cells, RBCs), leukocytes (white blood cells, WBCs) and platelets. RBCs are the most numerous cells in blood (around 50 % of whole blood volume) because they are needed to tissue respiration. They lack nuclei and contain hemoglobin (*Hb*), an iron-containing protein that transports oxygen and carbon dioxide (GREER et al., 2019).

From a rheological perspective, in complement to the previous paragraph, Merrill (1969) and Lowe (1988) emphasize that RBCs (see Fig. 6) dominate the rheological characteristics due to their volumetric concentration to the extent that the influence of WBCs and platelets becomes imperceptible.

Figure 6 – The normal mature erythrocyte (RBCs) as visualized by the scanning electron microscope. Source: Greer et al. (2019), Fig. 6.7

It is interesting to reproduce a passage from a lecture given in 1786 by John Hunter (PALMER, 2015):

> "In all inflammatory dispositions . . . blood has an increased disposition to separate into its component parts, the red globules become less uni-

> formly diffused and their attraction to one another becomes stronger, so that the blood . . . when spread over any surface, it appears mottled, the red blood attracting itself and forming spots of red."

This citation already demonstrates, long ago, the understanding of the tendency of RBCs to aggregate.

On the other hand, WBCs encompass a diverse array of cell types, each with distinct immune functions and characteristic morphological features. WBCs are nucleated and consist of neutrophils, lymphocytes, monocytes, eosinophils, and basophils. WBCs account for approximately 1 % of the whole blood volume.

And finally, the platelets, are cytoplasmic fragments originating from megakaryocytes in the bone marrow and play a crucial role in hemostasis.

Several preanalytical factors can impact hematologic measurements, and it is essential to collect specimens in a standardized manner to minimize data variability. Factors such as patient activity, hydration levels, medications, gender, age, race, smoking, and anxiety levels can notably influence hematologic parameters.

Additionally, we have plasma, which is a suspension of proteins (such as fibrinogen) and small molecules in water.

The fibrinogen contained in blood plasma, interacting with RBCs, can produce the following effects, according to Merrill (1969):

- Inconvenient rapid sedimentation of RBCs
- Syneresis of plasma next to boundary surfaces
- Densification of the red cell core (increase of HCT)

Merrill (1969) points out that the non-Newtonian behavior of human blood is dominated by the interaction of fibrinogen with RBCs. At normal hematocrit levels, no other plasma protein seems to have the capacity to promote the formation of a yield stress in RBCs.

3.2.1 Volume of packed red cells (Hematocrit)

Hematocrit (HCT) represents the percentage of a blood sample's volume occupied by red cells. The determination of HCT can be performed manually through centrifugation of blood in a standardized glass tube with a consistent bore, following the method initially outlined by Greer et al. (2019). The HCT is calculated by comparing the height of the column of red cells after centrifugation to the total volume of the blood sample.

In his paper, Merrill (1969) cites some medical sources of data, presenting some mathematical relationships for the viscosity of whole blood at high shear rates, as a function of HCT level. It also presents the relationship representing the variable yield stress for the range of shear rates corresponding to the non-Newtonian behavior of human blood.

3.2.2 Temperature

The rheological properties of normal human blood are less affected by temperature, at the non-Newtonian and zero shear rate regimes. Approximately 90 % of tested humans presented a yield stress of their blood independent of temperature, while other 10 % showed substantial increase of yield stress as temperature decreased from 37 °C to 25 °C (MERRILL, 1969).

3.2.3 Anticoagulants

Cokelet et al. (1963) studied both fresh human blood from a donor without anticoagulants and with anticoagulants in a Couette viscometer, and found that, at reasonable concentrations, anticoagulants such as heparin, sodium citrate, ACD, EDTA, and sodium oxalate did not promote significant changes in the rheological properties of whole blood. They do not play an observable significant role in the fibrinogen-RBCs structure.

3.3 Density of human blood

According to Pedrizzetti et al. (2022) and Pedrizzetti e Perktold (2003) blood density is approximately $1,050\,\mathrm{kg/m^3}$.

Trudnowski e Rico (1974) mentions that the relative density (see appendix B, sec. 14.2) of blood at 37 °C is 1.0506 (95 % confidence interval: $1.0537 - 1.0475$), yielding a density of human blood at 37 °C of $1,050.6\,\mathrm{kg/m^3}$. It is important to note that the relative specific mass is the ratio between the fluid's specific mass under consideration and the specific mass of water (Trudnowski e Rico (1974) considered $1,000\,\mathrm{kg/m^3}$ at 4 °C) at a given specific temperature.

Larkin e Banks (2016) and Hulse-Smith, Mehdizadeh e Chandra (2005) mention in their works that the relative density of human blood ranges between 1.052 e 1.063.

The relative density measured by Raymond, Smith e Liesegang (1996) for human blood containing ACD or EDTA anticoagulant was in the range $1.056 - 1.061$. The relative density of the blood was measured using a pyknometer graduated to hold a volume of 10 ml at 20 °C. The pyknometer was weighed dry at 37 °C with distilled water as a reference sample at 37 °C, with fresh human blood from a number of individuals.

Finally, Attinger et al. (2013) sheds light on a range of values for the density of human blood, from $1,052 - 1,063\ \mathrm{kg/m^3}$ at 37 °C, taking into account the works of James, Kish e Sutton (2005) and Rosina et al. (2007).

3.4 Blood viscosity

Blood viscosity is the result of several features like RBCs, aggregation and deformation, plasma viscosity, and RBCs-plasma coupling.

Whole blood viscosity varies in accordance with both physical conditions and its composition (LOWE, 1988). Temperature, HCT, plasma viscosity, and shear rate are physical conditions that affect blood viscosity. Regarding composition, viscosity is affected, for example, by the deformability of RBCs, flexibility of their membranes, and *Hb* concentration. When the shear rate is reduced, RBCs become less deformed and progressively aggregate through plasma globulins — especially fibrinogen — leading to an increase in bulk blood viscosity.

Quoting Lowe (1988) on the viscosity of human blood:

> Low blood viscosity at high shear rates is due to the considerable deformability of normal red cells. Under high-shear conditions, red cells are oriented in parallel with the flow streamlines, assume an ellipsoidal shape with their long axes parallel to the direction of flow, and participate in flow.

Merrill et al. (1966) showed that fibrinogen acts as an adhesive in the reversible clustering of RBCs. The yield stress, τ_y, rises with higher concentrations of fibrinogen and HCT composition. Additionally, they noted that the presence of other plasma proteins does not have an impact when fibrinogen is absent.

Merrill (1969) asserts that the non-Newtonian behavior of human blood regarding variations in applied shear rates on fluid elements is much more significant than the viscoelastic characteristic it also exhibits.

Merrill (1969) discusses the presence of a yield stress in human blood, of which I quote the following excerpt:

> A special problem is posed with blood because it exhibits a "yield stress". This means that, if in the playing card experiment, one increases from zero to stress, but keeps it less than a critical value, the response will be elastic, [...], and on removal of the stress, the shape of the blood film will be unaltered, i.e., no flow will have occurred. However, if the yield stress is exceeded, irreversible deformation will occur.

Merrill (1969) also mentions the value of $\tau_y = 0.04\,\mathrm{dynes/cm^2} = 0.004\,\mathrm{N/m^2}$.

In this context, Lowe (1988) also mention the reversible deformation (elasticity) of the bulk flow, but he is unaware of the reason, and presented a table of the yield stress for human blood from some previous studies:

Table 1 – Human blood yield stress values. Adapted from Lou e Yang (1993)

HCT (%)	τ_y (mN/m)	**Sources**
46	5	Cokelet et al. (1963)
Normal	10.89	Charm e Kurland (1965)
Normal	0.3-0.2	Charm e Kurland (1972)
42	14.4-25.6	Bate (1977)
	18.66	Blair (1959)

Baskurt e Meiselman (2003) states that at medium to high shear rates, there is about a 4 % increase of blood viscosity per unit increase of HCT (e.g., a change from 45 to 46 % in HCT increases blood viscosity by 4 %).

Merrill (1969) demonstrates through experimental data that the non-Newtonian behavior of human blood occurs approximately when $\dot{\gamma} \leq 100\,\mathrm{s}^{-1}$. In Fig. 7, it can be observed that for values of the shear rate higher than $100\,\mathrm{s}^{-1}$, the linear coefficient of the curve remains constant, highlighting the Newtonian characteristic of human blood. Due to this data overlap in Fig. 7 - at low shear rates - Merrill (1969) replotted the data using the double square root, as shown in Fig. 8. In this image, it is noticeable that at low shear rates ($\dot{\gamma}^{1/2} \leq 5.3\,\mathrm{s}^{-1/2}$), there is a constant linear coefficient, similar to what occurs for $\dot{\gamma}^{1/2} \geq 10.0\,\mathrm{s}^{-1/2}$, indicating Newtonian behavior both at low and high shear rates, with a transitional region in the middle range of shear rates, where human blood exhibits non-Newtonian behavior.

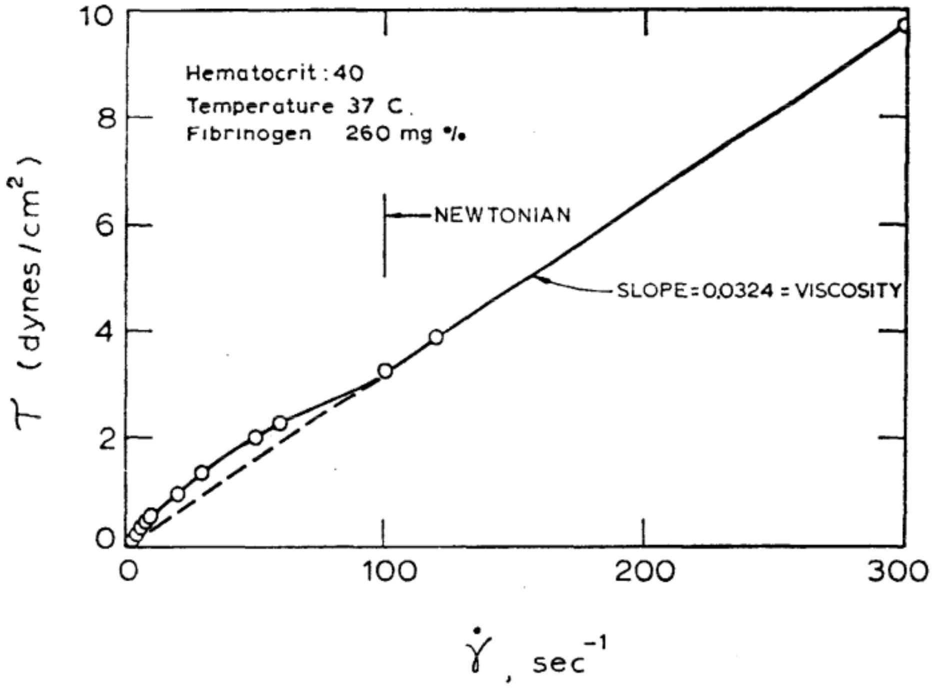

Figure 7 – Shear stress (τ) plotted vs. shear rate ($\dot{\gamma}$) for a typical normal blood (HCT = 40 % and T = 37 °C). Note confusion of points near origin. Source: Merrill (1969)

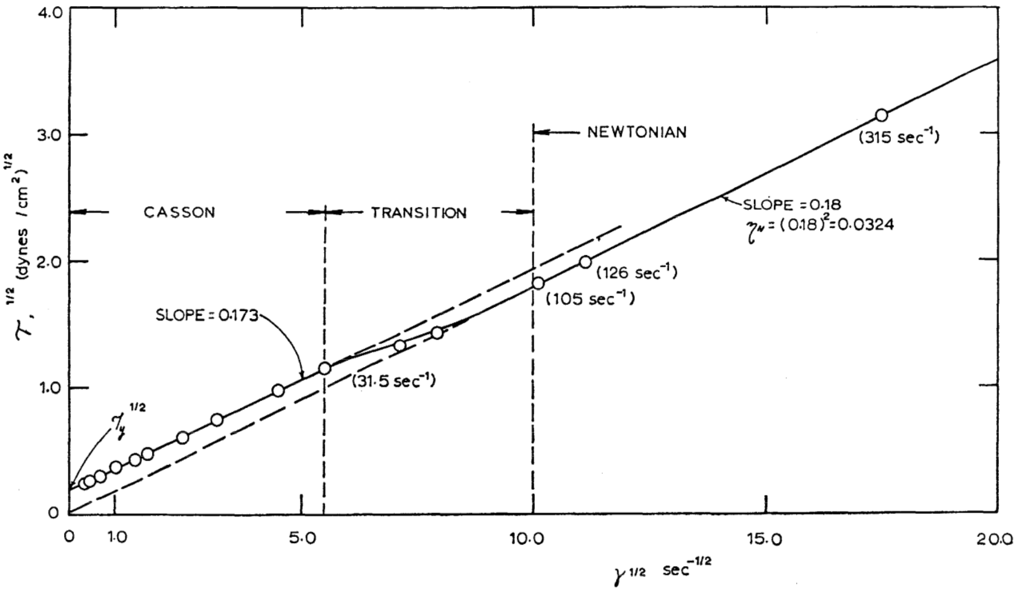

Figure 8 – Same data as in Fig. 7 replotted as square root of shear stress (τ) vs. square root of shear rate ($\dot{\gamma}$) for a typical normal blood (HCT = 40 % and T = 37 °C). Note determination of square root of yield stress $\tau_y^{1/2}$. Source: Merrill (1969)

As well noted by Merrill (1969), determining the correct viscosity of whole human blood at low shear rates is a challenging task, due to sedimentation processes and the formation of a clear plasma layer near the viscometer walls, leading to gross measurement errors. Therefore, the measurement speed becomes an important parameter to consider.

Moreover, Fåhraeus (1929) observed that under low flow conditions, RBCs in plasma form a structure of linear aggregates called *rouleaux* (figure 9), which result from the aggregation of RBCs by plasma proteins, especially fibrinogen, which form bridges between adjacent red cells.

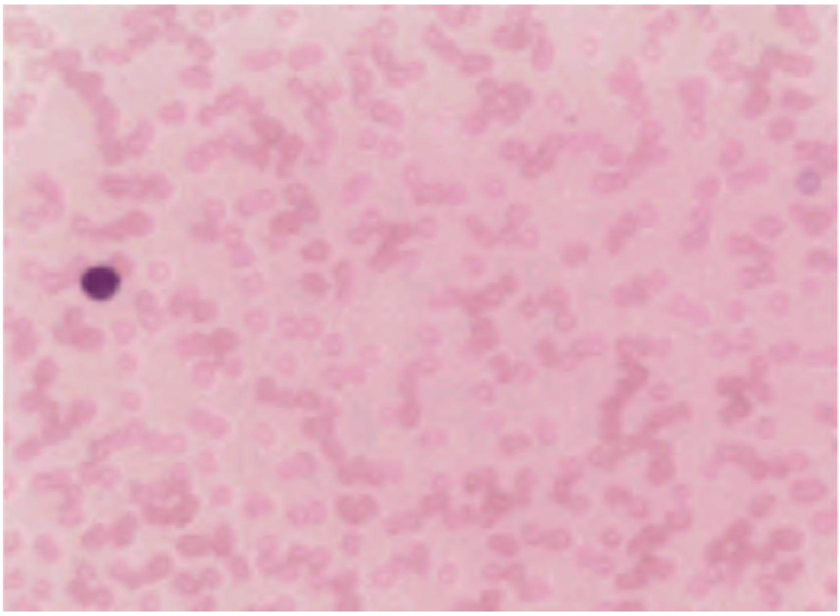

Figure 9 – Rouleaux formation. Source: Greer et al. (2019)

Some important considerations pertain to changes in whole blood viscosity in healthy individuals, supported by research findings. For instance, Lowe (1988) mentions that according to some studies, women — especially during reproductive years — exhibit lower blood viscosity than men, due to reduced HCT levels.

Regarding individuals' age, newborns have higher blood viscosity than adults due to elevated HCT levels. Conversely, children have lower viscosity than adults due to decreased HCT levels. During puberty, hormonal changes lead to increased RBC mass in males, altering viscosity compared to females.

Despite limited information in the field, Lowe (1988) anticipates lower blood viscosity values in underdeveloped countries due to lower HCT levels resulting from experiences of malnutrition, infections and infestations, as well as in regions with colder and extreme climates.

Moreover, women in menstrual cycles may exhibit high viscosity during the premenstrual period and low viscosity during menstruation.

Women taking oral contraceptives may experience increased blood viscosity due to elevated HCT and fibrinogen levels, but not plasma viscosity.

Pregnant women will experience decreased viscosity due to a drop in HCT levels.

Similarly, variations will be noticed in situations such as physical fitness, weight, blood pressure, blood lipids and lipoproteins, cigarette smoking, alcohol consumption, mental stress and individual differences.

3.5 Blood interfacial tension

According to Rosina et al. (2007), blood's interfacial tension is one of the most important parameters, in special from forensic perspective, due to bloodstain formation on crime scenes. Raymond, Smith e Liesegang (1996) mentioned that the interfacial tension pertinent to crime scene reconstruction is essentially that interfacial energy or tension characterised by a particular blood droplet and air's interfaces.

As elucidated by Tryggvason, Scardovelli e Zaleski (2011), interfacial tension can be understood from a molecular perspective, where the interface is not thermodynamically optimal. Molecularly, the preference of molecules is to exist at either gas or liquid specific mass, minimizing free energy. The non-optimal conditions near the interface result in excess energy. From a mechanical standpoint, interfacial tension can be perceived as a force per unit length acting perpendicularly on any line segment in the interface. These perspectives are equivalent: stretching the interface requires applying force to it.

Regarding some works on this property, Raymond, Smith e Liesegang (1996) employed interfacial tension, along with other physical parameters like viscosity and specific mass, to validate the use of porcine blood as a representative medium for freshly spilled human blood in crime-related investigations. The assessment of interfacial tension's impact and its correlation with the blood/bile ethanol ratio was explored by Winek, Henry e Kirkpatrick (1983).

Investigations into the suitability of alumina as a material for cardiovascular applications, incorporated interfacial tension as a critical parameter (QUEIROZ et al., 2014).

McCuaig et al. (1992) simulated blood flow to examine the influence of interfacial tension on slow venous bleeding, observing the coating of syringe interfaces and the formation of a dome over skin laceration bleeding sites.

The chemistry of blood platelet-rich plasma, including interfacial tension values at 37 °C and 25 °C, was scrutinized by Baier et al. (1985) to establish a method for estimating the apparent blood compatibility of new biomaterials.

As researched by Rosina et al. (2007), blood's interfacial tension can be expressed - for the range 20 °C ≤ T ≤ 40 °C - as:

$$\sigma(\mathrm{T}) = -0.473 \cdot \mathrm{T} + 70.105 \tag{3.1}$$

which give us the following graphic:

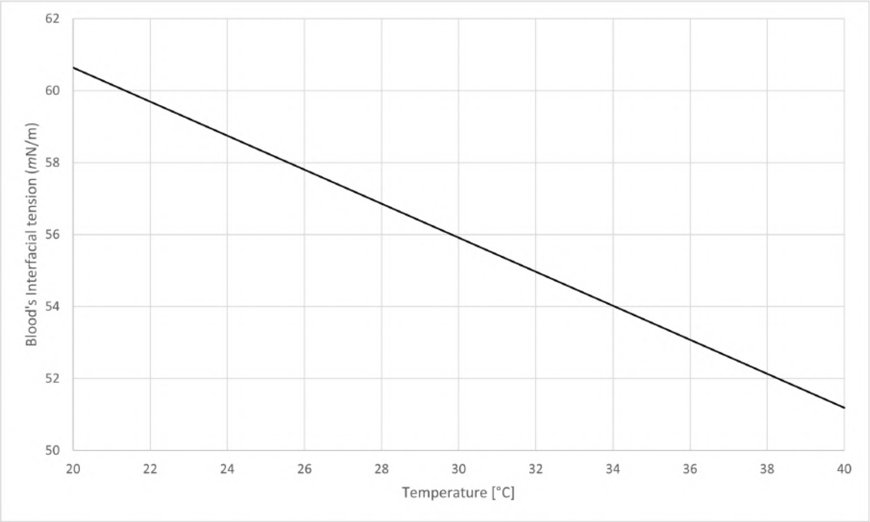

Figure 10 – Blood's interfacial tension according to Rosina et al. (2007)

Lee et al. (2020) studied blood substitutes and one of the properties simulated was interfacial tension that, for real human blood samples, was measured as 47.65 ± 1.25 mN/m at 20 °C.

Attinger et al. (2013) mentioned that at 20 °C, blood's interfacial tension in respect to the air is approximately 61 mN/m, and at 37 °C is close to 52 mN/m.

4 Fundamental equations of viscous flows

4.1 Introduction

The equations of viscous flows are known for beyond the last century. Current computational capability to solve numerical problems is limited and can easily become inefficient depending on the solving problem. For example, at high Reynolds number (turbulent flow), it's impossible to solve the complete viscous flows equations in their complete form.

The basic two balance equations considered here to solve fluids motion are:

- Mass balance (continuity equation)
- Linear momentum balance equation

4.2 Mass balance: Continuity equation

On Eulerian system - appropriated to fluid flow - the balance equations mentioned on sec. 4.1 must utilize the particle derivative:

$$\frac{D\rho}{Dt} + \rho\nabla \cdot \mathbf{u} = 0 \quad \text{or} \quad \frac{\partial \rho}{\partial t} + \nabla \cdot (\rho \mathbf{u}) = 0 \tag{4.1}$$

If the specific mass is constant (incompressible flow), the term $\partial\rho/\partial t$ is set to zero. Then:

$$\nabla \cdot \mathbf{u} = 0 \tag{4.2}$$

4.2.1 The stream function

The mathematician J. L. Lagrange, in 1755, defined the stream function ψ . The two-dimensional steady compressible flow in the xy plane, takes the continuity equation to:

$$\frac{\partial}{\partial x}(\rho u) + \frac{\partial}{\partial y}(\rho v) = 0 \tag{4.3}$$

If we define the stream function ψ as:

$$\rho u = \frac{\partial \psi}{\partial y} \quad \text{and} \quad \rho v = -\frac{\partial \psi}{\partial x} \tag{4.4}$$

it is noticed that Eq. 4.4 satisfies Eq. 4.3. It leads to a physical significance which means that lines of constant ψ ($d\psi = 0$) are lines across which there is no mass flow ($d\dot{m} = 0$), that is, they are streamlines of the flow. Also, between two streamlines, the value of ψ is numerically equal to the mass flow between these two streamlines.

4.3 Linear momentum balance

The Newton's second law is expressed as:

$$\mathbf{F} = m\,\mathbf{a} \tag{4.5}$$

Dividing all Eq. 4.5 by the volume of the particle, we have:

$$\rho\frac{D\mathbf{u}}{Dt} = \mathbf{f} = \mathbf{f}_{body} + \mathbf{f}_{interface} \tag{4.6}$$

where $\mathbf{f}$ is the applied force per unit of volume of the fluid particle. This force $\mathbf{f}$ is divided into two forces: body forces and interface forces.

The body forces are those applied on the entire fluid particle. This forces are usually the gravitational field, wrote as:

$$\mathbf{f}_{body} = \rho\mathbf{g} \tag{4.7}$$

being $\mathbf{g}$ the vector acceleration of gravity.

External stresses make up the interface forces when applied on the sides of the fluid particle. All stresses are positive, as the sign convention shown on following figure:

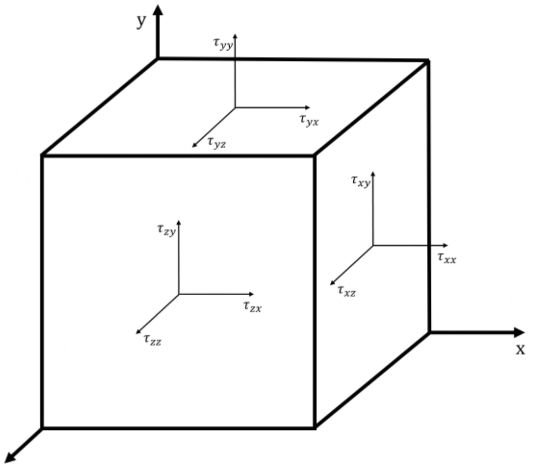

Figure 11 – Stresses convention notation

The quantity stress τ_{ij} is understood as the tension τ applied on a plane orthogonal to the i-axis, on j-axis direction. It is defined as:

$$\tau_{ij} = \begin{bmatrix} \tau_{xx} & \tau_{xy} & \tau_{xz} \\ \tau_{yx} & \tau_{yy} & \tau_{yz} \\ \tau_{zx} & \tau_{zy} & \tau_{zz} \end{bmatrix} \tag{4.8}$$

This tensor is symmetric to satisfy equilibrium of moments about the three axes of the element of fluid.

Considering Fig. 11, the total force on the frontal faces in each direction due to stress is:

$$\begin{aligned} dF_x &= \tau_{xx} dydz + \tau_{yx} dxdz + \tau_{zx} dxdy \\ dF_y &= \tau_{xy} dydz + \tau_{yy} dxdz + \tau_{zy} dxdy \\ dF_z &= \tau_{xz} dydz + \tau_{yz} dxdz + \tau_{zz} dxdy \end{aligned} \tag{4.9}$$

If the particle is in equilibrium, these forces in each direction would be balanced by equal and opposite forces applied on back faces. But, if the particle is accelerating, the front and back faces stresses will be different by an infinitesimal amount as, for example:

$$\tau_{xx,front} = \tau_{xx,back} + \frac{\partial \tau_{xx}}{\partial x} dx \tag{4.10}$$

So, the *net* force in x direction is:

$$F_{x,net} = \left(\frac{\partial \tau_{xx}}{\partial x} dx \right) dydz + \left(\frac{\partial \tau_{yx}}{\partial y} dy \right) dxdz + \left(\frac{\partial \tau_{zx}}{\partial z} dz \right) dxdy \tag{4.11}$$

or, per unit of volume of the fluid particle:

$$f_{x,net} = \frac{\partial \tau_{xx}}{\partial x} + \frac{\partial \tau_{yx}}{\partial y} + \frac{\partial \tau_{zx}}{\partial z} \tag{4.12}$$

The previous Eq. 4.12 is the divergent of the vector $(\tau_{xx}, \tau_{xy}, \tau_{xz})$, the upper row of the stress tensor (eq. 4.8). Similarly, f_y and f_z are divergent of the other two rows of the stress tensor, respectively. So, the total vector interface force can be written as:

$$\mathbf{f}_{interface} = \nabla \cdot \tau_{ij} = \frac{\partial \tau_{ij}}{\partial x_j} \tag{4.13}$$

In this way, the Newton's law presented on Eq. 4.5 becomes:

$$\rho \frac{D\mathbf{u}}{Dt} = \rho \mathbf{g} + \nabla \cdot \tau_{ij} \tag{4.14}$$

The above equation is also known as the Cauchy equation of motion, which represents the balance of linear momentum. It is one of the fundamental equations of continuum mechanics.

When the fluid is at rest, the viscous stresses vanishes; it has no velocity and no shear stresses, and the normal stresses become equal to hydrostatic pressure. So, Eq. 4.14 reduces to:

$$\begin{aligned}&\tau_{xx} = \tau_{yy} = \tau_{zz} = -p\\&\tau_{ij} = 0 \quad \text{for} \quad i \neq j\\&\nabla \mathrm{p} = \rho \mathbf{g}\end{aligned} \tag{4.15}$$

4.3.1 Deformation law for Newtonian fluid

As well explained by White (2006), a fluid element can undergo four types of motion or deformation:

- Translation
- Rotation
- Extensional strain or dilatation
- Shear strain

Consider a square particle of fluid initially positioned as $\overline{ABCD}$ at a random time t. After a infinitesimal time dt, the particle is positioned as $\overline{A'B'C'D'}$.

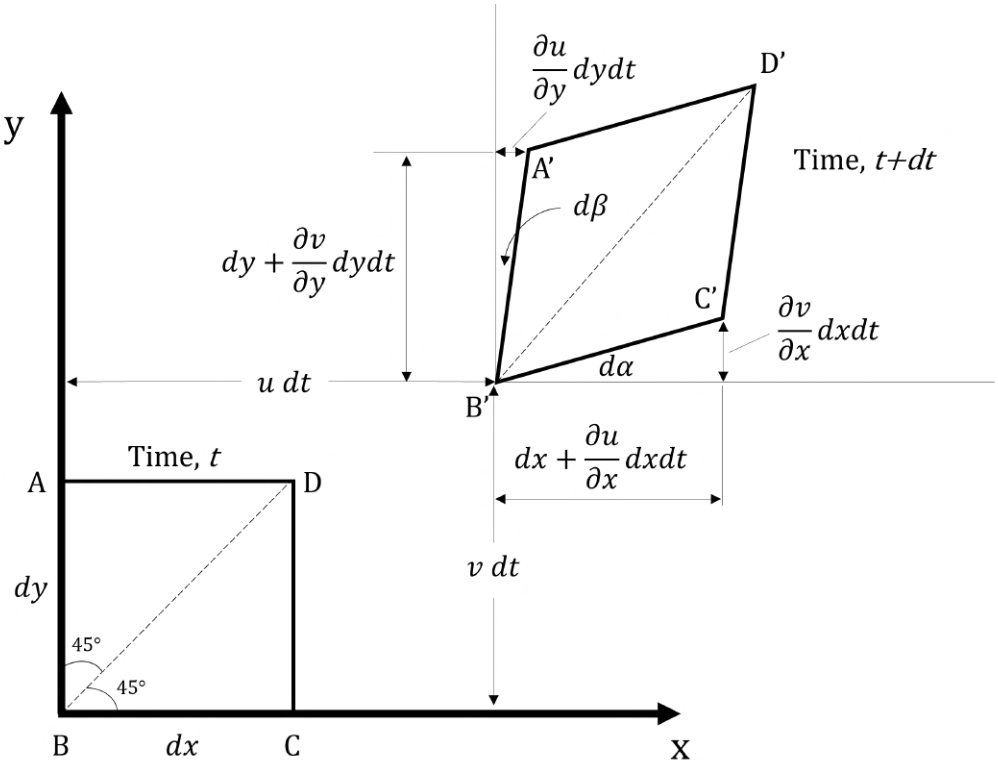

Figure 12 – Distortion of a moving fluid element

The *translation* is defined by the displacements $u\,dt$ and $v\,dt$ of the point B. The *rate of translation* are the velocities itself: u and v. In three-dimensional motion, the *rate of translation* is u, v and w.

The *angular rotation* of the particle about the z-axis is defined by the *average* counterclockwise rotation (by convention) of the two sides $\overline{BA}$ and $\overline{BC}$. It's visible in the Fig. 12 that the angle α performs a counterclockwise amount rotation of $d\alpha$, while angle β performs a clockwise amount rotation of $d\beta$. So, the counterclockwise amount rotation of the angle β is $-d\beta$. So, the *average rotation* is:

$$d\Omega_z = \frac{1}{2}(d\alpha - d\beta) \tag{4.16}$$

Now, let's find the angles $d\alpha$ and $d\beta$ in function of the velocity derivatives.

First, for an infinitesimal angles ϕ, we can assume that $tg\,\phi \approx \phi$. Then, looking at Fig. 12 we can do:

$$d\alpha = tg\,\alpha = \lim_{dt\to 0}\left(\frac{\frac{\partial v}{\partial x}dx\,dt}{dx + \frac{\partial u}{\partial x}dx\,dt}\right) = \frac{dv}{dx}dt \tag{4.17}$$

$$d\beta = tg\,\beta = \lim_{dt\to 0}\left(\frac{\frac{\partial u}{\partial y}dy\,dt}{dy + \frac{\partial v}{\partial y}dy\,dt}\right) = \frac{du}{dy}dt \tag{4.18}$$

Replacing the Eqs. 4.17 and 4.18 on Eq. 4.16, we find the *rate of rotation*, that is given by:

$$\frac{d\Omega_z}{dt} = \frac{1}{2}\left(\frac{dv}{dx} - \frac{du}{dy}\right) \tag{4.19}$$

Similarly, in three-dimensional motion, we have the *rate of rotation* about x and y axes, as:

$$\frac{d\Omega_x}{dt} = \frac{1}{2}\left(\frac{dw}{dy} - \frac{dv}{dz}\right) \tag{4.20}$$

$$\frac{d\Omega_y}{dt} = \frac{1}{2}\left(\frac{du}{dz} - \frac{dw}{dx}\right) \tag{4.21}$$

Now, we have the *shear strain*, which is commonly defined as the *average* decrease of the angle between two lines which are initially perpendicular in the unstrained state. As shown in Fig. 12, the initial lines are the segments $\overline{BA}$ and $\overline{BC}$. So, the *shear strain* is

$$\gamma_{xy} = \frac{1}{2}\left(d\alpha + d\beta\right) \tag{4.22}$$

So, the *shear strain rate* is:

$$\dot{\gamma}_{xy} = \frac{1}{2}\left(\frac{d\alpha}{dt} + \frac{d\beta}{dt}\right) = \frac{1}{2}\left(\frac{dv}{dx} + \frac{du}{dy}\right) \tag{4.23}$$

Similarly, on three-dimensional motion, we have:

$$\dot{\gamma}_{yz} = \frac{1}{2}\left(\frac{dv}{dz} + \frac{dw}{dy}\right) \tag{4.24}$$

$$\dot{\gamma}_{xz} = \frac{1}{2}\left(\frac{du}{dz} + \frac{dw}{dx}\right) \tag{4.25}$$

And for last, the fourth motion of a fluid particle is the *extensional strain* or *dilatation*. Looking into Fig. 12, the extensional strain on x direction is defined as the fractional increase in length of the horizontal side of the fluid particle, that is, segment $\overline{BC}$. As well explained by Malkin (1994), the absolute value of $\overline{B'C'} - \overline{BC}$ is not important, because the initial length $\overline{BC}$ might be quite arbitrary, only relative change of the distance between two sides is important:

$$\gamma_{xx} = \frac{\overline{B'C'} - \overline{BC}}{\overline{BC}} = \frac{(dx + \partial u/\partial x\, dx\, dt) - dx}{dx} = \frac{\partial u}{\partial x}dt \tag{4.26}$$

Similarly as we did on the other types of motion, we have the three-dimensional *shear strain rates* as:

$$\dot{\gamma}_{xx} = \frac{\partial u}{\partial x} \quad \dot{\gamma}_{yy} = \frac{\partial v}{\partial y} \quad \dot{\gamma}_{zz} = \frac{\partial w}{\partial z} \tag{4.27}$$

Join all *strain rate* components - extensional and shear - we can constitute a second-order strain rate tensor:

$$\begin{bmatrix} \dot{\gamma}_{xx} & \dot{\gamma}_{xy} & \dot{\gamma}_{xz} \\ \dot{\gamma}_{yx} & \dot{\gamma}_{yy} & \dot{\gamma}_{yz} \\ \dot{\gamma}_{zx} & \dot{\gamma}_{zy} & \dot{\gamma}_{zz} \end{bmatrix} \tag{4.28}$$

Regarding the deformation of a particle of fluid, Stokes (1845) developed the three following postulates:

- The fluid is continuous, and it's stress tensor, τ_{ij}, has a linear relation to strain rate tensor, $\dot{\gamma}_{ij}$
- The fluid is isotropic, i.e., it's properties are independent of the direction, and therefore the deformation law is independent of the coordinate axes in which it is expressed
- When do not have strain rate between adjacent particles of fluid, the deformation must reduce to the hydrostatic pressure, $\tau_{ij} = -p\delta_{ij}$, where δ_{ij} is the Kronecker delta function ($\delta_{ij} = 1$ if $i = j$ and $\delta_{ij} = 0$ if $i \neq j$)

Therefore, associating the mathematical developments presented earlier with the postulates of Stokes (1845), the following formulation for the stress tensor is achieved (further details in chapter 2 of White (2006)) from Eq. 4.14:

$$\tau_{ij} = -p\delta_{ij} + \mu\left(\frac{\partial u_i}{\partial x_j} + \frac{\partial u_j}{\partial x_i}\right) + \delta_{ij}\lambda\,\nabla\cdot u_i \tag{4.29}$$

4.3.2 The linear momentum balance equations

Now, it's possible to obtain the linear momentum balance equations by replacing the stress relations, equation 4.29, on Newton's law, as:

$$\rho\frac{Du_i}{Dt} = \rho g_i - \nabla \mathrm{p} + \frac{\partial}{\partial x_i}\left[\mu\left(\frac{\partial u_i}{\partial x_j} + \frac{\partial u_j}{\partial x_i}\right) + \delta_{ij}\lambda\,\nabla\cdot u_i\right] \tag{4.30}$$

Dismembering Eq. 4.30 in scalar form, we have:

$$\begin{aligned}
\rho\frac{Du}{Dt} &= \rho g_x - \frac{d\mathrm{p}}{dx} + \frac{\partial}{\partial x}\left(2\mu\frac{\partial u}{\partial x} + \lambda\,\nabla\cdot\mathbf{u}\right) + \frac{\partial}{\partial y}\left[\mu\left(\frac{\partial u}{\partial y} + \frac{\partial v}{\partial x}\right)\right] \\
&\quad + \frac{\partial}{\partial z}\left[\mu\left(\frac{\partial u}{\partial z} + \frac{\partial w}{\partial x}\right)\right] \\
\rho\frac{Dv}{Dt} &= \rho g_y - \frac{d\mathrm{p}}{dy} + \frac{\partial}{\partial x}\left[\mu\left(\frac{\partial v}{\partial x} + \frac{\partial u}{\partial y}\right)\right] + \frac{\partial}{\partial y}\left(2\mu\frac{\partial v}{\partial y} + \lambda\,\nabla\cdot\mathbf{u}\right) \\
&\quad + \frac{\partial}{\partial z}\left[\mu\left(\frac{\partial v}{\partial z} + \frac{\partial w}{\partial y}\right)\right] \\
\rho\frac{Dw}{Dt} &= \rho g_z - \frac{d\mathrm{p}}{dz} + \frac{\partial}{\partial x}\left[\mu\left(\frac{\partial w}{\partial x} + \frac{\partial u}{\partial z}\right)\right] + \frac{\partial}{\partial y}\left[\mu\left(\frac{\partial v}{\partial z} + \frac{\partial w}{\partial y}\right)\right] \\
&\quad + \frac{\partial}{\partial z}\left(2\mu\frac{\partial w}{\partial z} + \lambda\,\nabla\cdot\mathbf{u}\right)
\end{aligned} \tag{4.31}$$

The above equations can be simplified if we do some thermal decoupling, assuming ρ and μ constants. With $\rho = \mathit{constant}$, the term $\nabla\cdot\mathbf{u}$ vanishes from the Eqs. 4.30 and 4.31, due to continuity (Eq. 4.1), also eliminating the λ coefficient. Then, if we assume a fixed temperature and pressure, turning viscosity term constant, $\mu = \mathit{constant}$, so we have the simplified linear momentum balance equation for constants viscosity and specific mass:

$$\rho\frac{D\mathbf{u}}{Dt} = \rho\mathbf{g} - \nabla\mathrm{p} + \mu\nabla^2\mathbf{u} \tag{4.32}$$

Now, based on the considerations made in the previous paragraph, if we only disregard the physical and numerical constancy of viscosity μ, being able to vary it by some specific criterion, Eq. 4.30 returns to:

$$\rho\frac{Du_i}{Dt} = \rho g_i - \nabla\mathrm{p} + \frac{\partial}{\partial x_i}\left[\mu\left(\frac{\partial u_i}{\partial x_j} + \frac{\partial u_j}{\partial x_i}\right)\right] \tag{4.33}$$

For this specific case in which viscosity varies, the latter will be linked to the second Galilean invariant, as will be presented in chapter 5.

4.4 Nondimensional numbers

The dynamics of multifluid and multiphase flows are governed by a variety of nondimensional numbers, depending on the specific conditions driving the flow. Tryggvason, Scardovelli e Zaleski (2011) presented these nondimensional numbers on it's section 2.6.

4.4.1 Reynolds number

The Reynolds number is a dimensionless measure of the relative importance of inertial and viscous effects in fluid flow. It is defined as the ratio of inertial force to viscous force and is widely used to predict flow transitions, turbulence, and overall flow behavior.

$$\mathrm{Re} = \frac{\rho\, U\, L}{\mu} = \frac{U\, L}{\nu} \tag{4.34}$$

In the Eq. 4.34 above, U is the characteristic velocity of the flow and L is the characteristic length of the flow.

4.4.2 Weber number

The Weber number is a dimensionless number describing the relative importance of inertia and interfacial tension forces in a flow. It is often used in dynamic problems involving drops and bubbles. For liquids of low viscosity, the deformation of a drop is determined primarily by the ratio of the aerodynamic forces and the interfacial tension forces:

$$\mathrm{We} = \frac{\rho\, U^2\, L}{\sigma} \tag{4.35}$$

The higher the Weber number, the larger are the deforming external pressure forces compared with the reforming interfacial tension forces.

4.4.3 Ohnesorge number

The Ohnesorge number is a dimensionless number describing the relative importance of inertia, viscosity, and capillarity in viscous liquid flow problems. It is often used in contexts of spraying and atomization.

$$\mathrm{Oh} = \frac{\mu}{\sqrt{\rho\, \sigma\, L}} = \frac{\mu^*}{\sqrt{\rho^*}} \frac{\sqrt{We}}{Re} \tag{4.36}$$

where $\rho^* = \rho_d/\rho_c$ and $\mu^* = \mu_d/\mu_c$.

5 Rheology of non-Newtonian fluids

5.1 Introduction

Rheology is a science that deals with the deformation of any material as a result of the applied stress over it (CARREAU; KEE; CHHABRA, 2021).

It is possible to consider two extremes regarding the response of materials: first, a non-deformable body, and on the other hand, an inviscid fluid. For the former, the modulus of elasticity is infinite, while for the latter, the viscosity is zero. Real materials have properties of modulus of elasticity and viscosity that fluctuate within these two extremes.

Carreau, Kee e Chhabra (2021) consistently summarized, as shown in the table below, the possible behaviors of fluids between these two extremes:

Continuum mechanics	Fluids	Inviscid fluid (ideal case with $\mu = 0$)	None
		Linear viscous fluid (Newtonian behavior)	Water
		Non-linear viscous material	Suspensions in Newtonian media
		Linear viscoelastic material	Polymer under small deformation
		Non-linear viscoelastic material	Concentrated polymer solutions or plastics under large deformation
	Solids	Non-linear elastic material	Rubber
		Linear elastic solid	Linear Hookean spring
		Non-deformable solid (ideal case with $G = \infty$)	None

Table 2 – Summary of rheological behavior. Adapted from Carreau, Kee e Chhabra (2021)

In the development of his rheological model, Cross (1965) reinforces that a deep understanding of the relationship between viscosity and shear rate is a fundamental basis for comprehending non-Newtonian behavior.

5.2 Fluid behavior

5.2.1 Newtonian fluid

Barnes (2000) defines a Newtonian fluid as:

> A Newtonian liquid is one for which the viscosity—although varying with temperature and pressure—does not vary with shear rate or time; nor does such a liquid display any elastic properties or extensional anomalies.

And it's important establish that - as cited by Barnes (2000) - the word "non-Newtonian" has a lower case prefix "n" and the word is hyphenated.

According to Rao (1999), typical Newtonian foods are those containing compounds of low molecular weight, and that do not contain large concentrations of either dissolved polymers (e.g., pectins, proteins, starches) or insoluble solids.

Now, advancing on the subject, consider the laminar flow of a thin layer of an incompressible fluid between two parallel plates (see Fig. 13). The horizontal force imposed on the upper plate, creates an opposite friction force to balance the system. This friction force between the upper plate and the internal fluid may be expressed as a linear relation to the velocity gradient, as:

$$\frac{F}{A} = \tau_{yx} = \mu \left(-\frac{dV_x}{dy} \right) = \mu \dot{\gamma}_{yx} \tag{5.1}$$

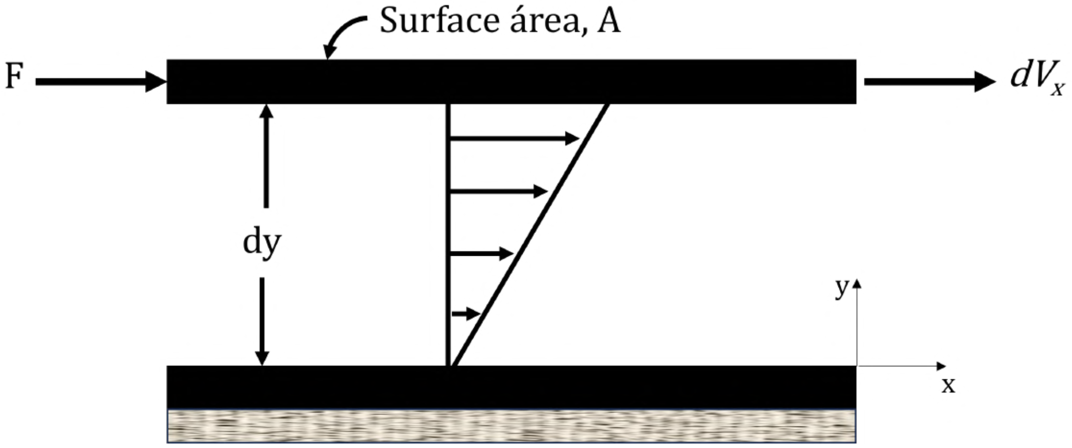

Figure 13 – Schematic representation of unidirectional shearing flow

The first subscript y on the variables τ and $\dot{\gamma}$ represents the interfacial plane where the shearing is happening, on a normal direction to the flow, while the second subscript x represents the direction of the force and flow.

The constant of proportionality, μ, is the ratio of shear stress to the shear rate, being called as the Newtonian viscosity. This constant of proportionality is independent of the shear stress or shear rate, only depending on the material and its temperature and pressure.

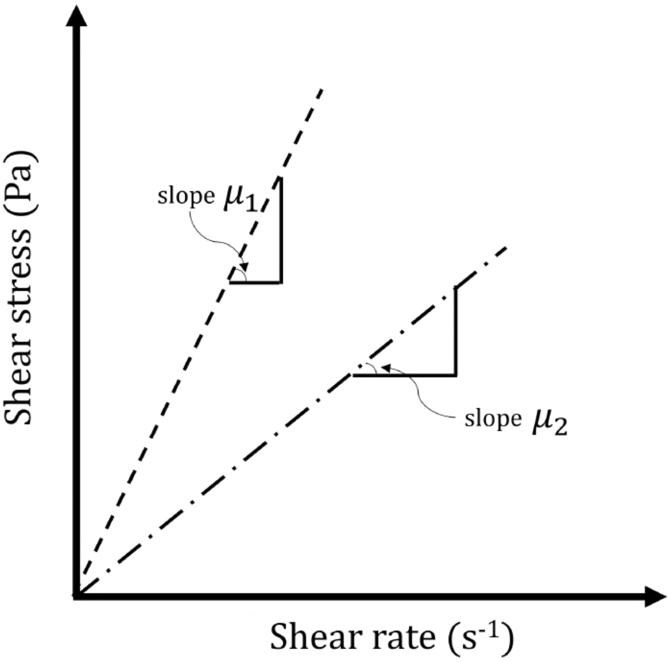

Figure 14 – Schematic representation of the constant of proportionality called viscosity, μ

On the above figure, it is notable that the slope of the curve that represents the relation between shear stress and shear rate is the viscosity μ, and that this one is constant for Newtonian fluids.

According to Barnes (2000), at high-enough shear rate, all liquids become non-Newtonian. But, for example, it has even been estimated that pentane becomes non-Newtonian above shear rates of $5 \cdot 10^6\,\mathrm{s}^{-1}$, while water has this non-linear behavior at an $10^{12}\,\mathrm{s}^{-1}$ shear rate order.

5.2.2 Non-Newtonian fluid

A Generalized Newtonian Fluid (GNF) is one defined as being purely viscous, depending solely on the shear rate or stress applied to the fluid element. In many flow configurations, viscoelasticity does not significantly influence the flow, and non-Newtonian viscosity, η, is sufficient to describe the fluid's rheology (BIRD, 1987; CARREAU; KEE; CHHABRA, 2021).

For this class of fluids, the curves of shear stress versus shear rate are non-linear and some can not starts from the origin. So, in this case, the slope of the curves are not constant, depending on factors as the flow geometry, pressure, temperature, shear rate and, sometimes, on the kinematic history of the fluid element.

As stated by Chhabra e Richardson (2011), the non-Newtonian fluids can be grouped in the three following classes:

- Time-independent fluids: The ones that the shear rate at any point is determined only by the value of the shear stress at that point. They are also called as "purely viscous", "inelastic" or "Generalized Newtonian Fluids" (GNF)

- Time-dependent fluids: The ones also depends on the duration of the shearing and their kinematic history
- Viscoelastic fluids: These fluids has characteristics of both ideal fluids and elastic solids, also showing partial elastic recovery, after deformation

Given that the focus of this study revolves particularly around human blood, the discussion will now delve deeper into time-independent fluids.

5.2.3 Time-independent fluid behavior

The flow behavior of this class of fluid may be described by this constitutive relation:

$$\boldsymbol{\tau} = \eta(\dot{\gamma}) \cdot \dot{\boldsymbol{\gamma}} \tag{5.2}$$

It means that the value of $\dot{\gamma}$ for each differential part of the fluid is determined by the shear stress on each one of this points.

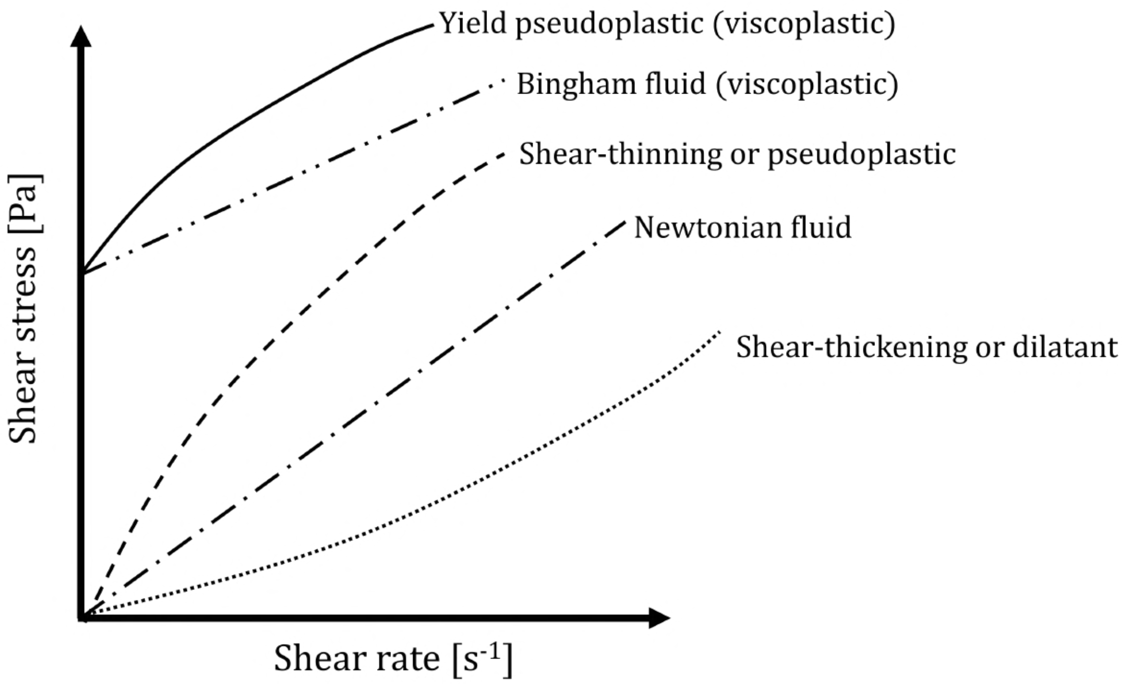

Figure 15 – Time-independent flow behavior

The shear-thinning fluid (figure 15) is the most common type fluid observed in non-Newtonian fluids, and is characterized by an apparent viscosity which decreases with increasing shear rate. Most of the shear-thinning fluids exhibits - both at very low and very high shear rates - Newtonian behavior, with a constant viscosity level.

Rao (1999) tells that is preferred the expression *shear-thinning* than *pseudoplastic*, because it is an accurate description of the shear stress *versus* shear rate curve.

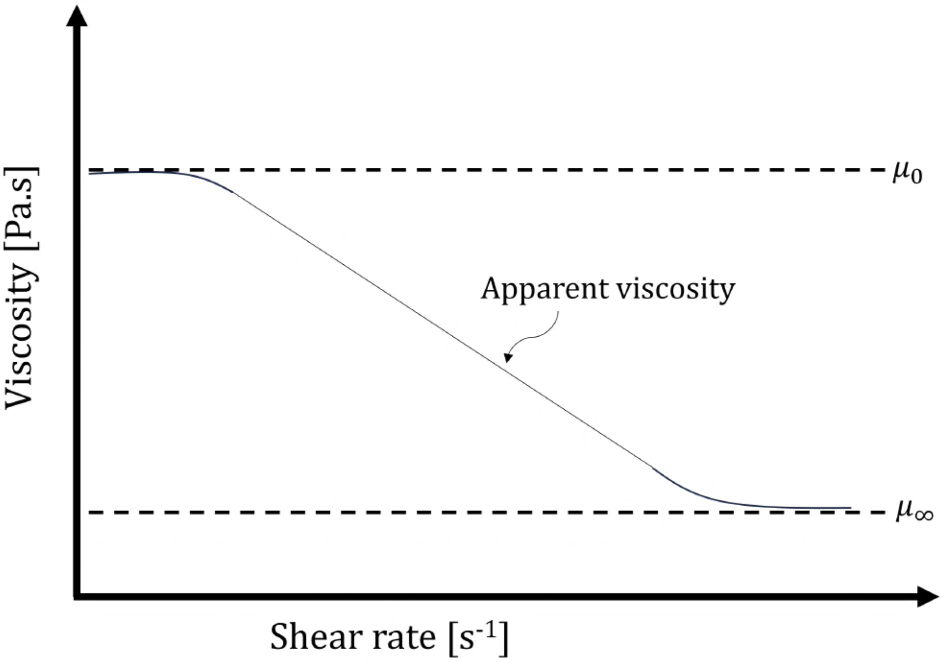

Figure 16 – Schematic shear-thinning viscosity profile

The viscoplastic fluid behavior is characterized by an yield stress (τ_0), below which flow does not occur. As this yield stress is overcome, the fluid starts to flow, which may be through a linear or non-linear relation, but it will not pass through the origin.

When the fluid has a linear curve when $|\tau_{yx}| > |\tau_0|$, it is called Bingham plastic fluid, and it's characterized by a constant viscosity after the flow starts. On the opposite, when the fluid has a non-linear curve when $|\tau_{yx}| > |\tau_0|$, it is called yield-pseudoplastic fluid.

Many workers in this field view the yield stress in terms of the transition from a solid-like (high viscosity) to a liquid-like (low viscosity) state which occurs abruptly over an extremely narrow range of shear rates or shear stress.

Common examples of viscoplastic fluid behaviour include particulate suspensions, emulsions, foodstuffs, blood and drilling muds (BARNES, 2000).

And finally, the shear-thickening or dilatant fluids has the behavior of increase viscosity with increasing shear rate. This sub-class, according to Chhabra e Richardson (2011), has received very little attention and is found very few reliable data about this subject.

5.3 The Galilean invariant

In the subsequent chapters, we will want to make constitutive equations independent of the coordinate system. It will be necessary to make scalar rheological parameters like the modulus or viscosity as a function of a tensor. To explain, consider how the kinetic energy depends on the vector velocity. The kinetic energy is given by:

$$E_k = \frac{1}{2} m V^2 \tag{5.3}$$

where $V^2 = \mathbf{u} \cdot \mathbf{u}$. Kinetic energy is a function of the scalar product of the velocity vector, the magnitude of the velocity squared. Thus, $\mathbf{u} \cdot \mathbf{u}$ does not depend on the coordinate system; it is the *invariant* of the vector $\mathbf{u}$.

Along the same line of reasoning, there is only one commonly used invariant of a vector: it's magnitude. However, there are three possible invariant scalar functions of a tensor.

For a generic tensor as:

$$\mathbf{T} = \begin{bmatrix} T_{11} & T_{12} & T_{13} \\ T_{21} & T_{22} & T_{23} \\ T_{31} & T_{32} & T_{33} \end{bmatrix} \tag{5.4}$$

the three invariants are:

$$I_{\mathbf{T}} = \mathrm{tr}\mathbf{T} = T_{11} + T_{22} + T_{33} \tag{5.5}$$

$$\begin{aligned} II_{\mathbf{T}} = \frac{1}{2}\left[I_{\mathbf{T}}^2 - \mathrm{tr}\mathbf{T}^2\right] &= T_{11}T_{22} + T_{11}T_{33} + T_{22}T_{33} \\ &- T_{12}T_{21} - T_{23}T_{32} - T_{13}T_{31} \end{aligned} \tag{5.6}$$

$$\begin{aligned} III_{\mathbf{T}} = \det\mathbf{T} &= T_{11}T_{22}T_{33} + T_{12}T_{23}T_{31} + T_{12}T_{32}T_{21} \\ &- T_{11}T_{23}T_{32} - T_{21}T_{12}T_{33} - T_{31}T_{22}T_{13} \end{aligned} \tag{5.7}$$

$I_{\mathbf{T}}$ is called the first invariant of the tensor $\mathbf{T}$, $II_{\mathbf{T}}$ the second invariant and $III_{\mathbf{T}}$ the third invariant. They are called invariants because no matter the coordinate system used, the invariants will lead to the same value ever.

Now, it is possible to construct similar measurement to the strain rate tensor, putting the shear rate in function of it's invariants, so that is possible to complete the three-dimensional linear momentum balance equation (eq. 4.30).

The strain rate tensor, $\mathbf{S}$, is given by:

$$\mathbf{S} = \frac{1}{2}\left[(\nabla\mathbf{u}) + (\nabla\mathbf{u})^T\right] \tag{5.8}$$

So:

$$\begin{aligned}
2\mathbf{S} = \left[(\nabla \mathbf{u}) + (\nabla \mathbf{u})^T\right] &= \begin{bmatrix} S_{11} & S_{12} & S_{13} \\ S_{21} & S_{22} & S_{23} \\ S_{31} & S_{32} & S_{33} \end{bmatrix} + \begin{bmatrix} S_{11} & S_{21} & S_{31} \\ S_{12} & S_{22} & S_{32} \\ S_{13} & S_{23} & S_{33} \end{bmatrix} \\
2\mathbf{S} &= \begin{bmatrix} S_{11} + S_{11} & S_{12} + S_{21} & S_{13} + S_{31} \\ S_{21} + S_{12} & S_{22} + S_{22} & S_{23} + S_{32} \\ S_{31} + S_{13} & S_{32} + S_{23} & S_{33} + S_{33} \end{bmatrix}
\end{aligned} \tag{5.9}$$

Since the strain rate tensor is symmetric, we can do $S_{12} = S_{21}$, $S_{13} = S_{31}$ and $S_{23} = S_{32}$. So:

$$2\mathbf{S} = \begin{bmatrix} 2S_{11} & 2S_{12} & 2S_{13} \\ 2S_{12} & 2S_{22} & 2S_{23} \\ 2S_{31} & 2S_{23} & 2S_{33} \end{bmatrix} \tag{5.10}$$

The second-order Galilean invariant of the strain rate tensor, $II_{2\mathbf{S}}$, is given by:

$$II_{2\mathbf{S}} = \frac{1}{2}\left[I_{2\mathbf{S}}^2 - \operatorname{tr}\left[(2\mathbf{S})^2\right]\right] \tag{5.11}$$

In turn, the first-order Galilean invariant of the strain rate tensor, $I_{2\mathbf{S}}$, is:

$$I_{2\mathbf{S}} = \operatorname{tr}(2\mathbf{S}) = 2S_{11} + 2S_{22} + 2S_{33} \tag{5.12}$$

Squaring, is obtained:

$$\begin{aligned}
I_{2\mathbf{S}}^2 &= (2S_{11} + 2S_{22} + 2S_{33}) \cdot (2S_{11} + 2S_{22} + 2S_{33}) \\
I_{2\mathbf{S}}^2 &= 4\left[S_{11}^2 + S_{22}^2 + S_{33}^2 + 2\left(S_{11}S_{22} + S_{22}S_{33} + S_{33}S_{11}\right)\right]
\end{aligned} \tag{5.13}$$

Solving now $\operatorname{tr}\left[(2\mathbf{S})^2\right]$, we have:

$$\operatorname{tr}\left[(2\mathbf{S})^2\right] = \operatorname{tr}\left[\begin{bmatrix} 2S_{11} & 2S_{12} & 2S_{13} \\ 2S_{12} & 2S_{22} & 2S_{23} \\ 2S_{31} & 2S_{23} & 2S_{33} \end{bmatrix} \cdot \begin{bmatrix} 2S_{11} & 2S_{12} & 2S_{13} \\ 2S_{12} & 2S_{22} & 2S_{23} \\ 2S_{31} & 2S_{23} & 2S_{33} \end{bmatrix}\right] \tag{5.14}$$

$$\begin{aligned}
\operatorname{tr}\left[(2\mathbf{S})^2\right] = &\left(2S_{11} \cdot 2S_{11} + 2S_{12} \cdot 2S_{12} + 2S_{13} \cdot 2S_{13}\right) \\
&+ \left(2S_{12} \cdot 2S_{12} + 2S_{22} \cdot 2S_{22} + 2S_{23} \cdot 2S_{23}\right) \\
&+ \left(2S_{31} \cdot 2S_{31} + 2S_{23} \cdot 2S_{23} + 2S_{33} \cdot 2S_{33}\right)
\end{aligned} \tag{5.15}$$

$$\operatorname{tr}\left[(2\mathbf{S})^2\right] = 4 \cdot \left[S_{11}^2 + S_{22}^2 + S_{33}^2 + 2\left(S_{12}^2 + S_{23}^2 + S_{13}^2\right)\right] \tag{5.16}$$

Join 5.13 and 5.16, is obtained:

$$\begin{aligned} II_{2\mathbf{S}} = \frac{1}{2}\Big\{ & 4\left[S_{11}^2 + S_{22}^2 + S_{33}^2 + 2\left(S_{11}S_{22} + S_{22}S_{33} + S_{33}S_{11}\right)\right] \\ & -4\left[S_{11}^2 + S_{22}^2 + S_{33}^2 + 2\left(S_{12}^2 + S_{23}^2 + S_{13}^2\right)\right]\Big\} \end{aligned}$$

$$II_{2\mathbf{S}} = 4\left[\left(S_{11}S_{22} + S_{22}S_{33} + S_{33}S_{11}\right) - \left(S_{12}^2 + S_{23}^2 + S_{13}^2\right)\right] \tag{5.17}$$

5.4 Shear rate in function of Galilean invariant

Here, it is important to emphasize that several different relationships have been found in the literature* between the scalar value $\dot{\gamma}$ and the second Galilean invariant, $II_{\mathbf{T}}$ (see Eq. 5.6). These variations can lead to different results, and the relationship used by the reference being employed should always be checked during validations of computational simulations.

For example, Cho e Kensey (1991) utilizes the following relationship between the scalar $\dot{\gamma}$ and the second Galilean invariant :

$$\dot{\gamma} = \sqrt{\frac{1}{2} II_{2\mathbf{D}}} = \sqrt{\frac{1}{2}\left[\sum_i \sum_j \dot{\gamma}_{ij}\dot{\gamma}_{ji}\right]} \tag{5.18}$$

This relationship results in the following final combination of the components of the strain rate tensor:

$$\dot{\gamma} = \sqrt{2\left[\left(S_{11}S_{22} + S_{22}S_{33} + S_{33}S_{11}\right) + 2\left(S_{12}^2 + S_{23}^2 + S_{13}^2\right)\right]} \tag{5.19}$$

Similar occurrences happen for the relationships used by Shibeshi e Collins (2005) (eq. 5.20), Siauw, Ng e Mazumdar (2000) (eq. 5.21), and Bilgi e Atalık (2020) (eq. 5.22), despite the diverse nomenclature:

$$\dot{\gamma} = \sqrt{\frac{1}{2}\left[\sum_i \sum_j D_{ij} D_{ji}\right]} \tag{5.20}$$

where $D_{ij} = \frac{1}{2}\left(\frac{\partial u_i}{\partial x_j} + \frac{\partial u_j}{\partial x_i}\right)$.

---

* In all the relationships presented, the original nomenclature used in the articles has been preserved.

$$\sqrt{\mathbf{J}_2} = \sqrt{\frac{1}{2} V_{ij}\, V_{ji}} \tag{5.21}$$

where $V_{ij} = \frac{1}{2}\left(\frac{\partial u_i}{\partial x_j} + \frac{\partial u_j}{\partial x_i}\right)$.

$$\dot{\gamma} = \sqrt{I_2/2} = \sqrt{II_{2\mathbf{D}}/2} \tag{5.22}$$

Additionally, Shateyi e Muzara (2020) achieved the same final relationship as Cho e Kensey (1991) through another proposal:

$$\dot{\gamma} = \left[\frac{1}{2} tr(\mathbf{A}^2)\right]^{\frac{1}{2}} \tag{5.23}$$

where $\mathbf{A} = \nabla \mathbf{v} + \nabla \mathbf{v}^T$.

On the other hand, Buchanan et al. (2003) caused significant confusion between terminologies, failing to properly define the relationships between viscosity, total shear rate, and the second Galilean invariant. The following relationships were indicated in their paper:

$$\eta(II_D) \quad and \quad \eta(\dot{\gamma}) \quad and \quad \dot{\gamma} = 2\mathbf{D} \tag{5.24}$$

$$\mathbf{D} = \frac{1}{2}\left[\nabla \mathbf{v} + (\nabla \mathbf{v})^T\right] \tag{5.25}$$

$$II_D = \frac{1}{2}\left[I_D^2 + \text{tr}\left[(D)^2\right]\right] \tag{5.26}$$

The scalar of the shear rate found by Eq. 5.26 results in:

$$II_{\mathbf{D}} = \left(S_{11}^2 + S_{22}^2 + S_{33}^2\right) + \left(S_{11}S_{22} + S_{22}S_{33} + S_{33}S_{11}\right) + \left(S_{12}^2 + S_{23}^2 + S_{13}^2\right) \tag{5.27}$$

Neofytou (2005), on the other hand, proceeded to use a different relationship to the second Galilean invariant, absorbing only the trace of the strain rate tensor, as follows:

$$|\dot{\gamma}| = \sqrt{2tr(\mathbf{D}^2)} \tag{5.28}$$

where $\mathbf{D} = \frac{1}{2}\left[\nabla \mathbf{v} + (\nabla \mathbf{v})^T\right]$.

This results in a scalar for $\dot{\gamma}$ as follows:

$$\dot{\gamma} = \sqrt{2\ (S_{11}^2 + S_{22}^2 + S_{33}^2) + 4\ (S_{12}^2 + S_{23}^2 + S_{13}^2)} \tag{5.29}$$

Papanastasiou (1987) utilized the following relationship, not specifying the equation - in terms of the strain rate tensor - used to calculate the second Galilean invariant.

$$\dot{\gamma} = \sqrt{II_{\mathbf{D}}} \tag{5.30}$$

Macosko (1994), on the other hand, indicates Eq. 5.31 for the scalar of the shear rate in terms of the Galilean invariant, besides presenting Eq. 5.11 - in the initial chapters of his book - for the second Galilean invariant:

$$\dot{\gamma} = \sqrt{II_{2\mathbf{S}}} \tag{5.31}$$

Nisco et al. (2023), with different nomenclature (eq. 5.32), and Skiadopoulos, Neofytou e Housiadas (2017) arrived at the same relationship for the scalar $\dot{\gamma}$ as described by Neofytou (2005):

$$\dot{\gamma} = \sqrt{2\,\mathbf{D}(\mathbf{v}) : \mathbf{D}(\mathbf{v})} = \sqrt{2\,tr(\mathbf{D}(\mathbf{v})^2)} \tag{5.32}$$

where $\mathbf{D}(\mathbf{v}) = \frac{\nabla\mathbf{v}+\nabla\mathbf{v}^T}{2}$.

Chandran et al. (2020), finally, also using varied nomenclature, achieved the same results as Neofytou (2005).

$$\overline{\overline{\dot{\gamma}}} = \frac{1}{2}(\nabla\mathbf{u} + \nabla\mathbf{u}^T) \tag{5.33}$$

where $\dot{\gamma} = \sqrt{2\,\overline{\overline{\dot{\gamma}}} : \overline{\overline{\dot{\gamma}}}}$.

In this dissertation, for all computational simulations performed, the relation 5.31 was used to model the shear rate as a function of the Galilean invariant, the latter being calculated as demonstrated in Eq. 5.17.

6 Rheological viscosity models for blood

6.1 Introduction

As well highlighted by Barnes (2000), care must be taken when working with rheological models that represent the physical viscosity of non-Newtonian fluids, as they are developed for a specific range of shear rates, usually those experienced in real fluid operations within human body.

For the present research, where blood operates outside human body, we will observe the behavior of rheological models outside their ranges of shear rates used in their conception, indicating avenues for further research into the different features promoted by different models.

Next, rheological models representing viscosity for time-independent non-Newtonian fluids will be presented, where the shear rate experienced by the fluid elements is the main factor of viscosity variation. All these models mentioned below have been used to model human blood viscosity.

To adhere to the most widely used nomenclature in the community (Barnes (2000), Rao (1999), Malkin (1994), Chhabra e Richardson (2011), Macosko (1994) and Papanastasiou (1987)), the symbol η will be used to represent the viscosity of a non-Newtonian fluid when the following rheological models are being considered.

6.2 Shear-thinning models

6.2.1 Power-law model of Oswald de Waele

According to Bird (1987), in the power-law model of Ostwald de Waele (OSTWALD, 1923), the relationship between shear stress and shear rate (both plotted on logarithmic coordinates) for shear-thinning fluids can be approximated by a straight line within a limited range of either of these coordinates. For this part of the curve, the following relationship is applied:

$$\boldsymbol{\tau} = m\,\dot{\boldsymbol{\gamma}}^{n} \tag{6.1}$$

In this case, the viscosity of the power-law fluid (or Ostwald de Waele fluid) is given by:

$$\eta = \boldsymbol{\tau}/\dot{\boldsymbol{\gamma}} = m\,\dot{\gamma}^{n-1} \tag{6.2}$$

If:

- $n < 1$, the fluid exhibits shear-thinning properties
- $n = 1$, the fluid exhibits Newtonian behavior
- $n > 1$, the fluid exhibits shear-thickening behavior

In Eq. 6.2, m and n are two empirical constants known as the *fluid consistency index* and the *fluid behavior index*, respectively. The constant m has the unit of measurement $\mathrm{Pa{\cdot}s}^n$ and the constant n is dimensionless.

Physically, the fluid behavior index n is related to the decay/growth of viscosity. Within a fixed range of shear rate, as the exponent n increases towards unity, viscosity undergoes a smoothing in its decline. On the other hand, an increase in the consistency index m indicates a reduction in the rate of viscosity variation with respect to the shear rate, resulting in a curve with higher extremities of viscosity values for the same operational region of shear rate.

While the power-law model provides a straightforward depiction of shear-thinning behavior, it is not without its limitations. Typically, its applicability is confined to a restricted range of shear rates, leading to the dependence of the fitted values of m and n on the considered shear rate range. Additionally, the model does not provide predictions for zero and infinite shear viscosities, η_0 and η_∞.

6.2.2 Carreau model

This is a four-parameter model and has a sufficient flexibility to fit a large range of shear rate ($\dot{\gamma}$). The model, according to Bird (1987) and Carreau (1968) is:

$$\eta = \eta_\infty + (\eta_0 - \eta_\infty)\left[1 + (\lambda\dot{\gamma})^2\right]^{\frac{n-1}{2}} \tag{6.3}$$

On (6.3), η_0 is the zero-shear rate viscosity, η_∞ is the infinite-shear rate viscosity, λ is a time constant and n is the power-law expoent.

6.2.3 Carreau-Yasuda model

According to Carreau (1968), this is a highly successful five-parameter model and also has a sufficient flexibility to fit a large range of shear rate ($\dot{\gamma}$). According to Bird (1987), Carreau (1968) and Yasuda (1979), this model is:

$$\eta = \eta_\infty + (\eta_0 - \eta_\infty)\frac{1}{\left[1 + (\lambda\dot{\gamma})^a\right]^{\frac{1-n}{a}}} \tag{6.4}$$

On (6.4), the first four parameters are the same from Carreau model and a is a dimensionless parameter that describes the transition region between zero-shear rate region and power-law region.

6.2.4 Cross model

Cross (1965) proposed this four-parameters model:

$$\eta = \eta_\infty + (\eta_0 - \eta_\infty)\,\frac{1}{1 + [\lambda\dot{\gamma}]^a} \tag{6.5}$$

According to Cross, λ represents a constant associated with the rupture of molecular linkages.

6.2.5 Simplified Cross model

According to Cross (1965), Steffan et al. (1990), Siauw, Ng e Mazumdar (2000) and Abbasian et al. (2020), simplified Cross model can be described as:

$$\eta = \eta_\infty + (\eta_0 - \eta_\infty)\,\frac{1}{1 + \lambda\dot{\gamma}} \tag{6.6}$$

6.2.6 Modified Cross model

Cho e Kensey (1991) presented a modification of the Carreau-Yasuda model, simplifying the expoent of the terms in brackets from $\frac{n-1}{a}$ to a single m. As expected, both a and m constants are dimensionless.

$$\eta = \eta_\infty + (\eta_0 - \eta_\infty)\,\frac{1}{[1 + [\lambda\dot{\gamma}]^a]^m} \tag{6.7}$$

6.2.7 Powell-Eyring model

Cho e Kensey used Powell e Eyring (1944) discussion about the relaxation theory of flow treated according to statistical mechanics, and applied the inverse hyperbolic-sine on shear rate terms, as:

$$\eta = \eta_\infty + (\eta_0 - \eta_\infty)\left[\frac{\sinh^{-1}\lambda\dot{\gamma}}{\lambda\dot{\gamma}}\right] \tag{6.8}$$

6.2.8 Modified Power-Eyring model

A modification on Powell-Eyring model was proposed by Cho e Kensey (1989) as:

$$\eta = \eta_\infty + (\eta_0 - \eta_\infty)\,\frac{\ln(\lambda\dot{\gamma} + 1)}{[\lambda\dot{\gamma}]^a} \tag{6.9}$$

6.3 Yield-shear-thinning models

6.3.1 Herschel-Bulkley model

In his article, Herschel e Bulkley (1926) says that the flow in a plastic material does not occur until a certain pressure is reached. This is the yield stress experimented by some yield-shear-thinning fluids. So, as explained by Rao (1999), it can be included in the power-law model as:

$$\boldsymbol{\tau} - \tau_0 = m\,\dot{\boldsymbol{\gamma}}^n \tag{6.10}$$

that with some mathematical manipulations is presented by Carreau (1968) and Antonova (2012) as:

$$\eta = \frac{\tau_0}{|\dot{\gamma}|} + \eta_0 |\dot{\gamma}|^{n-1} \tag{6.11}$$

6.3.2 Casson model

Cross (1965) mentioned in his article *Rheology of non-Newtonian fluids: A new flow equation for shear-thinning systems* that Casson has developed a theory, applicable to non-aqueous pigment suspensions, based on the assumption that particles aggregate into linear chains which can be treated as rigid rods. Abbasian et al. (2020) and Siauw, Ng e Mazumdar (2000) also described Casson relation on their researches under medical perspective. So, Casson model (CASSON, 1959) can be described as:

$$\eta = \left(\sqrt{\eta_c} + \sqrt{\tau_c/\dot{\gamma}}\right)^2 \tag{6.12}$$

where τ_c is the same as τ_0, the yield stress.

6.3.3 Modified Casson model

Abbasian et al. (2020) and Karimi et al. (2014) mentioned in their medical field articles the development of the modified Casson equation, devised by Popel e Enden (1993), who utilized parameters from the method of Quemada (1978):

$$\eta = \left(\sqrt{\eta_c} + \frac{\sqrt{\tau_c}}{\sqrt{\lambda} + \sqrt{\dot{\gamma}}}\right)^2 \tag{6.13}$$

6.3.4 K-L model

Abbasian et al. (2020) brought into play the K-L model mentioned by Karimi et al. (2014), which is nothing more than a mathematical manipulation of the Casson model.

$$\eta = \frac{1}{\dot{\gamma}} \left[\tau_c + \eta_c \left(\alpha_2 \sqrt{\dot{\gamma}} + \alpha_1 \dot{\gamma} \right) \right] \tag{6.14}$$

6.3.5 Papanastasiou regularization

Some viscosity models, such as Herschel-Bulkley, Casson, and K-L, can easily induce singularities in regions of the domain where there is no shear rate between adjacent discrete volumes due to the denominator of these models' relationships, resulting in an improper fraction. These singularities are avoided in computational simulations by adding to the numerator the regularization proposed by Papanastasiou (1987), the term $\left[1 - \exp\left(-n\,|II_{2\mathbf{S}}|^{1/2}\right)\right] = [1 - \exp(-n\,\dot{\gamma})]$.

According to Papanastasiou e Boudouvis (1997), the exponent n is responsible for providing a finite stress - at very low shear rates - when discrete elements are subjected to stresses below the yield limit, avoiding the mentioned singularities. The higher the value of n, the closer the *stress - shear rate* curve approaches the original curve, as shown in the Fig. 17.

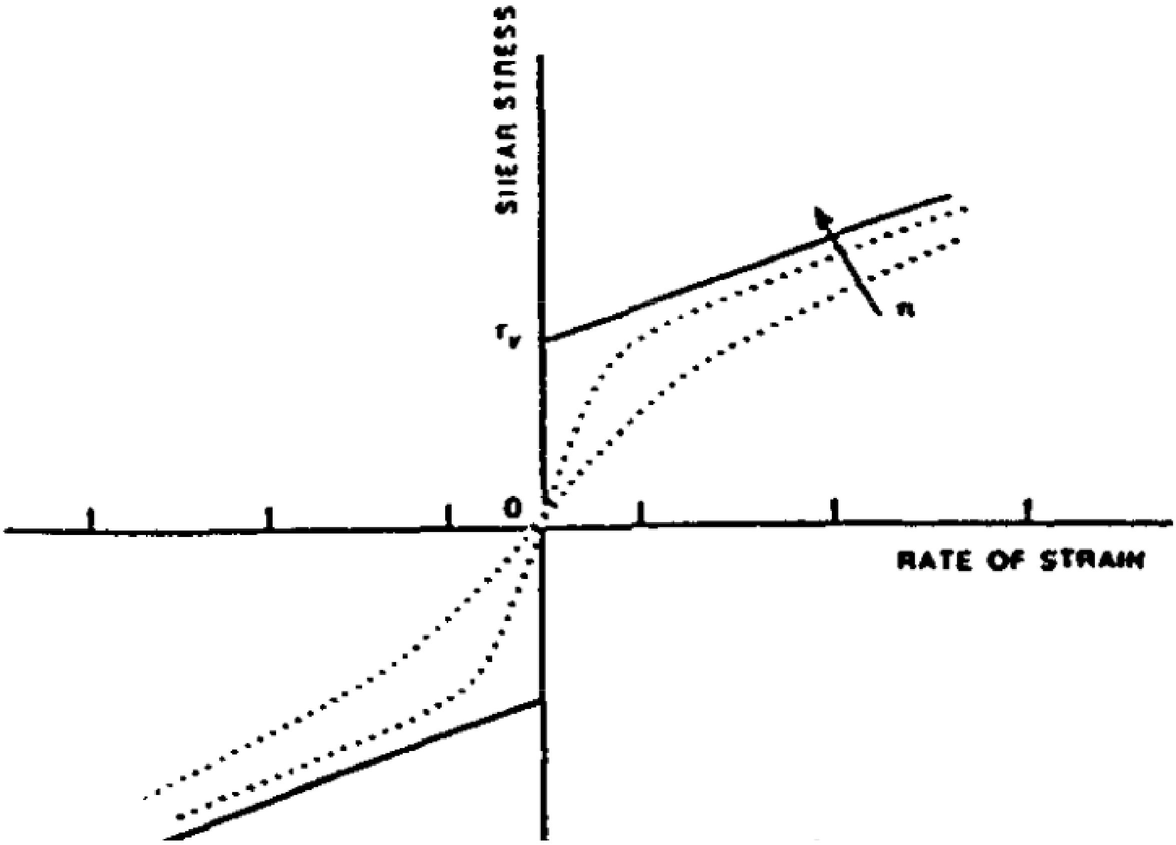

Figure 17 – Example curves for increasing values of n for viscoplastic models. Source: Papanastasiou e Boudouvis (1997)

7 Computational modeling

7.1 MFSim: CFD plataform

According to the user manual's own definition:

> MFSim is a Computational Fluid Dynamics (CFD) simulation software continuously developed since 2007 by the Fluid Mechanics Laboratory of the graduate program of the Mechanical Engineering Faculty (FEMEC) at the Federal University of Uberlândia (UFU).

Considering only the scope of this dissertation - three-dimensional, two-phase, isothermal and incompressible flows of immiscible Newtonian and non-Newtonian fluids - the functionalities incorporated by MFSim are as follows:

- Finite Volume Method (FVM) for discretization
- Pressure-velocity coupling by Fractional Step method
- Second-order divergent and non-divergent space and time discretization
- Implicit and semi-implicit discretization, fully parametric and variable time step
- Immersed Boundary Method (IBM) technique
- Multiphase simulation: Volume of Fluid (VoF), Front-Tracking and Level-set
- Simulation refinement via dynamic adaptive meshing

As presented by Villar (2007), in MFSim, the numerical discretization of balance equations is performed in an Eulerian grid, while the equations for the interface motion are discretized on a moving Lagrangian grid, independent of the Eulerian grid, with communication between them through interpolations and spreading. These peculiarities were exploited in the computational simulations carried out in this work.

Furthermore, for all carried out simulations, the temporal discretization was performed using the *Semi Backward Difference Formula* (SBDF) method (ASCHER; PETZOLD, 1998; BADALASSI; CENICEROS; BANERJEE, 2003). This method treats the diffusive term of the linear momentum balance equation implicitly and the advective term explicitly.

In the computational code MFSim, when solving the linear momentum balance equation, various interpolation schemes for the advective term are employed. Among these, the Barton scheme is renowned for its ability to capture variations in solutions with high resolution, minimizing numerical oscillations. This scheme has demonstrated excellent performance in several preliminary simulations, providing precise and stable results.

However, when applied to the primary problem of free fall of a human blood droplet onto a solid surface (see sec. 10.5), the Barton scheme proved unsatisfactory. The high density ratio ($\rho^* = 895.27$) and viscosity ratio ($\mu^* = 186.49$) present in this specific problem compromised the accuracy of the scheme, highlighting its limitations in scenarios with large gradients and discontinuities.

After identifying that the interpolation scheme of the advective term was the main issue, several other schemes were tested, resulting in the selection of the TVD SUPERBEE. This scheme, part of the Total Variation Diminishing (TVD) family, features a specific limiter that combines high resolution with the prevention of non-physical oscillations (HARTEN, 1983; BAI; YANG; ZHOU, 2018). The TVD SUPERBEE proved particularly effective in preserving the shape of the droplet during the simulation, even under challenging conditions of high density and viscosity ratios. By implementing the TVD SUPERBEE, it was possible to achieve more accurate and stable results, demonstrating its superiority compared to the Barton scheme for this specific type of fluid dynamics problem.

Regarding the computational domain, cubic domains of dimensions $[A_1, B_1, C_1] \times [A_2, B_2, C_2]$ were considered for all simulations. Concerning discretization, initially, the domain contains M, N, and L volumes in the x, y, and z directions, respectively, with computational cell spacings $\Delta x = \frac{A_2 - A_1}{M}$, $\Delta y = \frac{B_2 - B_1}{N}$, and $\Delta z = \frac{C_2 - C_1}{L}$.

As explained by Villar (2007), the center of each computational volume is described by:

$$\mathbf{x}_{i,j,k} = (x_i, y_j, z_k) = \left[A_1 + \left(i - \frac{1}{2}\right)\Delta x,\ B_1 + \left(j - \frac{1}{2}\right)\Delta y,\ C_1 + \left(k - \frac{1}{2}\right)\Delta z\right] \tag{7.1}$$

for $1 \leq i \leq M$, $1 \leq j \leq N$, and $1 \leq k \leq L$.

Also, it is important to emphasize that scalar variables are defined at the center of the computational volume, while vector variables are defined on faces (HARLOW; WELCH, 1965).

During master's research, although the primary objective was to simulate blood droplets in free fall onto a solid surface, it was necessary to conduct several preliminary simulations in the MFSim code to validate the implementation of rheological models for non-Newtonian fluids. In all these simulations, both for validation and those within the dissertation's scope, I opted to use the Fractional Step method instead of the SIMPLE or SIMPLEC methods.

Regarding the pressure-velocity coupling, the Fractional Step method takes into account the role of pressure in incompressible flows, as reported by Chorin (1968), which is to enforce the incompressibility condition, thus not having a thermodynamic role. The Fractional Step method proved particularly effective for pressure-velocity coupling in the linear momentum balance equations. This time discretization method decomposes the solution into sub-steps, separately addressing velocity updating and pressure correction. Initially, an intermediate velocity is calculated without the pressure contribution. Then, a

Poisson equation for pressure is solved to ensure mass conservation. Finally, the velocity is corrected using the obtained pressure. This approach not only increased the numerical stability of the simulations but also ensured the accuracy and efficiency required to handle the complex behaviors of non-Newtonian fluids under the investigated conditions.

Concerning the computational domain mesh, it consists of grouped meshes that are refined in zones of interest of the problem, such as refinement driven by density, vorticity or VoF interface criteria. This refinement occurs at a rate of 2 ($r = 2$), and as the flow progresses in time, the mesh is refined following the imposed refinement criteria.

The base mesh is called l_{base}, while the finest mesh is called l_{top}. Therefore, $l_{base} \leq l \leq l_{top}$, and the spacing of the other meshes is defined as:

$$\Delta x_{l+1} = \frac{\Delta x_l}{r} \tag{7.2}$$

$$\Delta y_{l+1} = \frac{\Delta y_l}{r} \tag{7.3}$$

$$\Delta z_{l+1} = \frac{\Delta z_l}{r} \tag{7.4}$$

In the meantime, the finest mesh is applied to the zones of interest, and the solution in the finer meshes can be approximated by finite differences using the base mesh that covers the entire domain.

The numerical resolution of fluid dynamics systems entails a high and often prohibitive computational cost due to the large number of equations to be solved. Therefore, one solution is the use of the *Multigrid* method, as pointed out by Maliska (2023). This method promotes agility in solving the linear systems linked to solving the fluid dynamics equations of the computational code, and this algorithm is considered one of the fastest and most efficient for solving the mentioned linear systems, as indicated by Zhang (1997).

Finally, for the final and main simulations of this work, blood droplets were defined within the computational domain using the Volume of Fluid (VoF) method, in which the indicator function ϕ was applied with harmonic mean to define the density at the interface, and with arithmetic mean for viscosity (DUAN et al., 2017; HALLMARK; CHEN; DAVIDSON, 2019), as follows:

$$\overline{\rho} = \frac{1}{\frac{(1-\phi)}{\rho_g} + \frac{\phi}{\rho_l}} \tag{7.5}$$

$$\overline{\mu} = \phi \, \mu_l + (1 - \phi) \, \mu_g \tag{7.6}$$

In the previous equations, the subscript l indicates the liquid phase (dispersed phase), while the subscript g indicates the gas phase (continuous phase).

Furthermore, regarding Immersed Boundary Method (IBM), this one allows for the efficient representation of complex boundary geometries within a fixed Cartesian grid by introducing additional force terms in the momentum equations, which mimic the effect of the solid boundaries. It is particularly useful for simulating fluid-structure interactions without the need for mesh conformity to the solid boundaries.

And finally, in all simulations conducted using the MFSim computational code, both for validation and within the scope of the dissertation, the following numerical methods were consistently employed: the Fractional Step method, the SBDF and TVD SUPERBEE schemes, and the Multigrid method for solving the pressure-velocity coupling.

8 Non-Newtonian viscosity models validation

8.1 Permanent Poiseuille flow

8.1.1 Phisycal modeling

This is an horizontal flow between parallel and fixed flat plates (no-slip), due to an imposed pressure gradient. Incompressible flow was assumed, in permanent regime, isothermal and also disregarding gravitational effects.

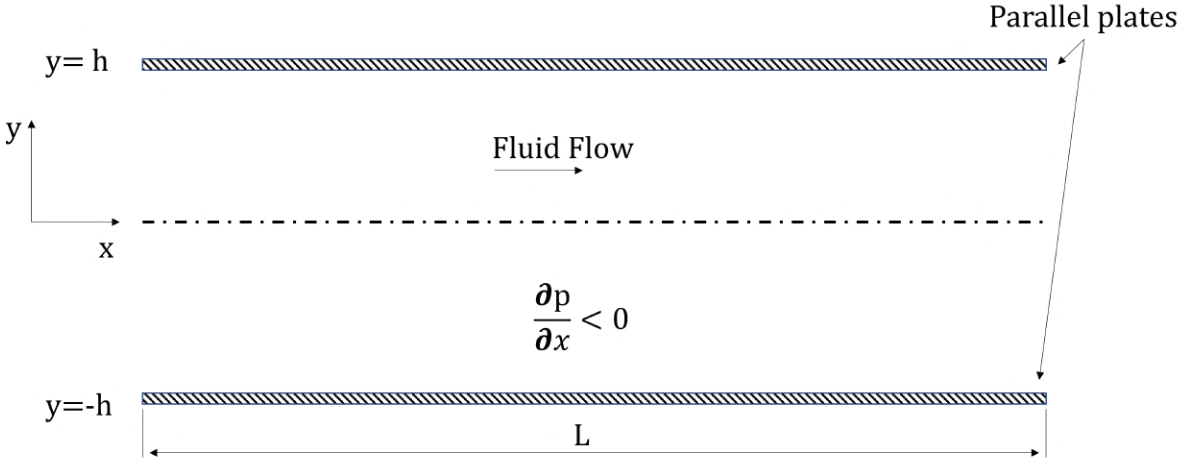

Figure 18 – Schematic diagram of Poiseuille flow

To maintain a laminar flow of Re = 100, was set $\rho = 1\,\mathrm{kg/m^3}$, $\overline{V} = 1\,\mathrm{m/s}$, $B = 1\,\mathrm{m}$ (depth) and $\mu = 0.01$ Pa·s.

The pressure difference between the fluid's inlet ($x = 0$) and outlet ($x = L$) was set to $-0.6\,\mathrm{Pa}$, calculated using Eqs. 13.20 (see Appendix A) and 8.4.

8.1.2 Algebraic-differential mathematical modeling

As the specific mass is constant (incompressible flow), the term $\partial\rho/\partial t$ of mass balance (eq. 4.1) is set to zero. Then we have:

$$\nabla \cdot \mathbf{u} = 0$$

Applying the physical modeling assumptions described in sec. 8.1.1, the linear momentum balance equation (eq. 4.33) results in:

$$\frac{\partial}{\partial y}\left(\boldsymbol{\tau}_{yx}\right) = \frac{\partial p}{\partial x} \tag{8.1}$$

The boundary conditions for this problem are:

$$\begin{cases} V(h) = 0 \\ V(-h) = 0 \end{cases} . \tag{8.2}$$

8.1.3 Continuous mathematical modeling

Solving the previous ODE, considering the imposed boundary conditions, it arrives at the following continuous solution for Newtonian fluids (see Appendix A):

$$u(y) = V_{\text{max}} \left[1 - \left(\frac{y}{h} \right)^2 \right] \tag{8.3}$$

where

$$V_{max} = -\frac{\varphi\, h^2}{2} \tag{8.4}$$

and

$$\varphi = \frac{1}{\mu} \frac{d\text{p}}{dx} \tag{8.5}$$

For non-Newtonian fluids (power-law model), the continuous solution (see Appendix A) found was:

$$u(y) = V_{max} \left[1 - \left(\frac{y}{h} \right)^{\frac{1}{n}+1} \right] \tag{8.6}$$

where

$$V_{max} = -\frac{n \cdot \varphi}{n+1} h^{1/n+1} \tag{8.7}$$

and

$$\varphi = \left[\frac{1}{m} \left(\frac{d\text{p}}{dx} \right) \right]^{1/n} \tag{8.8}$$

It is possible to notice and it was checked that, for the case of $n = 1$, Eq. 8.6 returns to the original equation for Newtonian fluids, Eq. 8.3.

8.1.4 Computational modeling

The domain was defined starting from the origin and extending to the coordinates $(L, H, B) = (5.0\,\text{m}, 1.0\,\text{m}, 1.0\,\text{m})$. The l_{bot} level was defined as $40 \times 8 \times 8$.

The boundary conditions for the parallelepiped domain were defined as follows for each of the three velocity components and for pressure.

For the velocity components u, v, and w, the south, north, bottom and top faces were set with Dirichlet conditions, indicating that the velocity is directly imposed on these faces (all zero in this case). The west and east faces were set with a Neumann condition.

For pressure, the south, north, bottom and top faces were set with Neumann conditions. The west and east faces were set with a Dirichlet condition, where the pressure is directly imposed, as specified in sec. 8.1.3. These configurations ensure an adequate representation of the variables of interest at the domain boundaries, allowing the flow to be directed based on the established pressure drop along the x-axis.

The Courant-Friedrichs-Lewy (CFL) number was set to 0.5. This value was chosen to ensure the stability of the simulation, ensuring that the time step was sufficiently small to accurately capture the rapid dynamics of the flow.

The total simulation time was set to 50 s, which is sufficient to reach the desired steady state.

8.1.5 Computational results

After performing the simulations on the MFSim, the results of the discrete solution converged to the continuous ones. As expected, for $n < 1$ (shear-thinning fluids) the high shear rates regions - occurring near the wall - promotes a reducing on local viscosity, allowing more fluid advection on flow direction, due to pressure imposed, as shown in Figs. 19 and 20. On the other hand, for $n > 1$ (shear-thickening fluids), the pressure applied on the fluid promotes a increasing on local viscosity, creating a imaginative obstacle to normal flow, reducing, therefore, advection on flow direction. For this last cases, the viscosity profiles invert on the graph.

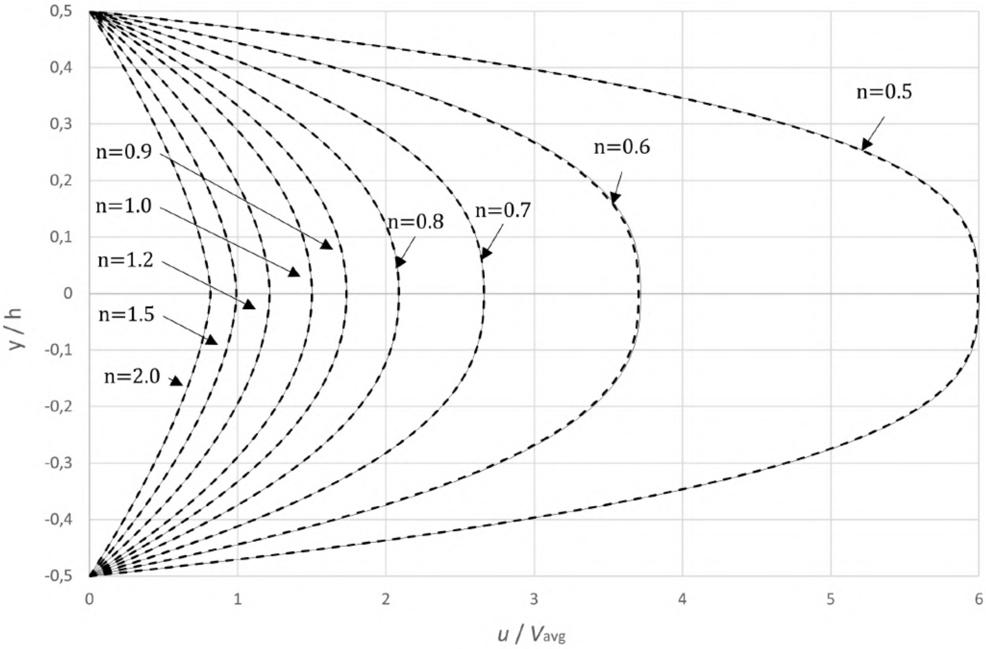

Figure 19 – Continuous (full lines) and discrete (dashed lines) solutions for the u-velocity profiles, for different values of the flow behavior index, n

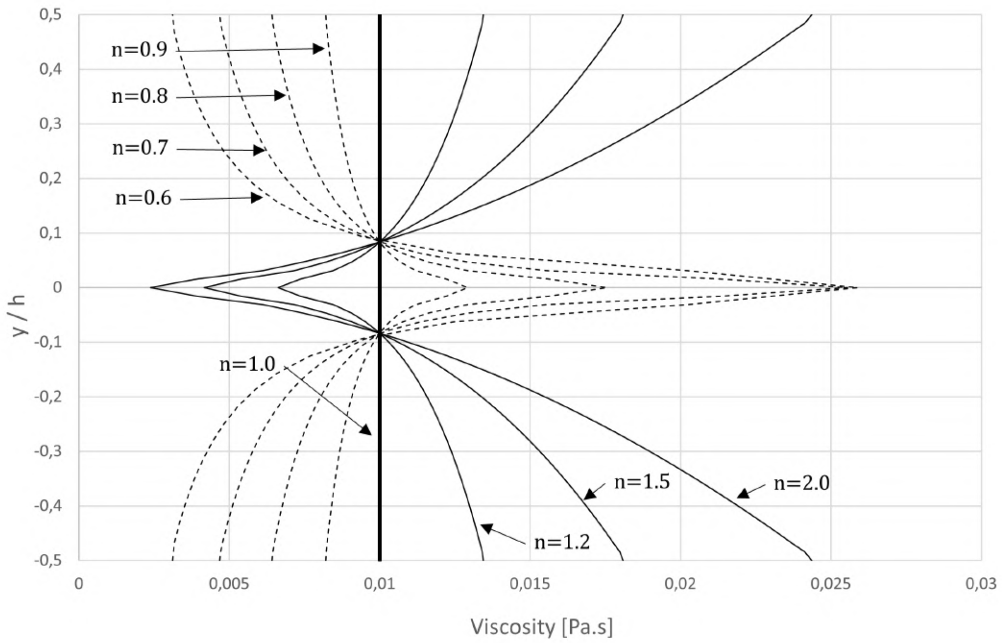

Figure 20 – Viscosity profiles for shear-thinning (dashed lines), shear-thickening (thin full lines) and Newtonian (straight full line) fluids, for different values of the flow behavior index, n

8.2 Transient Couette flow

8.2.1 Phisycal modeling

It is a horizontal flow between parallel flat plates (no-slip), with no pressure gradient in the flow direction, among which the upper plate moves at a constant velocity V. Incompressible and isothermal flow was assumed, in transient regime, disregarding the gravitational effects.

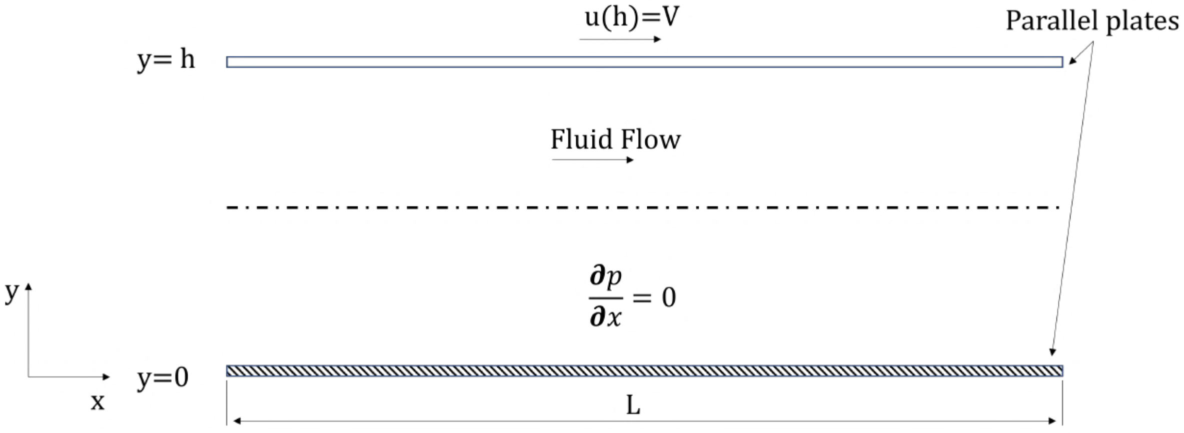

Figure 21 – Schematic diagram of transient Couette flow

8.2.2 Algebraic-differential mathematical modeling

As the specific mass is constant (incompressible flow), the term $\partial\rho/\partial t$ of mass balance (eq. 4.1) is set to zero. Then we have:

$$\nabla \cdot \mathbf{u} = 0$$

Applying the physical modeling assumptions described in sec. 8.2.1, the linear momentum balance equation (eq. 4.33) results in:

$$\frac{\partial u}{\partial t} = \frac{1}{\rho}\frac{\partial}{\partial y}\left(\boldsymbol{\tau}_{yx}\right) \tag{8.9}$$

The boundary conditions for this problem are:

$$\begin{cases} u(0,t) = 0 \\ u(h,t) = V \end{cases} \quad t > 0 \tag{8.10}$$

$$u(y,0) = 0 \quad 0 < y < h \tag{8.11}$$

8.2.3 Continuous mathematical modeling

Solving the previous ODE by Laplace transform (see Appendix A), considering the imposed boundary conditions, it reached the following continuous solution for Newtonian fluids:

$$u(y,t) = V \cdot \sum \left[\operatorname{erf}\left(\frac{2bn + a + b}{2\sqrt{t}}\right) - \operatorname{erf}\left(\frac{2bn - a + b}{2\sqrt{t}}\right)\right] \tag{8.12}$$

where

$$a = \frac{y}{\sqrt{\nu}}$$

and

$$b = \frac{h}{\sqrt{\nu}}$$

For non-Newtonian fluids it was not reached a continuous solution.

8.2.4 Computational modeling

The domain was defined starting from the origin and extending to the coordinates $(L, H, B) = (5.0\,\mathrm{m}, 1.0\,\mathrm{m}, 0.25\,\mathrm{m})$. The l_{bot} level was defined as $80 \times 16 \times 4$.

The boundary conditions for the parallelepiped domain were defined as follows for each of the three velocity components and for pressure.

For the velocity component u, the south and north faces were set with Dirichlet conditions, indicating that the velocity is directly imposed on these faces (zero at south and the unit at north). The bottom, top, west and east faces were set with a Neumann condition. For the velocity component v, the south and north faces were also set with Dirichlet conditions (all zero in this case). The bottom, top, west and east faces were set with a Neumann condition. For the velocity component w, the only difference on setup to v, is that bottom and top faces were set with Dirichlet conditions (all zero), indicating a pseudo-2D performing simulation.

For pressure, the south, north, bottom and top faces were set with Neumann conditions. The west and east faces were set with a Dirichlet condition, where the pressure is directly imposed (zero pressure gradient), as specified in sec. 8.2.3.

CFL number was set to 0.5. This value was also sufficiently small to accurately capture the dynamics of the flow.

The total simulation time was set to 250 s, which is sufficient to reach this problem steady condition.

8.2.5 Computational results

After performing the simulations on the MFSim platform, the results of the discrete solution also converged to the continuous ones, for Newtonian fluids, as shown in Fig. 22. On this case, is clearly observable the diffusion effect occurring from the upper flat plat to the fluid, until the steady state is reached. As time goes by, linear momentum is diffused on negative vertical direction, towards the bottom plate.

On the other hand, concerning non-Newtonian models, the power-law model was activated. For the times indicated in Fig. 22, flow development in relation to the flow behavior index, n, was analyzed. It is necessary to explain that flow behavior index higher than 2 it's unusual, but it was done exclusively to visualize, didactically, the physics perspective.

Considering that the region of the flow experiencing the highest shear rates is the one near the upper plate, the greater the value of the parameter n, the more resistance to flow is perceived in this region. This resistance is transferred to the lower portions of the domain through diffusion mechanisms, causing the steady-state regime to be reached more quickly.

In Fig. 23 is possible to verify the shear-thinning and shear-thickening behaviors, previously explained, for each time indicated in Fig. 22.

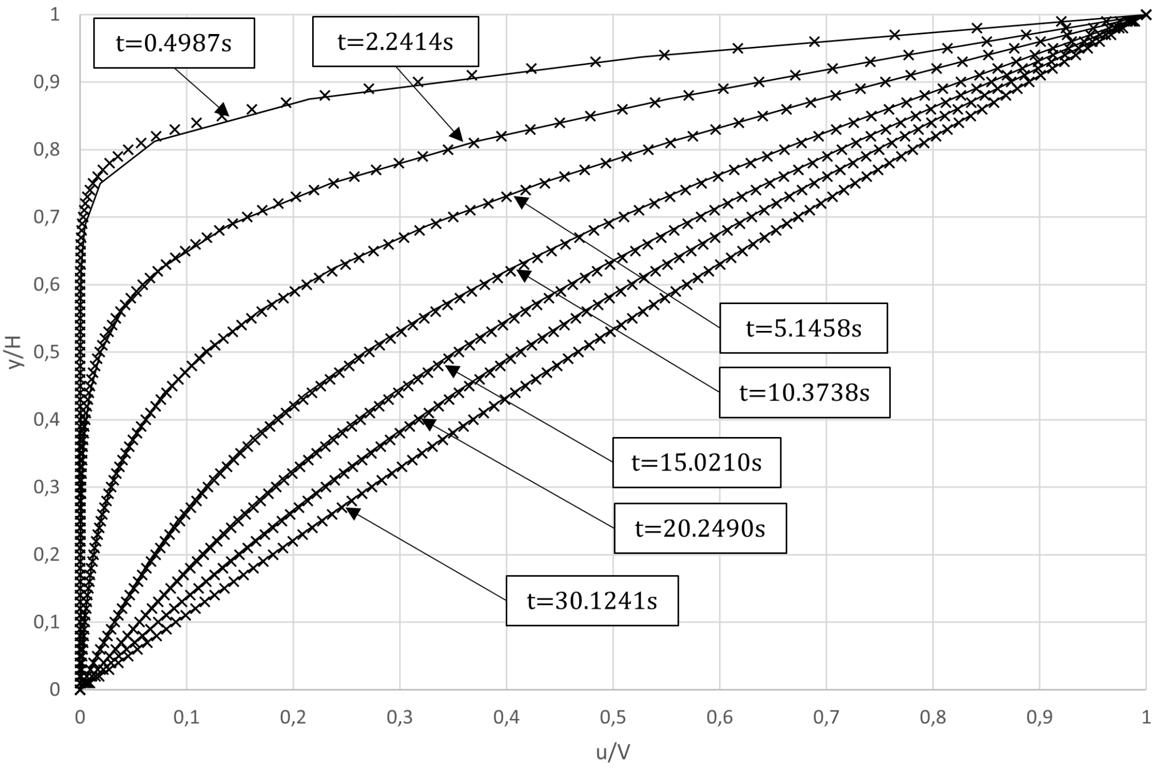

Figure 22 – Continuous (full lines) and discrete (x-symbols) solutions for the u-velocity profiles, at some specific times, for Newtonian fluid

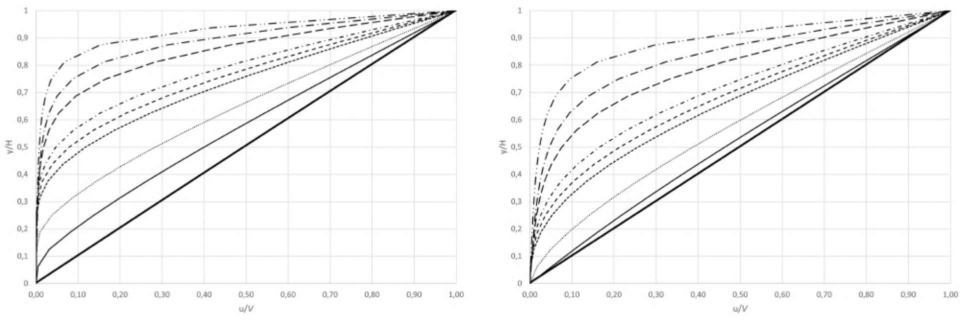

(a) Time 5.1458s

(b) Time 10.3738s

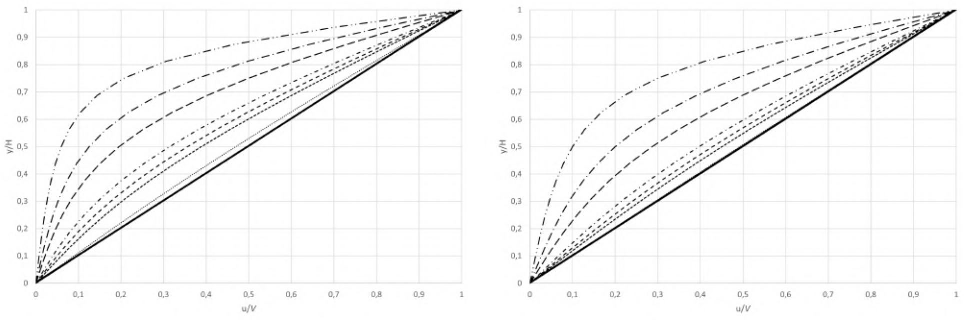

(c) Time 20.2490s

(d) Time 30.1241s

Figure 23 – u-velocity profiles for non-Newtonian fluids (power-law) at specific times: n=0.25 (long dash dot dot), n=0.5 (long dash dot), n=0.75 (long dash), n=1.25 (dash dot), n=1.5 (dashed), n=1.75 (square dot), n=3 (round dot), n=5 (thinner solid line) and n=10 (thicker solid line)

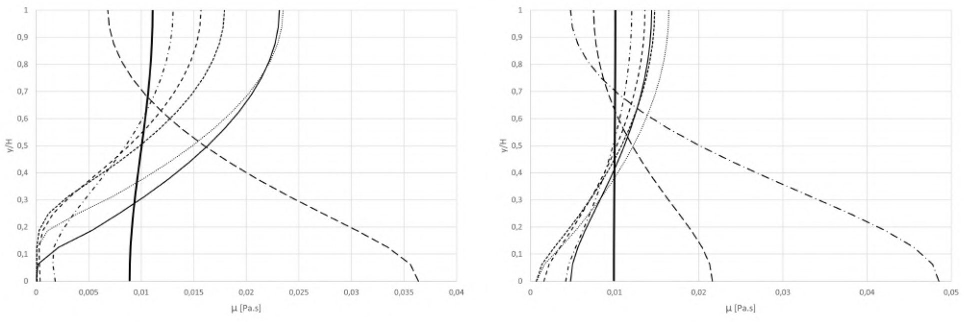

(a) Time 5.1458s

(b) Time 10.3738s

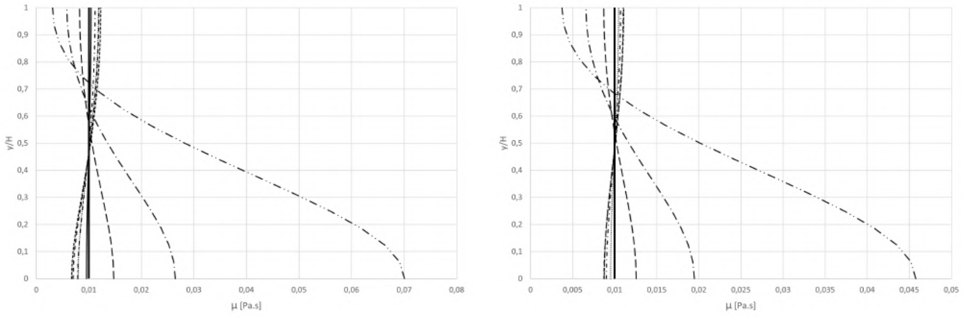

(c) Time 20.2490s

(d) Time 30.1241s

Figure 24 – Viscosity profiles for non-Newtonian fluids (power-law) at specific times: n=0.25 (long dash dot dot), n=0.5 (long dash dot), n=0.75 (long dash), n=1.25 (dash dot), n=1.5 (dashed), n=1.75 (square dot), n=3 (round dot), n=5 (thinner solid line) and n=10 (thicker solid line)

8.3 Lid-driven cavity flow

8.3.1 Phisycal modeling

The lid-driven cavity is another benchmark used to validate computational results and features a 1:1:1 cubic cavity on a $\mathbb{R}^3$ domain, with five walls set with no-slip boundary conditions (the vertical ones and the bottom one), while the top wall is defined as a fixed non-null velocity that drives the cavity flow, as shown in Fig. 25. Note that, using all the characteristic length, the lid-velocity and the specific mass equals to one, the Reynolds number is set as $\mathrm{Re} = 1/\mu$ for a Newtonian fluid. Incompressible and isothermal flow was assumed, in transient regime, disregarding the gravitational effects.

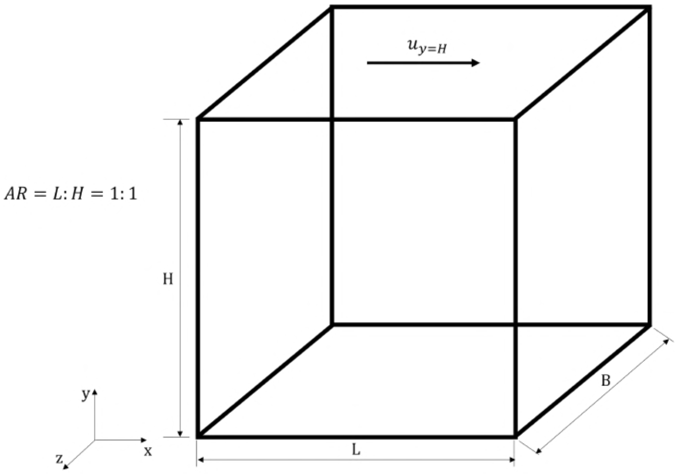

Figure 25 – Schematic diagram of the lid-driven cavity flow

8.3.2 Algebraic-differential mathematical modeling

As the specific mass is constant (incompressible flow), the term $\partial\rho/\partial t$ of mass balance (eq. 4.1) is set to zero. Then we have:

$$\nabla \cdot \mathbf{u} = 0$$

Applying the physical modeling assumptions described in the previous section, the lid-driven cavity problem will uses the full linear momentum balance equation (eq. 4.33) to be solved, as follows:

$$\rho\frac{Du_i}{Dt} = \rho g_i - \nabla \mathrm{p} + \frac{\partial}{\partial x_i}\left[\mu\left(\frac{\partial u_i}{\partial x_j} + \frac{\partial u_j}{\partial x_i}\right)\right]$$

For the flow of a non-Newtonian fluid inside the cavity, the only modification to the above equation is that the viscosity will no longer be a constant. This entails, in the discrete model, calculating its value for each volume of the computational domain by calling a subroutine within the MFSim code.

The boundary conditions for this problem are:

$$\begin{cases} u(x,H,z)=1, \quad v(x,H,z)=0, \quad w(x,H,z)=0, \quad \text{for} \quad 0\leq x\leq L \quad \text{and} \quad 0\leq z\leq B \\ u(0,y,z)=0, \quad v(0,y,z)=0, \quad w(0,y,z)=0, \quad \text{for} \quad 0\leq y\leq H \quad \text{and} \quad 0\leq z\leq B \\ u(L,y,z)=0, \quad v(L,y,z)=0, \quad w(L,y,z)=0, \quad \text{for} \quad 0\leq y\leq H \quad \text{and} \quad 0\leq z\leq B \\ u(x,y,0)=0, \quad v(x,y,0)=0, \quad w(x,y,0)=0, \quad \text{for} \quad 0\leq x\leq L \quad \text{and} \quad 0\leq y\leq H \\ u(x,y,B)=0, \quad v(x,y,B)=0, \quad w(x,y,B)=0, \quad \text{for} \quad 0\leq x\leq L \quad \text{and} \quad 0\leq y\leq H \\ u(x,0,z)=0, \quad v(x,0,z)=0, \quad w(x,0,z)=0, \quad \text{for} \quad 0\leq x\leq L \quad \text{and} \quad 0\leq z\leq B \end{cases} \tag{8.13}$$

8.3.3 Computational modeling

The domain was defined starting from the origin and extending to the coordinates $(L, H, B) = (1.0\,\mathrm{m}, 1.0\,\mathrm{m}, 1.0\,\mathrm{m})$. The l_{bot} level was defined as $60 \times 60 \times 60$.

The boundary conditions for the parallelepiped domain were defined as follows for each of the three velocity components and for pressure.

For the velocity components u, v and w, all faces were set with Dirichlet conditions, indicating that the velocity is directly imposed on them (all zero, except the lid with $u = 1\,\mathrm{m/s}$).

For pressure, they were all set with Neumann conditions.

CFL number was set to 0.5. This value was also sufficiently small to accurately capture the rapid dynamics of the flow.

The total simulation time was set to 400 s, which is sufficient to observe the dynamic flow behavior.

8.3.4 Computational results

After performing the simulations on the MFSim, the results obtained both for Newtonian and non-Newtonian fluids were validated with previous works (figure 26). Were extracted u-velocity and v-velocity profiles on z-mean symmetry plane, over a central vector on y and x directions, respectively. Simulations were conducted both at $\mathrm{Re} = 100$ and $\mathrm{Re} = 500$.

For a power-law non-Newtonian fluid, when $n < 1$ viscosity decreases, leading to a thinner boundary layer and less resistance near the lid. Conversely, for $n > 1$ viscosity increases with increasing shear rate, resulting in a thicker boundary layer and greater resistance near the lid.

Within the cavity, these viscosity variations influence vortex formation and flow resistance transmission. Shear-thinning fluids ($n < 1$) exhibit smoother flow with larger and more rapidly forming vortices, as the lower viscosity in high shear regions facilitates flow development. Shear-thickening fluids ($n > 1$), on the other hand, show more confined and less pronounced vortices due to higher viscosity in high shear regions, slowing flow stabilization. Thus, the power-law model significantly alters fluid dynamics compared to Newtonian fluids, affecting flow patterns and stabilization times in the cavity.

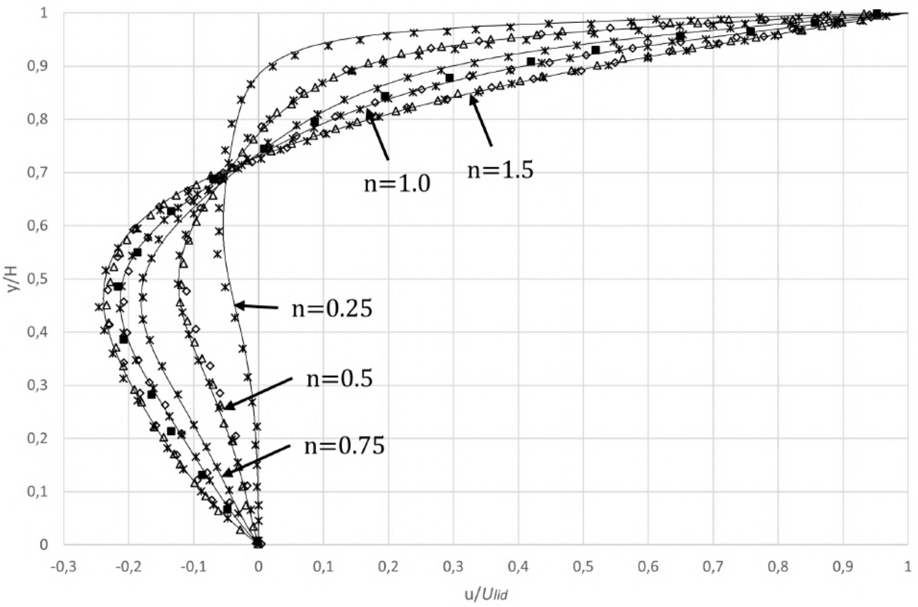

Figure 26 – u-velocity profiles for different values of the flow behavior index n, for Re $= 100$. MFSim solution: solid lines. References solutions (symbols): Ghia, Ghia e Shin (1982) (square), Tian, Bharti e Xu (2014) (asterisk), Chai et al. (2011) (diamond) and Wang et al. (2016) (triangle)

Likewise with the previous u-velocity profiles, the v-velocity following profiles keep the same physical behaviors.

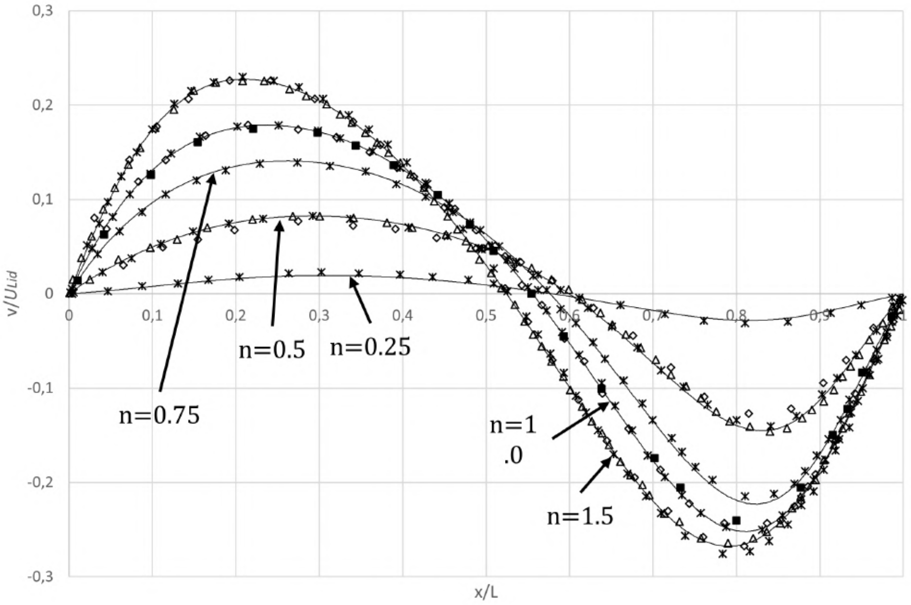

Figure 27 – v-velocity profiles for different values of the flow behavior index n, for Re $= 100$. MFSim solution: solid lines. References solutions (symbols): Ghia, Ghia e Shin (1982) (square), Tian, Bharti e Xu (2014) (asterisk), Chai et al. (2011) (diamond) and Wang et al. (2016) (triangle)

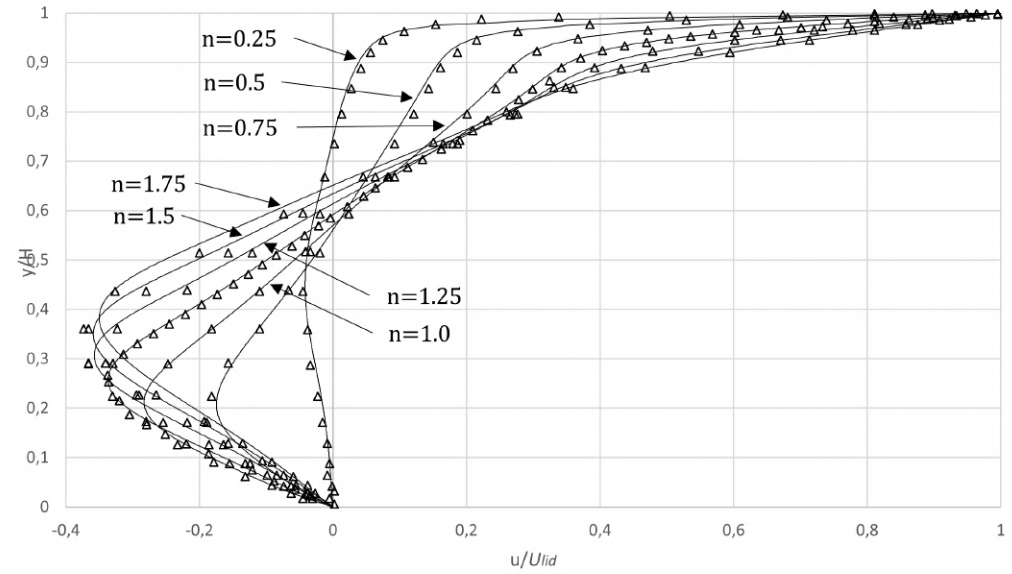

Figure 28 – u-velocity profiles for different values of the flow behavior index n, for Re = 500. MFSim solution: solid lines. References solutions (symbols): Aguirre et al. (2018) (triangle)

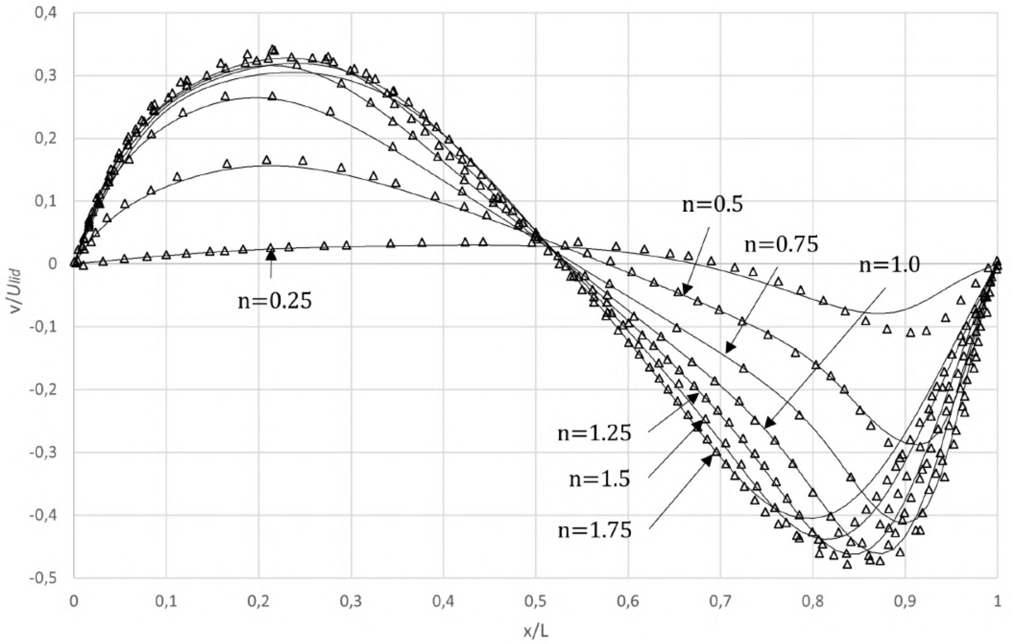

Figure 29 – v-velocity profiles for different values of the flow behavior index n, for Re = 500. MFSim solution: solid lines. References solutions (symbols): Aguirre et al. (2018) (triangle)

9 Performance analysis of blood's rheological models

9.1 Introduction

Lots of material experiments were conducted on last century about human blood viscosity - most of them under medical perspective - testing influence of some blood parameters, as RBCs aggregation, HCT, temperature, etc. Despite this many studies, the majority works at medium and high shear rate ranges. There are a just a few works on shear rates lower than $0.1\,\mathrm{s}^{-1}$.

In turn, when we discuss research on shear rate ranges within the human body, it is not perceived very low shear rates inside body organs. For example, Ronco et al. (2002), when investigating the flow inside a hemodialysis membrane module, found average wall shear rates from 160 to $760\,\mathrm{s}^{-1}$. Ecker et al. (2021) mentioned other medical researches as Yap, Saikrishnan e Yoganathan (2012), that found in an in vitro study of aortic valves $1,700$ to $2,600\,\mathrm{s}^{-1}$ of shear rate. Stone, Jr e Schmidt-Nielsen (1968) investigated blood viscosity of human and some animals (sheep, goat, dog and camel) with HCT level from $25\,\%$ to $69\,\%$ and shear rates from 5 to $230\,\mathrm{s}^{-1}$.

We still have Ethier e Simmons (2007), that realized that typical wall shear stresses are in the range 0.1 to 1.5 Pa for most arteries in humans, which corresponds to wall shear rates from approximately 30 to $450\,\mathrm{s}^{-1}$.

In addition to that explained in sec. 3.4, about the existence of blood's yield stress, it remains a controversial problem, according to Bird, Stewart e Lightfoot (1960).

So, on next table is presented several studies on human blood viscosity, carefully verified, that were conducted over many different ranges of shear rate and HCT.

As we are interested in the study of blood viscosity from a forensic perspective, the following figures present viscosity curves by shear rate specifically related to the studies in Tab. 3 that encompass $\mathrm{HCT} \geq 40\,\%$ and $\mathrm{T} \geq 37\,^{\circ}\mathrm{C}$.

In Fig. 30, are presented the studies where the HCT level is closest to what is considered normal for human blood, $45\,\%$, and, in Fig. 31, curves related to HCT in the range of $40\,\%$ are depicted.

Table 3 – Material experiments on blood viscosity

Reference	**Shear rate range** (s^{-1})	**Temperature (°C)**	**HCT (%)**
Eckmann et al. (2000)	4.5 to 450	10/15/25/37	22.5
Ecker et al. (2021)	10 to 1,000	37	40
Windberger et al. (2003)	0.7 to 94	37	40
Fossum et al. (1997)	0.5 to 201	37	40.9/42.5/44.2
Chien et al. (1966)	0.05 to 50	37	45
Merrill (1969)	1 to 300	37	40
Chien (1975)	0 to 300	37	45
Chien (1987)	1 to 1,000	37	44
Horner, Wagner e Beris (2021)	0.1 to 700	39	45
Rand et al. (1964)	21 to 212	22/27/32/37	20/40/60/80
Macosko (1994)	0.01 to 100	not informed	not informed
Barnes (2000)	0.01 to 100	not informed	not informed

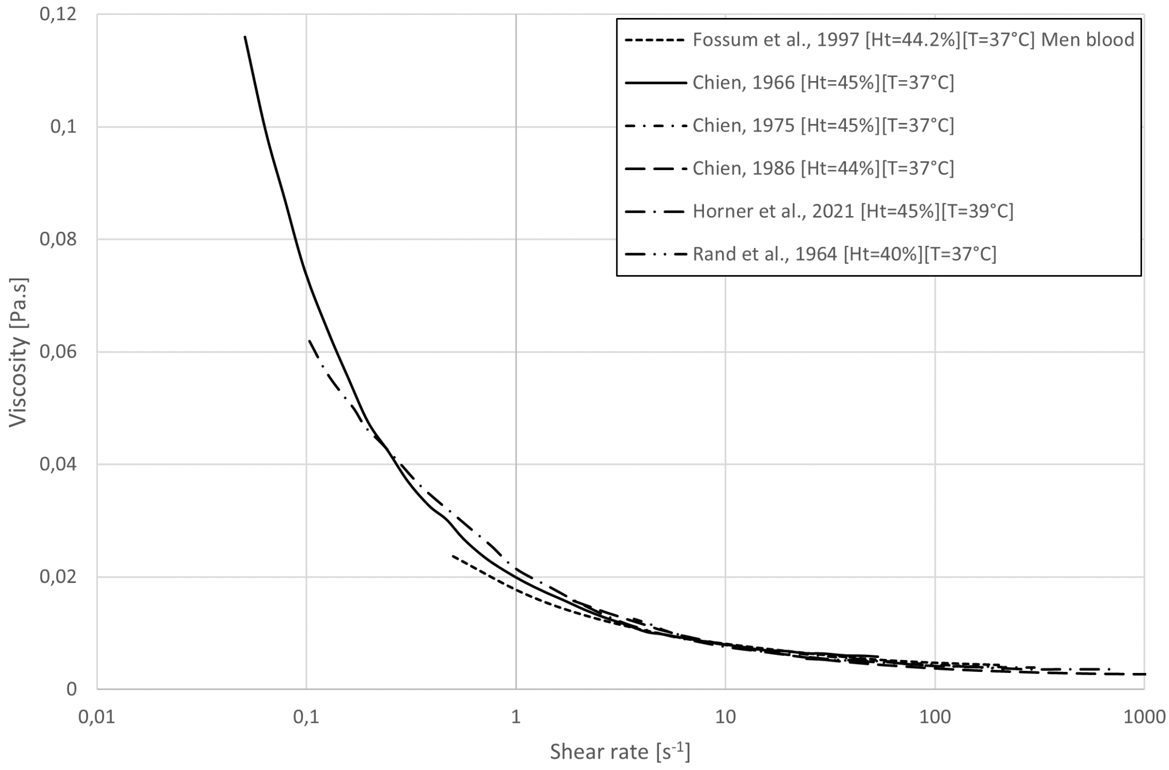

Figure 30 – Viscosity profiles as a function of the shear rate for some material experiments

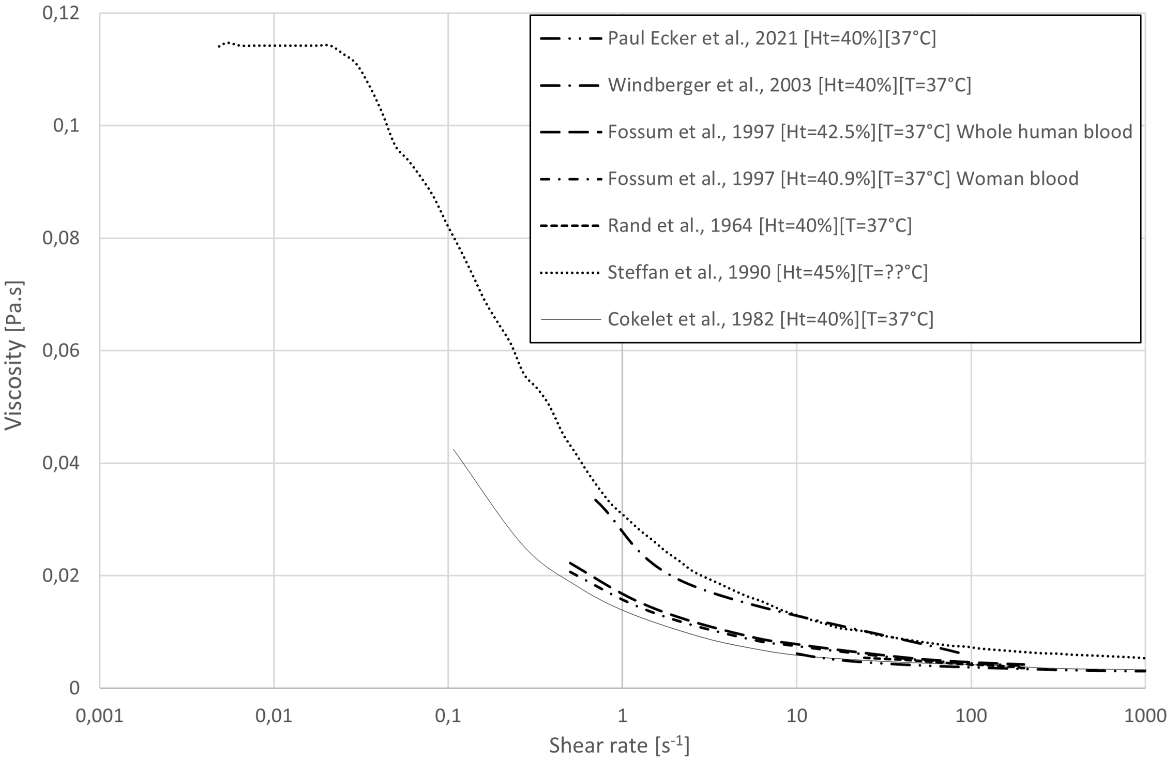

Figure 31 – Viscosity profiles as a function of the shear rate for some material experiments

An important point to be noted with Figs. 30 and 31 is the exponential growth of viscosity for $\dot{\gamma} \leq 1\,\mathrm{s}^{-1}$ and the lack of experimental data for shear rate ranges below this value. Proceeding with extrapolations to determine the parameters of each rheological model for blood - under the avaiable experimental shear rate range - may lead computational modeling to results that do not accurately represent physical reality, if lower shear rates are found within run simulations. This factor will be thoroughly explored in the simulations conducted on next sections.

9.2 Rheological models *versus* material experiments

The following three tables summarize the blood parameters for each model simulated in MFSim, categorized by model group:

- Table 4 contains values specifically related to the power-law model (eq. 6.1). This model exhibits shear-thinning behavior without Newtonian plateau regions for low and high shear rates
- Table 5 contains values specifically related to yield-shear-thinning models, characterized by a yield stress that must be exceeded for flow to occur
- Table 6 contains values specifically related to shear-thinning models with Newtonian plateau regions for low and high shear rates

Table 4 – Power-law rheological models' parameters for blood

Rheological model	**References**	**Blood parameters**
Power-law	Liepsch e Moravec (1984)	$m = 0.042\,[\mathrm{Pa} \cdot \mathrm{s}^n]$ $n = 0.61$
Power-law	Davies et al. (1990)	$m = 0.35\,[\mathrm{Pa} \cdot \mathrm{s}^n]$ $n = 0.6$
Power-law	Antonova (2012)	$m = 0.01318\,[\mathrm{Pa} \cdot \mathrm{s}^n]$ $n = 0.79$
Power-law	Karimi et al. (2014) Shibeshi e Collins (2005)	$m = 0.017\,[\mathrm{Pa} \cdot \mathrm{s}^n]$ $n = 0.708$
Power-law	Siauw, Ng e Mazumdar (2000) Walburn e Schneck (1976)	$m = 0.134\,[\mathrm{Pa} \cdot \mathrm{s}^n]$ $n = 0.785$
Power-law	Hussain, Kar e Puniyani (1999)	$m = 0.016915\,[\mathrm{Pa} \cdot \mathrm{s}^n]$ $n = 0.713$

Table 5 – Yield-shear-thinning models' parameters for blood

Rheological model	**References**	**Blood parameters**
Casson	Abbasian et al. (2020)	$\eta_0 = 0.0042\,[\mathrm{Pa} \cdot \mathrm{s}]$ $\tau_0 = 0.0038\,[\mathrm{Pa}]$
Casson	Siauw, Ng e Mazumdar (2000) Walburn e Schneck (1976)	$\eta_0 = 0.00414\,[\mathrm{Pa} \cdot \mathrm{s}]$ $\tau_0 = 0.0038\,[\mathrm{Pa}]$
Modified Casson	Karimi et al. (2014) Abbasian et al. (2020) Buchanan et al. (2003)	$\eta_0 = 0.002982\,[\mathrm{Pa} \cdot \mathrm{s}]$ $\lambda = 4.02\,[\mathrm{s}]$ $\tau_0 = 0.02876\,[\mathrm{Pa}]$
Herschel-Bulkley	Antonova (2012)	$n = 0.805$ $\eta_0 = 0.01189\,[\mathrm{Pa} \cdot \mathrm{s}]$ $\tau_0 = 0.00415\,[\mathrm{Pa}]$
K-L	Karimi et al. (2014) Abbasian et al. (2020)	$n = 1.19523$ $\eta_0 = 0.0035\,[\mathrm{Pa} \cdot \mathrm{s}]$ $a = 1$ $\tau_0 = 0.005\,[\mathrm{Pa}]$

Table 6 – Shear-thinning models' parameters for blood

Rheological model	**References**	**Blood parameters**
Cross	Abbasian et al. (2020) Karimi et al. (2014)	$n = 1.45$ $\eta_0 = 0.0364\,[\mathrm{Pa}\cdot\mathrm{s}]$ $\eta_\infty = 0.00345\,[\mathrm{Pa}\cdot\mathrm{s}]$ $\lambda = 0.38\,[\mathrm{s}]$
Cross	Cho e Kensey (1991) Bird (1987)	$n = 1.028$ $\eta_0 = 0.056\,[\mathrm{Pa}\cdot\mathrm{s}]$ $\eta_\infty = 0.00345\,[\mathrm{Pa}\cdot\mathrm{s}]$ $\lambda = 1.007\,[\mathrm{s}]$
Simplified Cross	Abbasian et al. (2020) Steffan et al. (1990) Siauw, Ng e Mazumdar (2000)	$\eta_0 = 0.13\,[\mathrm{Pa}\cdot\mathrm{s}]$ $\eta_\infty = 0.005\,[\mathrm{Pa}\cdot\mathrm{s}]$ $\lambda = 8\,[\mathrm{s}]$
Modified Cross	Cho e Kensey (1991)	$n = 2.406$ $\eta_0 = 0.056\,[\mathrm{Pa}\cdot\mathrm{s}]$ $\eta_\infty = 0.00345\,[\mathrm{Pa}\cdot\mathrm{s}]$ $\lambda = 3.736\,[\mathrm{s}]$ $a = 0.254$
Modified Cross	Abraham, Behr e Heinkenschloss (2005)	$n = 0.64$ $\eta_0 = 0.16\,[\mathrm{Pa}\cdot\mathrm{s}]$ $\eta_\infty = 0.0035\,[\mathrm{Pa}\cdot\mathrm{s}]$ $\lambda = 8.2\,[\mathrm{s}]$ $a = 1.23$
Carreau	Cho e Kensey (1991) Shibeshi e Collins (2005)	$n = 0.3568$ $\eta_0 = 0.056\,[\mathrm{Pa}\cdot\mathrm{s}]$ $\eta_\infty = 0.00345\,[\mathrm{Pa}\cdot\mathrm{s}]$ $\lambda = 3.313\,[\mathrm{s}]$
Carreau-Yasuda	Cho e Kensey (1991) Weddell et al. (2015) Aguirre et al. (2018)	$n = 0.22$ $\eta_0 = 0.056\,[\mathrm{Pa}\cdot\mathrm{s}]$ $\eta_\infty = 0.00345\,[\mathrm{Pa}\cdot\mathrm{s}]$ $\lambda = 1.902\,[\mathrm{s}]$ $a = 1.25$
Carreau-Yasuda	Abraham, Behr e Heinkenschloss (2005) Boyd, Buick e Green (2007)	$n = 0.2128$ $\eta_0 = 0.16\,[\mathrm{Pa}\cdot\mathrm{s}]$ $\eta_\infty = 0.0035\,[\mathrm{Pa}\cdot\mathrm{s}]$ $\lambda = 8.2\,[\mathrm{s}]$ $a = 0.64$
Powell-Eyring	Cho e Kensey (1991)	$\eta_0 = 0.056\,[\mathrm{Pa}\cdot\mathrm{s}]$ $\eta_\infty = 0.00345\,[\mathrm{Pa}\cdot\mathrm{s}]$ $\lambda = 5.383\,[\mathrm{s}]$
Modified Powell-Eyring	Cho e Kensey (1991)	$\eta_0 = 0.056\,[\mathrm{Pa}\cdot\mathrm{s}]$ $\eta_\infty = 0.00345\,[\mathrm{Pa}\cdot\mathrm{s}]$ $\lambda = 2.415\,[\mathrm{s}]$ $a = 1.089$

To facilitate the writing and reading of the data, the following correspondence will be made regarding the names of the models on Tab. 7 below.

Table 7 – Correspondence for the nomenclature of the models used

Model	**Reference**	**Nomenclature to be used**
Power-law	Liepsch e Moravec (1984)	PL1
Power-law	Davies et al. (1990)	PL2
Power-law	Antonova (2012)	PL3
Power-law	Karimi et al. (2014) Shibeshi e Collins (2005)	PL4
Power-law	Siauw, Ng e Mazumdar (2000) Walburn e Schneck (1976)	PL5
Power-law	Hussain, Kar e Puniyani (1999)	PL6
Casson	Abbasian et al. (2020)	Casson1
Casson	Siauw, Ng e Mazumdar (2000) Walburn e Schneck (1976)	Casson2
Modified Casson	Karimi et al. (2014) Abbasian et al. (2020) Buchanan et al. (2003)	ModCasson
Herschel-Bulkley	Antonova (2012)	HB
K-L	Karimi et al. (2014) Abbasian et al. (2020)	KL
Cross	Abbasian et al. (2020) Karimi et al. (2014)	Cross1
Cross	Cho e Kensey (1991) Bird (1987)	Cross2
Simplified Cross	Abbasian et al. (2020) Steffan et al. (1990) Siauw, Ng e Mazumdar (2000)	SimpCross
Modified Cross	Cho e Kensey (1991)	ModCross1
Modified Cross	Abraham, Behr e Heinkenschloss (2005)	ModCross2
Carreau	Cho e Kensey (1991) Shibeshi e Collins (2005)	Carreau
Carreau-Yasuda	Cho e Kensey (1991) Weddell et al. (2015) Aguirre et al. (2018)	CY1
Carreau-Yasuda	Abraham, Behr e Heinkenschloss (2005) Boyd, Buick e Green (2007)	CY2
Powell-Eyring	Cho e Kensey (1991)	PE
Modified Powell-Eyring	Cho e Kensey (1991)	ModPE

Figure 32 compares the viscosity profiles of blood - as a function of shear rate - obtained in material experiments with the power-law rheological model under coefficients from various references listed in Tab. 4. Figure 32a encompasses the shear rate range

$0.1 \leq \dot{\gamma} \leq 1,000\,\mathrm{s}^{-1}$, providing a closer visualization of the correspondence between the material experiments' curves and the curves of the rheological models. It can be observed that the parameters proposed by some references, such as Davies et al., Walburn e Schneck, and Liepsch e Moravec, did not exhibit good correspondence with material experiments for human blood under normal conditions (HCT $\approx 45\,\%$ and $T \approx 37\,°\mathrm{C}$). On the other hand, coefficients proposed by Hussain, Kar e Puniyani, Karimi et al., and Antonova showed good correspondence for the shear rate range $10 \leq \dot{\gamma} \leq 1,000\,\mathrm{s}^{-1}$ but fell short in the range $\dot{\gamma} \leq 10\,\mathrm{s}^{-1}$, as evident in Fig. 32b. Finally, Fig. 32c highlights the viscosity values reached by the models at $\dot{\gamma} = 0.001\,\mathrm{s}^{-1}$, where the model proposed by Davies et al. diverged from other models, reaching a viscosity value five times higher than the others.

Figure 33 juxtaposes the viscosity profiles of blood, influenced by shear rate, acquired through material experiments and through shear-thinning rheological models. The coefficients for these models are extracted from various references detailed in Tab. 6. The graphic in 33a illustrates that these shear-thinning models exhibit a satisfactory fit within the shear rate range of $0.1 \leq \dot{\gamma} \leq 1,000\,\mathrm{s}^{-1}$. However, they initiate their plateau region over low shear rate—associated with viscosity η_0—at approximately $\dot{\gamma} \approx 0.1\,\mathrm{s}^{-1}$.

In Fig. 33b, a notable discrepancy in viscosity profiles is observed between experimental and model data. Shear-thinning models reach a plateau, whereas experimental data demonstrates an exponential increase in viscosity for $\dot{\gamma} \leq 0.1\,\mathrm{s}^{-1}$. For instance, at $\dot{\gamma} \approx 0.05\,\mathrm{s}^{-1}$, ModCross1, Carreau, and PE models exhibit a $98\,\%$ deviation in viscosity compared to the experimental data presented by Chien et al. (1966) (represented by the full line).

For the second group of shear-thinning models presented in Fig. 34, the behavior of the models closely resembled the first group from Fig. 33. However, we can observe in Fig. 34a that the ModCross2, CY2 and SimpCross models exhibited the same exponential growth curve than experimental data toward $\dot{\gamma} = 0.1\,\mathrm{s}^{-1}$, in contrast to the CY1 and Cross models.

In Fig. 34b, we observe that the models, which exhibited exponential growth up to $\dot{\gamma} = 0.1\,\mathrm{s}^{-1}$, now begin to deviate significantly from the experimental data and initiate the formation of their viscosity plateaus for shear rate ranges of $\dot{\gamma} \leq 0.1\,\mathrm{s}^{-1}$. Figure 34c provides a broader view of the viscosity values reached by the models at $\dot{\gamma} = 0.001\,\mathrm{s}^{-1}$, where the SimpCross, ModCross2 and CY2 attained a value of approximately $\dot{\gamma} = 0.15\,\mathrm{s}^{-1}$.

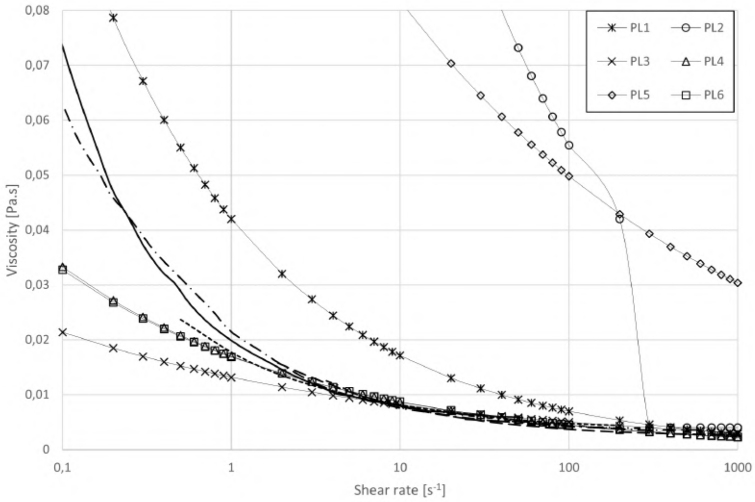

(a) Shear rate range from 0.1 to $1,000\,\mathrm{s}^{-1}$

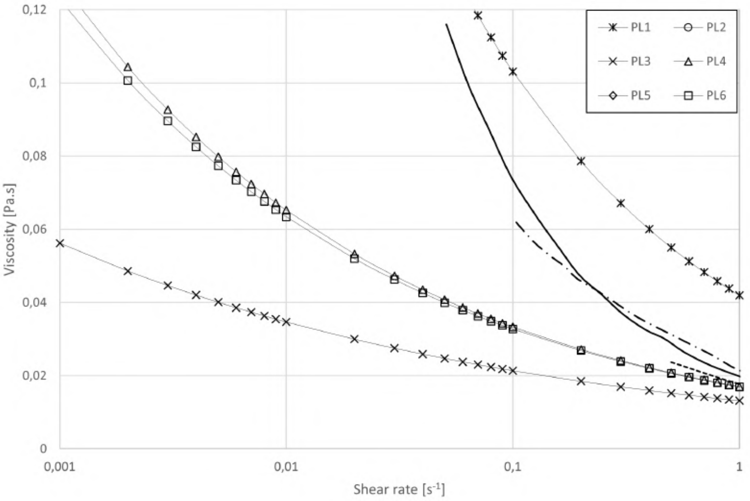

(b) Shear rate range from 0.001 to $1\,\mathrm{s}^{-1}$

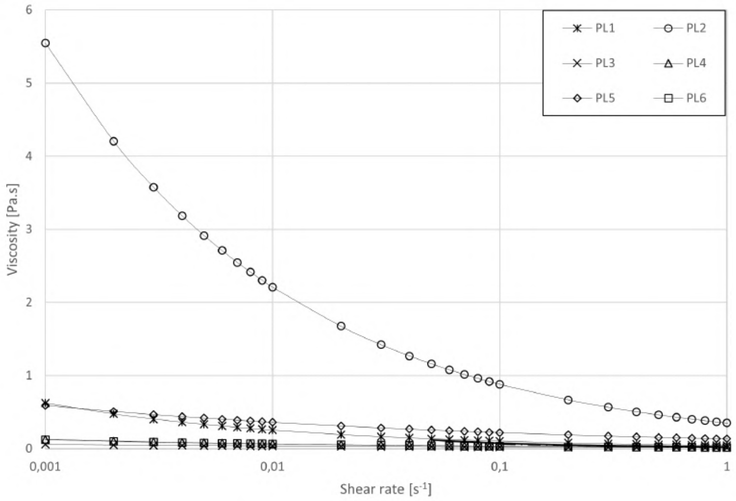

(c) Maximum viscosity reached by the models at $\dot{\gamma} = 0.001\,\mathrm{s}^{-1}$

Figure 32 – Power-law models *versus* material experiments

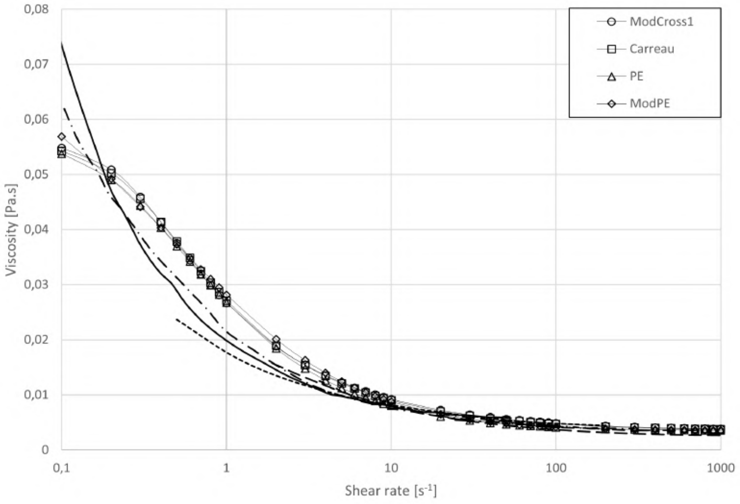

(a) Shear rate range from 0.1 to $1,000\,\mathrm{s}^{-1}$

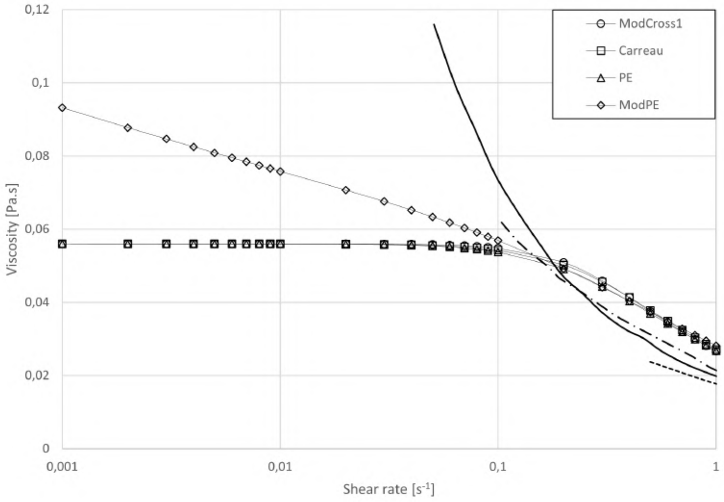

(b) Shear rate range from 0.001 to $1\,\mathrm{s}^{-1}$

Figure 33 – Shear-thinning models *versus* material experiments

Finally, in Fig. 35, we observe that, except for the modified Casson model, the yield-shear-thinning models were the ones that demonstrated the best correspondence with experimental data for human blood under normal conditions, across all experimentally available shear rate ranges. As mentioned earlier, the challenge lies in not fully understanding the real behavior of blood viscosity under low rates, $\dot{\gamma} \leq 0.05\,\mathrm{s}^{-1}$, which may be encountered in flow settings different from those that occur within the human body.

Charm e Kurland (1965) highlighted that Casson's equation can be applied for a wide range of $2 - 100,000\,\mathrm{s}^{-1}$ of shear rate, doing tests with a series of viscometers.

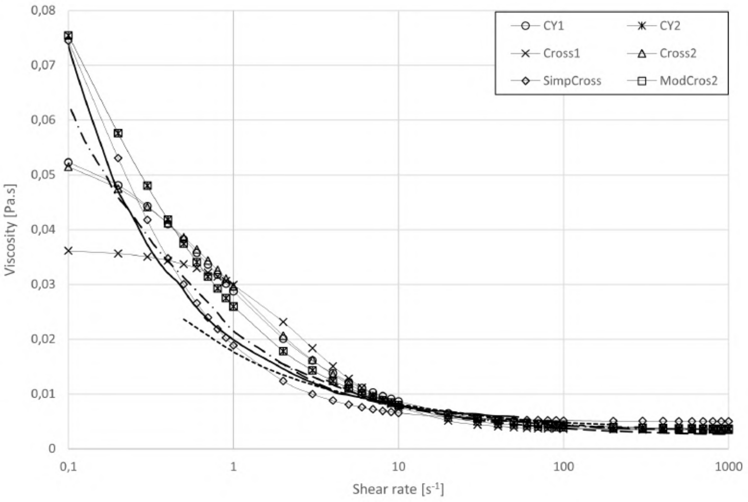

(a) Shear rate range from 0.1 to $1,000\,\mathrm{s}^{-1}$

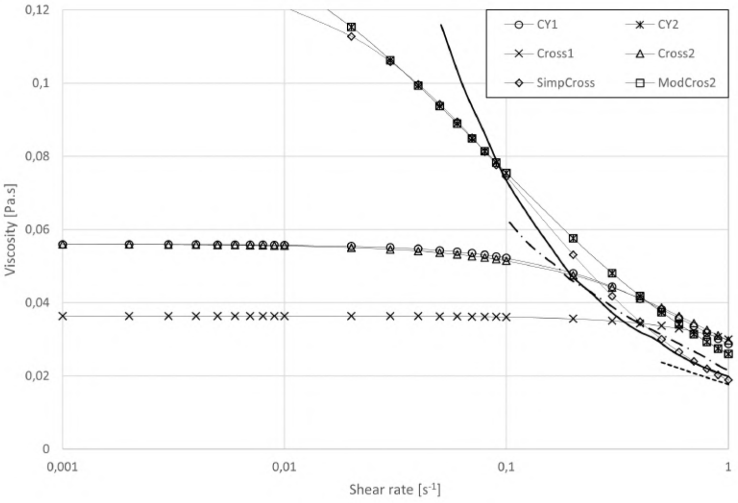

(b) Shear rate range from 0.001 to $1\,\mathrm{s}^{-1}$

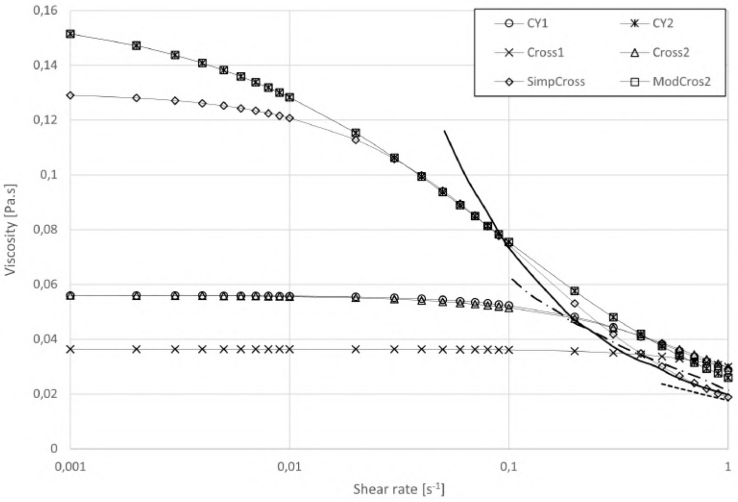

(c) Maximum viscosity reached by the models at $\dot{\gamma} = 0.001\,\mathrm{s}^{-1}$

Figure 34 – Shear-thinning models *versus* material experiments

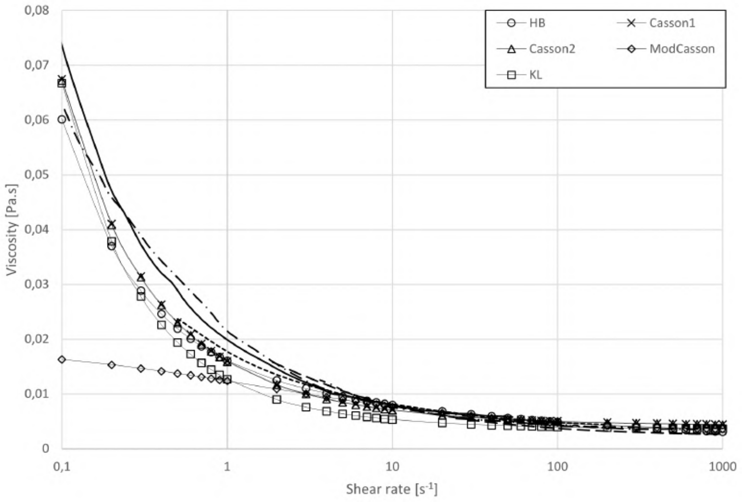

(a) Shear rate range from 0.1 to $1,000\,\mathrm{s}^{-1}$

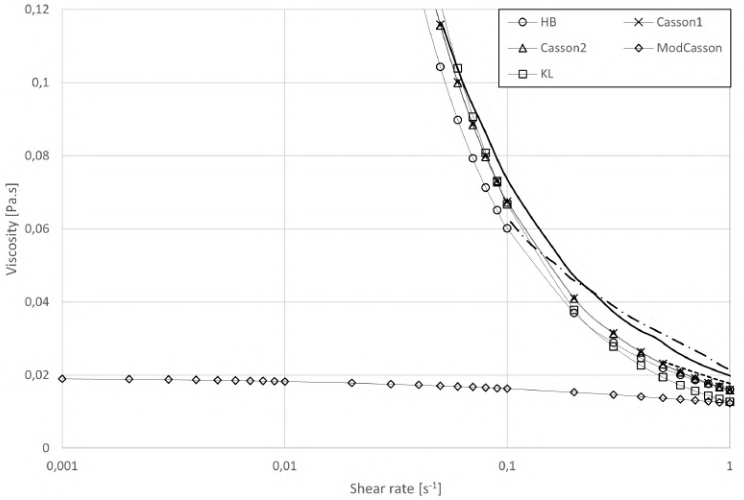

(b) Shear rate range from 0.001 to $1\,\mathrm{s}^{-1}$

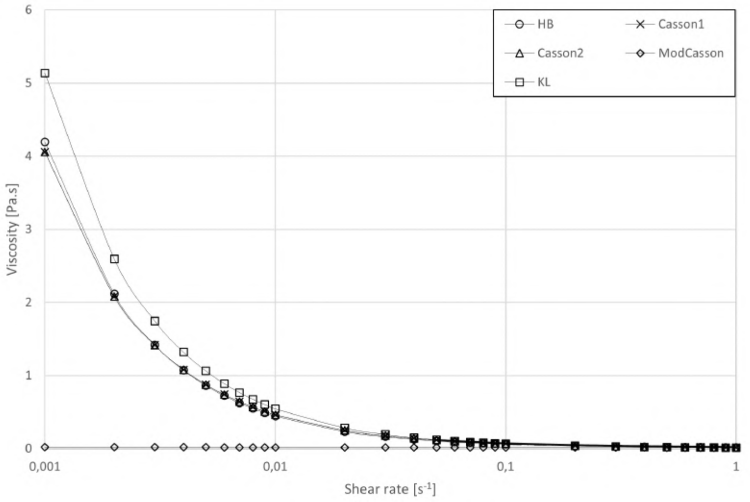

(c) Maximum viscosity reached by the models at $\dot{\gamma} = 0.001\,\mathrm{s}^{-1}$

Figure 35 – Yield-shear-thinning models *versus* material experiments

10 Blood drop's modeling

10.1 Introduction

Getting close to the purpose of the entire project, is required to run and study some falling drop simulations. In that regard, MacDonell (2009) points that the degree of spatter that results when a drop of blood falls onto a surface is far more dependent upon the nature of the surface than it is on the distance the drop has fallen before it impacted the surface. But due to the fact that we are simulating 21 cases with different rheological models and parameters, limitations are necessary due to the available time for the completion of the work. So, the purpose of this chapter is isolate as many variables as possible, that allows for a minimally adequate comparison of the non-Newtonian viscosity models implemented in MFSim, for instance, regarding the pattern formed after impact and the relative diameter reached after impact, etc.

In that regard, some previous cases were carried out on MFSim, primarily aiming MFSim's validation to do this type of modeling, that involves VoF and IBM techniques and, just after that, activate the non-Newtonian models for blood.

To validate MFSim for VoF and IBM techniques, were used the work provided by Deen, Annaland e Kuipers (2009). This article presents a complex multifluid flow simulation, using the previous methods cited.

10.2 Deformation and fragmentation of drops

The breakup process of a drop has been studied since the beginning of the twenty century, theoretically and experimentally. Hinze (1955) mentioned that the investigation into the bursting of drops in air stream started before 1904, with the publishing of Lenard experiments, and mentions in his article three basic types of droplet deformation (see Fig. 36), due to the action of aerodynamic force:

- The droplet undergoes flattening, taking on the shape of a flattened ellipsoid (lenticular deformation). The subsequent changes depend on the internal forces' magnitude driving the deformation. It is suggested that the ellipsoid transforms into a torus, which undergoes stretching and breaks into smaller droplets. This deformation occurs under the influence of aerodynamic pressures or viscous stresses generated by parallel and rotating flows
- The initial droplet elongates, forming an extended cylindrical thread or ligament that eventually breaks into smaller droplets (cigar-shaped deformation). This type

of deformation requires specific flow conditions such as plane hyperbolic and Couette flows

- Localized deformations on the droplet interface result in bulges and protuberances that detach from the parent droplet, forming smaller droplets. This deformation occurs within irregular flow patterns

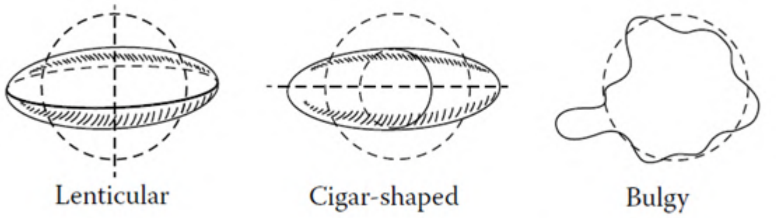

Figure 36 – Drop deformation. Source: Hinze (1955)

Hence, the predilection for a particular deformation and breakup type is influenced by the physical characteristics of the gas and liquid phases, including their specific masses, viscosities and interfacial tension, as well as the flow pattern surrounding the droplet. In general, the breakup of a droplet in a flowing stream is guided by dynamic pressure, interfacial tension and viscous forces.

Hinze has shown theoretically that We_{crit} depends not only on Ohnesorge number, Oh, but also on the way in which the relative velocity changes with time. For Oh = 0 and true shock exposure, $We_{crit} \approx 13$ whereas for a falling drop $We_{crit} \approx 22$.

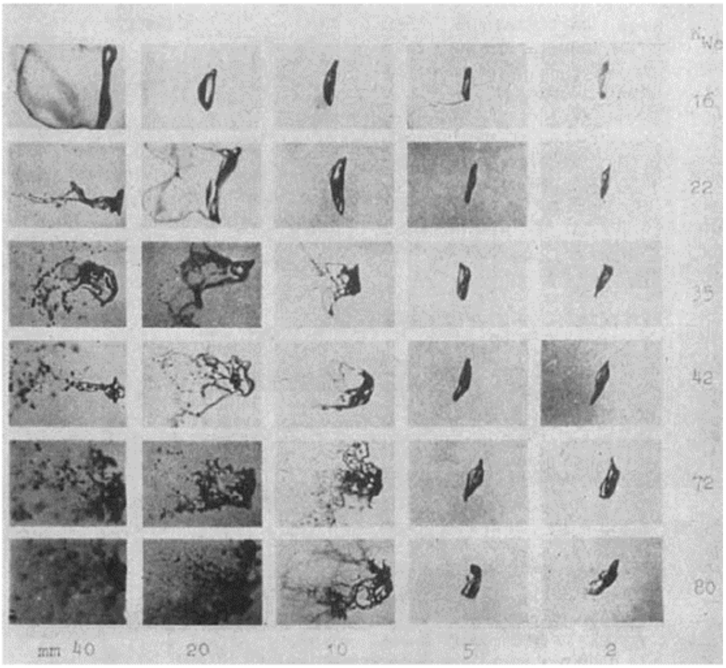

Figure 37 – Short-flash photographs showing the breakup of a drop at increasing values of We. Gas oil, $D = 39\,\text{mm}$. $We_{crit} = 13$. Source: Hinze (1955)

According to Lane (1951), three stages can be distinguished in the shatter process:

- Initiation of small disturbances at the interface of the liquid, in the form of local ripples or protuberances
- Action of air pressure and tangential forces on these disturbances, forming ligaments which may break up into drops
- Further breakup of these drops in movement through the air

For the first mode of breakup, Lane (1951) has established that at normal atmospheric conditions there is a limiting value of the relative velocity $U_{R_{crit}}$ below which breakup does not occur. For phases whose interfacial tension (σ) lie in the range $0.028 - 0.475\,\mathrm{N/m^2}$ - as the system air-blood -, the relationship is given by:

$$U_{R_{crit}} \propto \left(\frac{\sigma}{D_{drop}}\right)^{0.5} \tag{10.1}$$

Concerning the breakup of drops in steady stream of air, Lane (1951) made a series of experiments where large drops of known size were allowed to fall down the axis of a small vertical wind tunnel in which a steady downward stream of air of measured velocity could be maintained. As it came under the influence of the air stream, the drop was seen to become increasingly flattened, and at a critical velocity of the air it was blown out into the form of a hollow bag attached to a roughly circular rim. Bursting of this bag produced a shower of very fine droplets, and the rim, which contained at least 70 % of the mass of the original spherical drop, broke up later into much larger drops.

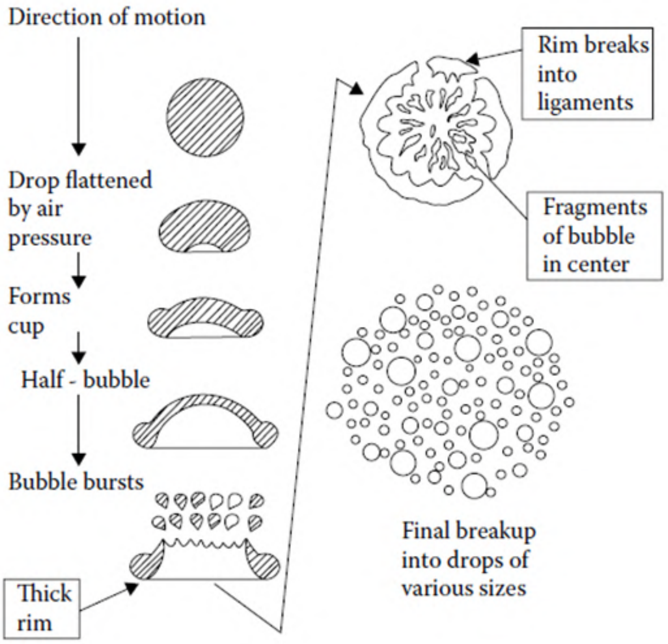

Figure 38 – Breakup of a spherical drop by interaction with ambient air. Source: Lefebvre e McDonell (2017)

According to Lane (1951), some characteristics of the bursting drop can be interpreted using established principles of fluid mechanics. When examining the pressure distribution on the surface of a rigid sphere in a wind tunnel, it is observed that the front of the sphere experiences positive pressure, while the sides and rear are subjected to reduced pressure (refer to Fig. 39). Consequently, a liquid drop introduced into an airstream is expected to flatten on the side facing the positive pressure and elongate at the sides and rear. This deformation is counteracted by the interfacial tension, which strives to maintain the drop's spherical shape, potentially leading to a depression at the center of the drop's upper interface.

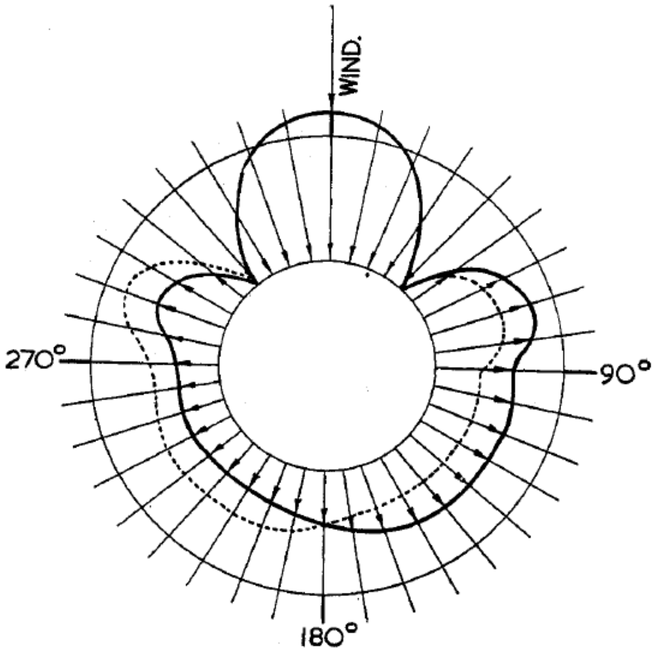

Figure 39 – Distribution of pressure over interface of rigid sphere in wind tunnel. Source: Lane (1951)

The deformation of the drop leading to its ultimate breakup is resisted by the force of interfacial tension, making it important to study the effect of this property of the liquid. Simple dimensional analysis suggests, and experiments confirmed, this relationship by using various liquids that cover a wide range of interfacial tensions (from < 0.028 to $0.475\,\mathrm{N/m}$). In each case tested by Lane, the air flow velocity in the wind tunnel, required to shatter drops of known size, was measured. Anomalous results were observed with drops of aqueous solutions of interface-active substances, but these could be explained based on the known variation of the interfacial tension of such solutions over time. Viscosity appeared to influence the breakup process only when it was very high, as in the case of glycerol drops, where it tended to retard the breakup of the drop.

According to Hinze (1949), the forces exerted on the surface of the globule include a tangential component due to the viscosity of the surrounding fluid, and a normal component resulting from the velocity pressures of the surrounding fluid. For high Reynolds numbers (e.g., Re > 1,000), the influence of the tangential forces on deformation is minimal compared to that of the normal forces and can be disregarded.

Liquid drops released individually from pipettes exhibit initial vibrations. As noted by Hauser et al. (1935), at the moment of separation, the drop assumes a slightly ellipsoidal shape with the major axis oriented vertically. This initial deformation triggers free vibrations.

According to Hsiang e Faeth (1995), at low Ohnesorge numbers (Oh < 0.1), significant drop deformation (approximately 5 %) commenced at Weber numbers around unity, with the deformation phase concluding due to breakup onset at Weber numbers between 10 and 20. These transitions were relatively stable regardless of the Ohnesorge number for steady disturbances. However, higher Ohnesorge numbers extended the Weber number range for both deformation and breakup regimes when exposed to shock wave disturbances, an effect explained by phenomenological theory. Another transition, from dome-shaped to bowl-shaped drops (analogous to the shift between bag and shear breakup), was primarily associated with Weber and Reynolds numbers under the given conditions. For steady disturbances, drop deformation was relatively independent of the specific mass ratio between dispersed and continuous phases but was generally less than that for shock wave disturbances due to the absence of inertial overshoot. Conversely, drop drag coefficients, when normalized by the drag coefficient of a solid sphere at the same Reynolds number, showed strong correlation with the degree of deformation alone.

For any given liquid, the initial condition for breakup is achieved when the aerodynamic drag is just equal to the surface tension force, that is:

$$C_D \, \frac{\pi \, D_{drop}^2}{4} \, 0.5 \, \rho_c \, U_{rel}^2 = \pi \, D_{drop} \, \sigma \tag{10.2}$$

Rearranging the terms, we have:

$$\left(\frac{\rho_c \, U_{rel}^2 \, D_{drop}}{\sigma} \right)_{crit} = We_{crit} = \frac{8}{C_D} \tag{10.3}$$

According to Hinze (1949), splitting-up occurs if We is greater than this critical value We_{crit}, and this value has to be determined experimentally. However, such a critical Weber's number appears to depend on the variation with time of the air forces and on the viscosity of the liquid. Now, putting this equations in therms of the maximum stable drop size:

$$D_{max} = \frac{8\sigma}{C_D \, \rho_c \, U_{rel}^2} \tag{10.4}$$

and the critical velocity is obtained as:

$$U_{rel_{crit}} = \left(\frac{8\sigma}{C_D \, \rho_c \, D_{drop}} \right)^2 \tag{10.5}$$

10.3 VoF and IBM validation

Direct Numerical Simulation (DNS) of complex multi-fluid flows where it is present deformable (drops or bubbles) and non-deformable elements (any object's random-shaped and impenetrable interfaces) is possible to be solved with Volume of Fluid (VoF) method and the Immersed Boundary Method (IBM) technique, to represent the dispersed phase and the impenetrable interfaces, respectively. As presented on chapter 7, MFSim has both techniques implemented within the computational code and it'll be validated here, with the simulation of a falling drop over a rigid and stationary spherical particle, proposed by Deen, Annaland e Kuipers (2009).

10.3.1 Falling drop over sphere

10.3.1.1 Physical modeling

This concerns the free fall of a drop initially positioned at $\mathbf{S}_\mathrm{p} = (0.025\,\mathrm{m}, 0.075\,\mathrm{m}, 0.025\,\mathrm{m})$ within a domain of dimensions $0.05\,\mathrm{m} \times 0.1\,\mathrm{m} \times 0.05\,\mathrm{m}$, over a rigid and stationary spherical particle positioned at $\mathbf{S}_\mathrm{p} = (0.025\,\mathrm{m}, 0.025\,\mathrm{m}, 0.025\,\mathrm{m})$. The radius of the drop and rigid sphere are, respectively, $0.01\,\mathrm{m}$ and $0.005\,\mathrm{m}$, and the physical properties of the drop and the surrounding continuous phase were considered constants, with $\rho_d = 1,000\,\mathrm{kg/m^3}$, $\rho_c = 100\,\mathrm{kg/m^3}$, $\mu_d = 0.1$ Pa·s and $\mu_c = 0.01$ Pa·s. The interfacial tension between continuous and dispersed phases were considered as $\sigma = 0.1\mathrm{N/m}$. The flow was considered incompressible and isothermal. Gravitational effects were taken into account, with $g = 10\,\mathrm{m/s^2}$.

10.3.1.2 Algebraic-differential mathematical modeling

As the specific mass is constant (incompressible flow), the term $\partial\rho/\partial t$ of mass balance (eq. 4.1) is set to zero. Then we have:

$$\nabla \cdot \mathbf{u} = 0$$

Applying the physical modeling assumptions described in the previous section, this problem will uses the full linear momentum balance equation (eq. 4.33) to be solved, as follows:

$$\rho \frac{Du_i}{Dt} = \rho g_i - \nabla \mathrm{p} + \frac{\partial}{\partial x_i}\left[\mu\left(\frac{\partial u_i}{\partial x_j} + \frac{\partial u_j}{\partial x_i}\right)\right]$$

For the fall of a non-Newtonian droplet, the only modification to the above equation is that the viscosity will no longer be a constant. This entails, in the discrete model, calculating its value for each internal droplet volume of the computational domain by calling a subroutine within the MFSim code.

The boundary conditions for this problem are:

$$\begin{cases} \frac{\partial p}{\partial y}=0, & \text{for} \quad y=H \quad \text{and} \quad 0\leq x\leq L \quad \text{and} \quad 0\leq z\leq B \\ u(0,y,z)=0, \quad v(0,y,z)=0, \quad w(0,y,z)=0, & \text{for} \quad 0\leq y\leq H \quad \text{and} \quad 0\leq z\leq B \\ u(L,y,z)=0, \quad v(L,y,z)=0, \quad w(L,y,z)=0, & \text{for} \quad 0\leq y\leq H \quad \text{and} \quad 0\leq z\leq B \\ u(x,y,0)=0, \quad v(x,y,0)=0, \quad w(x,y,0)=0, & \text{for} \quad 0\leq x\leq L \quad \text{and} \quad 0\leq y\leq H \\ u(x,y,B)=0, \quad v(x,y,B)=0, \quad w(x,y,B)=0, & \text{for} \quad 0\leq x\leq L \quad \text{and} \quad 0\leq y\leq H \\ u(x,0,z)=0, \quad v(x,0,z)=0, \quad w(x,0,z)=0, & \text{for} \quad 0\leq x\leq L \quad \text{and} \quad 0\leq z\leq B \\ \mathbf{u}_{drop}=0, & \text{for} \quad t=0 \end{cases} \tag{10.6}$$

10.3.1.3 Computational modeling

The domain was defined starting from the origin and extending to the coordinates $(L, H, B) = (0.048\,\mathrm{m}, 0.096\,\mathrm{m}, 0.048\,\mathrm{m})$. The l_{bot} level was defined as $24 \times 48 \times 24$. There were 3 more refinement levels.

The boundary conditions for the parallelepiped domain were defined as follows for each of the three velocity components and for pressure.

For the velocity components u, v, and w, the west, east, south, bottom, and top faces were set with Dirichlet conditions, indicating that the velocity is directly imposed on these faces (all zero in this case). The north face was set with a Neumann condition.

For pressure, the west, east, south, bottom, and top faces were set with Neumann conditions. The north face was set with a Dirichlet condition (zero in this case).

The droplet was represented using the VoF method, which is suitable for accurately capturing the interface between two fluids. Within the VoF settings, the Continuum Surface Force (CSF) model was used to solve for interfacial tension. This model is effective in representing the interfacial forces, ensuring that interfacial effects are correctly incorporated into the simulation.

The rigid and stationary sphere was represented using the IBM technique.

A remeshing procedure was established every 50 iterations. This procedure ensures that the VoF interface remains covered by the finest available mesh, allowing for an adequate resolution of the interface and, consequently, an accurate capture of the associated physical phenomena. The criteria for remeshing were based on the specific mass and immersed boundary points, ensuring that regions with significant changes in these properties (tolerance < 0.05) received finer mesh refinement.

CFL number was set to 0.2. This lower value was chosen to ensure the stability of the simulation, ensuring that the time step was sufficiently small to accurately capture the rapid dynamics of the flow. With this configuration, the simulation was able to progress without introducing numerical instabilities, even in regions with high velocity gradients.

The total simulation time was set to 20 ms, which is sufficient to observe the dynamic behavior of the droplet during the period of interest.

10.3.1.4 Results

After performing the computational simulation in MFSim, the frames corresponding to the times indicated in Tab. 8 were extracted, which composes Fig. 41.

Qualitatively, by comparing Figs. 40 and 41, it can be observed that the computational simulation run in MFSim performed satisfactorily, achieving the same results as Deen, Annaland e Kuipers (2009).

Table 8 – Deen, Annaland e Kuipers (2009) and MFSim's simulation times for comparison

Snapshot	**Reference time from Deen, Annaland e Kuipers (2009) (s)**	**Time from MFSim (s)**
1	0.050	0.0493
2	0.075	0.0757
3	0.100	0.0994
4	0.125	0.1251
5	0.150	0.1502
6	0.175	0.1753

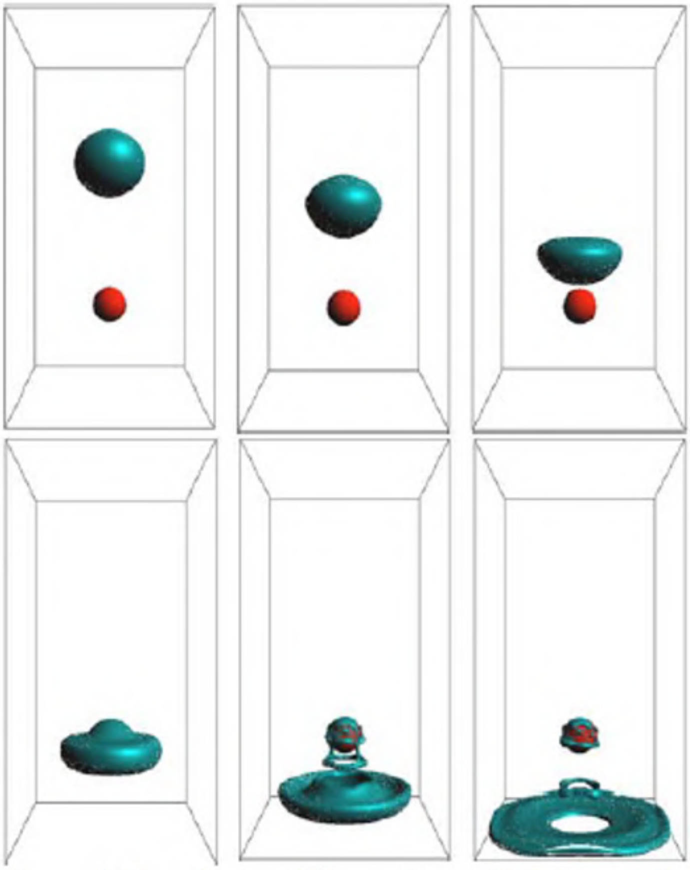

Figure 40 – 3D snapshots from Deen, Annaland e Kuipers (2009) at specific times presented at Tab. 8

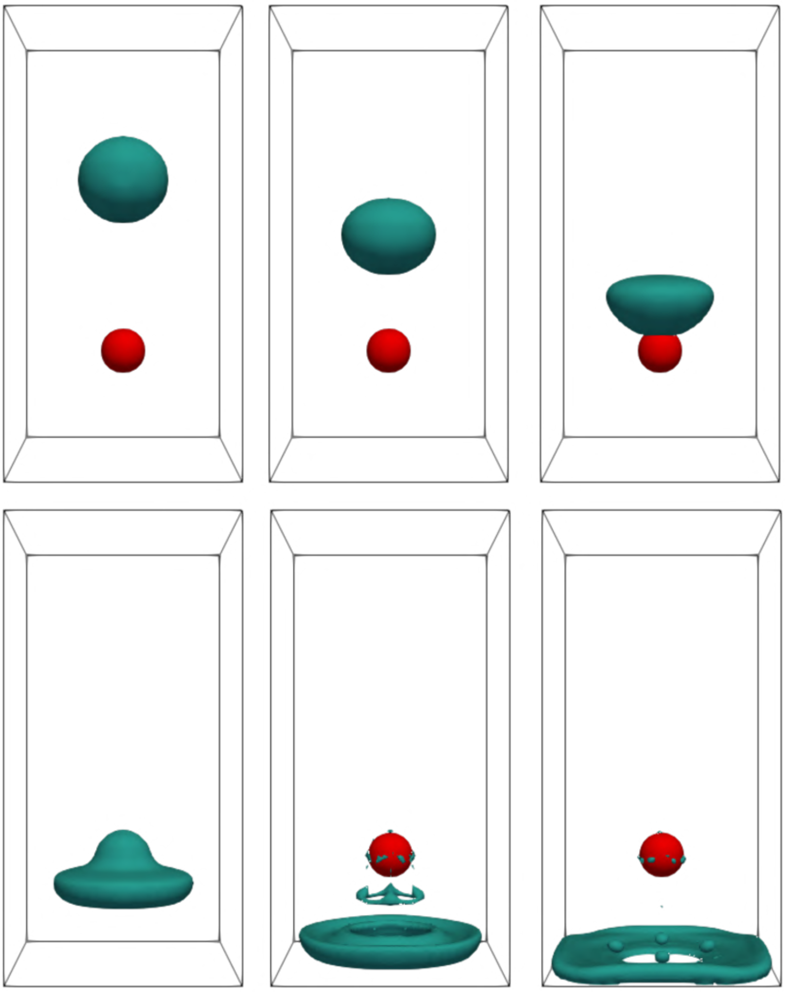

Figure 41 – 3D snapshots from MFSim at specific times presented at Tab. 8

Furthermore, the computational simulation of a fluid drop falling onto a sphere revealed distinct fluid dynamic behaviors for Newtonian and non-Newtonian fluids when the power-law model was activated. For the Newtonian fluid with constant viscosity $mu = 0.1$, the drop maintained predictable behavior, with the constant viscosity resulting in uniform flow and stable interaction with the sphere. In contrast, when the power-law non-Newtonian fluid model was activated, physically consistent differences were observed, particularly in regions of high shear rate.

In the case of non-Newtonian fluids, the simulations demonstrated that the drop's viscosity varied according to the shear rate, significantly influencing the drop's behavior upon contact with the sphere. For the simulation with $n = 0.25$ (simulation 2), the drop exhibited pronounced shear-thinning behavior, where the viscosity drastically decreased in regions of high shear rate. This effect resulted in a considerable increase in the drop's velocity, as the reduction in viscosity facilitated the flow. The simulation with $n = 0.5$ (simulation 3) displayed similar behavior, although less pronounced, resulting in a lower velocity compared to simulation 2, but still higher than that of the Newtonian fluid.

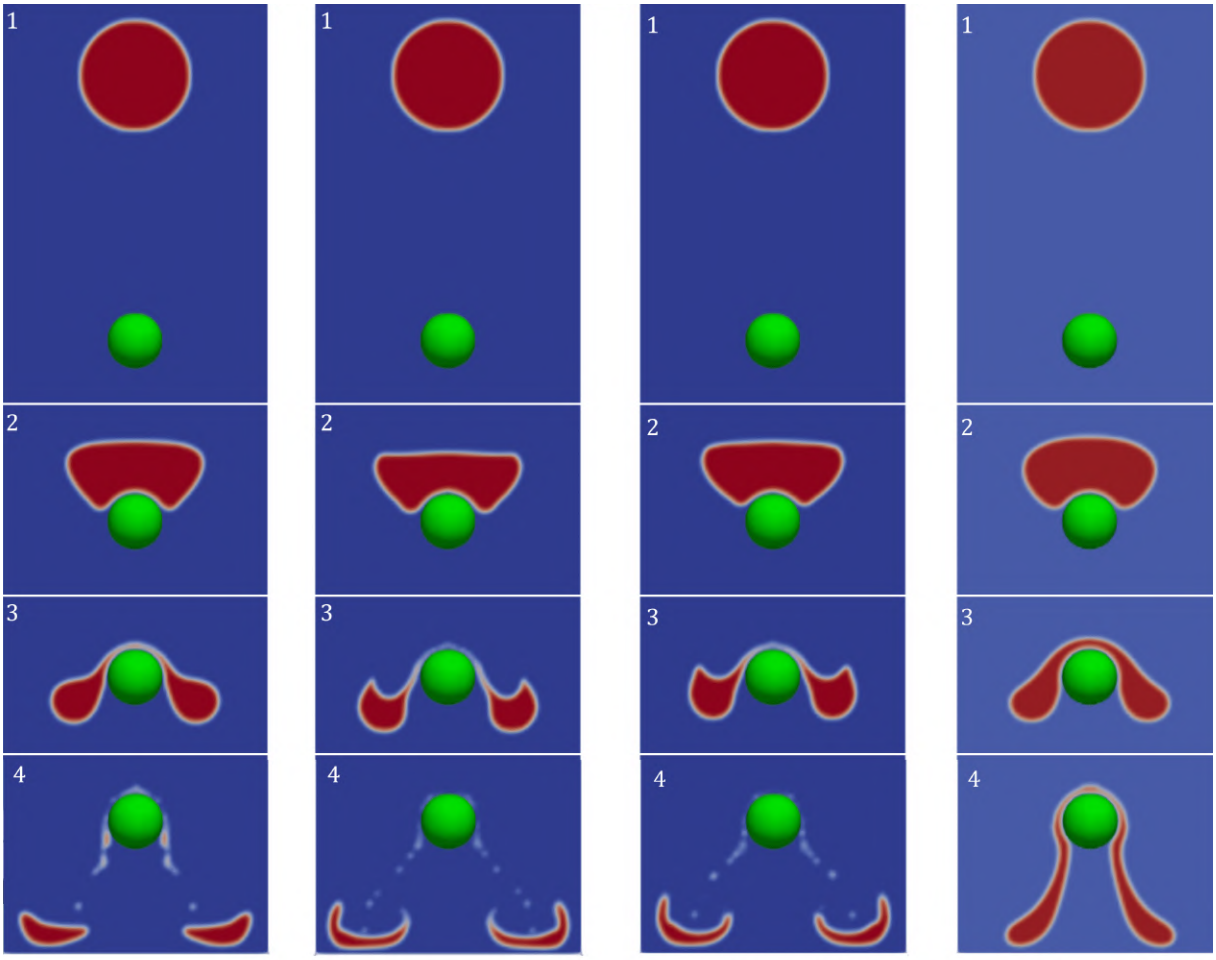

Newtonian m=0.1 n=0.25 m=0.1 n=0.50 m=0.1 n=1.50

Figure 42 – Comparison between Newtonian fluid (left) and power-law non-Newtonian fluids with different flow index behavior, n

Conversely, the simulation with $n = 1.5$ (simulation 4) exhibited behavior opposite to shear-thinning, known as shear-thickening, as introduced in sec. 5.2.3. In this case, the viscosity significantly increased in regions of high shear rate around the sphere, creating greater resistance to flow. This behavior resulted in a sharp decrease in the drop's velocity and greater difficulty in flowing over the rigid sphere. These observed and demonstrated characteristics underscore the importance of considering the rheological behavior of non-Newtonian fluids in fluid dynamic simulations, especially in applications where shear rates vary significantly, as the fluid's viscous response can drastically alter the flow dynamics.

10.4 Falling drop deformation

Now that the VoF method and the IBM technique have been properly validated, we will take another step forward by validating the deformation of a droplet in free fall, according to its Weber number. Were used the article presented by Kékesi, Amberg e Wittberg (2014).

10.4.1 Physical modeling

This concerns the free fall of a particle initially positioned at $\mathbf{S}_{\mathrm{p}} = (x_i, y_i, z_i)$ within a domain of dimensions L × H × B, with AR of L:H:B=1:1:1 and with south ($y = 0$) and north ($y = \mathrm{H}$) faces with no pressure difference with the external environment. The flow was considered incompressible and isothermal. Physical properties are assumed to be constant. Gravitational effects were taken into account, with $g = 9.80665\,\mathrm{m/s^2}$.

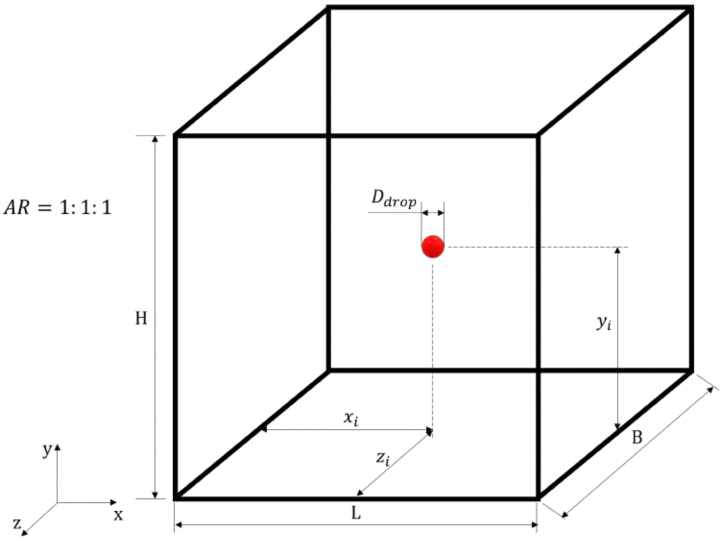

Figure 43 – Schematic diagram of falling drop physical modeling

The dimensionless fluid dynamic parameters used in the simulations conducted are presented in the table below, in accordance with the work of Kékesi, Amberg e Wittberg (2014):

Table 9 – Single drop simulations parameters (KéKESI; AMBERG; WITTBERG, 2014)

Parameter	**Abbr.**	**Numerical value**
Weber number	We	0.1, 1, 5, 10 and 12
Reynolds number	*Re*	100
Specific mass ratio	ρ^*	80
Viscosity ratio	μ^*	55.6

10.4.2 Algebraic-differential mathematical modeling

As the specific mass is constant (incompressible flow), the term $\partial\rho/\partial t$ of mass balance (eq. 4.1) is set to zero. Then we have:

$$\nabla \cdot \mathbf{u} = 0$$

Applying the physical modeling assumptions described in the previous section, this problem will uses the full linear momentum balance equation (eq. 4.33) to be solved, as follows:

$$\rho\frac{Du_i}{Dt} = \rho g_i - \nabla \mathrm{p} + \frac{\partial}{\partial x_i}\left[\mu\left(\frac{\partial u_i}{\partial x_j} + \frac{\partial u_j}{\partial x_i}\right)\right]$$

As previously mentioned, for the fall of a non-Newtonian droplet, the only modification to the above equation is that the viscosity will no longer be a constant. This entails, in the discrete model, calculating its value for each internal droplet volume of the computational domain by calling a subroutine within the MFSim code.

The boundary conditions for this problem are:

$$\begin{cases} \frac{\partial p}{\partial y}{=}0, \quad \text{for} \quad y{=}H \quad \text{and} \quad 0{\le}x{\le}L \quad \text{and} \quad 0{\le}z{\le}B \\ u(0{,}y{,}z){=}0, \quad v(0{,}y{,}z){=}0, \quad w(0{,}y{,}z){=}0, \quad \text{for} \quad 0{\le}y{\le}H \quad \text{and} \quad 0{\le}z{\le}B \\ u(L{,}y{,}z){=}0, \quad v(L{,}y{,}z){=}0, \quad w(L{,}y{,}z){=}0, \quad \text{for} \quad 0{\le}y{\le}H \quad \text{and} \quad 0{\le}z{\le}B \\ u(x{,}y{,}0){=}0, \quad v(x{,}y{,}0){=}0, \quad w(x{,}y{,}0){=}0, \quad \text{for} \quad 0{\le}x{\le}L \quad \text{and} \quad 0{\le}y{\le}H \\ u(x{,}y{,}B){=}0, \quad v(x{,}y{,}B){=}0, \quad w(x{,}y{,}B){=}0, \quad \text{for} \quad 0{\le}x{\le}L \quad \text{and} \quad 0{\le}y{\le}H \\ \frac{\partial p}{\partial y}{=}0, \quad \text{for} \quad y{=}0 \quad \text{and} \quad 0{\le}x{\le}L \quad \text{and} \quad 0{\le}z{\le}B \\ \mathbf{u}_{drop}{=}0, \quad \text{for} \quad t{=}0 \end{cases} \tag{10.7}$$

10.4.3 Computational modeling

The domain was defined starting from the origin and extending to the coordinates $(L, H, B) = (0.16\,\text{m}, 0.16\,\text{m}, 0.16\,\text{m})$. The l_{bot} level was defined with 20 volumes in each direction ($20 \times 20 \times 20$). There were 7 more refinement levels, allowing - at its finest level - the passage of 80 volumes across the droplet diameter. The latter was defined at $D_{drop} = 5\,\text{mm}$ with its initial position at $(L/2, 5H/8, B/2)$.

The boundary conditions for the parallelepiped domain were defined as follows for each of the three velocity components and for pressure.

For the velocity components u, v, and w, the west, east, bottom and top faces were set with Dirichlet conditions, indicating that the velocity is directly imposed on these faces (all zero in this case). The south and north faces were set with a Neumann condition.

For pressure, the west, east, bottom and top faces were set with Neumann conditions. The north and south faces were set with a Dirichlet condition (all zero in this case). These configurations ensure an adequate representation of the variables of interest at the domain boundaries, allowing for the correct simulation of the flow within the domain.

The droplet was represented using the VoF method; within the VoF settings, the Continuum Surface Force (CSF) model was used to solve for interfacial tension.

A remeshing procedure was established every 20 iterations. This procedure ensures that the VoF interface remains covered by the finest available mesh, allowing for an adequate resolution of the interface and, consequently, an accurate capture of the associated physical phenomena. The criteria for remeshing were based on the VoF and vorticity, ensuring that regions with significant changes in these properties (tolerance < 0.01) received finer mesh refinement.

CFL number was set to 0.5. This value was chosen to ensure the stability of the simulation, ensuring that the time step was sufficiently small to accurately capture the rapid dynamics of the flow.

The total simulation time was set to 14 ms, which is sufficient to observe the dynamic behavior of the droplet during the period of interest.

10.4.4 Results for a Newtonian fluid drop

Firstly, it was observed that for simulations with We = 0.1 and We = 1, the simulation time was relatively much longer compared to higher We numbers, except for We = 12, where the droplet breaks, resulting in a significantly longer simulation time.

Table 10 – Simulation time for each Weber number

Weber number	**Simulation time (h)**
0.1	≈ 15.00
1	9.84
5	4.32
10	3.48
12	≈ 24.00

Qualitatively comparing the images obtained in the MFSim simulations, it is possible to align them with the images obtained by Kékesi, Amberg e Wittberg (2014).

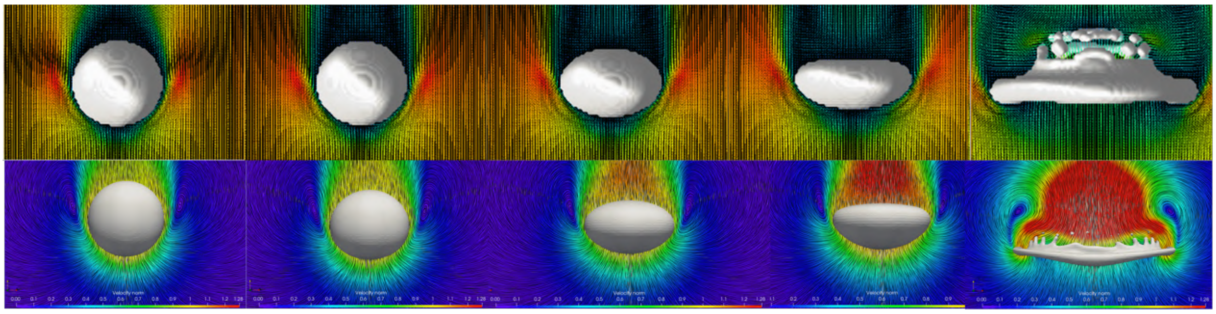

Figure 44 – Qualitatively results of simulating Newtonian fluid. We equal to 0.1, 1, 5, 10 and 12, from left to right

10.4.5 Results of simulating non-Newtonian models as Newtonian fluids

With the aim of validating - once again - the non-Newtonian models, they were configured to represent the same Newtonian fluid as in the previous simulation, in sec. 10.4.1, by appropriately selecting their respective parameters. The configuration of these parameters is presented in Tab. 11. A value of We = 10 was chosen to visualize a greater deformation of the droplet.

After running all the mentioned simulations, the images in Fig. 45 were generated, showing the same drop shape at We = 10.

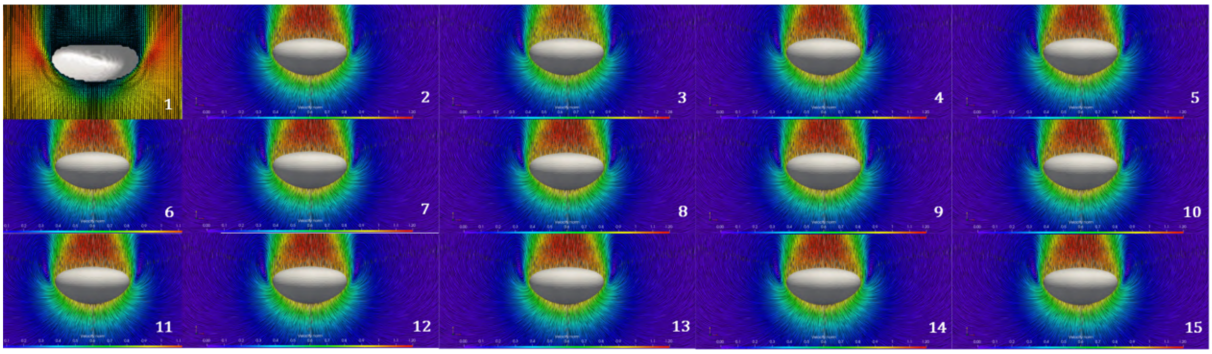

Figure 45 – Qualitatively results of non-Newtonian models simulating Newtonian fluid at the falling drop case

Table 11 – Non-Newtonian models' parameters to simulate Newtonian fluid at the present falling drop case

Figure	Rheological model	Model's parameters	Simulation time
1	Kékesi, Amberg e Wittberg (2014)	–	–
2	Newtonian fluid	–	–
3	Power-law	$m = 0.00556\,[\mathrm{Pa}\cdot\mathrm{s}^n]$ $n = 1$	4.42h pc-MFLab
4	Power-law (Davies)	$m = 0.00556\,[\mathrm{Pa}\cdot\mathrm{s}^n]$ $n = 1$	4.90h Cluster
5	Carreau	$n = 1 \quad \lambda = 0\,[\mathrm{s}]$ $\eta_0 = 0.00556\,[\mathrm{Pa}\cdot\mathrm{s}]$ $\eta_\infty = 0\,[\mathrm{Pa}\cdot\mathrm{s}]$	4.95h Cluster
6	Carreau-Yasuda	$n = 1 \quad a = 2$ $\eta_0 = 0.00556\,[\mathrm{Pa}\cdot\mathrm{s}]$ $\eta_\infty = 0\,[\mathrm{Pa}\cdot\mathrm{s}]$ $\lambda = 0\,[\mathrm{s}]$	4.92h Cluster
7	Cross	$n = 1 \quad \lambda = 0\,[\mathrm{s}]$ $\eta_0 = 0.00556\,[\mathrm{Pa}\cdot\mathrm{s}]$ $\eta_\infty = 0\,[\mathrm{Pa}\cdot\mathrm{s}]$	4.25h pc-MFLab
8	Simplified Cross	$\eta_0 = 0.00556\,[\mathrm{Pa}\cdot\mathrm{s}]$ $\eta_\infty = 0\,[\mathrm{Pa}\cdot\mathrm{s}]$ $\lambda = 0\,[\mathrm{s}]$	4.25h pc-MFLab
9	Modified Cross	$n = 1 \quad a = 1$ $\eta_0 = 0.00556\,[\mathrm{Pa}\cdot\mathrm{s}]$ $\eta_\infty = 0\,[\mathrm{Pa}\cdot\mathrm{s}]$ $\lambda = 0\,[\mathrm{s}]$	4.25h pc-MFLab
10	Herschel-Bulkley	$n = 1 \quad \tau_0 = 0\,[\mathrm{Pa}]$ $\eta_0 = 0.00556\,[\mathrm{Pa}\cdot\mathrm{s}]$	4.25h pc-MFLab
11	Bingham	$\eta_0 = 0.00556\,[\mathrm{Pa}\cdot\mathrm{s}]$ $\tau_0 = 0\,[\mathrm{Pa}]$	4.33h pc-MFLab
12	Casson	$\eta_0 = 0.00556\,[\mathrm{Pa}\cdot\mathrm{s}]$ $\tau_0 = 0\,[\mathrm{Pa}]$	4.38h pc-MFLab
13	Modified Casson	$\eta_0 = 0.00556\,[\mathrm{Pa}\cdot\mathrm{s}]$ $\lambda = 1\,[\mathrm{s}] \quad \tau_0 = 0\,[\mathrm{Pa}]$	4.91h Cluster
14	Powell-Eyring	$\eta_0 = 0.00556\,[\mathrm{Pa}\cdot\mathrm{s}]$ $\eta_\infty = 0.00556\,[\mathrm{Pa}\cdot\mathrm{s}]$ $\lambda = 1\,[\mathrm{s}]$	4.91h Cluster
15	Modif. Powell-Eyring	$\eta_0 = 0.00556\,[\mathrm{Pa}\cdot\mathrm{s}]$ $\eta_\infty = 0.00556\,[\mathrm{Pa}\cdot\mathrm{s}]$ $\lambda = 1\,[\mathrm{s}] \quad a = 0$	4.91h Cluster

10.5 Blood modeling

10.5.1 Physical modeling

This concerns the free fall of an initially spherical particle of human blood (incompressible flow), at a constant external temperature of 25 °C (isothermal flow), positioned at $\mathbf{S}_\mathrm{p} = (x_i, y_i, z_i)$ within a domain of dimensions L × H × B, whose upper interface has no pressure difference with the external environment (see Fig. 43). Physical properties are considered constant, except for the viscosity of the blood particle, which, depending on the rheological model used in the simulation, will vary with the shear rate. The interfacial tension of the blood-air system was considered $\sigma = 5.2604 \cdot 10^{-2}\,\mathrm{N/m}$ (calculated by Eq. 3.1, at 37 °C), the specific mass of the surrounding air was considered $1.184\,\mathrm{kg/m^3}$ (at 25 °C), while the density of human blood was considered $1,060\,\mathrm{kg/m^3}$ (at 37 °C). Gravitational effects were considered, with $g = 9.80665\,\mathrm{m/s^2}$.

Regarding the parameters for each viscosity model, the ones presented in Tabs. 4, 5 and 6 were considered.

10.5.2 Algebraic-differential mathematical modeling

As the specific mass is constant (incompressible flow), the term $\partial\rho/\partial t$ of mass balance (eq. 4.1) is set to zero. Then we have:

$$\nabla \cdot \mathbf{u} = 0$$

Applying the physical modeling assumptions described in the previous section, this problem will uses the full linear momentum balance equation (eq. 4.33) to be solved, as follows:

$$\rho\frac{Du_i}{Dt} = \rho g_i - \nabla \mathrm{p} + \frac{\partial}{\partial x_i}\left[\mu\left(\frac{\partial u_i}{\partial x_j} + \frac{\partial u_j}{\partial x_i}\right)\right]$$

As previously mentioned, for the fall of a non-Newtonian droplet, the only modification to the above equation is that the viscosity will no longer be a constant. This entails, in the discrete model, calculating its value for each internal droplet volume of the computational domain by calling a subroutine within the MFSim code.

The boundary conditions for this problem are:

$$\begin{cases} \frac{\partial p}{\partial y}=0, & \text{for} \quad y=H \quad \text{and} \quad 0\leq x\leq L \quad \text{and} \quad 0\leq z\leq B \\ u(0,y,z)=0, \quad v(0,y,z)=0, \quad w(0,y,z)=0, & \text{for} \quad 0\leq y\leq H \quad \text{and} \quad 0\leq z\leq B \\ u(L,y,z)=0, \quad v(L,y,z)=0, \quad w(L,y,z)=0, & \text{for} \quad 0\leq y\leq H \quad \text{and} \quad 0\leq z\leq B \\ u(x,y,0)=0, \quad v(x,y,0)=0, \quad w(x,y,0)=0, & \text{for} \quad 0\leq x\leq L \quad \text{and} \quad 0\leq y\leq H \\ u(x,y,B)=0, \quad v(x,y,B)=0, \quad w(x,y,B)=0, & \text{for} \quad 0\leq x\leq L \quad \text{and} \quad 0\leq y\leq H \\ u(x,0,z)=0, \quad v(x,0,z)=0, \quad w(x,0,z)=0, & \text{for} \quad 0\leq x\leq L \quad \text{and} \quad 0\leq z\leq B \\ \mathbf{u}_{drop}=0, & \text{for} \quad t=0 \end{cases} \tag{10.8}$$

10.5.3 Computational modeling

The domain was defined starting from the origin and extending to the coordinates $(L, H, B) = (0.16\,\text{m}, 0.16\,\text{m}, 0.16\,\text{m})$. The l_{bot} level was defined with 20 volumes in each direction ($20 \times 20 \times 20$). There were 7 more refinement levels, allowing - at its finest level - the passage of 80 volumes across the droplet diameter ($D_{drop}/\Delta = 80$).

Kant e Banerjee (2023), for instance, used a $D_{drop}/\Delta = 75$ resolution in an uniform grid. In addition, the grid resolution is comparable or even better then some previous studies, i.e., Han e Tryggvason (2001) ($D_{drop}/\Delta = 100$), Wadhwa, Magi e Abraham (2007) ($D_{drop}/\Delta = 35$), Kékesi, Amberg e Wittberg (2014) ($D_{drop}/\Delta = 32$), Shao, Luo e Fan (2017) ($D_{drop}/\Delta = 50$), Yang et al. (2016) ($D_{drop}/\Delta = 128$), Jain et al. (2019) ($D_{drop}/\Delta = 410$).

Thus, defining $D_{drop} = 5\,\text{mm}$ with its initial position at $(L/2, 5H/8, B/2)$, the finest mesh in the present simulation gives $D_{drop}/\Delta = 80$.

The boundary conditions for the parallelepiped domain were defined as follows for each of the three velocity components and for pressure.

For the velocity components u, v, and w, the west, east, south, bottom, and top faces were set with Dirichlet conditions, indicating that the velocity is directly imposed on these faces (all zero in this case). The north face was set with a Neumann condition.

For pressure, the west, east, south, bottom, and top faces were set with Neumann conditions. The north face was set with a Dirichlet condition, where the pressure is directly imposed (zero in this case). These configurations ensure an adequate representation of the variables of interest at the domain boundaries, allowing for the correct simulation of the flow within the domain.

The droplet was represented using the VoF method, which is suitable for accurately capturing the interface between two fluids. Within the VoF settings, the Continuum Surface Force (CSF) model was used to solve for interfacial tension. This model is effective in representing the interfacial forces, ensuring that interfacial effects are correctly incorporated into the simulation.

A remeshing procedure was established every 5 iterations. This procedure ensures that the VoF interface remains covered by the finest available mesh, allowing for an adequate resolution of the interface and, consequently, an accurate capture of the associated physical phenomena. The criteria for remeshing were based on the VoF, ensuring that regions with significant changes in these properties (tolerance < 0.05) received finer mesh refinement.

CFL number was set to 0.1. This lower value was chosen to ensure the stability of the simulation, ensuring that the time step was sufficiently small to accurately capture the rapid dynamics of the flow. With this configuration, the simulation was able to progress without introducing numerical instabilities, even in regions with high velocity gradients.

The total simulation time was set to 15 ms, which is sufficient to observe the dynamic behavior of the droplet during the period of interest.

10.5.4 Influence of the viscosity model: fall

First, all models were assessed — both quantitatively and qualitatively — when a mean velocity about $\|\mathbf{u}\| \approx 1.00\,\mathrm{m/s}$ was reached. Figures 46 to 49 evidence the preserved spherical shape of the droplet at this instant and the different viscosity patterns promoted inside it, by a z-mean symmetry plane view (at B/2 in Fig. 43).

First, evaluating the viscosity distribution and imposing a range of $1.85 \cdot 10^{-5}$ to 0.01 Pa·s, for better visualization of intensities by the color palette, it is evident from Figs. 46 and 47 that each computationally simulated model has its intrinsic particularities in the internal viscosity distribution of the drop. However, it is possible to notice a region (to the east) with higher intensity in almost all models, which corresponds to the highest measured viscosities. This indicates low shear rates on fluid elements in this region, mainly related to the internal circulation promoted during the free fall of the drop. Additionally, greater uniformity and attenuation are perceptible in the K-L, Casson, Modified Casson and Herschel-Bulkley models, indicating consistency in the results, given that these models are characterized by a yield stress that prevents fluid movement if this stress is not reached, despite the use of Papanastasiou regularization (see sec. 6.3.5).

It is important to note that out of the six references found for the power-law model, only three were successfully executed (as predicted in chapter 9), but not without imposing minimum and maximum viscosity limits. This is because power-law models promote an exponential increase in viscosity with the decrease in shear rate, which results in poorly represented fluid dynamics, where solid-like viscosities are reached. Furthermore, all the papers reviewed focus on specific situations of internal fluid circulation, where a specific range of shear rate is fixed. With these considerations, in the free fall of a drop of this fluid, undoubtedly, shear rates outside this range occur and lead to the discrepancies observed in the simulations, which necessitated the aforementioned viscosity limitations.

Moving on to the analysis of the internal pressure distribution within the drop (figures 48 and 49), a range of 0 to 50.00 Pa was fixed for better visualization of intensities using the color palette. When the drop reaches $\|\mathbf{u}\| \approx 1.00\,\mathrm{m/s}$, almost the same internal pressure distribution is observed in all models, with the upper portion of the drop exhibiting a little higher pressure. Although counterintuitive, this is physically consistent, as the pressure jump between the dispersed and continuous phases needs to remain constant. Since the drop is in free fall, a higher upstream pressure and a lower downstream pressure are observed externally, resulting in a internal little smaller upstream pressure jump and a internal little larger downstream pressure jump.

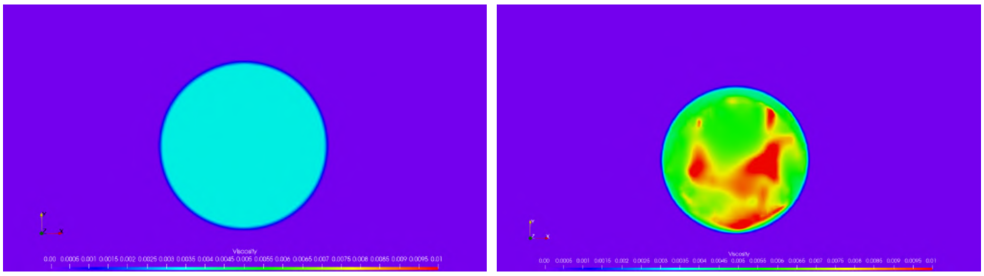

(a) Newtonian (b) Carreau

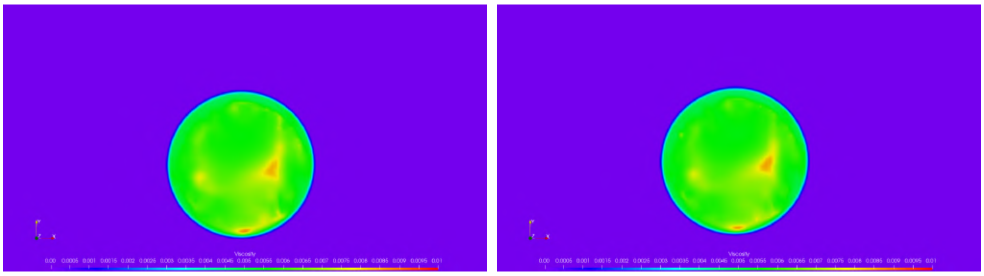

(c) Casson1 (d) Casson2

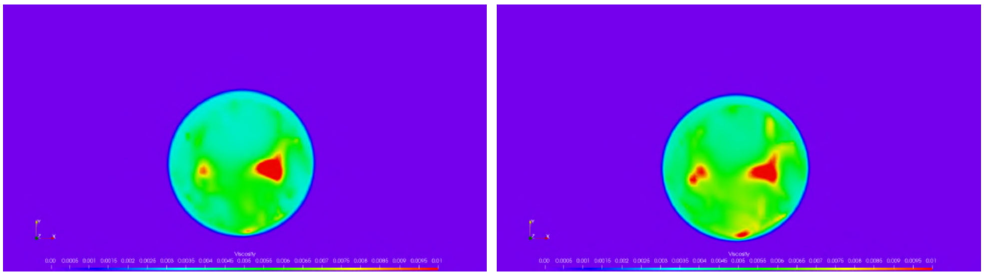

(e) Cross1 (f) Cross2

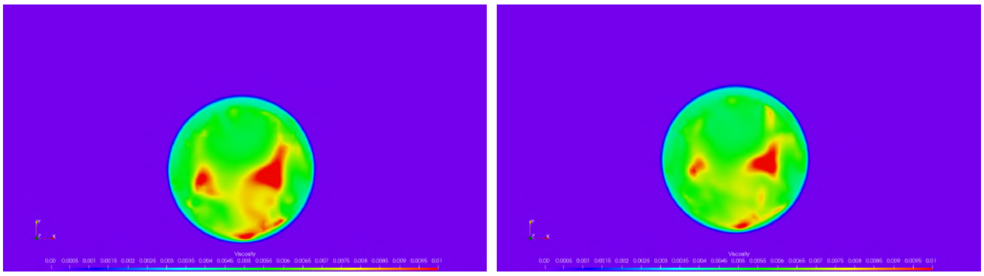

(g) CY1 (h) CY2

Figure 46 – Viscosity distribution in the human blood droplet at $\|\mathbf{u}\| \approx 1\,\mathrm{m/s}$, in the z-mean symmetry plane

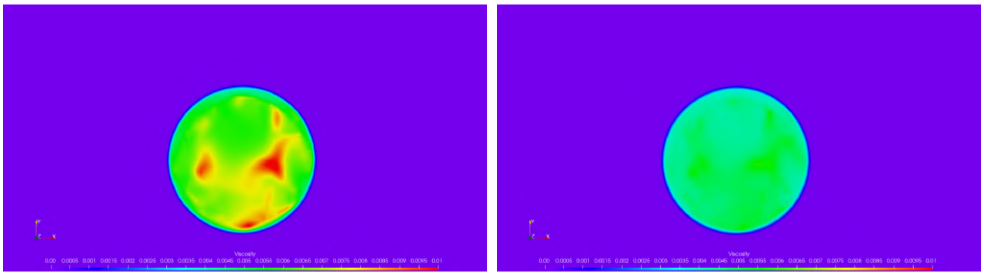

(a) HB (b) KL

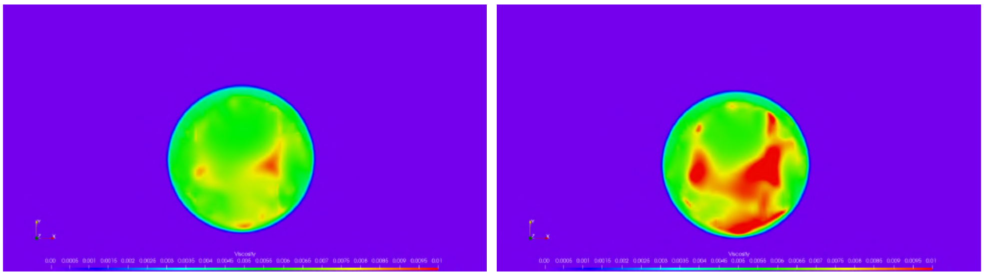

(c) ModCasson (d) ModCross1

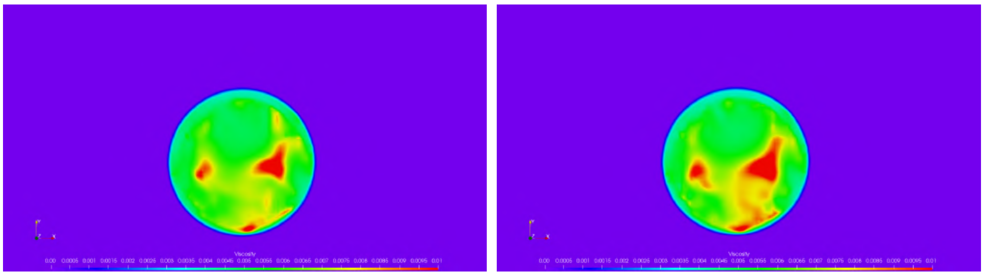

(e) ModCross2 (f) ModPE

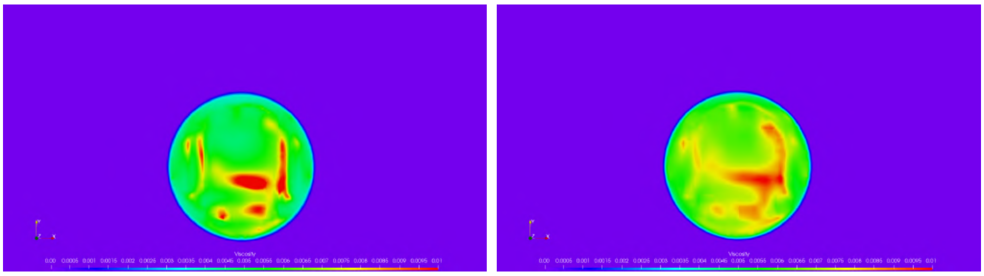

(g) PE (h) PL3

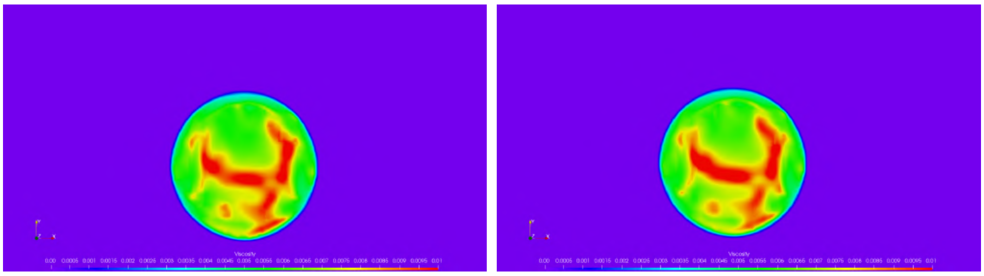

(i) PL4 (j) PL6

Figure 47 – Viscosity distribution in the human blood droplet at $\|\mathbf{u}\| \approx 1\,\mathrm{m/s}$, in the z-mean symmetry plane

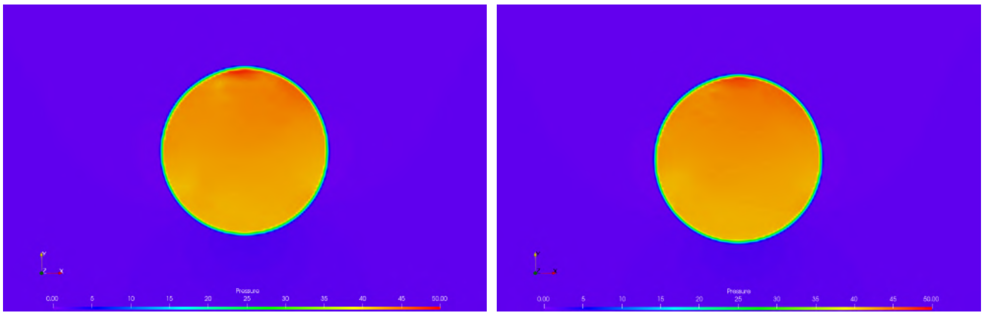

(a) Newtonian (b) Carreau

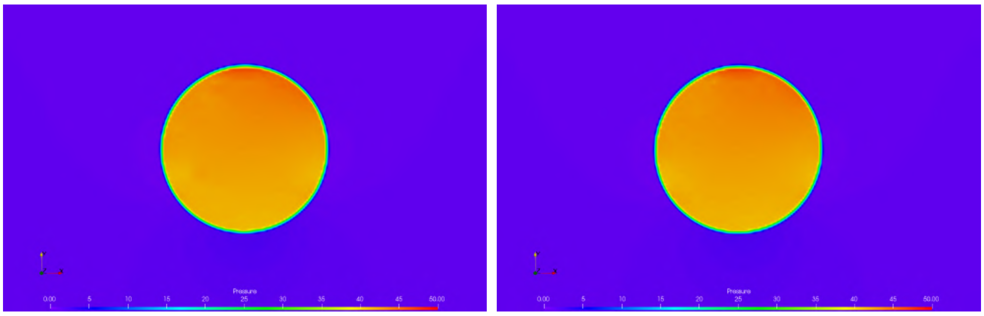

(c) Casson1 (d) Casson2

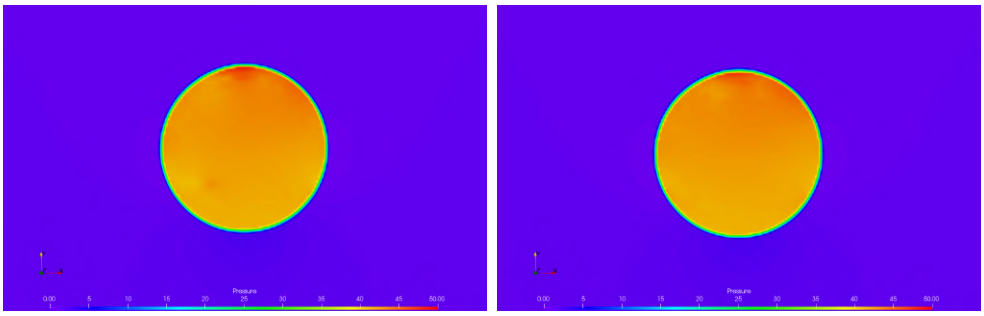

(e) Cross1 (f) Cross2

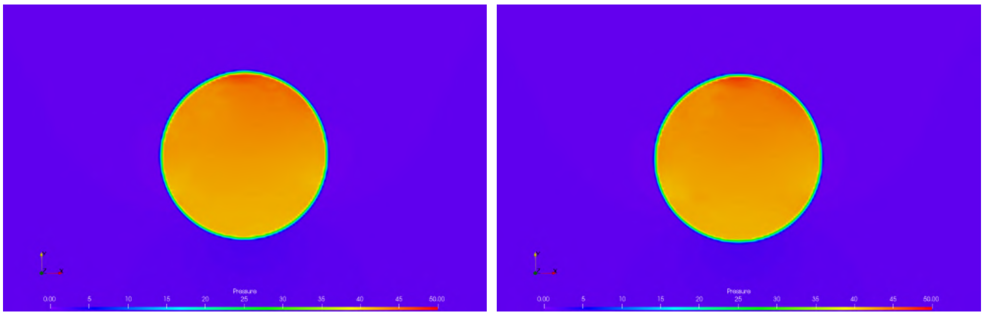

(g) CY1 (h) CY2

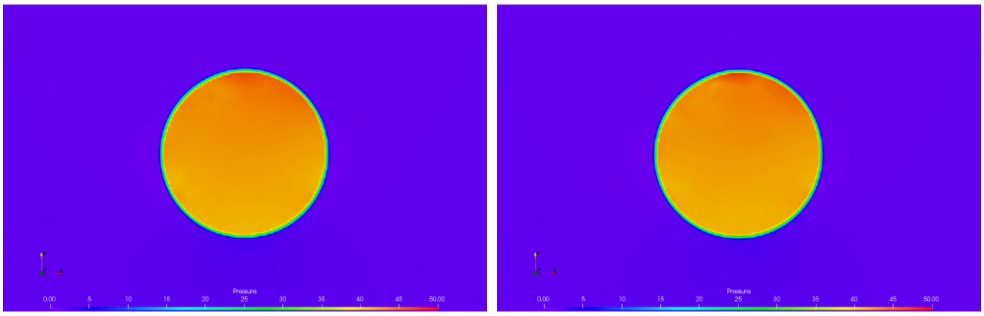

(i) HB (j) KL

Figure 48 – Pressure distribution in the human blood droplet at $\|\mathbf{u}\| \approx 1\,\mathrm{m/s}$, in the z-mean symmetry plane

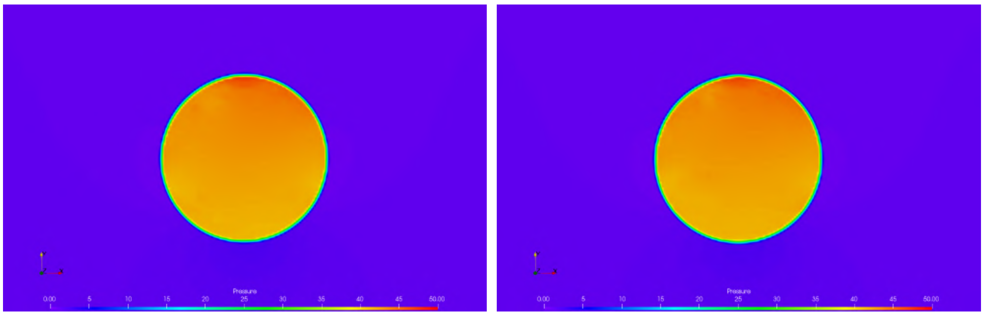

(a) ModCasson (b) ModCross1

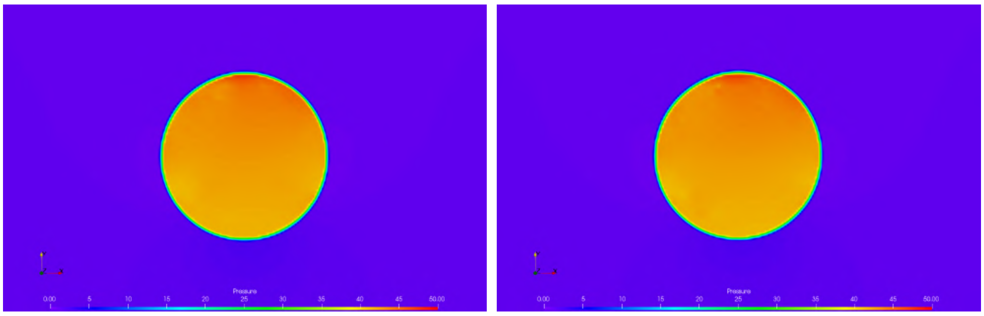

(c) ModCross2 (d) ModPE

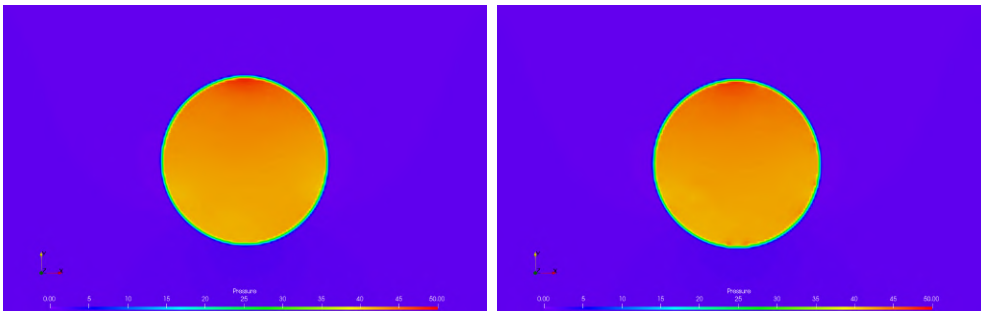

(e) PE (f) PL3

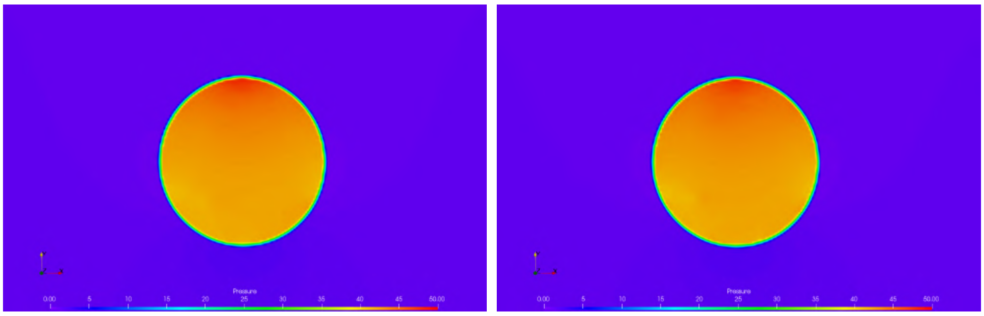

(g) PL4 (h) PL6

Figure 49 – Pressure distribution in the human blood droplet at $\|\mathbf{u}\| \approx 1\,\mathrm{m/s}$, in the z-mean symmetry plane

10.5.5 Influence of the viscosity model: impact

In second place, all models were assessed on the imminence of the impact, when a mean velocity about $\|\mathbf{u}\| \approx 1.43\,\mathrm{m/s}$ was reached. Again, the following tables and figures show the previous analysis at this specific moment of the simulation. It is important to note that at the moment of impact, $\mathrm{We} = 0.23$ and $\mathrm{Oh} = 6.53 \cdot 10^{-3}$, which implies virtually no deformation of the drop, as explained in sec. 10.2.

In figures 50 and 51, the maximum viscosity limit imposed, to the collor pallete, to improve the visualization of the internal distribution of this parameter was reduced to 0.0085 Pa·s. Again, the lowest viscosities were observed in the models with yield stress (K-L, Casson, Modified Casson and Herschel-Bulkley). However, at the moment of impact, the models began to exhibit their differences more intensively. There is no longer a specific region in almost all models where a pattern can be observed. The differences at this instant are more pronounced.

The PE model, in contrast to all other models, observed a maximum viscosity at the impact greater than that observed at $\|\mathbf{u}\| \approx 1.00\,\mathrm{m/s}$, jumping from $\eta \approx 16.20$ mPa·s to $\eta \approx 27.25$ mPa·s. This can be justified due to its constitutive equation (eq. 6.8), which includes an inverse hyperbolic sine term.

Figures 54 and 55 illustrate the internal circulation occurring within the drop for each computationally simulated model and both the internal vortices and those formed downstream. The color palette aligns with the previously presented viscosity distribution.

The analysis of streamlines, particularly in relation to the stagnation point of the drop, provides valuable insight into the internal recirculation and its interaction with the viscosity distribution. Blood, due to its non-Newtonian nature, exhibits viscosity that varies with the shear rate. Each simulated model represents the relationship between shear stress and shear rate differently, influencing the viscosity distribution within the free-falling drop.

The visualization of streamlines reveals regions of recirculation where the internal flow of the drop deviates and reorganizes due to the interaction between inertia and viscosity. These recirculations are particularly significant near the stagnation point, where the fluid decelerates and the shear rate can change drastically.

In the context of models such as power-law, viscosity is strongly dependent on the shear rate, decreasing as this rate increases. During the fall, regions with a high shear rate, near the boundaries of the drop, exhibit reduced viscosity, facilitating recirculation. Conversely, areas of very low shear rate, such as the internal stagnation point of the drop or those farther from the internal vortices, display higher viscosity, influencing the recirculation pattern.

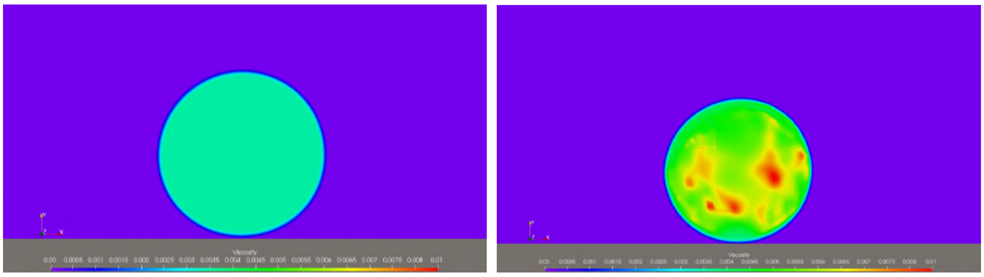

(a) Newtonian (b) Carreau

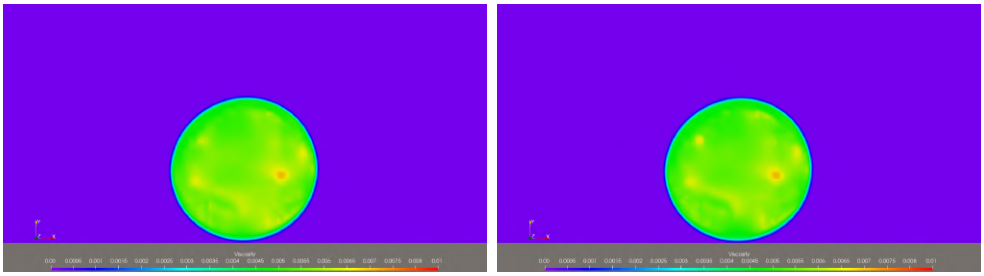

(c) Casson1 (d) Casson2

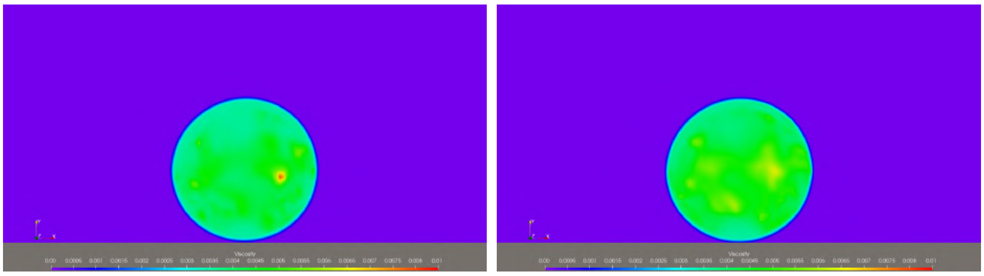

(e) Cross1 (f) Cross2

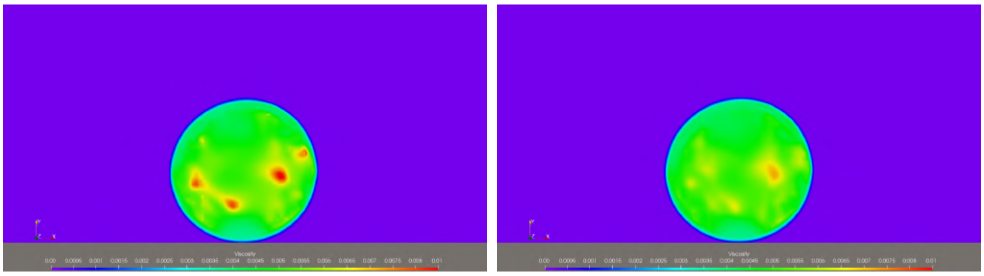

(g) CY1 (h) CY2

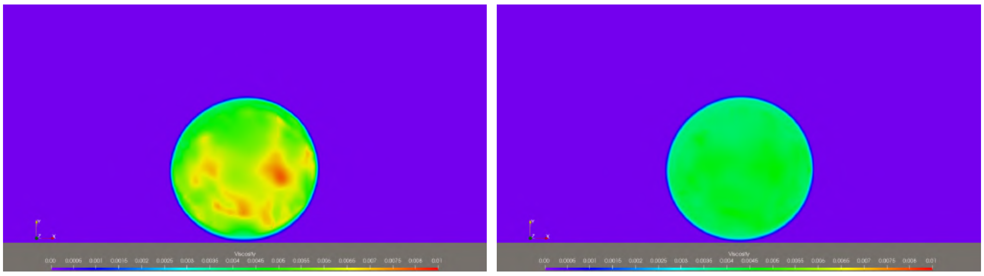

(i) HB (j) KL

Figure 50 – Viscosity distribution in the human blood at the verge of droplet impact, in the z-mean symmetry plane

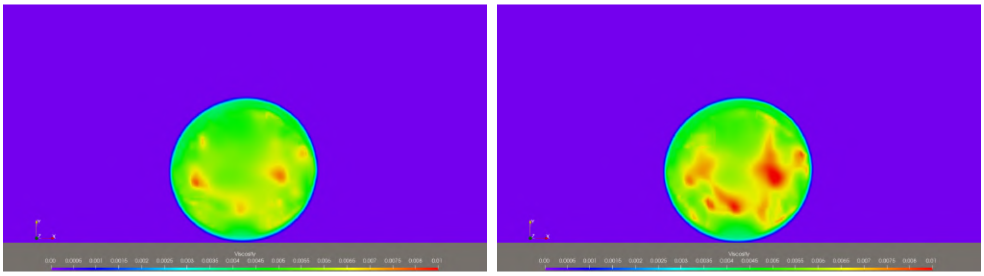

(a) ModCasson (b) ModCross1

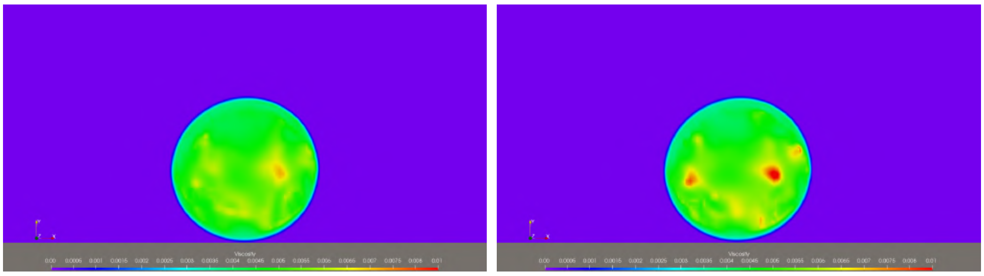

(c) ModCross2 (d) ModPE

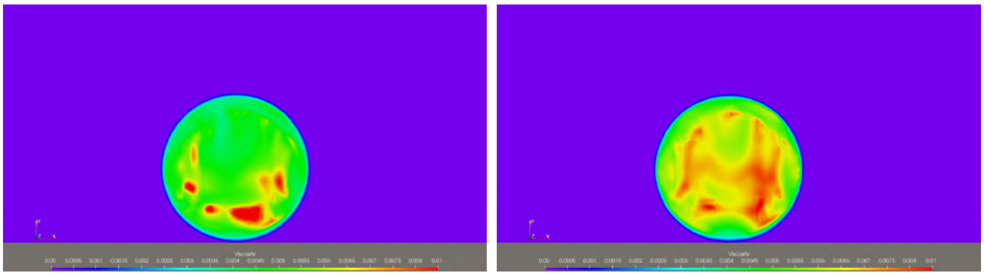

(e) PE (f) PL3

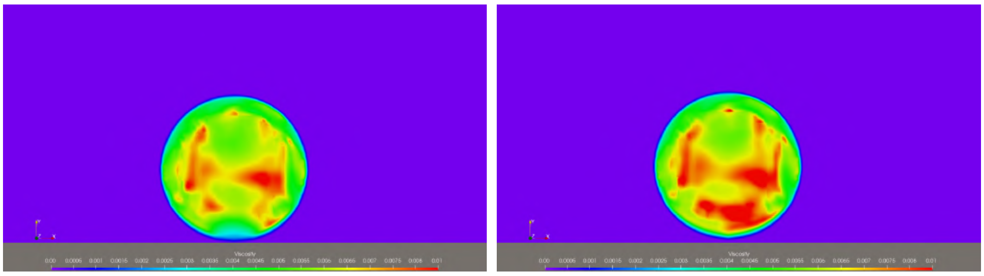

(g) PL4 (h) PL6

Figure 51 – Viscosity distribution in the human blood at the verge of droplet impact, in the z-mean symmetry plane

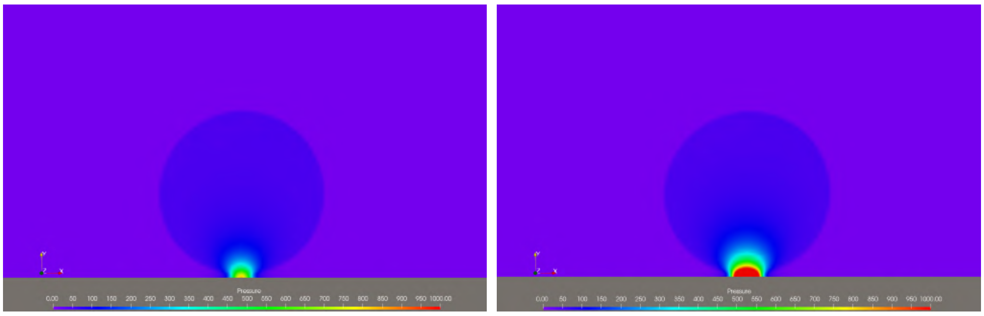

(a) Newtonian (b) Carreau

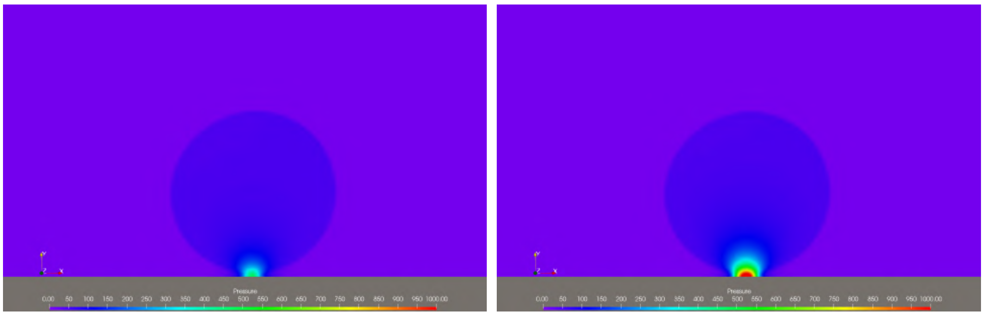

(c) Casson1 (d) Casson2

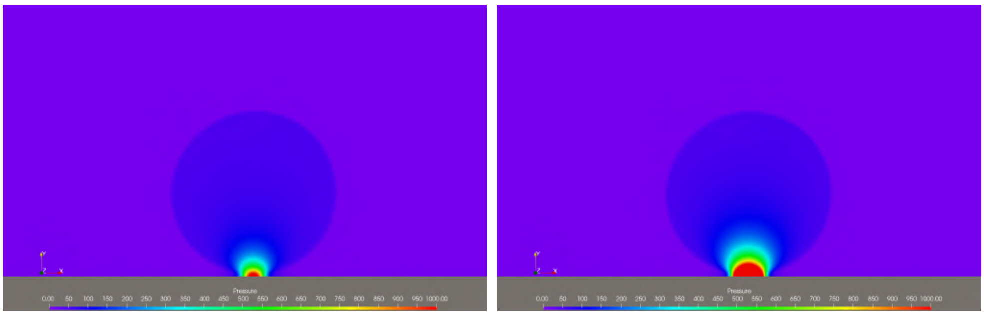

(e) Cross1 (f) Cross2

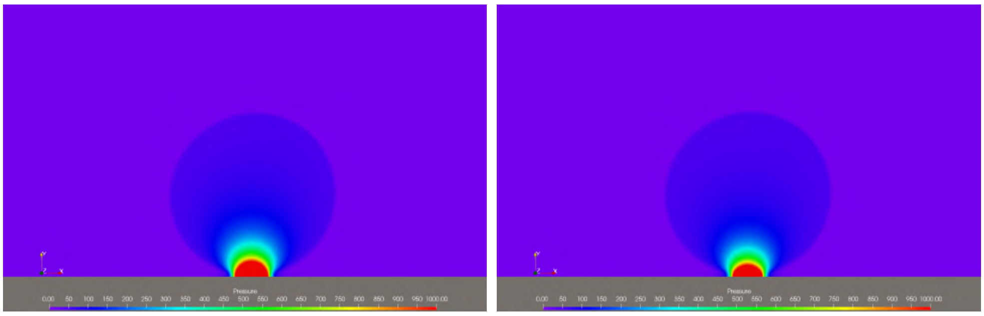

(g) CY1 (h) CY2

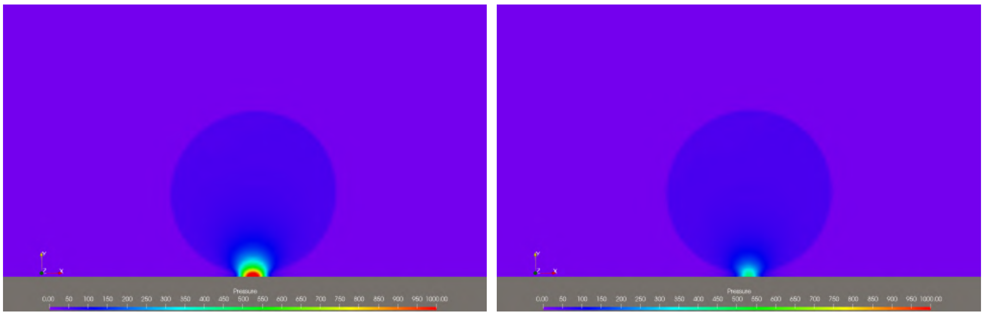

(i) HB (j) KL

Figure 52 – Pressure distribution in the human blood at the verge of droplet impact, in the z-mean symmetry plane

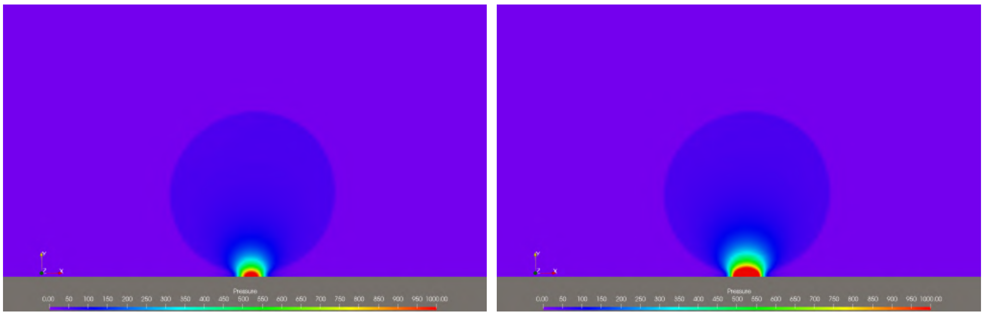

(a) ModCasson (b) ModCross1

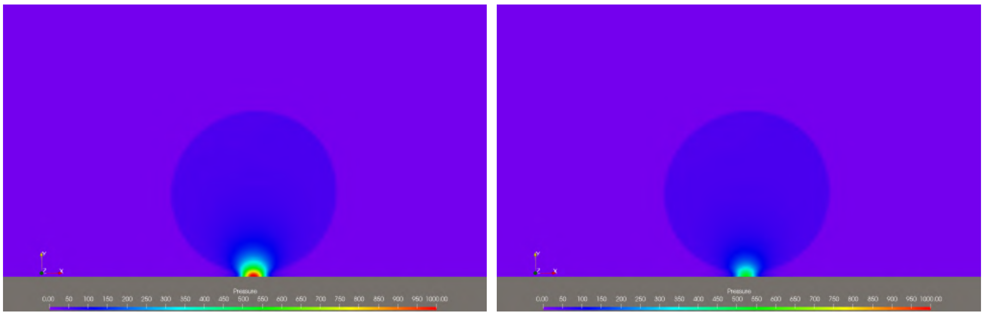

(c) ModCross2 (d) ModPE

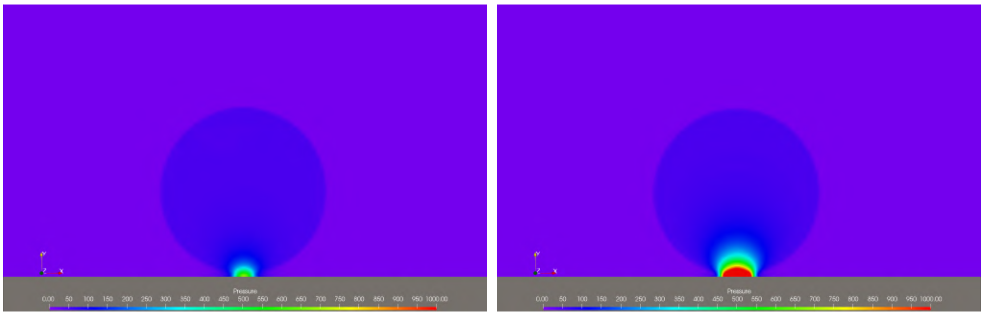

(e) PE (f) PL3

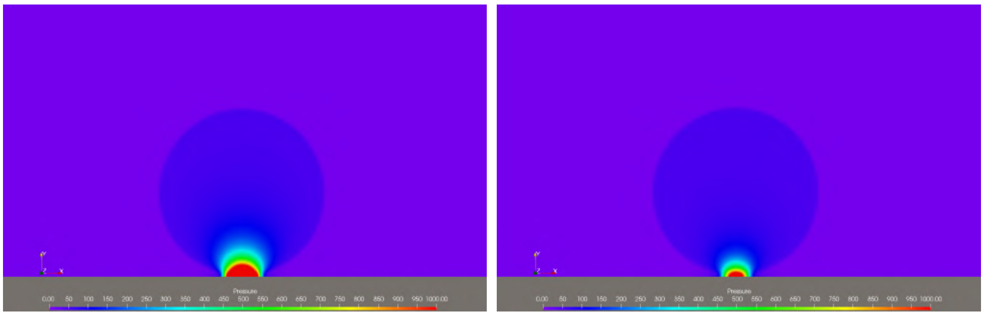

(g) PL4 (h) PL6

Figure 53 – Pressure distribution in the human blood at the verge of droplet impact, in the z-mean symmetry plane

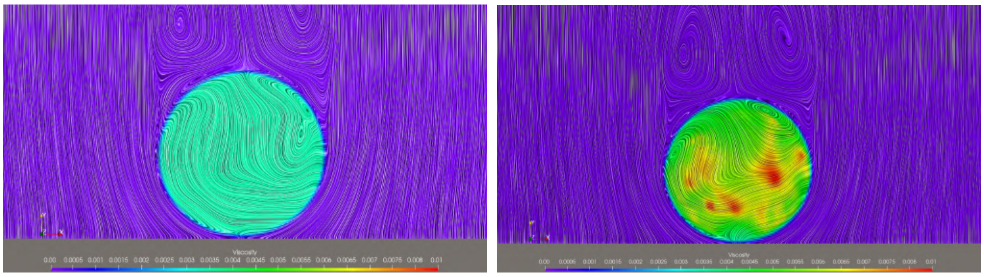

(a) Newtonian (b) Carreau

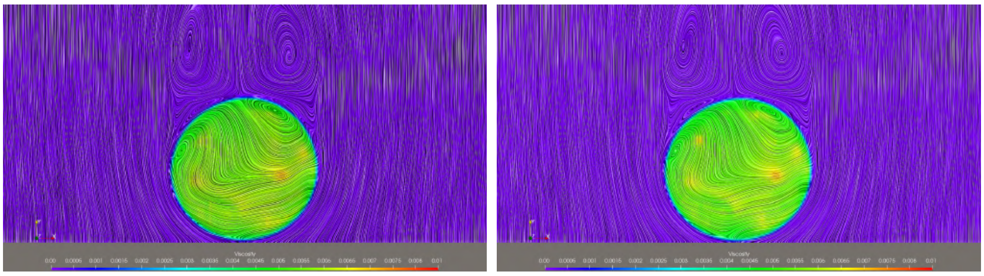

(c) Casson1 (d) Casson2

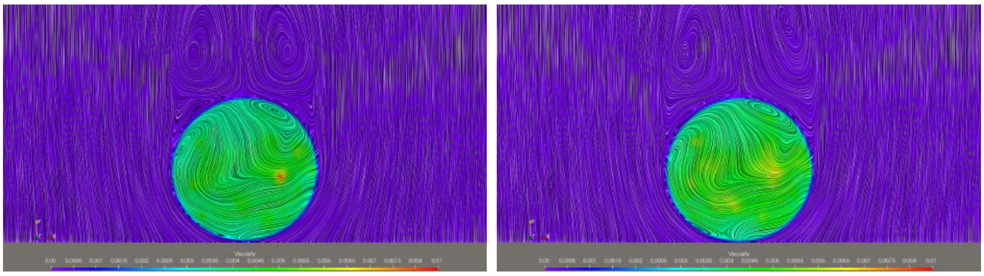

(e) Cross1 (f) Cross2

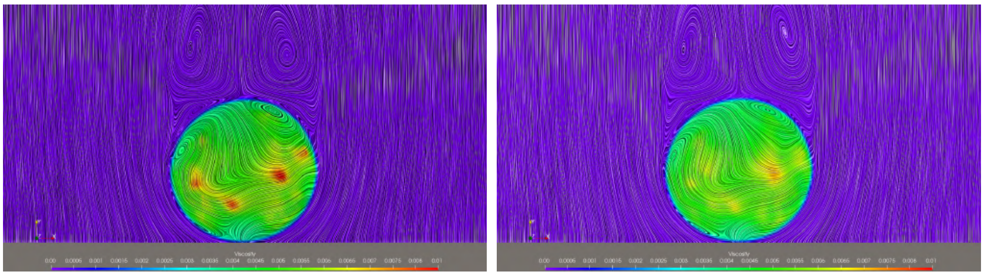

(g) CY1 (h) CY2

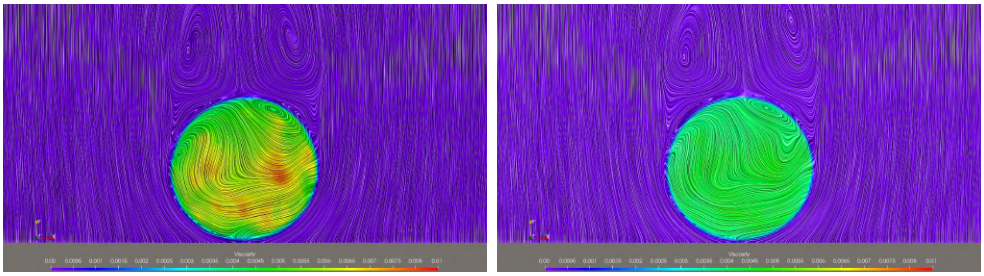

(i) HB (j) KL

Figure 54 – Streamlines along the human blood at the verge of droplet impact, in the z-mean symmetry plane

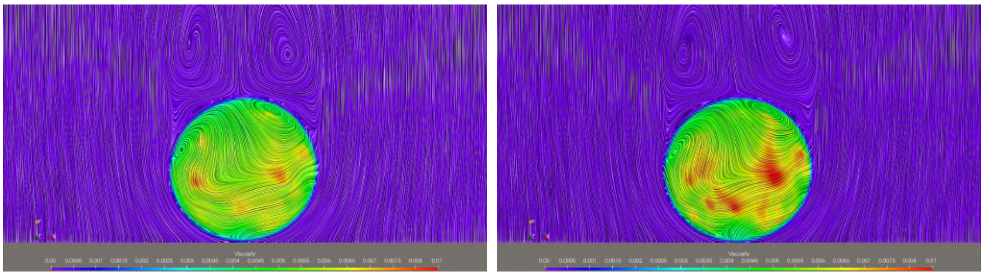

(a) ModCasson (b) ModCross1

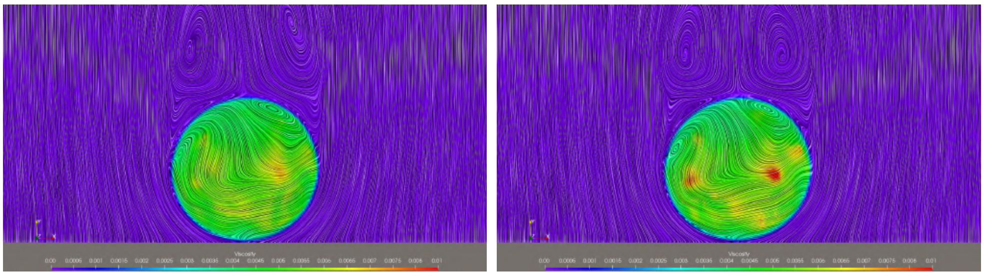

(c) ModCross2 (d) ModPE

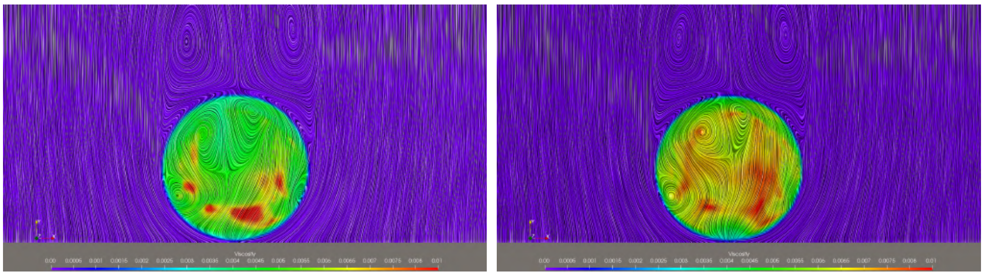

(e) PE (f) PL3

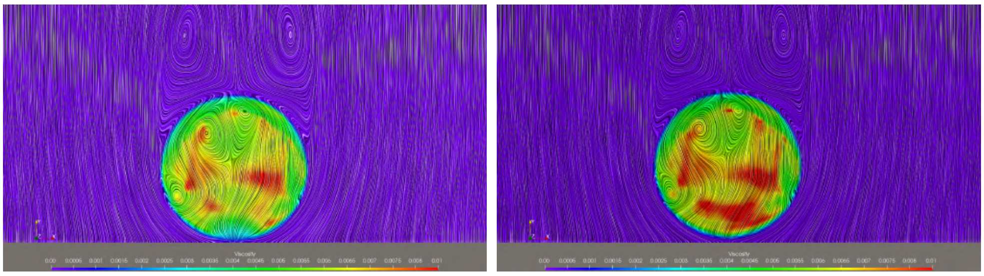

(g) PL4 (h) PL6

Figure 55 – Streamlines along the the human blood at the verge of droplet impact, in the z-mean symmetry plane

Yield-shear-thinning models as Herschel-Bulkley, Casson, modified Casson and K-L introduce a yield stress that must be overcome for the fluid to begin flowing. This implies that in recirculation regions where shear stress is insufficient to surpass this yield stress, viscosity can be significantly elevated, resulting in more restricted flow and greater resistance to shear. This behavior can cause an accumulation of high-viscosity fluid in certain regions, affecting the overall dynamics of the drop. This phenomenon was difficult to observe in these yield-shear-thinning models due to low yield stress and the Papanastasiou regularization term, which, in discrete terms, does not necessarily prevent blood flow within the drop if the yield stress is not exceeded.

Additionally, shear-thinning models such as Cross, Carreau, Powell-Eyring and others, predict viscosity that transitions between two asymptotic limits of high and low shear rates. During recirculation, as the drop accelerates and decelerates, the viscosity of blood can vary substantially between these regions, influencing the stability and shape of the recirculation.

Regarding interfacial tension, it tends to keep the drop cohesive and spherical, while internal viscosity resists movement and shear. In free fall, the blood drop encounters inertial forces that attempt to deform it. The viscosity of blood helps to dampen these deformations, while interfacial tension works to restore the spherical shape. In non-Newtonian models, the variability of viscosity with shear rate can result in different deformation and recirculation responses. Within the drop, fluid recirculation is influenced by the interfacial tension acting on the edges of the drop. Regions of high curvature, where interfacial tension is more pronounced, can cause pressure variations that affect internal flow. The viscosity of blood, which can vary with the shear rate, interacts with these pressure variations to form complex recirculation patterns. For instance, in regions near the surface of the drop, where the shear rate may be high due to interaction with the surrounding air, viscosity tends to be lower. In contrast, at the center of the drop, where the shear rate is lower, viscosity tends to be higher. These viscosity gradients contribute to the formation of recirculation patterns.

In summary, the internal viscosity distribution of the blood drop is intrinsically linked to the recirculation patterns, which are driven both by the characteristics of the non-Newtonian viscosity models used and by the dynamic conditions imposed by free fall.

Finally, the shape of the drop after the impact was evaluated at the instant $t \approx 150\,\mathrm{ms}$. At this moment, the drop reaches its maximum relative diameter and is on the verge of retracting due to the imbalance of interfacial forces.

For didactic purposes, Fig. 56 illustrates the physical mechanism of the drop's edge filling and its starting retraction in 6 stages.

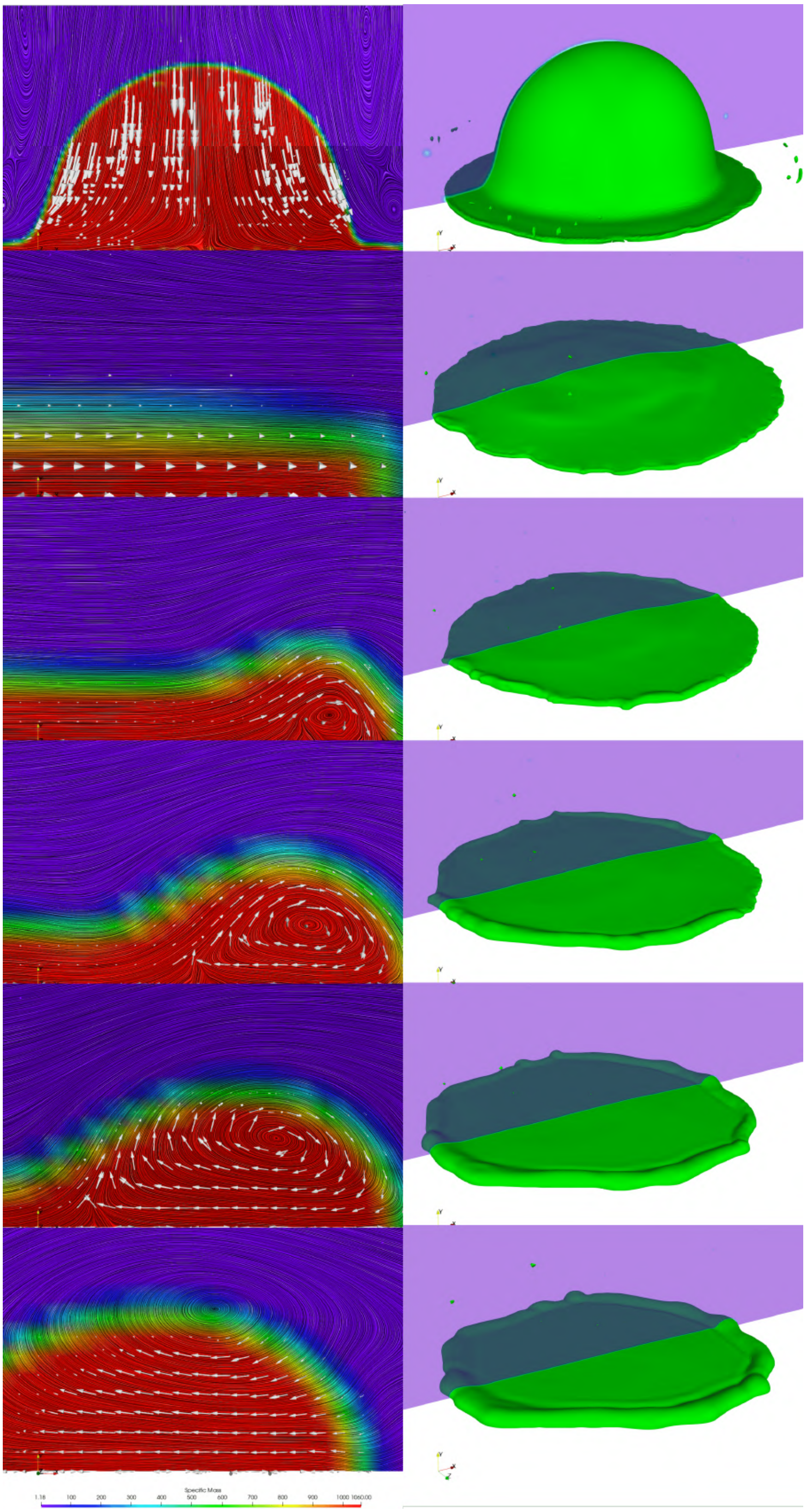

Figure 56 – Droplet thick rim formation after impact

Stage 1 illustrates the initial moments post-impact of the droplet on the surface, during which it is possible to observe the change in direction of the fluid flow that constitutes the droplet, while always preserving the balance of linear momentum.

In stage 2, the drop is still increasing in diameter, with the fluid initially located at the center of the drop moving radially towards the edges. At this instant, the force exerted by the fluid on the interface is greater than the force exerted by the interface in the opposite direction on the fluid, but not sufficient to break the interface and allow the expulsion of part of this fluid from the interior of the drop.

In stage 3, the drop has already reached its relative diameter; the interfacial forces are sufficient to prevent further increase in the drop's diameter. However, the fluid from the center of the drop is still moving towards and accumulating at the edge. The beginning of a physically consistent internal circulation at the edge of the drop is noted at this instant.

In stages 4 and 5, the volume at the edge of the drop increases to its limit, with the aforementioned circulation still occurring.

Finally, in stage 6, it is observed that the interfacial forces have started the return of the fluid accumulated at the edge back to the center of the drop, restoring its interfacial equilibrium. Nearly all vectors indicate the fluid's movement towards the center of the drop.

To perform a qualitative analysis regarding the impact of the droplets, Tab. 12 presents variations in the aforementioned maximum relative diameter of the droplets compared to that of a Newtonian blood droplet. The calculation of the relative diameter was based on the impact area of the droplet on the surface.

The analysis of the differences in maximum relative droplet diameters after impact, reveals several insights into the performance of various non-Newtonian models compared to the Newtonian baseline. Starting with the Newtonian model, which has a relative diameter of 15.79 mm, it is evident that most non-Newtonian models produced diameters close to this baseline. This indicates that the fundamental dynamics of droplet impact are preserved across different fluid behaviors, albeit with subtle variations.

Models such as Carreau, Cross2, and KL exhibit minimal variations in diameter ($-0.63\,\%$, $-0.19\,\%$, and $-0.19\,\%$, respectively). These small deviations suggest that while these models capture non-Newtonian behavior, they do not significantly alter the impact dynamics compared to a Newtonian fluid. In contrast, models like Casson1, Casson2, and ModCasson show moderate reductions in relative diameters ($-3.16\,\%$, $-3.10\,\%$, and $-2.03\,\%$, respectively). This indicates that yield stress and shear-thinning behaviors, common in Casson and power-law models, moderately influence the spreading behavior of droplets upon impact.

Table 12 – Relative diameter reached by the droplet after impact

Model	**Relative diameter (mm)**	**Percentage difference**
Newtonian	15.79	–
Carreau	15.68	-0.63 %
Casson1	15.29	-3.16 %
Casson2	15.30	-3.10 %
Cross1	15.92	0.82 %
Cross2	15.76	-0.19 %
CY1	15.91	0.76 %
CY2	15.81	0.13 %
HB	16.35	3.55 %
KL	15.76	-0.19 %
ModCasson	15.47	-2.03 %
ModCross1	15.80	0.06 %
ModCross2	15.85	0.38 %
ModPE	15.43	-2.28 %
PE	15.60	-1.20 %
PL3	15.72	-0.44 %
PL4	16.25	2.91 %
PL6	16.12	2.09 %
SimpCross	14.91	-5.57 %

Significant increases in relative diameters are observed in models such as HB (Herschel-Bulkley) and PL4 (3.55 % and 2.91 %, respectively). These results suggest that incorporating yield stress and shear-thinning behaviors, especially those with higher power-law indices, can significantly affect droplet spreading. This likely results from the complex interactions between the fluid's resistance to deformation and its flow characteristics under high shear conditions. On the other hand, the SimpCross model shows the largest reduction in relative diameter ($-5.57\,\%$). This pronounced difference could indicate that the simplifications inherent in this model fail to capture some critical aspects of droplet impact dynamics, leading to an underestimation of the spreading diameter.

Understanding these differences is crucial for applications where precise control of droplet spreading is necessary, as BPA activity. Selecting an appropriate non-Newtonian model can lead to better predictive capabilities and optimized process parameters. In conclusion, while many non-Newtonian models exhibit minor to moderate deviations from the Newtonian baseline, certain models show significant differences that are critical for applications requiring precise control of droplet behavior. This analysis underscores the importance of selecting appropriate fluid models to accurately capture the complex dynamics of non-Newtonian droplet impact, thereby enhancing predictive accuracy and practical outcomes in relevant engineering applications.

(a) Newtonian (b) Carreau

(c) Casson1 (d) Casson2

(e) Cross1 (f) Cross2

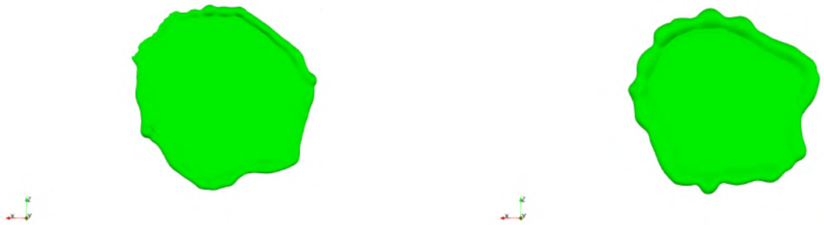

(g) CY1 (h) CY2

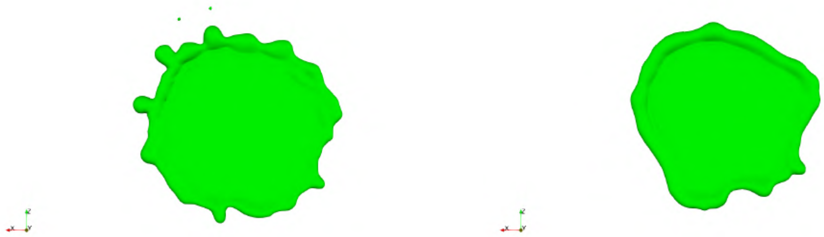

(i) HB (j) KL

Figure 57 – Droplet's shape after impact, at $t \approx 150\,\mathrm{ms}$

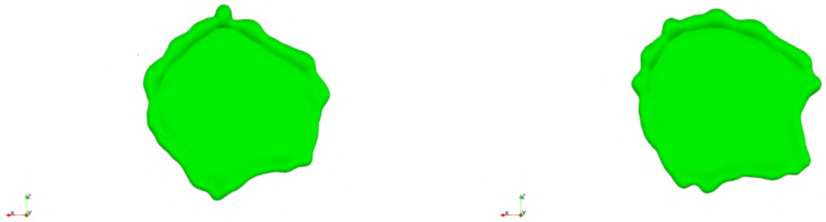

(a) ModCasson (b) ModCross1

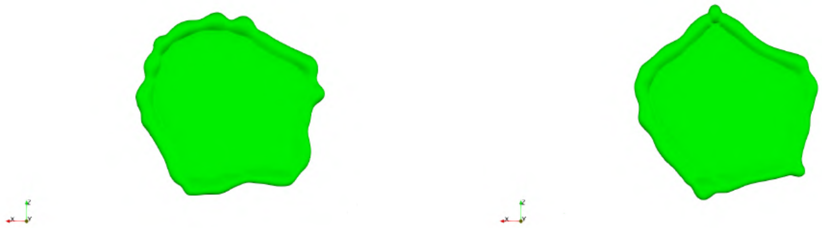

(c) ModCross2 (d) ModPE

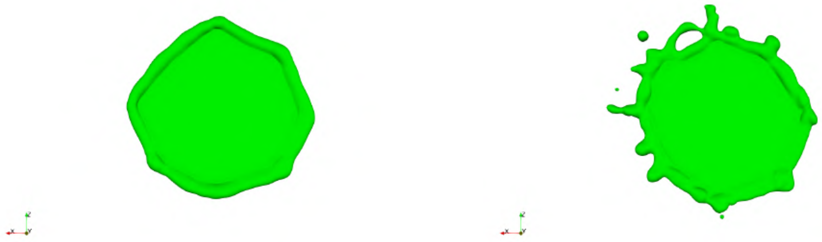

(e) PE (f) PL3

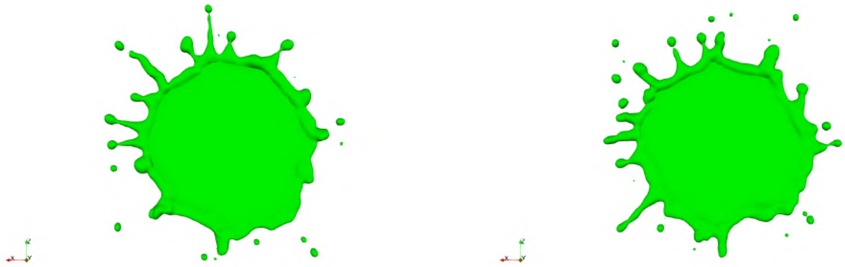

(g) PL4 (h) PL6

Figure 58 – Droplet's shape after impact, at $t \approx 150\,\mathrm{ms}$

Furthermore, concerning splash characteristics, all power-law models (PL3, PL4 and PL6) accurately replicated the formation of liquid fingers described by Adam (2012). Despite that, imposing minimum and relative limits on viscosity (with the aim of just running computational simulations of power-law models) resulted in qualitatively significant differences in the final shape of the droplet, thereby disproportionately failing to accurately represent the physics of human blood.

These models effectively captured the projection of thin jets of liquid beyond the stain's edge, resulting in a crown-like appearance along its circumference. This aligns with the observation that such splash features are predominantly associated with higher impact velocities. Conversely, under lower speed conditions, the stain's edge may exhibit a scalloped appearance, resembling splash patterns without liquid ejection from the stain's main body.

That said, the inefficiency of power-law models in representing the behavior of human blood becomes clear, as they provide dissatisfactory qualitative results primarily due to the simplicity of their rheological model architecture, which necessitates restrictions for their appropriate use.

11 Human blood substitutes

11.1 Introduction

Discussing the use of non-human blood sources, Raymond, Smith e Liesegang (1996) wrote:

> It is common knowledge that pig organ substitution in humans is being trialled successfully both in Australia and America and that pig and human blood have very similar Haematocrit (HCT) or Packed Cell Volumes (PCVs) when fresh. Porcine (pig) blood has been cited by some as a reasonable alternative to human blood, but a comparison between the physical parameters of ageing pig and fresh human blood has not been documented in the literature.

In contrast, in *Animal blood in translational research: How to adjust animal blood viscosity to the human standard*, Ecker et al. addresses the challenge of these fluids accurately replicating the physical properties and behavior of human blood. For instance, it highlights that pig blood is not recommended for material experiments at low shear rates ($\dot{\gamma} \leq 200\,\mathrm{s}^{-1}$). Similarly, horse blood is not recommended as a representative model in material experiments for this purpose.

Furthermore, Windberger et al. conducted material experiments measuring the yield stress of human, horse, and sheep blood at temperatures of 7 °C, 22 °C, and 37 °C, for HCT levels of 40 %, 50 %, and 60 %. As shown in Tab. 13, Windberger et al. (2017) demonstrates that at 37 °C, there is no yield stress for human blood with a 40 % HCT. This underscores the need for accurate modeling of human blood, as in forensic applications, blood leaving the human body at 37 °C undergoes thermal variations on the way to reaching any surface, potentially leading to the eventual appearance of yield stress in blood droplets ejected during the process. This oversimplification can significantly impact results.

Table 13 – Yield stress (τ_y) for different temperatures and HCT levels

τ_y (Pa)	Temperature (°C)	Hematocrit		
		40 %	50 %	60 %
Human	7	0.021	0.033	0.046
Horse	7	0.033	0.021	0.072
Sheep	7	-	-	0.464
Human	22	0.003	0.021	0.021
Horse	22	0.027	0.020	0.060
Sheep	22	-	-	0.214
Human	37	-	0.009	0.009
Horse	37	-	0.010	0.054
Sheep	37	-	-	0.097

On the other hand, Horner, Wagner e Beris (2021) conducted measurements on seven different mammalian species under permanent and transient shear rate conditions. They also mention that human blood exhibits complex behavior, including shear-thinning behavior, viscoelasticity, and thixotropy (COKELET et al., 1963; APOSTOLIDIS; MOYER; BERIS, 2016; THURSTON, 1972; KOLBASOV et al., 2016; BRUST et al., 2013; CHIEN et al., 1975; PICART et al., 1998; HORNER et al., 2018). Horner, Wagner e Beris (2021) compared these seven mammalian species using a protocol developed to produce reproducible and precise measurements of human hemorheology. Their work aimed to raise awareness among readers about the significant and complex differences in blood from different species.

Raymond, Smith e Liesegang (1996) also mentions the need for due attention regarding that the most obvious difference across species occurs at the low shear rates. Certain species such as humans, pigs, and horses demonstrate pronounced shear-thinning characteristics, which is indicated by a significant reduction in viscosity. Conversely, species like chickens, sheep, and cows display nearly constant viscosity. In species whose blood shows notable shear-thinning, RBCs tend to form rouleaux at low shear rates, leading to a behavior akin to yielding. This yielding phenomenon is due to the formation of an aggregate network among the rouleaux in a stationary state, which can withstand a finite applied stress.

11.2 Ecker viscosity models

The viscosity of animal blood is often used as a substitute for human blood in these experiments, but it is important to note that the properties of erythrocytes differ among species, resulting in species-specific shear-thinning behavior of blood suspensions (ECKER et al., 2021). Therefore, it is not enough to adjust the HCT of an animal blood sample to mimic the behavior of human blood over the entire range of shear rates present in the body. Increasing HCT increases viscosity due to the added solid fraction in the suspension. The human blood reacts differently to changes in shear rate, temperature or HCT than animal blood, as reported by Stone, Jr e Schmidt-Nielsen (1968), who investigated blood viscosity of human, sheep, goat, dog and camel with HCT levels ranging from 25 to 70 % and shear rates from 5 to 230 s^{-1}. A comprehensive comparison of nine mammalian species, including shear rate variations from 0.7 to 97 s^{-1}, showed no uniform relation of whole blood viscosity (WBV), plasma viscosity and RBCs aggregation, emphasizing the complexity of inter species hemorheology (WINDBERGER et al., 2017).

According to measurements made by Ecker et al. (2021) on human and horse bloods, for example, the human blood didn't presented difference on WBV irrespective of the starting temperature point of the experimental setting, which was not observed on horse blood, that showed differences on viscosity measurements during increasing or decreasing temperatures.

11.2.1 Mathematical models from Ecker

Ecker et al. (2021) offered mathematical models derived for some species using a multi-linear regression approach to describe the influence of shear rate ($\dot{\gamma}$), HCT and temperature (T) on blood viscosity.

Human blood's constitutive equation:

$$\begin{aligned}\ln(\eta) = {} & C_1\mathrm{HCT} + C_2\dot{\gamma} + C_3T - C_4\sqrt{\dot{\gamma}} \\ & - C_5\sqrt{T} + C_6e^{1/\mathrm{HCT}} + C_7e^{1/\dot{\gamma}} - C_8e^{1/T} \\ & - C_9e^{1/(\mathrm{HCT}\cdot\dot{\gamma})} + C_{10}\end{aligned} \tag{11.1}$$

Porcine blood's constitutive equation:

$$\begin{aligned}\ln(\eta) = {} & [C_1\ln(\mathrm{HCT})\ln(\dot{\gamma}) - C_2]\ln(T) + C_3\mathrm{HCT} \\ & - C_4\dot{\gamma} - C_5T - C_6\sqrt{\mathrm{HCT}} + C_7\sqrt{\dot{\gamma}} \\ & - C_8e^{1/(\mathrm{HCT}+\dot{\gamma})} + C_9e^{1/(\dot{\gamma}+T)} + C_{10}\ln(\mathrm{HCT}) - C_{11}\ln(\dot{\gamma}) + C_{12}\end{aligned} \tag{11.2}$$

Ovine blood's constitutive equation:

$$\begin{aligned}\ln(\eta) = {} & C_1\mathrm{HCT} + C_2\dot{\gamma} + C_3T - C_4\sqrt{\dot{\gamma}} \\ & - C_5\sqrt{T} + C_6e^{1/\mathrm{HCT}} + C_7e^{1/\dot{\gamma}} \\ & - C_8e^{1/(\mathrm{HCT}\cdot\dot{\gamma})} - C_9e^{1/(\mathrm{HCT}\cdot T)} + C_{10}e^{1/(\mathrm{HCT}\cdot T\cdot\dot{\gamma})} - C_{11}\end{aligned} \tag{11.3}$$

Equine blood's constitutive equation:

$$\begin{aligned}\ln(\eta) = {} & [(-C_1\ln(\mathrm{HCT}) + C_2)\ln(\dot{\gamma}) + C_3\ln(\mathrm{HCT}) - C_4]\ln(T) \\ & + C_5\mathrm{HCT} - C_6\dot{\gamma} - C_7T - C_8\sqrt{\mathrm{HCT}} + C_9\sqrt{\dot{\gamma}} \\ & + C_{10}\ln(\mathrm{HCT}) - C_{11}\ln(\dot{\gamma}) + C_{12}\end{aligned} \tag{11.4}$$

Ecker et al. showed that pig blood cannot be recommended for experiments at low flow conditions ($\dot{\gamma} < 200\,\mathrm{s}^{-1}$) even though RBCs properties are similar in pigs and humans (figure 59). However, pig blood mimics human blood excellently at high flow conditions. Horse blood is unsuitable as an experimental model in this regard. For several studied conditions, sheep blood was the closest match to human blood viscosity among the tested species.

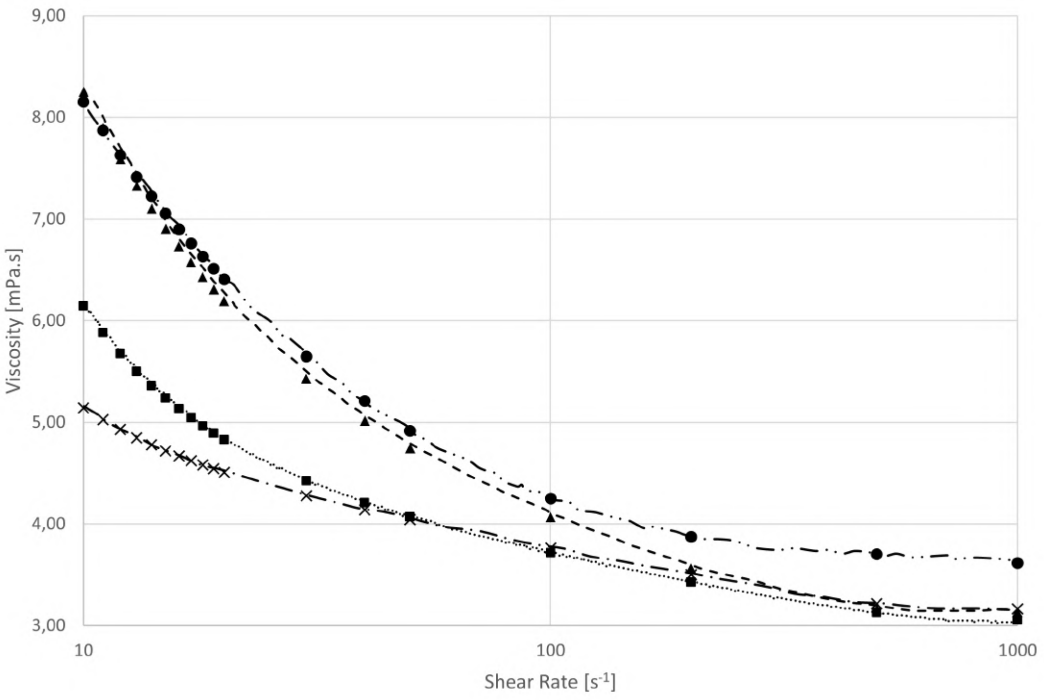

Figure 59 – Experimental (solid lines) and numerical (symbols) data of human and animals blood's viscosity in function of shear rate. Source: Ecker et al. (2021). Human blood (square), porcine blood (triangle), ovine blood (cross marker) and equine blood (circle)

11.2.2 About interfacial tension

It is crucial to remember that interfacial tension is also a parameter that influences the shape the droplet will acquire after impact, as it is one of the components of the force balance at the blood-air interface.

That said, the interfacial tension for porcine blood was set at 0.057 N/m (RAYMOND; SMITH; LIESEGANG, 1996), for ovine blood it was set at 0.0480165 N/m (JABER; VAYRON; HARMAND, 2022) and for equine blood it was set at 0.072309 N/m (ZAITSEV et al., 2011).

For this round of computational simulations, the interfacial tension of human blood was also tested on animal blood viscosity models for purely didactic purposes.

11.2.3 Comparison between human and animal's blood simulations

As was done on last chapter, first, all models were assessed — both quantitatively and qualitatively — when a mean velocity about $\|\mathbf{u}\| \approx 1.00\,\mathrm{m/s}$ was reached.

Figures 60 to 61 evidence the preserved spherical shape of the droplet at $\|\mathbf{u}\| \approx 1.0\,\mathrm{m/s}$ and the different viscosity patterns promoted inside it, by a z-mean symmetry plane view (at B/2 in Fig. 43).

Qualitatively, we observe in all animal blood models a reduction in the internal viscosity of the drop, with an even greater proportion seen in Ecker's human blood model.

When examining the distribution of internal pressure (figure 61), it is physically perceptible and consistent that, as the interfacial tension of the drop-air system is higher (in porcine and equine blood), there is a corresponding increase in internal pressure to reestablish the force balance. The inverse also occurs in ovine blood.

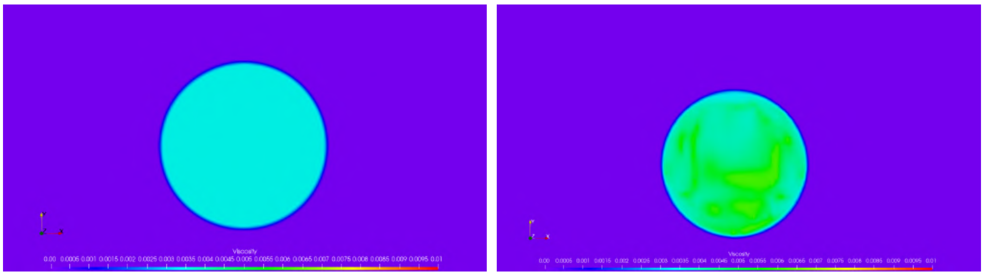

(a) Newtonian (b) Ecker human

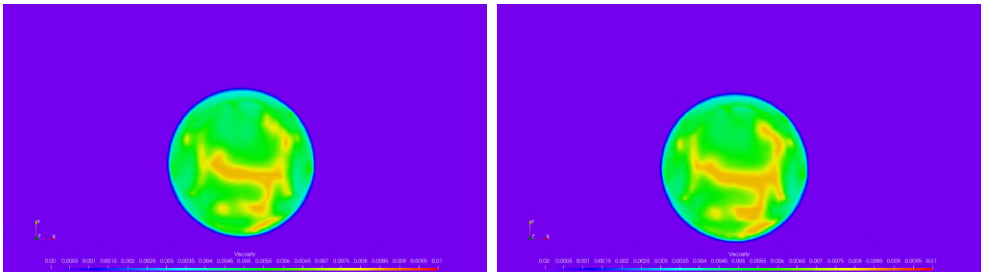

(c) Ecker porcine (d) Ecker porcine*

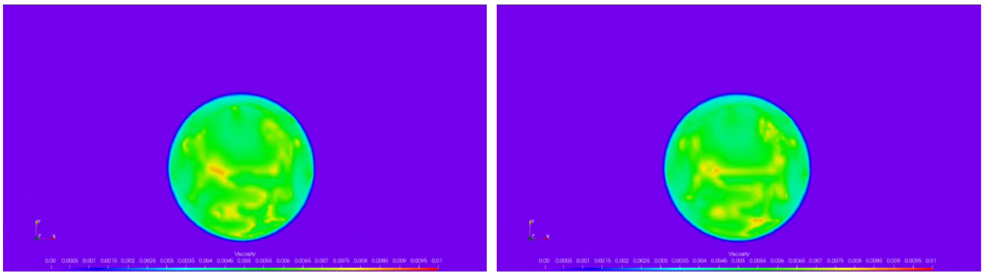

(e) Ecker ovine (f) Ecker ovine*

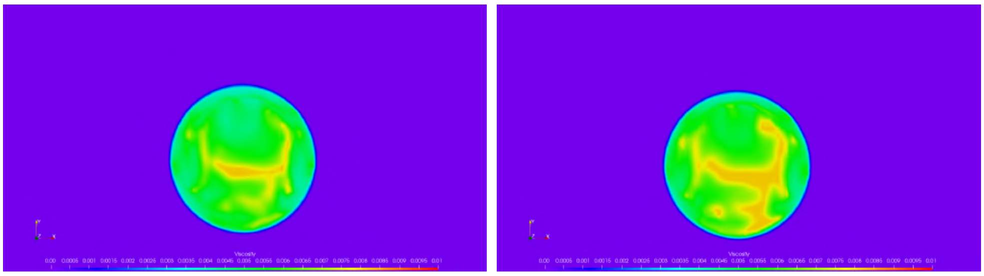

(g) Ecker equine (h) Ecker equine*

Figure 60 – Viscosity distribution in the human and animal's blood droplet at $\|\mathbf{u}\| \approx 1\,\mathrm{m/s}$, in the z-mean symmetry plane

* Human blood's interfacial tension was used in these simulations.

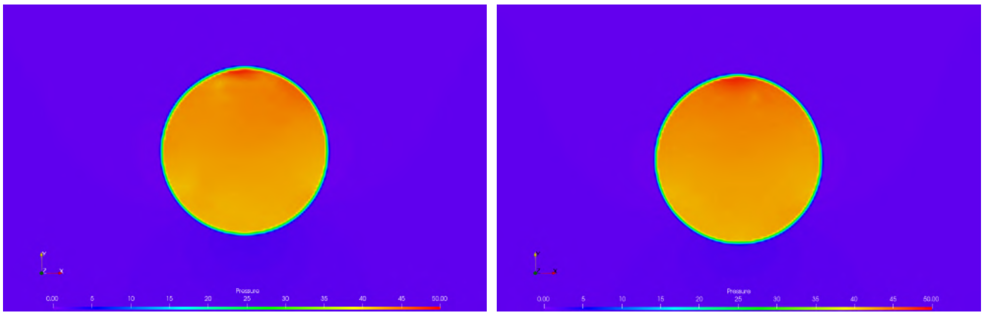

(a) Newtonian (b) Ecker human

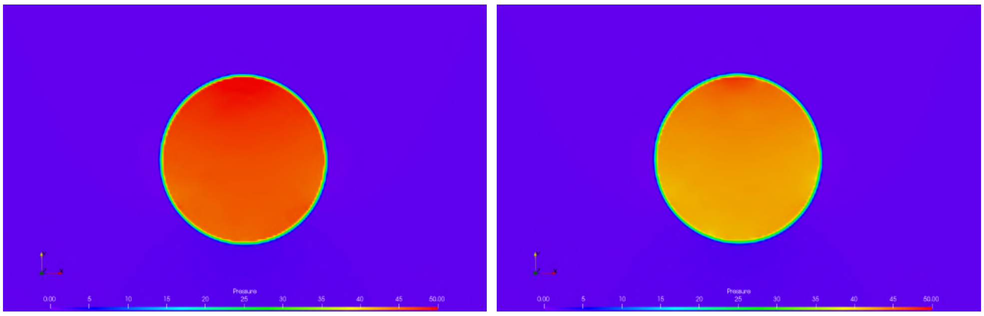

(c) Ecker porcine (d) Ecker porcine*

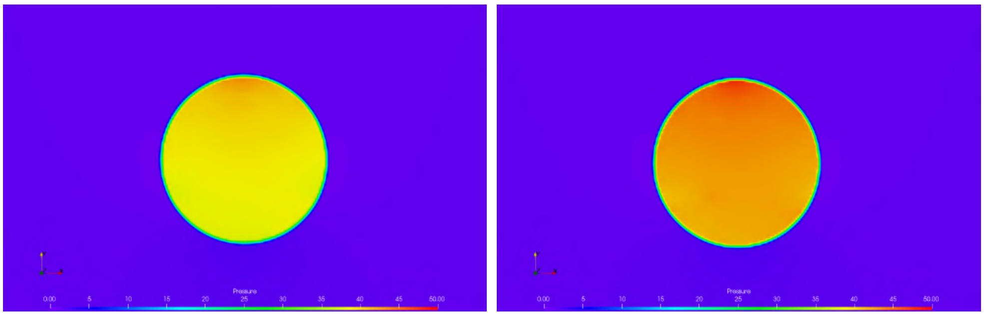

(e) Ecker ovine (f) Ecker ovine*

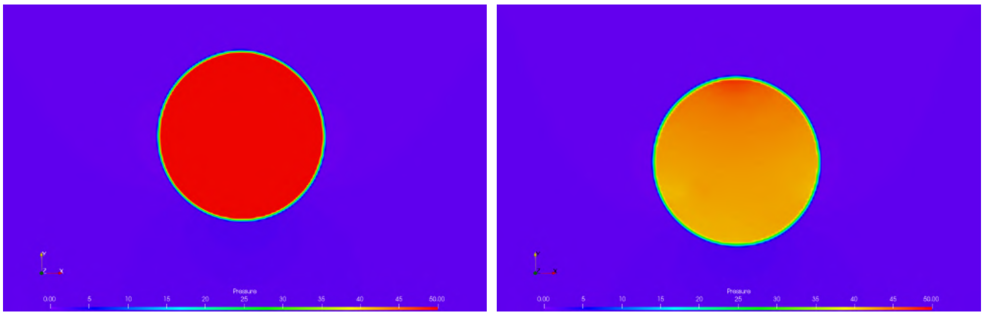

(g) Ecker equine (h) Ecker equine*

Figure 61 – Pressure distribution in the human and animal's blood droplet at $\|\mathbf{u}\| \approx 1\,\mathrm{m/s}$, in the z-mean symmetry plane

* Human blood's interfacial tension was used in these simulations.

In second place, all models were assessed on the imminence of the impact, when a mean velocity about $\|\mathbf{u}\| \approx 1.43\,\mathrm{m/s}$ was reached. Again, the following tables and figures show the previous analysis at this specific moment (impact) of the droplet.

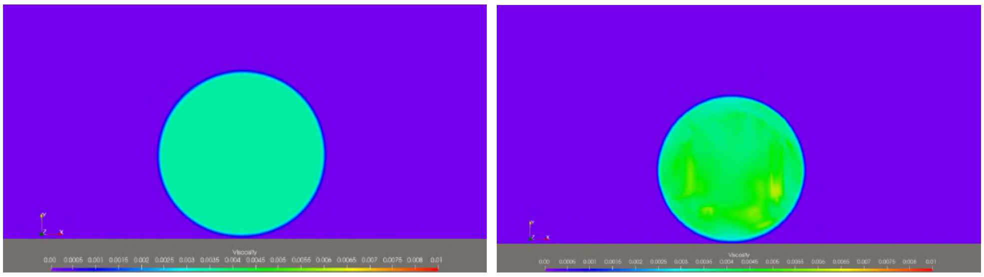

(a) Newtonian (b) Ecker human

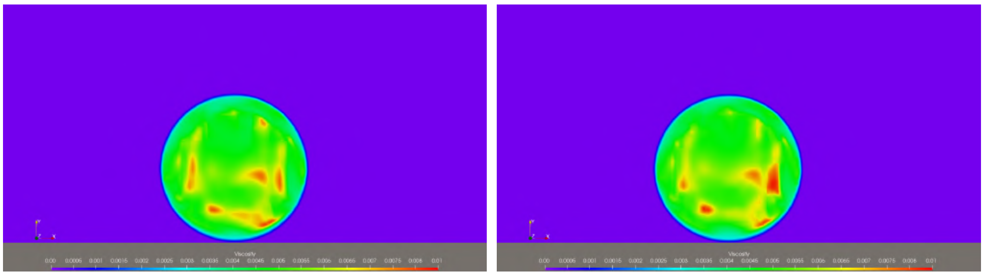

(c) Ecker porcine (d) Ecker porcine*

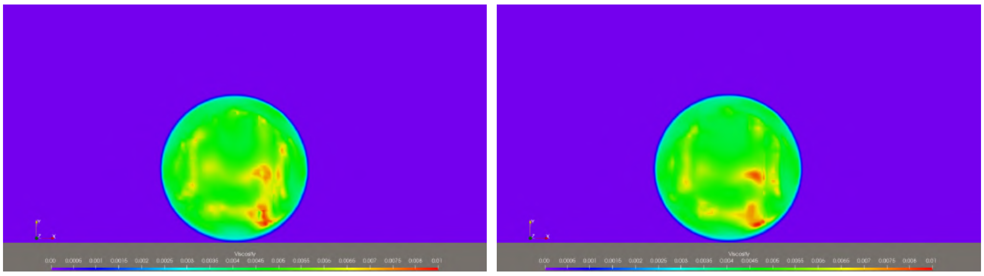

(e) Ecker ovine (f) Ecker ovine*

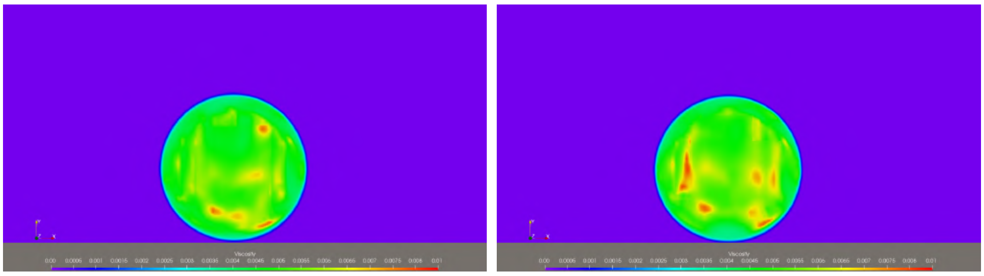

(g) Ecker equine (h) Ecker equine*

Figure 62 – Viscosity distribution in the human and animal's blood at the verge of droplet impact, in the z-mean symmetry plane

* Human blood's interfacial tension was used in these simulations.

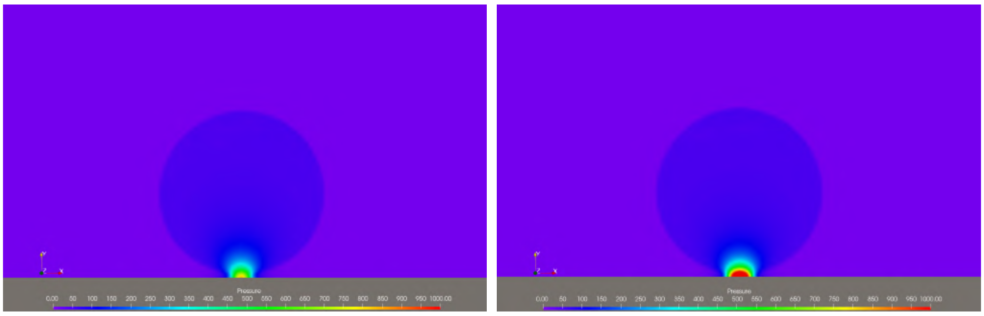

(a) Newtonian (b) Ecker human

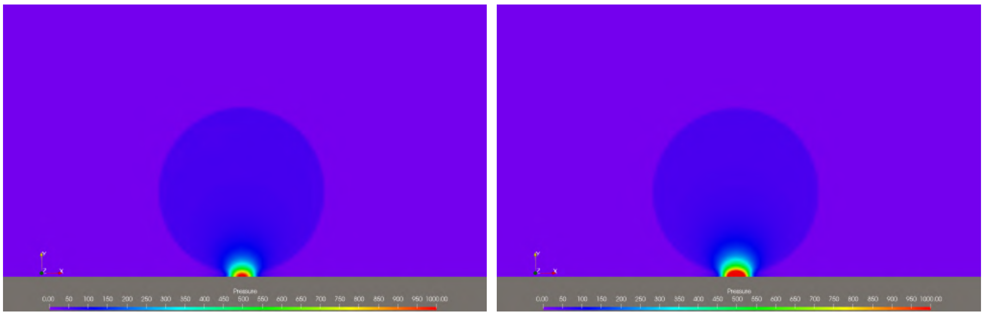

(c) Ecker porcine (d) Ecker porcine*

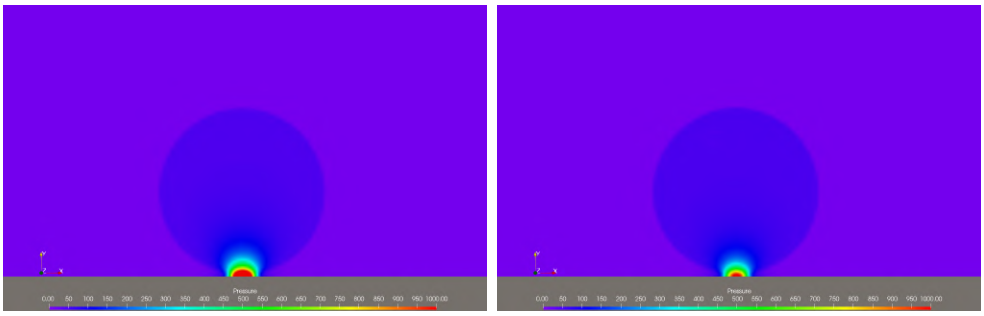

(e) Ecker ovine (f) Ecker ovine*

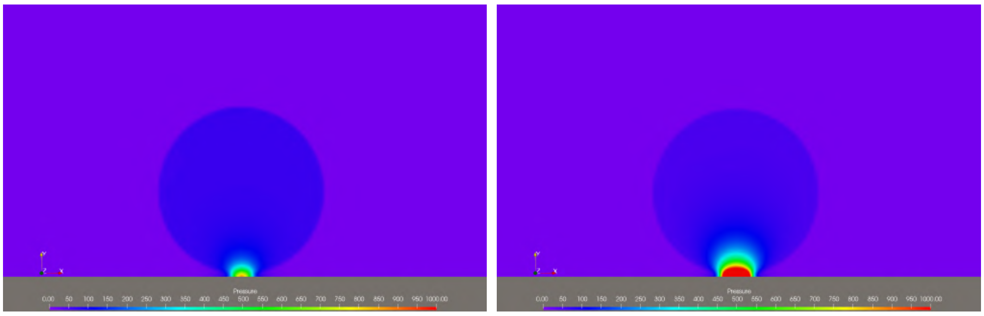

(g) Ecker equine (h) Ecker equine*

Figure 63 – Pressure distribution in the human and animal's blood at the verge of droplet impact, in the z-mean symmetry plane

* Human blood's interfacial tension was used in these simulations.

(a) Newtonian (b) Ecker human

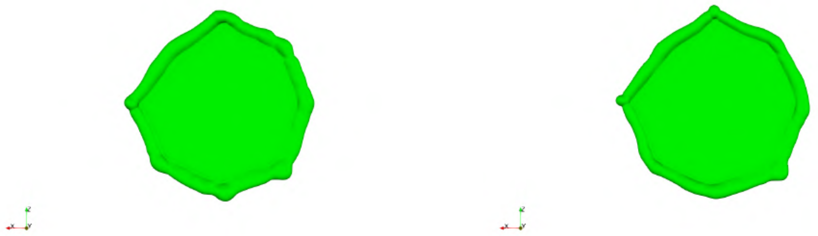

(c) Ecker porcine (d) Ecker porcine*

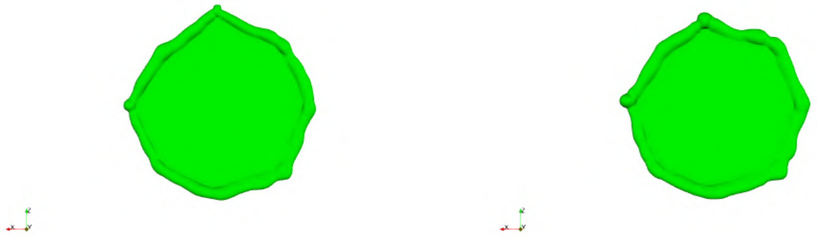

(e) Ecker ovine (f) Ecker ovine*

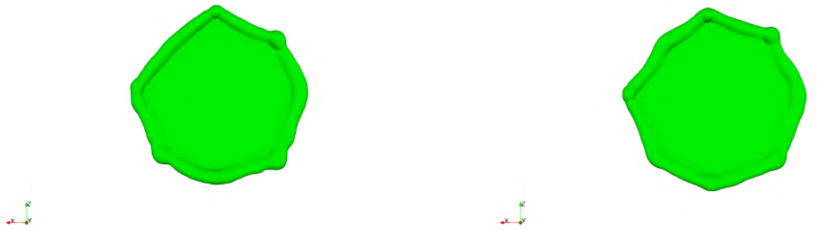

(g) Ecker equine (h) Ecker equine*

Figure 64 – Relative diameter reached after impact, at $t \approx 150\,\mathrm{ms}$

* Human blood's interfacial tension was used in these simulations.

To conduct a qualitative analysis regarding the impact of droplets, following Tab. 14 presents the variations in the maximum relative diameter of droplets.

Table 14 – Maximum relative diameter reached by the droplet after impact

Model	**Relative diameter (mm)**	**Difference**
Newtonian	15.79	–
Ecker's human model	15.83	0.25 %
Ecker's porcine model	15.69	-0.63 %
Ecker's ovine model	15.94	0.95 %
Ecker's equine model	14.51	-8.11 %
Ecker's porcine model*	15.84	0.32 %
Ecker's ovine model*	15.71	-0.51 %
Ecker's equine model*	15.38	-2.60 %

* Human blood's interfacial tension was used in these simulations.

As shown in the Tab. 14, the Newtonian model has a reference relative diameter of 15.79 mm. Ecker's human blood model shows a slight increase to 15.83 mm, representing a 0.25 % difference, indicating that the human blood model behaves very similarly to the Newtonian model under these conditions. In contrast, Ecker's porcine model, without any modification to interfacial tension, shows a slight decrease to 15.69 mm, a -0.63 % difference, suggesting minor variations in impact dynamics when compared to human blood.

Interestingly, Ecker's ovine model exhibits a relative diameter of 15.94 mm, which is a 0.95% increase from the Newtonian model. This suggests that the ovine blood has slightly different spreading characteristics, likely due to its specific rheological properties. On the other hand, Ecker's equine model shows a significant decrease to 14.51 mm, an -8.11% difference, indicating a substantial divergence in impact behavior from both the Newtonian and human blood models.

As previously mentioned, to isolate the effect of interfacial tension, further tests were conducted using human blood's interfacial tension in the animal blood models. The results for Ecker's porcine, ovine, and equine models with this adjustment show diameters of 15.84 mm (0.32%), 15.71 mm (-0.51%), and 15.38 mm (-2.60%), respectively. These adjusted results highlight that while interfacial tension plays a role, the inherent rheological properties of each animal's blood are crucial in determining the droplet's impact behavior. For instance, the significant improvement in the equine model's diameter from -8.11% to -2.60% with adjusted interfacial tension highlights the importance of accurately modeling both viscosity and interfacial tension to predict droplet behavior.

Therefore, this analysis demonstrates that while some animal blood models show minor differences in relative diameter compared to human blood, others exhibit significant deviations. These findings underscore the importance of considering both viscosity and interfacial tension in computational models to accurately capture the complex dynamics of droplet impact.

12 Conclusion

The initial objectives of this project were to conduct groundbreaking computational simulations within the realm of fluid mechanics, focusing specifically on the forensic analysis of bloodstain patterns. Our study aimed to address a significant gap in scientific understanding due to the scarcity of comprehensive investigations into computational fluid dynamics within the forensic domain on a global scale.

We set out to achieve well-defined objectives: to execute computational simulations of both human and animal blood droplets in free fall and to scrutinize their impact upon a solid surface. These simulations were intended to facilitate a deeper comprehension of the non-Newtonian properties of blood and their repercussions on the bloodstain patterns discernible at crime scenes.

In terms of the results, it is important to note that nearly all research on human blood has been conducted from the perspective of hemodynamics, focusing on blood circulation within the human body. This inherently limits the shear rates experienced by human blood. Few studies have examined shear rates of human blood outside these limits. In the forensic context, human blood is subjected to shear rates vastly different from those within the body.

In this dissertation, various models from the literature that represent human blood were compared. Each model yielded different results concerning the internal viscosity distribution of the droplet and the final shape of the droplet upon impact with a solid surface. While the shapes may appear similar to a layperson, they become distinctly different upon deeper analysis, considering the constitutive model used, its capabilities, and its complexities.

Simpler constitutive models, with lower complexity, such as the power-law, which perform well when representing blood under internal circulation conditions within the human body, encountered shear rates in typical forensic contexts (free-falling droplet) that led to non-physical viscosity levels. This rendered the use of this model infeasible in forensic contexts.

Regarding the animal blood models tested, the resulting shapes after impact were significantly different from those produced by human blood. This underscores the necessity for special considerations when using animal blood to study bloodstain patterns at crime scenes.

These findings are crucial for advancing the forensic analysis of bloodstain patterns, providing a more scientifically robust framework for interpreting blood evidence at crime scenes. The distinct behaviors observed in different blood models highlight the importance of choosing appropriate models for accurate forensic investigations.

12.1 Discussion of implications

The findings of this study have several theoretical and practical implications.

Firstly, the computational simulations conducted in this research provide a deeper understanding of the non-Newtonian properties of blood under forensic conditions. This expands the current body of knowledge, which predominantly focuses on hemodynamic conditions within the human body, by introducing insights into the behavior of blood at higher shear rates typical in forensic scenarios.

Moreover, the comparison of various constitutive models revealed significant differences in the internal viscosity distribution and final shape of blood droplets upon impact. This highlights the necessity for careful selection of models in forensic analysis to ensure accurate interpretation of bloodstain patterns. The inadequacy of simpler models like the power-law in forensic contexts underscores the importance of using more complex and accurate models that can handle the low and high shear rates experienced by blood droplets in free fall.

12.1.1 Contributions of Computational Fluid Dynamics

Constitutive models for representing the viscosity of non-Newtonian fluids were successfully implemented and validated within the MFSim code.

Computational simulations of forensic scenarios, grounded in the laws of physics, were executed. Although these simulations were simple at this initial stage, they are of extreme interest to forensic experts working at crime scenes.

From a forensic perspective, this dissertation stands as one of the few studies worldwide to employ computational fluid dynamics, establishing a fertile ground for the continuation of this work.

For the international forensic community involved in bloodstain pattern analysis, computational fluid dynamics emerges as a promising assistant tool for in-depth studies of bloodstains in various situations.

12.1.2 Contributions of the obtained results

Quantitative and qualitative results were provided, supported by the laws of physics and of significant interest to the international community of bloodstain pattern analysts. These results demonstrate the ability to generate diverse final outcomes when using substances with different intrinsic properties.

Practically, these findings can enhance forensic methodologies by providing a more robust scientific basis for analyzing bloodstain patterns. Forensic investigators can use these insights to more accurately determine the origin and trajectory of blood droplets at crime scenes, leading to more precise reconstructions of criminal events. This can ultimately contribute to the resolution of criminal cases and the advancement of justice.

Furthermore, the use of internally developed computational codes at MFLab enables highly detailed and accurate simulations that surpass the capabilities of empirical experiments. This methodological advancement positions this research at the forefront of forensic fluid mechanics, setting a new standard for future studies.

Therefore, this study not only starts filling a critical gap in the forensic analysis of bloodstain patterns but also provides a foundation for future research that can further refine and expand upon these findings.

12.2 Limitations and future work

12.2.1 Limitations

Several limitations were encountered during this research. Regarding the implementation of viscosity models for non-Newtonian fluids in the MFSim computational code, only models for time-independent fluids were implemented. Models for time-dependent and viscoelastic fluids remain to be implemented. As discussed in chapters 3 and 11, blood exhibits complex behavior that includes viscoelasticity and thixotropy in addition to shear-thinning feature, as reported by Cokelet et al. (1963), Apostolidis, Moyer e Beris (2016), Thurston (1972), Kolbasov et al. (2016), Brust et al. (2013), Chien et al. (1975), Picart et al. (1998), and Horner et al. (2018).

Due to the extensive number of models tested, only one scenario was examined within the available timeframe: the impact of a free-falling droplet on a solid surface. Even within this specific scenario, there were limitations regarding the physical representation, which require further improvements:

- During the impact, a static contact angle was considered, without accounting for the dynamic contact line or triple contact line
- Small ejected droplets from the main structure were not analyzed, as this information was dissipated due to the insufficient mesh resolution, despite being fine. There is potential to adapt the code to track these small particles using techniques already implemented in MFSim, such as the *dpm* method
- Adhesion to the impact surface of the droplet was not considered, which necessitates appropriate implementation and validation in the MFSim computational code
- The simulations conducted in this dissertation were considered isothermal in their physical model. However, for a human blood droplet expelled from the body due to a crime, there is thermal exchange with the environment from expulsion until impact, which cannot be disregarded. As observed in chapter 11, human blood with $\text{HCT} = 40\,\%$ at a temperature of $37\,^{\circ}\text{C}$ (the internal body temperature) exhibits no

yield stress, while at 22 °C it does, completely changing the internal fluid dynamics of the expelled blood droplet

- No turbulence model was activated during the simulation. Despite the laminar regime of the computational modeling conducted in this dissertation, other scenarios may require the activation of turbulence models to capture fluid dynamic phenomena that cannot be ignored
- Wind effects, under different orientations, were not considered for evaluating their quantitative and qualitative impacts on results

Another significant limitation was the difficulty in finding well-documented experimental data with the aim of computational modeling them. While there are material experiments involving blood conducted by the forensic community (LABER; EPSTEIN; TAYLOR, 2006), they are often poorly documented for the specific purpose of reproducting them via computational modeling. There is a lack of information on the type of blood used (whether human, animal or synthetic) and its physical properties; temperature (ROSINA et al., 2007) and relative humidity of the environment where the experiment was conducted (BENABDELHALIM; BRUTIN, 2023), which have a profound impact on the final shape of the blood droplet after impact; dimensional information of the experiment, droplet release height, and the units of measurement used (SI, imperial or US customary units); and the positioning of vertical and frontal cameras that captured the impact, suggesting parallax issues that hinder the understanding of results.

12.2.2 Future work

Future research directions based on the findings and limitations of this study include:

- Investigation of droplets falling on inclined planes at various angles
- Application of the Immersed Boundary Method technique (see chapter 7) to represent various objects within the domain
- Tracking of small droplets detached from the main droplet structure using the *dpm* method
- Use of *wettability* and *adhesion* techniques to improve the physical representation of the impact and post-impact moments
- Conducting thermal balance in the computational modeling, imposing thermal boundary and initial conditions compatible with real situations
- Incorporating wind effects into the modeling and evaluating their impacts on the results

- Performing material experiments with human blood of specific physical properties, under specific and controlled thermal and fluid dynamic conditions, well-documented for subsequent computational modeling.

These suggestions aim to address the identified limitations and pave the way for more comprehensive and accurate forensic simulations using computational fluid dynamics.

12.3 Closing remarks

In conclusion, this research project represents a pioneering effort in computational fluid dynamics applied to forensic bloodstain pattern analysis. Our objectives were aimed at filling critical gaps in understanding the behavior of blood under non-hemodynamic conditions, specifically in forensic contexts where high and very low shear rates play a decisive role in pattern formation.

We successfully executed computational simulations of blood droplets in free fall, employing various viscosity models to capture the complex non-Newtonian behavior of blood. The comparison of these models revealed significant differences in droplet shape and internal viscosity distribution upon impact, emphasizing the need for accurate model selection in forensic investigations.

Despite encountering several challenges and limitations, such as the need for more comprehensive viscosity models and better-documented experimental data, this study has laid a solid foundation for future advancements in forensic fluid mechanics. The insights gained here can significantly enhance the accuracy and reliability of bloodstain pattern analysis, ultimately aiding forensic experts in reconstructing crime scenes with greater precision.

The theoretical and practical contributions of this research extend beyond academia, offering tangible benefits to forensic practitioners worldwide. By integrating computational fluid dynamics into forensic science, we open new avenues for detailed and systematic analysis of bloodstain patterns, thereby supporting the pursuit of justice and truth in criminal investigations.

Looking ahead, further research should focus on refining existing models to encompass additional fluid properties like viscoelasticity and thixotropy, addressing thermal effects during droplet flight, and incorporating environmental factors such as wind. Additionally, conducting well-documented material experiments with human blood under controlled conditions will be crucial for validating and expanding the applicability of computational models in forensic settings.

In summary, this dissertation marks a significant step forward in the application of computational fluid dynamics to forensic science, paving the way for more sophisticated methodologies and tools that can revolutionize how blood evidence is analyzed and interpreted in criminal investigations.

Bibliography

ABBASIAN, M. et al. Effects of different non-newtonian models on unsteady blood flow hemodynamics in patient-specific arterial models with in-vivo validation. *Computer Methods and Programs in Biomedicine*, v. 186, p. 105185, 2020. ISSN 0169-2607. Disponível em: <https://doi.org/10.1016/j.cmpb.2019.105185>.

ABRAHAM, F.; BEHR, M.; HEINKENSCHLOSS, M. Shape optimization in steady blood flow: A numerical study of non-newtonian effects. *Computer methods in biomechanics and biomedical engineering*, v. 8, p. 127–37, 05 2005. Disponível em: <https://doi.org/10.1080/10255840500180799>.

ADAM, C. D. Fundamental studies of bloodstain formation and characteristics. *Forensic science international*, Elsevier, v. 219, n. 1-3, p. 76–87, 2012. Disponível em: <https://doi.org/10.1016/j.forsciint.2011.12.002>.

AGUIRRE, A. et al. Stationary and time-dependent numerical approximation of the lid-driven cavity problem for power-law fluid flows at high reynolds numbers using a stabilized finite element formulation of the vms type. *Journal of Non-Newtonian Fluid Mechanics*, v. 257, p. 22–43, 2018. ISSN 0377-0257. Disponível em: <https://doi.org/10.1016/j.jnnfm.2018.03.014>.

ANTONOVA, N. On some mathematical models in hemorheology. *Biotechnology & Biotechnological Equipment*, Taylor & Francis, v. 26, p. 3286–3291, 2012. Disponível em: <https://doi.org/10.5504/BBEQ.2012.0069>.

APOSTOLIDIS, A. J.; MOYER, A. P.; BERIS, A. N. Non-newtonian effects in simulations of coronary arterial blood flow. *Journal of Non-Newtonian Fluid Mechanics*, v. 233, p. 155–165, 2016. Disponível em: <https://doi.org/10.1016/j.jnnfm.2016.03.008>.

ASCHER, U. M.; PETZOLD, L. R. *Computer methods for ordinary differential equations and differential-algebraic equations*. SIAM, 1998. Disponível em: <https://books.google.com.br/books/about/Computer_Methods_for_Ordinary_Differenti.html?id=2iXovtfcL74C&redir_esc=y>.

ATTINGER, D. et al. Fluid dynamics topics in bloodstain pattern analysis: Comparative review and research opportunities. *Forensic science international*, Elsevier, v. 231, n. 1-3, p. 375–396, 2013. Disponível em: <https://doi.org/10.1016/j.forsciint.2013.04.018>.

BACON, F. *The Works of Francis Bacon*. Cambridge University Press, 2011. Disponível em: <https://doi.org/10.1017/CBO9781139149549.019>.

BADALASSI, V.; CENICEROS, H.; BANERJEE, S. Computation of multiphase systems with phase field models. *Journal of Computational Physics*, Elsevier, v. 190, n. 2, p. 371–397, 2003. Disponível em: <https://doi.org/10.1016/S0021-9991(03)00280-8>.

BAI, F. peng; YANG, Z. hua; ZHOU, W. gang. Study of total variation diminishing (tvd) slope limiters in dambreak flow simulation. *Water Science and Engineering*, v. 11, n. 1, p. 68–74, 2018. ISSN 1674-2370. Disponível em: <https://doi.org/10.1016/j.wse.2017.09.004>.

BAIER, R. et al. Human platelet spreading on substrata of known surface chemistry. *Journal of biomedical materials research*, Wiley Online Library, v. 19, n. 9, p. 1157–1167, 1985. Disponível em: <https://doi.org/10.1002/jbm.820190922>.

BARNES, H. A. *A handbook of elementary rheology*. University of Wales, Institute of Non-Newtonian Fluid Mechanics, 2000. Disponível em: <https://books.google.com.br/books/about/A_Handbook_of_Elementary_Rheology.html?id=zBYvAQAAIAAJ&redir_esc=y>.

BASKURT, O. K.; MEISELMAN, H. J. Blood rheology and hemodynamics. In: COPYRIGHT© 2003 BY THIEME MEDICAL PUBLISHERS, INC., 333 SEVENTH AVENUE, NEW .... *Seminars in thrombosis and hemostasis*. 2003. v. 29, p. 435–450. Disponível em: <https://doi.org/10.1055/s-2003-44551>.

BATE, H. Blood viscosity at different shear rates in capillary tubes. *Biorheology*, v. 14, n. 5-6, p. 267–275, 1977. Disponível em: <https://doi.org/10.3233/bir-1977-145-607>.

BENABDELHALIM, H.; BRUTIN, D. Influence of the relative humidity on the blood drip stain formation on jeans fabrics. *Forensic Science International*, v. 350, p. 111808, 2023. ISSN 0379-0738. Disponível em: <https://doi.org/10.1016/j.forsciint.2023.111808>.

BEVEL, T.; GARNER, R. M. *Bloodstain Pattern Analysis: With an Introduction to Crime Scene Reconstruction*. CRC Press, 2008. 440 p. ISBN 9780429248870. Disponível em: <https://doi.org/10.1201/9781420052725>.

BILGI, C.; ATALIK, K. Effects of blood viscoelasticity on pulsatile hemodynamics in arterial aneurysms. *Journal of Non-Newtonian Fluid Mechanics*, Elsevier, v. 279, p. 104263, 2020. Disponível em: <https://doi.org/10.1016/j.jnnfm.2020.104263>.

BIRD, R. *Dynamics of Polymeric Liquids, Volume 1: Fluid Mechanics*. Wiley, 1987. (Dynamics of Polymeric Liquids). ISBN 9780471802457. Disponível em: <https://books.google.com.br/books?id=posvAQAAIAAJ>.

BIRD, R. B.; STEWART, W. E.; LIGHTFOOT, E. N. *Transport Phenomena*. [S.l.]: John Wiley & Sons, 1960. ISBN 9780471073925, 047107392X.

BLAIR, G. W. S. An equation for the flow of blood, plasma and serum through glass capillaries. *Nature*, v. 183, n. 4661, p. 613–614, 1959. Disponível em: <https://doi.org/10.1038/183613a0>.

BOYD, J.; BUICK, J. M.; GREEN, S. Analysis of the casson and carreau-yasuda non-newtonian blood models in steady and oscillatory flows using the lattice boltzmann method. *Physics of Fluids*, AIP Publishing, v. 19, 2007. Disponível em: <https://doi.org/10.1063/1.2772250>.

BRUST, M. et al. Rheology of human blood plasma: Viscoelastic versus newtonian behavior. *Physical review letters*, APS, v. 110, n. 7, p. 078305, 2013. Disponível em: <https://doi.org/10.1103/PhysRevLett.110.078305>.

BUCHANAN, J. et al. Hemodynamics simulation and identification of susceptible sites of atherosclerotic lesion formation in a model abdominal aorta. *Journal of biomechanics*, Elsevier, v. 36, p. 1185–1196, 2003. Disponível em: <https://doi.org/10.1016/s0021-9290(03)00088-5>.

CARREAU, P. J. *Ph.D. Thesis*. Tese (Doutorado) — University of Wisconsin, Madison, 1968. Disponível em: <https://search.library.wisc.edu/catalog/999638316602121>.

CARREAU, P. J.; KEE, D. C. D.; CHHABRA, R. P. *Rheology of Polymeric Systems: Principles and Applications*. Carl Hanser Verlag GmbH & Co KG, 2021. Disponível em: <https://doi.org/10.1016/C2018-0-01790-9>.

CASSON, N. Rheology of disperse systems. In: MILL, C. C. (Ed.). *Rheology of Disperse Systems*. New York, NY: Pergamon Press, 1959. p. 291–300.

CERQUEIRA, D. R. d. C. C. et al. Atlas da violência 2023. *Fórum Brasileiro de Segurança Pública*, Instituto de Pesquisa Econômica Aplicada (Ipea), 2023. Disponível em: <https://dx.doi.org/10.38116/riatlasdaviolencia2023>.

CHAI, Z. et al. Multiple-relaxation-time lattice boltzmann model for generalized newtonian fluid flows. *Journal of Non-Newtonian Fluid Mechanics*, v. 166, p. 332–342, 2011. ISSN 0377-0257. Disponível em: <https://doi.org/10.1016/j.jnnfm.2011.01.002>.

CHALMERS, A. F. *What Is This Thing Called Science?* Indianapolis: Hackett Publishing Company, 1999. ISBN 0-87220-453-7.

CHANDRAN, K. et al. Numerical simulation of blood flow modeled as a fluid-particulate mixture. *Journal of Non-Newtonian Fluid Mechanics*, Elsevier, v. 285, p. 104383, 2020. Disponível em: <https://doi.org/10.1016/j.jnnfm.2020.104383>.

CHARM, S.; KURLAND, G. Viscometry of human blood for shear rates of 0-100,000 sec^{-1}. *Nature*, v. 206, n. 4984, p. 617–618, 1965. Disponível em: <https://doi.org/10.1038/206617a0>.

CHARM, S. E.; KURLAND, G. S. Blood rheology. In: BERGEL, D. H. (Ed.). *Cardiovascular Fluid Dynamics, Vol. 2*. London: Academic Press, 1972. cap. 15, p. 157–203. Disponível em: <https://www.librarysearch.manchester.ac.uk/discovery/fulldisplay/alma9930594644401631/44MAN_INST:MU_NUI>.

CHHABRA, R. P.; RICHARDSON, J. F. *Non-Newtonian flow and applied rheology: engineering applications*. Butterworth-Heinemann, 2011. Disponível em: <https://doi.org/10.1016/B978-0-7506-8532-0.X0001-7>.

CHIEN, S. Shear dependence of effective cell volume as a determinant of blood viscosity. *Science*, v. 168, n. 3934, p. 977–979, 1970. Disponível em: <https://doi.org/10.1126/science.168.3934.977>.

CHIEN, S. Biophysical behavior of red cells in suspensions. *The red blood cell*, Academic New York, v. 2, p. 1031–1133, 1975. Disponível em: <https://doi.org/10.1016/B978-0-12-677202-9.50019-8>.

CHIEN, S. Physiological and pathophysiological significance of hemorheology. In: *Clinical Hemorheology: Applications in Cardiovascular and Hematological Disease, Diabetes, Surgery and Gynecology*. Springer, 1987. p. 125–164. Disponível em: <https://doi.org/10.1007/978-94-009-4285-1_5>.

CHIEN, S. et al. Viscoelastic properties of human blood and red cell suspensions. *Biorheology*, IOS Press, v. 12, n. 6, p. 341–346, 1975. Disponível em: <https://doi.org/10.3233/bir-1975-12603>.

CHIEN, S. et al. Effects of hematocrit and plasma proteins on human blood rheology at low shear rates. *Journal of applied physiology*, v. 21, n. 1, p. 81–87, 1966. Disponível em: <https://doi.org/10.1152/jappl.1966.21.1.81>.

CHO, Y.; KENSEY, K. *Effects of the non-Newtonian viscosity of blood on hemodynamics of diseased arterial flows*. [S.l.]: Prat, 1989. v. 1.

CHO, Y. I.; KENSEY, K. R. Effects of the non-newtonian viscosity of blood on flows in a diseased arterial vessel. part 1: Steady flows. *Biorheology*, IOS Press, v. 28, p. 241–262, 1991. Disponível em: <https://doi.org/10.3233/bir-1991-283-415>.

CHORIN, A. J. Numerical solution of the navier-stokes equations. *Mathematics of Computation*, American Mathematical Society, v. 22, n. 104, p. 745–762, October 1968. Disponível em: <https://www.jstor.org/stable/2004575>.

COKELET, G. R. et al. The rheology of human blood—measurement near and at zero shear rate. *Transactions of the Society of Rheology*, v. 7, n. 1, p. 303–317, 1963. Disponível em: <https://doi.org/10.1122/1.548959>.

CROSS, M. M. Rheology of non-newtonian fluids: a new flow equation for pseudoplastic systems. *Journal of colloid science*, Elsevier, v. 20, p. 417–437, 1965. Disponível em: <https://doi.org/10.1016/0095-8522(65)90022-X>.

DAVIES, P. et al. Effects of non-newtonian fluid behavior on wall shear in a separated flow region. *First World Congress of Biomechanics*, v. 1, p. 301, 1990.

DEEN, N. G.; ANNALAND, M. van S.; KUIPERS, J. Direct numerical simulation of complex multi-fluid flows using a combined front tracking and immersed boundary method. *Chemical Engineering Science*, v. 64, p. 2186–2201, 2009. ISSN 0009-2509. Disponível em: <https://doi.org/10.1016/j.ces.2009.01.029>.

DUAN, G. et al. Stable multiphase moving particle semi-implicit method for incompressible interfacial flow. *Computer Methods in Applied Mechanics and Engineering*, v. 318, p. 636–666, 2017. ISSN 0045-7825. Disponível em: <https://doi.org/10.1016/j.cma.2017.01.002>.

ECKER, P. et al. Animal blood in translational research: How to adjust animal blood viscosity to the human standard. *Physiological Reports*, Wiley Online Library, v. 9, p. e14880, 2021. Disponível em: <https://doi.org/10.14814/phy2.14880>.

ECKMANN, D. M. et al. Hematocrit, volume expander, temperature, and shear rate effects on blood viscosity. *Anesthesia & Analgesia*, LWW, v. 91, p. 539–545, 2000. Disponível em: <https://doi.org/10.1097/00000539-200009000-00007>.

ETHIER, C. R.; SIMMONS, C. A. *Introductory biomechanics: from cells to organisms*. Cambridge University Press, 2007. Disponível em: <https://doi.org/10.1017/CBO9780511809217>.

FÅHRAEUS, R. The suspension stability of the blood. *Physiological reviews*, v. 9, n. 2, p. 241–274, 1929. Disponível em: <https://doi.org/10.1152/physrev.1929.9.2.241>.

FOSSUM, E. et al. Whole blood viscosity, blood pressure and cardiovascular risk factors in healthy blood donors. *Blood pressure*, Taylor & Francis, v. 6, p. 161–165, 1997. Disponível em: <https://doi.org/10.3109/08037059709061932>.

GHIA, U.; GHIA, K.; SHIN, C. High-re solutions for incompressible flow using the navier-stokes equations and a multigrid method. *Journal of Computational Physics*, v. 48, p. 387–411, 1982. ISSN 0021-9991. Disponível em: <https://doi.org/10.1016/0021-9991(82)90058-4>.

GREER, J. P. et al. *Wintrobe's Clinical Hematology*. 14th. ed. Wolters Kluwer, 2019. Disponível em: <https://mayoclinic.elsevierpure.com/en/publications/wintrobes-clinical-hematology-fourteenth-edition>.

HALLMARK, B.; CHEN, C.-H.; DAVIDSON, J. Experimental and simulation studies of the shape and motion of an air bubble contained in a highly viscous liquid flowing through an orifice constriction. *Chemical Engineering Science*, v. 206, p. 272–288, 2019. ISSN 0009-2509. Disponível em: <https://doi.org/10.1016/j.ces.2019.04.043>.

HAN, J.; TRYGGVASON, G. Secondary breakup of axisymmetric liquid drops. ii. impulsive acceleration. *Physics of Fluids*, v. 13, p. 1554–1565, 2001. Disponível em: <https://doi.org/10.1063/1.1370389>.

HARLOW, F. H.; WELCH, J. E. Numerical calculation of time-dependent viscous incompressible flow of fluid with free surface. *Phys. Fluids*, v. 8, p. 2182–2189, 1965. Disponível em: <https://doi.org/10.1063/1.1761178>.

HARTEN, A. High resolution schemes for hyperbolic conservation laws. *Journal of Computational Physics*, v. 49, n. 3, p. 357–393, 1983. ISSN 0021-9991. Disponível em: <https://doi.org/10.1016/0021-9991(83)90136-5>.

HAUSER, E. A. et al. The application of the high-speed motion picture camera to research on the surface tension of liquids. *The Journal of Physical Chemistry*, v. 40, n. 8, p. 973–988, 1935. Disponível em: <https://doi.org/10.1021/j150377a003>.

HERSCHEL, W. H.; BULKLEY, R. Konsistenzmessungen von gummi-benzollösungen. *Kolloid-Zeitschrift*, Springer, v. 39, p. 291–300, 1926. Disponível em: <https://doi.org/10.1007/BF01432034>.

HINZE, J. O. Critical speeds and sizes of liquid globules. *Flow, Turbulence and Combustion*, v. 1, n. 1, 1949. Disponível em: <https://doi.org/10.1007/bf02120335>.

HINZE, J. O. Fundamentals of the hydrodynamic mechanism of splitting in dispersion processes. *AIChE J.*, v. 1, n. 3, p. 289–295, 1955. Disponível em: <https://doi.org/10.1002/aic.690010303>.

HORNER, J. S. et al. Investigation of blood rheology under steady and unidirectional large amplitude oscillatory shear. *Journal of Rheology*, AIP Publishing, v. 62, n. 2, p. 577–591, 2018. Disponível em: <https://doi.org/10.1122/1.5017623>.

HORNER, J. S.; WAGNER, N. J.; BERIS, A. N. A comparative study of blood rheology across species. *Soft Matter*, Royal Society of Chemistry, v. 17, p. 4766–4774, 2021. Disponível em: <https://doi.org/10.1039/D1SM00258A>.

HSIANG, L.-P.; FAETH, G. Drop deformation and breakup due to shock wave and steady disturbances. *International Journal of Multiphase Flow*, v. 21, n. 4, p. 545–560, 1995. ISSN 0301-9322. Disponível em: <https://doi.org/10.1016/0301-9322(94)00095-2>.

HULSE-SMITH, L.; MEHDIZADEH, N. Z.; CHANDRA, S. Deducing drop size and impact velocity from circular bloodstains. *Journal of Forensic Sciences*, ASTM International, v. 50, n. 1, p. JFS2003224, 2005. Disponível em: <https://doi.org/10.1520/JFS2003224>.

HUSSAIN, M. A.; KAR, S.; PUNIYANI, R. R. Relationship between power law coefficients and major blood constituents affecting the whole blood viscosity. *Journal of Biosciences*, Springer, v. 24, p. 329–337, 1999. Disponível em: <https://doi.org/10.1007/BF02941247>.

IABPA. 2023 annual iabpa conference. In: INTERNATIONAL ASSOCIATION OF BLOODSTAIN PATTERN ANALYSTS. *Proceedings of the 2023 Annual IABPA Conference*. Baltimore, MD, USA, 2023. Disponível em: <https://www.iabpa.org/>.

JABER, A.; VAYRON, R.; HARMAND, S. Effect of temperature on evaporation dynamics of sheep's blood droplets and topographic analysis of induced patterns. *Heliyon*, Elsevier, v. 8, n. 7, p. e11258, 2022. Disponível em: <https://doi.org/10.1016/j.heliyon.2022.e11258>.

JAIN, S. et al. Secondary breakup of drops at moderate weber numbers: Effect of density ratio and reynolds number. *International Journal of Multiphase Flow*, v. 117, p. 25–41, 2019. Disponível em: <https://doi.org/10.1016/j.ijmultiphaseflow.2019.04.026>.

JAMES, S. H.; KISH, P. E.; SUTTON, T. P. *Principles of Bloodstain Pattern Analysis: Theory and Practice*. 2nd. ed. Boca Raton, FL: CRC Press, 2005. Disponível em: <https://doi.org/10.1201/9781420039467>.

KANT, K.; BANERJEE, R. Effect of density ratios on droplet breakup for newtonian and power-law fluids. *International Journal of Multiphase Flow*, v. 167, p. 104561, 2023. ISSN 0301-9322. Disponível em: <https://doi.org/10.1016/j.ijmultiphaseflow.2023.104561>.

KARIMI, S. et al. Effect of rheological models on the hemodynamics within human aorta: Cfd study on ct image-based geometry. *Journal of Non-Newtonian Fluid Mechanics*, v. 207, p. 42–52, 2014. ISSN 0377-0257. Disponível em: <https://doi.org/10.1016/j.jnnfm.2014.03.007>.

KIELY, T. F. *Forensic Evidence: Science and the Criminal Law*. 2nd. ed. CRC Press, 2005. 536 p. ISBN ISBN 13: 9780849328589. Disponível em: <https://doi.org/10.1201/9781420038064>.

KOLBASOV, A. et al. Blood rheology in shear and uniaxial elongation. *Rheologica Acta*, Springer, v. 55, p. 901–908, 2016. Disponível em: <https://doi.org/10.1007/s00397-016-0964-1>.

KUHN, T. S. *The Structure of Scientific Revolutions*. 3rd. ed. Chicago: University of Chicago Press, 1996. ISBN 0-226-45807-5. Disponível em: <https://doi.org/10.7208/chicago/9780226458106.001.0001>.

KéKESI, T.; AMBERG, G.; WITTBERG, L. P. Drop deformation and breakup. *International Journal of Multiphase Flow*, v. 66, p. 1–10, 2014. ISSN 0301-9322. Disponível em: <https://doi.org/10.1016/j.ijmultiphaseflow.2014.06.006>.

LABER, T. L.; EPSTEIN, B. P.; TAYLOR, M. C. *High Speed Digital Video Analysis of Bloodstain Pattern Formation from Common Bloodletting Mechanisms*. [S.l.], 2006. Disponível em: <https://bit.ly/highspeedvideo>.

LANE, W. R. Shatter of drops in streams of air. *Industrial & Engineering Chemistry*, v. 43, n. 6, p. 1312–1317, 1951. Disponível em: <https://doi.org/10.1021/ie50498a022>.

LARKIN, B. A.; BANKS, C. E. Exploring the applicability of equine blood to bloodstain pattern analysis. *Medicine, Science and the Law*, SAGE Publications Sage UK: London, England, v. 56, n. 3, p. 190–199, 2016. Disponível em: <https://doi.org/10.1177/0025802414542456>.

LAUDAN, L. *Progress and Its Problems: Toward a Theory of Scientific Growth*. Berkeley: University of California Press, 1978. Disponível em: <https://doi.org/10.2307/2184465>.

LEE, S.-Y. et al. Study on development of forensic blood substitute: focusing on bloodstain pattern analysis. *Forensic Science International*, Elsevier, v. 316, p. 110461, 2020. Disponível em: <https://doi.org/10.1016/j.forsciint.2020.110461>.

LEFEBVRE, A. H.; MCDONELL, V. G. *Atomization and Sprays*. 2nd. ed. Boca Raton: CRC Press, 2017. ISBN 978-1498736251. Disponível em: <https://doi.org/10.1201/9781315120911>.

LENARD, P. Raindrops terminal velocity measurements. *Meteor. Zs.*, v. 21, p. 249, 1904.

LIEPSCH, D.; MORAVEC, S. Pulsatile flow of non-newtonian fluid in distensible models of human arteries. *Biorheology*, IOS Press, v. 21, p. 571–586, 1984. Disponível em: <https://doi.org/10.3233/bir-1984-21416>.

LOU, Z.; YANG, W.-J. A computer simulation of the non-newtonian blood flow at the aortic bifurcation. *Journal of biomechanics*, Elsevier, v. 26, n. 1, p. 37–49, 1993. Disponível em: <https://doi.org/10.1016/0021-9290(93)90611-H>.

LOWE, G. D. O. *Clinical Blood Rheology: Volume 2*. Boca Raton, FL: CRC Press, 1988. v. 1. Disponível em: <https://doi.org/10.1201/9780429261183>.

MACDONELL, H. et al. *Flight Characteristics and Stain Patterns of Human Blood*. U.S. Department of Justice, Law Enforcement Assistance Administration [and the] National Institute of Law Enforcement and Criminal Justice, 1971. Disponível em: <https://books.google.com.br/books?id=O54KMgEACAAJ>.

MACDONELL, H. L. Bloodstain pattern interpretation. In: ______. *Wiley Encyclopedia of Forensic Science*. John Wiley & Sons, Ltd, 2009. p. 37. ISBN 9780470061589. Disponível em: <https://doi.org/10.1002/9780470061589.fsa066>.

MACOSKO, C. *Rheology: Principles, Measurements, and Applications*. VCH, 1994. (Advances in interfacial engineering series). ISBN 9781560815792. Disponível em: <https://books.google.com.br/books?id=XXspAQAAMAAJ>.

MALISKA, C. R. *Fundamentals of Computational Fluid Dynamics: The Finite Volume Method*. Springer, 2023. v. 135. (Fluid Mechanics and Its Applications, v. 135). Disponível em: <https://doi.org/10.1007/978-3-031-18235-8>.

MALKIN, A. I. *Rheology Fundamentals*. ChemTec Piblishing, 1994. (Fundamental Topics in Rheology). ISBN 1-895198-09-7. Disponível em: <https://books.google.com.br/books/about/Rheology_Fundamentals.html?id=NZFpZuoP2kkC&redir_esc=y>.

MCCUAIG, K. et al. Simulation of blood flow in microgravity. *The American journal of surgery*, Elsevier, v. 164, n. 2, p. 119–123, 1992. Disponível em: <https://doi.org/10.1016/s0002-9610(05)80368-x>.

MERRILL, E. W. Rheology of blood. *Physiological Reviews*, v. 49, n. 4, p. 863–888, 1969. Disponível em: <https://doi.org/10.1152/physrev.1969.49.4.863>.

MERRILL, E. W. et al. Blood rheology: Effect of fibrinogen deduced by addition. *Circulation Research*, v. 18, n. 4, p. 437–446, 1966. Disponível em: <https://doi.org/10.1161/01.RES.18.4.437>.

NEOFYTOU, P. A 3rd order upwind finite volume method for generalised newtonian fluid flows. *Advances in Engineering Software*, Elsevier, v. 36, n. 10, p. 664–680, 2005. Disponível em: <https://doi.org/10.1016/j.advengsoft.2005.03.011>.

NISCO, G. D. et al. Modelling blood flow in coronary arteries: Newtonian or shear-thinning non-newtonian rheology? *Computer Methods and Programs in Biomedicine*, Elsevier, v. 242, p. 107823, 2023. Disponível em: <https://doi.org/10.1016/j.cmpb.2023.107823>.

OSTWALD, W. Kolloid-z., 36, 99-117 (1925); a. de waele. *Oil Color Chem. Assoc. J*, v. 6, p. 33–88, 1923.

PALMER, J. F. *The Works of John Hunter, F.R.S.* Cambridge University Press, 2015. v. 3. Disponível em: <https://doi.org/10.1017/CBO9781316034804>.

PAPANASTASIOU, T.; BOUDOUVIS, A. Flows of viscoplastic materials: models and computations. *Computers & Structures*, Elsevier, v. 64, n. 1-4, p. 677–694, 1997. Disponível em: <https://doi.org/10.1016/S0045-7949(96)00167-8>.

PAPANASTASIOU, T. C. Flows of materials with yield. *Journal of rheology*, The Society of Rheology, v. 31, n. 5, p. 385–404, 1987. Disponível em: <https://doi.org/10.1122/1.549926>.

PEDRIZZETTI, G. et al. *Fluid Mechanics for Cardiovascular Engineering*. Springer, 2022. Disponível em: <https://doi.org/10.1007/978-3-030-85943-5>.

PEDRIZZETTI, G.; PERKTOLD, K. *Cardiovascular fluid mechanics*. Springer, 2003. Disponível em: <https://doi.org/10.1007/978-3-7091-2542-7>.

PERKTOLD, K.; RAPPITSCH, R. B.; GRASSER, F. A. P. T. A. Computer simulation of local blood flow and vessel mechanics in a compliant carotid artery bifurcation model. *Journal of Biomechanics*, 1998. Disponível em: <https://doi.org/10.1016/0021-9290(95)95273-8>.

PICART, C. et al. Human blood shear yield stress and its hematocrit dependence. *Journal of Rheology*, The Society of Rheology, v. 42, n. 1, p. 1–12, 1998. Disponível em: <https://doi.org/10.1122/1.550883>.

POPEL, A.; ENDEN, G. An analytical solution for steady flow of a quemada fluid in a circular tube. *Rheologica acta*, Springer, v. 32, p. 422–426, 1993. Disponível em: <https://doi.org/10.1007/BF00435088>.

POPPER, K. *The Logic of Scientific Discovery*. New York: Basic Books, 1959. Disponível em: <https://doi.org/10.4324/9780203994627>.

POWELL, R. E.; EYRING, H. Mechanisms for the relaxation theory of viscosity. *nature*, Nature Publishing Group UK London, v. 154, p. 427–428, 1944. Disponível em: <https://doi.org/10.1038/154427a0>.

QUEIROZ, A. et al. The interaction of blood proteins with alpha alumina. *Brazilian journal of medical and biological research*, 2014. Disponível em: <https://repositorio-api.ipen.br/server/api/core/bitstreams/9e0737a8-0e51-48e6-b45a-a4bea0493780/content>.

QUEMADA, D. Rheology of concentrated disperse systems iii. general features of the proposed non-newtonian model. comparison with experimental data. *Rheologica Acta*, Springer, v. 17, n. 6, p. 643–653, 1978. Disponível em: <https://doi.org/10.1007/BF01522037>.

RAND, P. W. et al. Viscosity of normal human blood under normothermic and hypothermic conditions. *Journal of Applied Physiology*, v. 19, n. 1, p. 117–122, 1964. Disponível em: <https://doi.org/10.1152/jappl.1964.19.1.117>.

RAO, M. A. *Rheology of fluid and semisolid foods: principles and applications.* Aspen Publishers, Inc., 1999. 441 p. ISBN 0-8342-1264-1. Disponível em: <https://doi.org/10.1007/978-0-387-70930-7>.

RAYMOND, M.; SMITH, E.; LIESEGANG, J. The physical properties of blood–forensic considerations. *Science & justice: journal of the Forensic Science Society*, v. 36, n. 3, p. 153–160, 1996. Disponível em: <https://doi.org/10.1016/S1355-0306(96)72590-X>.

RONCO, C. et al. Blood and dialysate flow distributions in hollow-fiber hemodialyzers analyzed by computerized helical scanning technique. *Journal of the American Society of Nephrology*, LWW, v. 13, n. suppl_1, p. S53–S61, 2002. Disponível em: <https://doi.org/10.1681/ASN.V13suppl_1s53>.

ROSINA, J. et al. Temperature dependence of blood surface tension. *Physiological Research*, v. 56, n. 1, p. S93, 2007. Disponível em: <https://doi.org/10.33549/physiolres.931306>.

SHAO, C.; LUO, K.; FAN, J. Detailed numerical simulation of unsteady drag coefficient of deformable droplet. *Chemical Engineering Journal*, v. 308, p. 619–631, 2017. Disponível em: <https://doi.org/10.1016/j.cej.2016.09.062>.

SHATEYI, S.; MUZARA, H. On numerical analysis of carreau–yasuda nanofluid flow over a non-linearly stretching sheet under viscous dissipation and chemical reaction effects. *Mathematics*, MDPI, v. 8, n. 7, p. 1148, 2020. Disponível em: <https://doi.org/10.3390/math8071148>.

SHIBESHI, S. S.; COLLINS, W. E. The rheology of blood flow in a branched arterial system. *Applied rheology*, Sciendo, v. 15, p. 398–405, 2005. Disponível em: <https://doi.org/10.1901/jaba.2005.15-398>.

SIAUW, W.; NG, E.; MAZUMDAR, J. Unsteady stenosis flow prediction: a comparative study of non-newtonian models with operator splitting scheme. *Medical Engineering & Physics*, v. 22, p. 265–277, 2000. ISSN 1350-4533. Disponível em: <https://doi.org/10.1016/S1350-4533(00)00036-9>.

SILVA, T.; BASTOS, V.; OLIVEIRA, F. Mendes de. Perícia criminal e a legislação brasileira. *Revista Brasileira de Criminologia*, Revista Brasileira de Criminalística, v. 11, n. 2, p. 14–23, 2022. ISSN 2237-9223. Disponível em: <https://doi.org/10.15260/rbc.v11i2.415>.

SKIADOPOULOS, A.; NEOFYTOU, P.; HOUSIADAS, C. Comparison of blood rheological models in patient specific cardiovascular system simulations. *Journal of Hydrodynamics*, Springer, v. 29, n. 2, p. 293–304, 2017. Disponível em: <https://doi.org/10.1016/S1001-6058(16)60739-4>.

STEFFAN, H. et al. Comparison of newtonian and non-newtonian blood flow in stenotic vessels using numerical simulation. In: SPRINGER. *Biofluid Mechanics: Blood Flow in Large Vessels*. 1990. p. 479–485. Disponível em: <https://doi.org/10.1007/978-3-642-52338-0_61>.

STOKES, G. G. On the theories of the internal friction of fluids in motion, and of the equilibrium and motion of elastic solids. *Mathematical and Physical Papers*, Vol.1, p. 75–129, 1845. Disponível em: <https://doi.org/10.1017/cbo9780511702242.005>.

STONE, H.; JR, H. T.; SCHMIDT-NIELSEN, K. Influence of erythrocytes on blood viscosity. *American Journal of Physiology-Legacy Content*, American Physiological Society, v. 214, p. 913–918, 1968. Disponível em: <https://doi.org/10.1152/ajplegacy.1968.214.4.913>.

THURSTON, G. B. Viscoelasticity of human blood. *Biophysical journal*, Elsevier, v. 12, n. 9, p. 1205–1217, 1972. Disponível em: <https://doi.org/10.1016/S0006-3495(72)86156-3>.

TIAN, F.-B.; BHARTI, R.; XU, Y.-q. Deforming-spatial-domain/stabilized space–time (dsd/sst) method in computation of non-newtonian fluid flow and heat transfer with moving boundaries. *Computational Mechanics*, v. 53, p. 257–271, 02 2014. Disponível em: <https://doi.org/10.1007/s00466-013-0905-0>.

TRUDNOWSKI, R. J.; RICO, R. C. Specific gravity of blood and plasma at 4 and 37 c. *Clinical chemistry*, Oxford University Press, v. 20, n. 5, p. 615–616, 1974. Disponível em: <https://doi.org/10.1093/clinchem/20.5.615>.

TRYGGVASON, G.; SCARDOVELLI, R.; ZALESKI, S. *Direct numerical simulations of gas–liquid multiphase flows*. Cambridge university press, 2011. Disponível em: <https://doi.org/10.1017/CBO9780511975264>.

VILLAR, M. M. *Análise numérica detalhada de escoamentos multifásicos bidimensionais*. Tese (Tese) — Universidade Federal de Uberlândia, 2007. Disponível em: <https://repositorio.ufu.br/handle/123456789/14664>.

WADHWA, A.; MAGI, V.; ABRAHAM, J. Transient deformation and drag of decelerating drops in axisymmetric flows. *Physics of Fluids*, v. 19, 2007. Disponível em: <https://doi.org/10.1063/1.2800038>.

WALBURN, F. J.; SCHNECK, D. J. A constitutive equation for whole human blood. *Biorheology*, IOS Press, v. 13, n. 3, p. 201–210, 1976. Disponível em: <https://doi.org/10.3233/bir-1976-13307>.

WANG, Y. et al. A decoupling multiple-relaxation-time lattice boltzmann flux solver for non-newtonian power-law fluid flows. *Journal of Non-Newtonian Fluid Mechanics*, v. 235, p. 20–28, 2016. ISSN 0377-0257. Disponível em: <https://doi.org/10.1016/j.jnnfm.2016.03.010>.

WEBER, A. R.; LEDNEV, I. K. Crime clock–analytical studies for approximating time since deposition of bloodstains. *Forensic Chemistry*, Elsevier, v. 19, p. 100248, 2020. Disponível em: <https://doi.org/10.1016/j.forc.2020.100248>.

WEDDELL, J. C. et al. Hemodynamic analysis in an idealized artery tree: differences in wall shear stress between newtonian and non-newtonian blood models. *PloS one*, Public Library of Science San Francisco, CA USA, v. 10, p. e0124575, 2015. Disponível em: <https://doi.org/10.1371/journal.pone.0124575>.

WHITE, F. M. *Viscous fluid flow*. 3th. ed. McGraw-Hill New York, 2006. Disponível em: <https://www.amazon.com/Viscous-Fluid-McGraw-Hill-Mechanical-Engineering/dp/007124493X>.

WINDBERGER, U. et al. Whole blood viscosity, plasma viscosity and erythrocyte aggregation in nine mammalian species: reference values and comparison of data. *Experimental physiology*, Wiley Online Library, v. 88, p. 431–440, 2003. Disponível em: <https://doi.org/10.1113/eph8802496>.

WINDBERGER, U. et al. Measurement of whole blood of different mammalian species in the oscillating shear field: Influence of erythrocyte aggregation. In: IOP PUBLISHING. *Journal of Physics: Conference Series*. 2017. v. 790, p. 012035. Disponível em: <https://doi.org/10.1088/1742-6596/790/1/012035>.

WINEK, C. L.; HENRY, D.; KIRKPATRICK, L. The influence of physical properties and lipid content of bile on the human blood/bile ethanol ratio. *Forensic Science International*, Elsevier, v. 22, n. 2-3, p. 171–178, 1983. Disponível em: <https://doi.org/10.1016/0379-0738(83)90010-5>.

YANG, W. et al. Influence of density ratio on the secondary atomization of liquid droplets under highly unstable conditions. *Fuel*, v. 174, p. 25–35, 2016. Disponível em: <https://doi.org/10.1016/j.fuel.2016.01.078>.

YAP, C. H.; SAIKRISHNAN, N.; YOGANATHAN, A. P. Experimental measurement of dynamic fluid shear stress on the ventricular surface of the aortic valve leaflet. *Biomechanics and modeling in mechanobiology*, Springer, v. 11, p. 231–244, 2012. Disponível em: <https://doi.org/10.1007/s10237-011-0306-2>.

YASUDA, K. *Ph.D. Thesis*. Tese (Doutorado) — Massachusetts Institute of Technology, Cambridge, 1979. Disponível em: <https://dspace.mit.edu/handle/1721.1/16043>.

ZAITSEV, S. et al. Investigation of dynamic surface tension of biological liquids for animal blood diagnostics. *Colloids and Surfaces A: Physicochemical and Engineering Aspects*, Elsevier, v. 384, n. 1-3, p. 170–176, 2011. Disponível em: <https://doi.org/10.1016/j.colsurfa.2011.02.009>.

ZHANG, J. *Multigrid Acceleration Techniques and Applications to the Numerical Solution of Partial Differential Equations*. Tese (Doutorado) — The George Washington University, Washington, D.C., USA, May 1997. Disponível em: <http://ftp.demec.ufpr.br/CFD/bibliografia/MULTIGRID/Zhang_disserta%C3%A7%C3%A3o_1997.pdf>.

13 Appendix A

13.1 Poiseuille flow continuous mathematical modeling

13.1.1 Newtonian fluid solution

According to Eq. 4.1, the mass balance in a system is given by:

$$\frac{D\rho}{Dt} + \rho\nabla \cdot \mathbf{u} = 0 \tag{13.1}$$

As the specific mass is constant (incompressible flow), the term $\partial\rho/\partial t$ is set to zero. Then:

$$\nabla \cdot \mathbf{u} = 0 \tag{13.2}$$

This leads to:

$$\frac{\partial\rho}{\partial t} + \rho\frac{\partial u}{\partial x} + \rho\frac{\partial v}{\partial y} + \rho\frac{\partial w}{\partial z} = 0 \tag{13.3}$$

Considering the initially stated assumptions, Eq. 13.3 reduces to:

$$\frac{\partial u}{\partial x} = 0 \tag{13.4}$$

which translates to there being no gradient, upon reaching the steady flow regime, of the horizontal component of velocity, u, in the horizontal flow direction, x.

The linear momentum balance is given by Eq. 4.29:

$$\rho\frac{Du_i}{Dt} = \rho\mathbf{g} - \nabla \mathrm{p} + \frac{\partial}{\partial x_i}\left[\mu\left(\frac{\partial u_i}{\partial x_j} + \frac{\partial u_j}{\partial x_i}\right) + \delta_{ij}\lambda\,\nabla \cdot u_i\right] \tag{13.5}$$

Expanding the axial component of Eq. 13.5, we have:

$$\begin{split}\rho\frac{Du}{Dt} = \rho g_x - \frac{d\mathrm{p}}{dx} + \frac{\partial}{\partial x}\left(2\mu\frac{\partial u}{\partial x} + \lambda\,\nabla \cdot u_i\right) + \frac{\partial}{\partial y}\left[\mu\left(\frac{\partial u}{\partial y} + \frac{\partial v}{\partial x}\right)\right] \\ + \frac{\partial}{\partial z}\left[\mu\left(\frac{\partial u}{\partial z} + \frac{\partial w}{\partial x}\right)\right]\end{split} \tag{13.6}$$

Again, considering the initially stated assumptions, Eq. 13.6 reduces to:

$$\frac{d\mathrm{p}}{dx} = \mu\,\frac{\partial^2 u}{\partial y^2} \tag{13.7}$$

Reorganizing the terms, we have:

$$\frac{\partial^2 u}{\partial y^2} = \frac{1}{\mu}\frac{d\mathrm{p}}{dx} \tag{13.8}$$

Letting $\frac{1}{\mu}\frac{d\mathrm{p}}{dx} = \varphi$, we get:

$$\frac{\partial^2 u}{\partial y^2} = \varphi \tag{13.9}$$

Integrating with respect to y, we get:

$$\frac{\partial u}{\partial y} = \varphi\, y + C_1 \tag{13.10}$$

As $\left.\frac{\partial u}{\partial y}\right|_{y=0} = 0$, then $C_1 = 0$. Hence:

$$\frac{\partial u}{\partial y} = \varphi\, y \tag{13.11}$$

Integrating once more, we get:

$$u(y) = \frac{\varphi\, y^2}{2} + C_2 \tag{13.12}$$

Applying the boundary condition $u(+h) = 0$, Eq. 13.12 reduces to:

$$0 = \frac{\varphi\, h^2}{2} + C_2 \tag{13.13}$$

which gives us $C_2 = -\frac{\varphi\, h^2}{2}$.

Therefore, returning to Eq. 13.12, we have:

$$u(y) = \frac{\varphi\, y^2}{2} - \frac{\varphi\, h^2}{2}$$

$$u(y) = \frac{\varphi\, h^2}{2}\left[\left(\frac{y}{h}\right)^2 - 1\right] \tag{13.14}$$

As the maximum velocity is reached at the center of the geometry, we have:

$$u(0) = V_{max} = -\frac{\varphi\, h^2}{2} \tag{13.15}$$

Thus, we can rearrange Eq. 13.14 as follows:

$$u(y) = V_{max}\left[1 - \left(\frac{y}{h}\right)^2\right] \tag{13.16}$$

For the calculation of the average flow velocity, we can integrate the found velocity, $u(y)$, over the cross-sectional area of the flow, as follows.

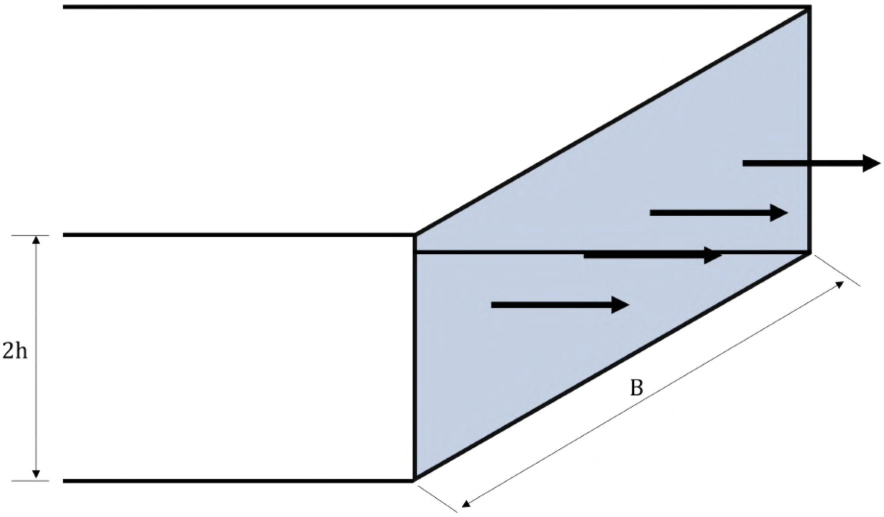

Figure 65 – Cross-sectional area of Poiseuille flow

Figure 65 illustrates - in blue - the cross-sectional area of the flow, through which the fluid flows in the direction indicated by the black arrows. The average flow velocity, when in steady state, can be represented by:

$$\overline{u} = \frac{1}{A_t} \int u \, dA_t \tag{13.17}$$

Substituting $A_t = B \cdot 2y$, $dA_t = B \cdot dy$, and substituting u by the relationship found in Eq. 13.16, we get:

$$\overline{u} = \frac{1}{B \cdot 2y} \int_{-h}^{h} V_{max} \left[1 - \left(\frac{y}{h} \right)^2 \right] B \, dy \tag{13.18}$$

Rearranging, we have:

$$\begin{aligned} \overline{u} &= \frac{V_{max}}{2\,h} \int_{-h}^{h} \left(1 - \frac{y^2}{h^2} \right) dy \\ &= \frac{V_{max}}{2\,h} \left[y \Big|_{-h}^{h} - \frac{1}{h^2} \left(\frac{y^3}{3} \Big|_{-h}^{h} \right) \right] \\ &= \frac{V_{max}}{2\,h} \left[2h - \frac{1}{h^2} \left(\frac{2h^3}{3} \right) \right] \\ &= \frac{V_{max}}{2\,h} \left(\frac{4h}{3} \right) \end{aligned} \tag{13.19}$$

Thus:

$$\overline{u} = \frac{2}{3} V_{max} \tag{13.20}$$

13.1.2 Non-newtonian fluid solution

Now, starting from Eq. 13.6, seeking a continuous solution for non-Newtonian fluid using the power-law model, we can no longer take the variable μ out of the divergence, replacing it with the constitutive equation of the power-law model below:

$$\eta = m\,\dot{\gamma}^{n-1} \tag{13.21}$$

which reduces Eq. 13.6 to:

$$\frac{d\mathrm{p}}{dx} = \frac{\partial}{\partial y}\left[m\left(\frac{du}{dy}\right)^{n-1} \cdot \frac{du}{dy}\right]$$

$$\frac{d\mathrm{p}}{dx} = m\left[\frac{\partial}{\partial y}\left(\frac{du}{dy}\right)^{n}\right] \tag{13.22}$$

Rearranging, we have:

$$\left[\frac{\partial}{\partial y}\left(\frac{du}{dy}\right)^{n}\right] = \frac{1}{m}\frac{d\mathrm{p}}{dx} \tag{13.23}$$

Integrating with respect to y, we get:

$$\left(\frac{du}{dy}\right)^{n} = \frac{1}{m}\,\frac{d\mathrm{p}}{dx}\,y + C_1 \tag{13.24}$$

Raising both sides to the power of $1/n$:

$$\frac{du}{dy} = \left[\frac{1}{m}\,\frac{d\mathrm{p}}{dx}\,y + C_1\right]^{1/n} \tag{13.25}$$

As $\left.\frac{\partial u}{\partial y}\right|_{y=0} = 0$, then $C_1 = 0$. Hence:

$$\frac{du}{dy} = \left[\frac{1}{m}\,\frac{d\mathrm{p}}{dx}\,y\right]^{1/n} \tag{13.26}$$

Making:

$$du = \left[\frac{1}{m}\,\frac{d\mathrm{p}}{dx}\right]^{1/n} \cdot y^{1/n}\,dy \tag{13.27}$$

Let $\left[\frac{1}{m}\,\frac{d\mathrm{p}}{dx}\right] = \lambda$, thus:

$$du = \lambda^{1/n} \cdot y^{1/n}\,dy \tag{13.28}$$

Integrating, we get:

$$u(y) = \lambda\,\frac{y^{\frac{1}{n}+1}}{\frac{1}{n}+1} = \frac{n\lambda}{n+1}\,y^{\frac{1}{n}+1} + C_2 \tag{13.29}$$

Applying the boundary condition $u(+h) = 0$, temos:

$$u(h) = 0 = \frac{n\lambda}{n+1}\, h^{\frac{1}{n}+1} + C_2 \tag{13.30}$$

which provides:

$$C_2 = -\frac{n\,\lambda\, h^{\frac{1}{n}+1}}{n+1} \tag{13.31}$$

Substituting into Eq. 13.29, we get:

$$u(y) = \frac{n\,\lambda}{n+1} y^{\frac{1}{n}+1} - \frac{n\,\lambda}{n+1}\, h^{\frac{1}{n}+1} \tag{13.32}$$

$$u(y) = \frac{n\,\lambda}{n+1}\, h^{\frac{1}{n}+1} \left[\left(\frac{y}{h}\right)^{\frac{1}{n}+1} - 1 \right] \tag{13.33}$$

The maximum velocity occurs at $u(0) = V_{\mathrm{max}}$:

$$u(0) = V_{max} = -\frac{n\,\lambda}{n+1} h^{\frac{1}{n}+1} \tag{13.34}$$

Thus:

$$u(y) = V_{max} \left[1 - \left(\frac{y}{h}\right)^{\frac{1}{n}+1} \right] \tag{13.35}$$

13.2 Transient Couette flow continuous mathematical modeling

13.2.1 Newtonian fluid solution

Starting from the linear momentum balance Eq. 4.29 and assuming the physical model considerations described in sec. 8.2.1, we arrive at the following ODE a be resolved:

$$\frac{\partial u}{\partial t} = \nu\, \frac{\partial^2 u}{\partial y^2} \tag{13.36}$$

or yet:

$$u_t = \nu\, u_{yy} \tag{13.37}$$

First, let's consider the following Laplace transform:

$$\mathscr{L}\left\{u(y,t)\right\} = U(y,s) \tag{13.38}$$

Applying the transform to the Eq. 13.37, we have:

$$\mathscr{L}\left\{u_t\right\} = \mathscr{L}\left\{\nu\, u_{yy}\right\} \tag{13.39}$$

which provides

$$s\,U(y,s) - u(y,0) = \nu \frac{\partial^2}{\partial y^2} \mathscr{L}\left\{u(y,t)\right\} \tag{13.40}$$

As $u(y,0) = 0$ (boundary condition), then:

$$s\,U(y,s) = \nu \frac{\partial^2}{\partial y^2} U(y,s) \tag{13.41}$$

Rearranging:

$$\nu \frac{\partial^2}{\partial y^2} U(y,s) - s\,U(y,s) = 0 \tag{13.42}$$

Now, the ODE of the Eq. 13.42 is a second-order homogeneous. Solving it, we have:

$$\nu\lambda^2 - s = 0 \tag{13.43}$$

Then:

$$\lambda = \pm\sqrt{\frac{s}{\nu}} \tag{13.44}$$

So the solution becomes:

$$U(y,s) = C_1\, e^{\sqrt{\frac{s}{\nu}}\, y} + C_2\, e^{-\sqrt{\frac{s}{\nu}}\, y} \tag{13.45}$$

Now, applying the Laplace transform to the boundary conditions, we have, in the first:

$$\mathscr{L}\left\{u(0,t)\right\} = U(0,s) \tag{13.46}$$

$$\mathscr{L}\left\{0\right\} = U(0,s)$$

$$0 = U(0,s)$$

which provides:

$$U(0,s) = 0 \tag{13.47}$$

The second boundary condition is:

$$\mathscr{L}\left\{u(h,t)\right\} = U(h,s) \tag{13.48}$$

$$\mathscr{L}\left\{V\right\} = U(h,s)$$

$$V\,\mathscr{L}\left\{1\right\} = U(h,s)$$

$$V\,\frac{1}{s} = U(h,s)$$

which provides

$$U(h,s) = \frac{V}{s} \tag{13.49}$$

Substituting the Eqs. 13.47 and 13.49 into 13.45, we have:

$$\begin{cases} U(0,s) = C_1 + C_2 = 0 \\ U(h,s) = C_1\, e^{\sqrt{\frac{s}{\nu}}\,h} + C_2\, e^{-\sqrt{\frac{s}{\nu}}\,h} = \frac{V}{s} \end{cases} \tag{13.50}$$

Solving C_1 and C_2, we have:

$$C_1 = \frac{V}{2s\sinh\left(\sqrt{\frac{s}{\nu}}h\right)} \tag{13.51}$$

$$C_2 = -\frac{V}{2s\sinh\left(\sqrt{\frac{s}{\nu}}h\right)} \tag{13.52}$$

Returning the Eqs. 13.51 and 13.52 into the Eq. 13.45, we have:

$$U(y,s) = \frac{V}{2s\sinh\left(\sqrt{\frac{s}{\nu}}\,h\right)}\left[e^{\sqrt{\frac{s}{\nu}}y} - e^{-\sqrt{\frac{s}{\nu}}y}\right] \tag{13.53}$$

Using the definition of hyperbolic sine, we adjust the previous equation to:

$$U(y,s) = \frac{V}{2s\sinh\left(\sqrt{\frac{s}{\nu}}\,h\right)}\left[2\,\sinh\left(\sqrt{\frac{s}{\nu}}y\right)\right] \tag{13.54}$$

Simplifying, we have:

$$U(y,s) = V\,\frac{\sinh\left(\sqrt{\frac{s}{\nu}}y\right)}{s\sinh\left(\sqrt{\frac{s}{\nu}}\,h\right)} \tag{13.55}$$

Making $a = \frac{y}{\sqrt{\nu}}$ and $b = \frac{h}{\sqrt{\nu}}$, we have:

$$U(y,s) = V\,\frac{\sinh\left(a\,\sqrt{s}\right)}{s\sinh\left(b\,\sqrt{s}\right)} \tag{13.56}$$

Now opening the hyperbolic terms, we have:

$$\frac{\sinh\left(a\,\sqrt{s}\right)}{s\sinh\left(b\,\sqrt{s}\right)} = \frac{e^{a\sqrt{s}} - e^{-a\sqrt{s}}}{s\,\left(e^{b\sqrt{s}} - e^{-b\sqrt{s}}\right)} \tag{13.57}$$

Multiplying both the numerator and denominator by $e^{-b\sqrt{s}}$, we have:

$$\frac{\sinh\left(a\,\sqrt{s}\right)}{s\sinh\left(b\,\sqrt{s}\right)} = \frac{e^{-b\sqrt{s}}\left(e^{a\sqrt{s}} - e^{-a\sqrt{s}}\right)}{s\,e^{-b\sqrt{s}}\left(e^{b\sqrt{s}} - e^{-b\sqrt{s}}\right)} = \frac{e^{(a-b)\sqrt{s}} - e^{-(a+b)\sqrt{s}}}{s\,\left(1 - e^{-2b\sqrt{s}}\right)} \tag{13.58}$$

Now matching the previous term with geometric series, we have:

$$\frac{1}{1-e^{-2b\sqrt{s}}}=\sum_{n=0}^{\infty}e^{-2bn\sqrt{s}} \tag{13.59}$$

So:

$$\frac{\sinh\left(a\sqrt{s}\right)}{s\sinh\left(b\sqrt{s}\right)}=\left(\sum_{n=0}^{\infty}e^{-2bn\sqrt{s}}\right)\cdot\left(\frac{e^{(a-b)\sqrt{s}}-e^{-(a+b)\sqrt{s}}}{s}\right) \tag{13.60}$$

Since the term outside the summation does not affect the summation itself (as it does not depend on the index n), we will include it within the summation:

$$\frac{\sinh\left(a\sqrt{s}\right)}{s\sinh\left(b\sqrt{s}\right)}=\sum_{n=0}^{\infty}\left[\frac{e^{(-2bn+a-b)\sqrt{s}}}{s}-\frac{e^{(-2bn-a-b)\sqrt{s}}}{s}\right] \tag{13.61}$$

With this, we can return to the Eq. 13.56, which is:

$$U(y,s)=V\sum_{n=0}^{\infty}\left[\frac{e^{(-2bn+a-b)\sqrt{s}}}{s}-\frac{e^{(-2bn-a-b)\sqrt{s}}}{s}\right] \tag{13.62}$$

Now, to obtain the function $u(y,t)$, we simply apply the inverse Laplace transform to $U(y,s)$:

$$u(y,t)=\mathscr{L}^{-1}\left\{U(y,s)\right\}=\mathscr{L}^{-1}\left\{V\sum_{n=0}^{\infty}\left[\frac{e^{(-2bn+a-b)\sqrt{s}}}{s}-\frac{e^{(-2bn-a-b)\sqrt{s}}}{s}\right]\right\}$$

$$u(y,t)=V\,\mathscr{L}^{-1}\left\{\sum_{n=0}^{\infty}\left[\frac{e^{(-2bn+a-b)\sqrt{s}}}{s}-\frac{e^{(-2bn-a-b)\sqrt{s}}}{s}\right]\right\} \tag{13.63}$$

which provides in the end:

$$u(y,t)=V\sum_{n=0}^{\infty}\left[\operatorname{erfc}\left(\frac{2bn-a+b}{2\sqrt{t}}\right)-\operatorname{erfc}\left(\frac{2bn+a+b}{2\sqrt{t}}\right)\right] \tag{13.64}$$

As $\operatorname{erfc}(x)=1-\operatorname{erf}(x)$, therefore:

$$u(y,t)=V\sum_{n=0}^{\infty}\left[\operatorname{erf}\left(\frac{2bn+a+b}{2\sqrt{t}}\right)-\operatorname{erf}\left(\frac{2bn-a+b}{2\sqrt{t}}\right)\right] \tag{13.65}$$

14 Appendix B

14.1 Introduction

The careful use of appropriate nomenclature in scientific discourse is paramount for ensuring precision, clarity, and effective communication. Terms that accurately reflect the physical reality of phenomena under study are essential for avoiding misunderstandings and misinterpretations. In fields such as engineering and physics, where complex interactions and precise measurements are routine, the correct terminology not only facilitates better comprehension but also promotes consistency in research and application.

Moreover, using nomenclature that faithfully represents physical concepts helps in standardizing scientific language across different disciplines and geographical regions. This standardization is crucial for the reproducibility of experiments and the validation of theoretical models. By adhering to terms that accurately describe the phenomena, researchers can more effectively communicate their findings, build upon each other's work, and advance the collective knowledge within the scientific community.

14.2 Relative specific mass *versus* specific gravity

The term **specific gravity** is widely used, especially in industrial and commercial contexts. However, this term is somewhat misleading, as it may suggest a direct relationship with gravitational force, which is not the case. Specific gravity refers to the ratio between the specific mass of a substance and the specific mass of a reference substance, typically water at $4\,^{\circ}\mathrm{C}$, where the specific mass is at its maximum and very close to $1,000\,\mathrm{kg/m^3}$.

In contrast, the term **relative specific mass** is more physically consistent and precise. This term highlights that we are dealing with a ratio of specific masses, eliminating any ambiguity associated with the erroneous interpretation of a relationship with gravity. Relative specific mass, defined as:

$$\text{Relative Specific Mass} = \frac{\rho_{\text{substance}}}{\rho_{\text{reference}}} \tag{14.1}$$

where $\rho_{\text{substance}}$ is the specific mass of the substance in question and $\rho_{\text{reference}}$ is the specific mass of the reference substance (usually water), clearly expresses the comparison between the specific masses of two substances.

Furthermore, the use of the term **relative specific mass** aligns with the nomenclature used in various international standards and technical norms, promoting uniformity in scientific and technical discourse. Adopting this term contributes to clearer communication and avoids confusion that may arise from imprecise terminology.

Therefore, it is strongly recommended to adopt the term **relative specific mass** in scientific and technical publications, as well as in educational environments, to ensure the precision and clarity necessary for scientific rigor.

14.3 Surface Tension x Interfacial Tension

Another common misnomer in this area is the use of the term **surface tension** instead of the more precise **interfacial tension**.

The term **surface tension** is often used to describe the force per unit length acting along the surface of a liquid in contact with another phase (typically a gas). While widely understood, this term is not entirely accurate when describing phenomena involving interfaces between two immiscible liquids or between a liquid and a solid. Surface tension primarily pertains to the interface between a liquid and a gas, and using it in other contexts can lead to misunderstandings.

Conversely, the term **interfacial tension** is more physically consistent and precise. Interfacial tension refers to the force per unit length existing at the interface between two different phases, which can be liquid-liquid, liquid-solid, or even liquid-gas. This term more accurately captures the complexities and nuances of interactions at various types of interfaces. Interfacial tension, defined as:

$$\text{Interfacial Tension} = \frac{F}{L}, \tag{14.2}$$

where F is the force acting along the interface and L is the length over which this force acts, provides a clear and unambiguous description of the force balance at the interface.

14.4 Yield-pseudoplastic *versus* yield-shear-thinning

And finally, the last commonly misused term in this field is **yield-pseudoplastic**, which should be replaced with the more physically consistent term **yield-shear-thinning**.

The term **yield-pseudoplastic** is often used to describe fluids that exhibit a yield stress followed by shear-thinning behavior. However, this term is somewhat misleading and less precise. Pseudoplasticity is a general term that denotes shear-thinning behavior without necessarily implying the presence of a yield stress. Therefore, using **yield-pseudoplastic** can cause confusion, as it does not clearly differentiate between simple shear-thinning fluids and those that exhibit both yield stress and shear-thinning characteristics.

On the other hand, the term **yield-shear-thinning** is more physically consistent and precise. This term accurately describes fluids that exhibit a yield stress (a threshold stress that must be exceeded before flow begins) and shear-thinning behavior (a decrease in viscosity with increasing shear rate) after yielding. Yield-shear-thinning fluids are characterized by a transition from a solid-like state to a fluid-like state upon the application of a stress greater than the yield stress, followed by a reduction in viscosity with further increases in shear rate. This term, defined as:

$$\text{Yield-shear-thinning} = \begin{cases} \tau < \tau_y & : \text{No flow} \\ \tau \geq \tau_y & : \text{Shear-thinning behavior} \end{cases} \tag{14.3}$$

where τ is the applied shear stress and τ_y is the yield stress, provides a clear and unambiguous description of the fluid's behavior.